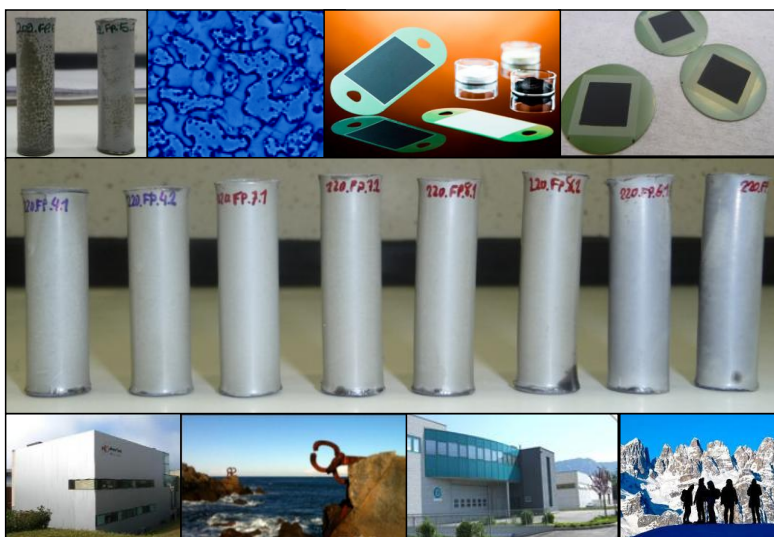




Stability studies of critical components in SOFC technologies

Amaia Arregui Buldain



April 2013

TITLE

STABILITY STUDIES OF CRITICAL COMPONENTS IN SOFC TECHNOLOGIES

Amaia Arregui

E-mail: amaia.arreguibuldain@unitn.it

Approved by:

PhD. Lide M. Rodriguez-Martinez,
Advisor
Energy Division
IK4-Ikerlan, Spain.

Prof. Vincenzo Maria Sglavo, Advisor
Department of Materials Engineering
and Industrial Technologies (DIMTI)
University of Trento, Italy.

Ph.D. Commission:

Prof. Gian Domenico Sorarù,
Department of Industrial Engineering
University of Trento, Italy.

Prof. Paolo Colombo,
Department of Mechanical Engineering
University of Padova, Italy.

Prof. Monica Ferraris,
Department of Applied Science and
Technology
Polytechnic University of Turin, Italy.

University of Trento,
Department of Materials Engineering and Industrial Technologies (DIMTI)

April 2013

**University of Trento - Department of Materials Engineering and
Industrial Technologies (DIMTI)**

Doctoral Thesis

Name - 2013

Published in Trento (Italy) – by University of Trento

ISBN: 978-88-8443-470-8

A la mémoire de Richard Kahn

*Ama, aita eta ahizpari
Paki eta Maxuxi Areson pasa genuen egunaz oroitzuz*

ABSTRACT

Solid Oxide Fuel Cells are highly efficient and clean energy conversion devices that during the last few decades have attracted increasingly interest of investors and governmental institutions. This emerging technology exhibits smart properties as compared to other type of fuel cells. Above all, characteristic fuel flexibility of SOFCs (i.e. hydrogen, carbon monoxide, methane) and the possibility to use high temperature exhaust gases for co-generation or hybrid applications are key factors for SOFC market introduction. In addition, at high temperature, non precious catalysts can be used, thus, reducing costs. In view of these merits, SOFCs applicability extends from distributed generation to auxiliary power units in transportation. More recently, SOFC miniaturization has opened a new way for its use also in portable applications.

Even if SOFCs demonstrated high electrochemical efficiencies and performances in a variety of cell configurations, cost and durability constraints have prevented SOFC commercialization up to now. The high operation temperature that SOFCs require, limits material selection fundamentally to metal oxides or ceramics. The earliest developed line at high temperatures (HT-SOFCs) is fully based on ceramic components (i.e. support, functional layers and interconnects). However, ceramics are expensive, susceptible to thermal gradients and very fragile under mechanical stress. Therefore, more recently developed efforts pursue to lowering operation to intermediate temperature (IT-SOFC), this allowing the use of widely adopted cheaper ferritic stainless steel as interconnect material. These steels are mechanically robust, exhibit matching TEC with cell components as well as an excellent thermal and electrical conductivity. Though anode-supported cell configuration with metal interconnects is the preferred design at intermediate temperature, an innovative metal-supported SOFC concept which uses similar ferritic stainless steels has been introduced in the SOFC field. Currently used ferritic stainless steels, whether as interconnect or metal-support, are chromia based ferritic alloys which form a protective chromia scale with good conductive properties in the surface of steel. This oxide layer is primordial but not sufficient to guarantee corrosion resistance and long life of the metal substrate.

Nevertheless, reactivity among cell materials and degradation is not completely eradicated at intermediate temperature. Chromium evaporation from ferritic components (i.e. interconnect or support) during fabrication and operation is especially harmful for the electrochemical performance of functional electrodes. According to the observed degradation, contact coating and diffusion barrier layers have been developed for both, oxidizing and reducing atmospheres, to block the chromium diffusion in the cathode and anode, respectively. Among the electrodes, it

is commonly accepted that limitations in the electrochemical performance and degradation during operation arise mainly at the cathode. Chromium evaporation is higher under oxidizing atmosphere and hence, Cr-poisoning is more severe in the cathode.

This thesis work was born as a collaboration project between two entities currently involved in the development and commercialization of IT-SOFC technology, IK4-Ikerlan and SOFCpower with a valuable contribution of Materials Department in the University of Trento and EPFL. IK4-Ikerlan, is a reference research institution in Spain which has largely invested in the development of metal-supported tubular SOFCs. SOFCpower, is a newly emerging Italian company currently involved in the research and commercialization of anode-supported IT-SOFC technology. Whereas IK4-Ikerlan has emphasized in the robustness through a metal-supported cell (MSC); SOFCpower, has prioritized electrochemical performance and, thus, it has adopted the anode-supported cell (ASC). Both centers pursue the final application of the SOFC product in the framework of domestic cogeneration.

In relation to degradation issues, cathode stability under operation is a general concern for IT-SOFC developers. In the first part of this thesis work, the stability of ferritic perovskite cathodes currently implemented at IK4-Ikerlan and SOFCpower (LSF-SDC and LSCF-GDC, respectively) was studied in a specific experimental DoE design. The influence of cathode processing and operation conditions together with intrinsic degradation mechanisms and extrinsic ones related to chromium poisoning and air humidification were analyzed in detail. Moreover, the effectiveness of two interconnect coating materials, MCO spinel and novel LNC perovskite against chromium poisoning of the cathode was studied. With this commitment, anode-supported half-cells manufactured by SOFCpower were used making profit of the verified high reproducibility of these cells.

In parallel, work at IK4-Ikerlan in tubular MSC technology demonstrated critical instability related to the operation under high fuel utilization and deficient diffusion barrier layer (DBL) implementation. This allowed element interdiffusion during the manufacturing process between the metal support and the anode. In the second part of this thesis work, a second generation (G2) of tubular MSCs based on an innovative DBL has been developed in all aspects. This includes processing parameters optimization and stability studies. During this work, an intrinsic variable degradation mechanism related to the DBL and manufacturing process of MSC turned out to be critical in G2 cells stability during operation. At this point, understanding such a mechanism and determining its origin became the most fascinating challenge of my investigation.

Overall, this thesis work focuses in the study of critical parameters in SOFCs stability. Factors affecting the stability of cell components over a wide range of operation conditions and degradation mechanisms related to the manufacturing process and operation are studied.

Table of contents

Abstract.....	5
---------------	---

Chapter I

Theoretical background/State of the art	12
1.1 Type of fuel cells.....	12
1.1.1 Low temperature Fuel Cells.....	12
1.1.2 High temperature Fuel Cells.....	13
1.2 Solid Oxide Fuels Cells	16
1.2.1 Basic principles.....	16
1.2.2 Open Circuit Voltage and Irreversibilities.....	17
1.2.3 Efficiency	19
1.2.4 SOFC targets.....	21
1.3 State of the art SOFC materials	21
1.3.1 Electrolytes	22
1.3.2 Anode	24
1.3.3 Cathode	25
1.3.4 Interconnector.....	28
1.4 SOFC designs	29
1.4.1 Planar design.....	31
1.4.2 Tubular design.....	33
1.5 Stability issues of IT-SOFCs	35
1.5.1 Degradation mechanisms of cell components	35
1.5.2 Implications of IT-SOFC metal components	37
1.6 Metal-supported SOFC overview	40
1.6.1 Technology and approach	40
1.6.2 Ceria-based MS-SOFC.....	41
1.6.3 YSZ-based MS-SOFC	41
1.6.4 Key problems and degradation mechanisms in current MSC concepts	42

Chapter II

Experimental techniques.....	50
2.1 Electrochemical characterization.....	50

2.1.1	Test furnaces	50
2.1.2	Air humidification	51
2.1.3	Fuel humidification	51
2.1.4	IV curves	52
2.1.5	Electrochemical Impedance Spectroscopy	53
2.2	<i>Microstructural characterization</i>	56
2.2.1	Scanning Electron Microscopy (SEM) and Energy Dispersive X-ray analysis (EDS)	56
2.2.2	X-ray Diffraction	58
2.3	<i>MSC fabrication and characterization</i>	59
2.3.1	Processing techniques and equipment	59
2.3.2	Processing characterization and equipment	66
Chapter III		
Cathode stability in anode-supported cells		70
3.1	<i>SOFCpower ASC-Technology</i>	70
3.1.1	Introduction	70
3.1.2	Anode-supported SOFC	72
3.2	<i>Ferritic cathodes stability study</i>	73
3.2.1	Introduction	73
3.2.2	Experimental procedure	74
3.2.3	Overview of cathode processing and operation parameters under analysis - Considerations on degradation	76
3.2.4	Design of experiments and durability tests	79
3.2.5	Degradation mechanisms	94
3.3	<i>Metal interconnect coatings against chromium poisoning</i>	105
3.3.1	Introduction	105
3.3.2	Experimental procedure	107
3.3.3	Analysis of results	108
3.3.4	Overall discussion and conclusions	114
3.4	<i>Appendix III</i>	116
	<i>Taguchi matrix</i>	116

Chapter IV

Metal-supported cell fabrication and operation	118
4.1 IK4-Ikerlan MSC-Technology.....	118
4.1.1 Introduction	118
4.1.2 Fabrication of tubular metal-supported SOFC	122
4.1.3 Differences between G1 and G2 cells	131
4.2 Second generation cells optimization	134
4.2.1 Introduction	134
4.2.2 Experimental set-up.....	134
4.2.3 Effect of sintering temperature and metal powder particle fraction	135
4.2.4 Diffusion barrier layer thickness.....	142
4.2.5 Optimization of electrochemically active electrodes	157
4.3 G2 cells degradation mechanisms during fabrication	164
4.3.1 Introduction	164
4.3.2 Stains identification.....	169
4.3.3 Titanium activation mechanisms.....	184
4.4 Robustness of second generation cells under operation ..	204
4.4.1 Thermal cycles.....	204
4.4.2 Redox tolerance.....	210
4.4.3 Performance and stability under fuel utilization	220

Chapter V

Conclusions and future perspectives	235
--	------------

List of abbreviation and acronyms	241
--	------------

References	244
-------------------------	------------

Scientific Production	260
------------------------------------	------------

Participation to Congresses, Schools and Workshops.....	261
--	------------

Other activities 262

Acknowledgments..... 263

Chapter I

THEORETICAL BACKGROUND/STATE OF THE ART

1.1 Type of fuel cells

Fuel cells share the characteristics of high efficiency, no moving parts, quiet operation and low (as compared to heat engines) or zero emissions. Potential markets of these devices include battery replacement in small portable electronic devices, auxiliary power units in vehicles, residential combined heat and power (CHP) and large-scale megawatt (MW) electrical power generation [1]. As a general rule, fuel cells are classified according to the type of electrolyte that they use. The electrolyte material conditions the charge carrier and chemical reaction but also the kind of catalysts required and the operation temperature. The latter has many implications in the functionality and determines the most appropriate application for each fuel cell. Figure I - 1 summarizes some of the issues related to operating temperature. Main characteristics of each fuel cell technology are presented in Table I - 1.

1.1.1 Low temperature Fuel Cells

Polymer electrolyte membrane fuel cells (PEM or PEFC), alkaline fuel cells (AFC) and phosphoric acid fuel cells (PAFC) operate, in general, at low temperatures. This allows fast start-up and therefore causes less wear of system components. However, at those temperatures, noble-metal catalyst (i.e. platinum) is required to promote hydrogen oxidation. Not only platinum catalyst adds extra cost to the system, it is

also extremely susceptible to CO poisoning and makes it necessary to use an additional reactor to reduce CO in the fuel gas if the hydrogen is derived from an alcohol or hydrocarbon fuel.

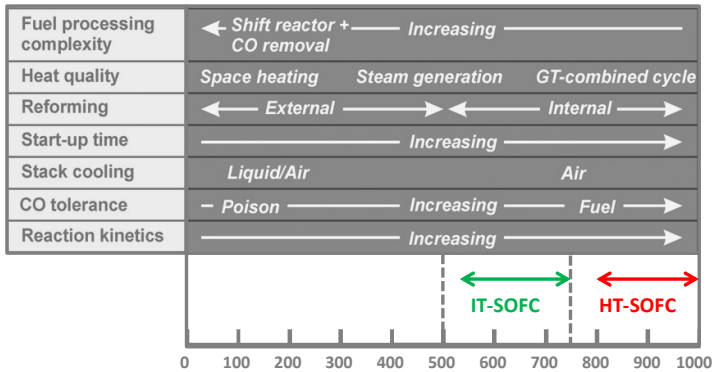


Figure I - 1. Summary of generic fuel cell issues related to temperature of operation [2].

AFCs were one of the pioneer cell technologies used in spacecrafts for electricity and water production. Despite the fast electrochemical activity and high performance, AFC is susceptible to little amounts of CO₂ in hydrogen and air, which add extra cost due to purification processes. Cheaper PEM fuel cells work below 100°C and are mainly used for transportation applications thanks to a favourable power-to-weight ratio. AFCs are more tolerant to CO impurities compared to PEM but less efficient generating electricity alone.

1.1.2 High temperature Fuel Cells

Molten carbonate fuel cell (MCFC) and solid oxide fuel cell (SOFC) work at very high temperatures. The electrochemical reaction is faster and no precious-metal catalysts are necessary at high temperature, thus reducing costs. High working temperature also allows SOFCs to reform fuels internally, which enables the use of a variety of fuels and reduces the cost associated with an integrated reformer. SOFCs are capable of internally reforming light hydrocarbons such as methane (natural gas), propane and butane. However, water must be added to the fuel to avoid carbon deposition (i.e. carbon coking) and resultant slowing of internal reforming. MCFC is not prone to carbon coking and it is especially attractive to work with coal gases thanks to the high tolerance to CO and CO₂ gases. However, the development of low-cost materials with stable performance at high operating temperatures is still challenging. This is especially true for MCFCs as the corrosive electrolyte used accelerates component breakdown and corrosion. In addition, MCFCs show lower

efficiencies. Alternative SOFCs can operate over a wide range of temperature (500°C to 1000°C). For high-temperature SOFCs (HT-SOFCs), high efficiencies can be reached from integration with gas-turbines for large-scale stationary applications.

	Electrolyte	Operating T(°C)	Stack Size	Overall efficiency	Applications	Advantages	Disadvantages
Low Temperature	PEM	50-100	<10kW-100kW	60% 35% stationary transportation	<ul style="list-style-type: none"> - Backup power - Portable power - Distributed generation - Transportation - Specialty vehicles 	<ul style="list-style-type: none"> -Solid electrolyte reduces corrosion and electrolyte management problems - Low temperature - Quick start-time 	<ul style="list-style-type: none"> -Expensive catalysts -Sensitive to fuel impurities -Low temperature waste heat
	PAFC	Phosphoric acid	150-200	400 kW 100 kW module	40%	<ul style="list-style-type: none"> - Distributed generation 	<ul style="list-style-type: none"> - Higher temperature enables CHP -Higher tolerance to fuel impurities
High Temperature	SOFC	500-1000	1kW-2MW	60%	<ul style="list-style-type: none"> - Auxiliary power - Electric utility - Distributed generation 	<ul style="list-style-type: none"> - High efficiency - Fuel flexibility - Can use a variety of catalysts - Suitable for CHP 	<ul style="list-style-type: none"> -High temperature corrosion and breakdown -Long start-up time -Low power

Table I - 1. Comparison of Fuel Cell technologies [3].

For smaller scale stationary applications, such as micro-CHP, APU and small electrical generators, there is a trend to move towards lower temperature of operation, into the so called intermediate temperatures (IT-SOFC, 500°C-750°C) [2]. Those temperatures are still considered too high for portable applications as they involve slow start-up times and thermal shielding that is necessary to ensure isolation. However, SOFC can be used as standalone system (APU) to supply auxiliary power to selected vehicles.

In general, high-temperature fuel cells (MCFC, SOFC) together with PAFC produce waste heat that can be use to reform fuels, provide heat and drive engines. Those technologies are therefore especially attractive for co-generation and hybrid system applications (i.e. gas turbine).

On the various cell technologies, PEM (low temperature) and SOFCs (high temperature) are currently attracting more attention and development budget. Until recently, PEM had the exclusivity of portable applications. In this context, however, SOFC supporters are enthusiastic towards newly developed micro-scale cells. Thanks to fast start-up times and high volumetric power densities, small-scale portable SOFCs aim to compete, in the near future, with PEMs in all fronts. Even laptops fuelled with SOFCs are contemplated [4].

The end-uses of SOFC systems may be classified into three main groups: stationary applications (large stationary power generation of over 10 KW and small stationary power generation of under 10 KW), niche transportation applications and portable applications. In 2007, the majority of SOFC units installed over the world were being used for small stationary applications which include domestic power supply, industrial applications requiring uninterrupted power supply (UPS) and military applications. The use of SOFC in the niche transport was higher than that in large stationary applications [5].

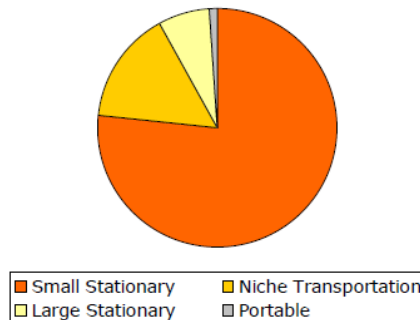


Figure I - 2. Total number of SOFC units installed over the world by 2007.

1.2 Solid Oxide Fuels Cells

1.2.1 Basic principles

Solid Oxide Fuel Cells (SOFC) consist of an electrolyte made of a non-porous ceramic oxide that becomes an ionic conductor for oxygen ions (O^{2-}) as the temperature increases. The electrolyte is sandwiched between two electrodes, cathode and anode, and together compose the electrochemically functional body of the cell. The overall electrochemical reaction is illustrated in Figure I - 3.

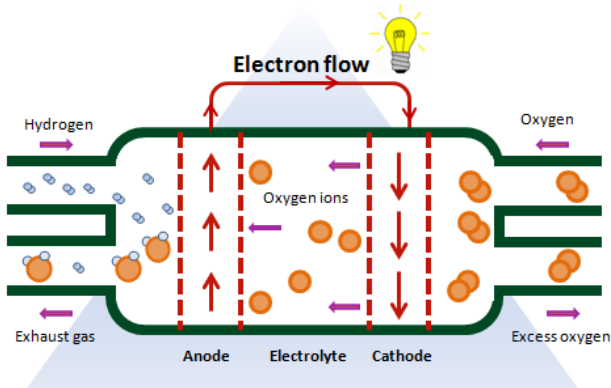
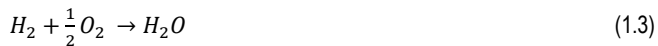


Figure I - 3. Operating principle of a Solid Oxide Fuel Cell.

Half-cell reactions at the electrodes occur according to



At the cathode, oxygen atoms are reduced according to Eq. (1.1) and resulting oxide ions are conducted through the ceramic electrolyte to the porous anode where they react with hydrogen according to Eq. (1.2), giving water and electrons which are conducted to the cathode through an external circuit. Another way of looking at the fuel cell is to say that hydrogen fuel is being “burnt” or combusted in the simple reaction:



However, instead of simple heat energy being liberated, electrical energy is produced.

This holds for an ideal situation where cells are fed with pure hydrogen. However, the actual hydrogen industry is based on steam reforming of fossil fuels which renders more attractive their direct use. In effect, fuel flexibility (i.e. hydrogen, carbon monoxide, methane) is an essential advantage of SOFCs. For the sake of simplicity, electrochemical reaction for hydrogen is described here but in a reasonable situation, additional CO and/or methane oxidation must be considered.

1.2.2 Open Circuit Voltage and Irreversibilities

At equilibrium, the Open Circuit Voltage (OCV), E , is given by the Nernst equation:

$$E = E_0 + \frac{RT}{2F} \ln \left(\frac{P_{H_2} P_{O_2}^{1/2}}{P_{H_2O}} \right) \quad (1.4)$$

where E_0 is the standard potential, R is the ideal gas constant, F is the Faraday constant, 2 is the number of exchanged electrons and the terms under the logarithm are the partial pressure of reactants and product of the electrochemical reaction (Eq(1.3)). The electromotive force (EMF) calculated from such equation, E , is known as “Nernst potential” and it is the reversible cell voltage at a given temperature and pressure. Note that Nernst potential, E , increases as reactant activities increase. E_0 is the EMF at standard pressure and it is given by the fundamental equation:

$$E_0 = -\frac{\Delta G^0}{2F} \quad (1.5)$$

where G^0 is the Gibbs free energy released in 1mol H_2 conversion and $-2 F E$ is the electrical work done moving the corresponding charge $2 F$ round the circuit. Even if the OCV is lower than the theoretical potential E_0 , during operation, when current flows through the cell, potential is lower than the OCV due to irreversibilities which cause the voltage drop. The characteristic voltage versus current density curve takes the shape shown in Figure I - 4.

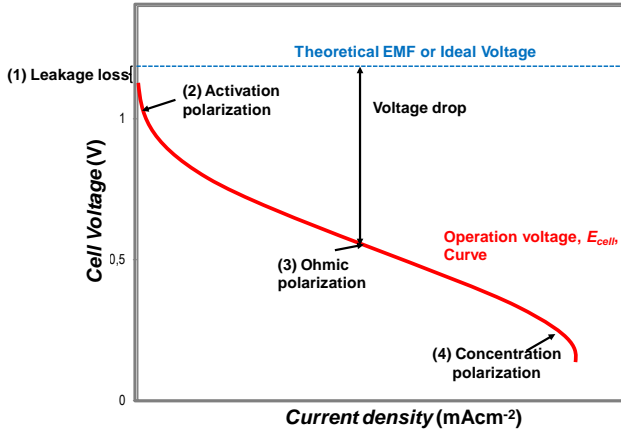


Figure I - 4. Typical fuel cell IV curve.

Four major irreversibilities or losses are distinguished and the real cell potential, E_{cell} , is expressed as follows:

$$E_{cell} = E_0 - E_{leak} - \eta_{act} - \eta_{ohm} - \eta_{conc} \quad (1.5)$$

The leakage loss, E_{leak} , is mainly caused by electrolyte imperfections (i.e. porosity, interconnectivity) which are directly related to the manufacturing process. This is traduced in a voltage drop from theoretical OCV. Even when non-porous electrolyte with excellent quality is processed, this ionic conductor is still able to support very small amounts of electron conduction or fuel crossover, typically in the order of few mAcm^{-2} . This voltage drop is inevitable but at the high operation temperature of SOFCs is modest in the order of few mV.

The activation polarization, η_{act} , is associated with charge transfer processes which take place in the electrodes and it is the dominant resistive mechanism at low current density. The size of the voltage drop is related to the current density, J , by the Tafel equation:

$$\eta_{act} = A \ln\left(\frac{J}{b}\right) \quad (1.6)$$

where A and b are constants related to the electrode (i.e. composition and microstructure) and cell conditions (i.e. temperature). For a given composition, activation losses are lower for fine electrode microstructures and high operation temperature. While an electrode with fine microstructure extends the electrochemically active area, increasing temperature accelerates charge transfer

kinetics. Generally, *triple phase boundary* (TPB) is used to describe the electrode zone where oxygen reduction and hydrogen oxidation half-reactions occur. It is essentially the meeting point of ion conducting electrolyte, electrically connected catalytic regions and gas space.

Ohmic polarization, η_{ohm} , is the voltage drop due to ohmic resistance and it is mainly produced in the electrolyte. As a matter of fact, thickness but especially the ionic conductivity of electrolyte material characterize the operation window of cells as it is related later on. Low ionic and electronic conductivity of electrodes (depending on material, thickness and microstructure) and poor interface contacts further increase ohmic polarization. The size of the voltage drop is simply proportional to the current; $V=I R$.

Concentration polarization, η_{conc} , is the result of practical limitations in the mass transport within the electrodes, when reactants are consumed faster than they can diffuse into the porous electrode. η_{conc} is also affected by variations in the bulk concentration of reactants. This is particularly important in the anode as the fuel utilization increases and hydrogen concentration reduces in the fuel stream due to steam production. Electrode microstructure (i.e. pore size and distribution) and thickness further influence concentration overvoltage.

1.2.3 Efficiency

The efficiency of a fuel-cell system, ε , can be written as the product of three contributing efficiencies as described in Eq.(1.7) [6]: the reversible efficiency, ε_R , the voltage or part-load efficiency, ε_V , and the fuel utilization, ε_U .

$$\varepsilon = \varepsilon_R \varepsilon_V \varepsilon_U \quad (1.7)$$

The ideal or reversible efficiency, ε_R , relates the electrical energy produced in an ideally reversible system with the energy that would be produced by burning the fuel, and can be thermodynamically calculated by

$$\varepsilon_R = \frac{\Delta G}{\Delta H} = 1 - \frac{T\Delta S}{\Delta H} \quad (1.8)$$

where ΔG , ΔH , and ΔS are changes in molar free energy, enthalpy, and entropy, respectively, associated with the full oxidation of fuel. This efficiency is thus directly related to fuel composition and temperature. As already mentioned, irreversibilities within the fuel cell reduce the cell potential when it is operated under load. The voltage efficiency, ε_V , depends on the operating cell potential E_{cell} and it is defined as

$$\varepsilon_V = \frac{E_{cell}}{E_0} \quad (1.9)$$

where E_0 is the reversible (Nernst) potential. Fuel utilization (FU) strongly affects the efficiency. One H_2 molecule oxidation liberates 2 electrons and thus hydrogen used can be directly calculated by dividing the current generated with $2F$, the current generated by 1 mol H_2 . Fuel utilization can be, thus, expressed as:

$$\varepsilon_U = \frac{I/2F}{n_{H_2}} \quad (1.10)$$

where n_{H_2} is the molar hydrogen supplied to the cell. For high system efficiency, the fuel utilization should be as high as possible. However, as the fuel concentration decreases along the length of the anode channel, the reversible “Nernst potential” decreases at high fuel utilizations according to Eq. (1.4). In Figure I - 5, the typical behaviour of the fuel cell efficiency and fuel utilization as a function of operating cell voltage is represented. Operating at low cell potential, the fuel can be fully utilized and the fuel cell efficiency is a linear function of cell potential E_{cell} . The slope of this function depends on the fuel composition as well as operating temperature and pressure. The reversible efficiency, ε_R , which would be achieved by operating the cell at its reversible potential, cannot be reached in practise due to the low fuel utilization at high operating potential. The exact conditions for maximum efficiency depend on fuel composition, temperature and pressure. In Figure I - 5, maximum efficiency is reached around 0.8V at 800°C for a given reformed gas composition (50% CO and 50% H_2).

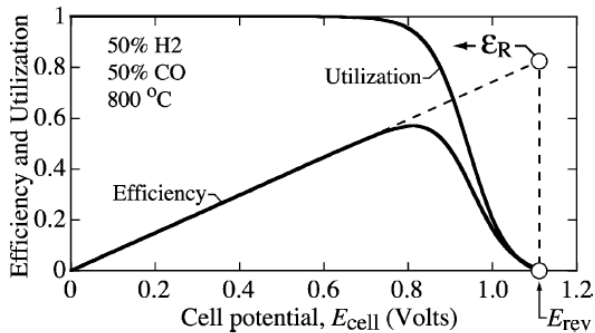


Figure I - 5. Fuel-cell efficiency and fuel utilizations as a function of operating cell voltage in an SOFC operated at 800°C with fuel composed of 50% CO and 50% H_2 at atmospheric pressure [6].

SOFCS attain efficiencies over 60% when converting fuel to electricity. If the heat they produce is also harnessed, the overall efficiency in converting fuel to energy can be over 80% in a combined heat and power (CHP) system.

1.2.4 SOFC targets

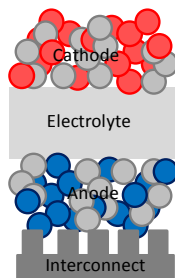
In addition to efficiency and power density, in general, other requirements such as long term stability, thermal and redox cycling capability, short start-up time and operation on different fuels at high fuel utilization have to be fulfilled. Table I - 2 gives an overview of the estimated targets for stationary and mobile applications. While performance requirements for stationary SOFC systems are more flexible, stability is an essential prerequisite. Chemical instability in the interface of cell components is considered key on this subject. On the other hand, for transportation applications, rapid start-up times and thus, lower operation temperature are essential. In addition, thermomechanical instability is a key issue because of frequent thermal cycling [7]. Regarding the fuel composition, micro-CHP systems fed with natural gas are planned for domestic co-generation. On the other hand, auxiliary power system designed for transportation should work with gasoline or diesel.

Table I - 2. Target areas for mobile and stationary SOFC systems [1].

Application	Stationary	Mobile
Operation temperature (°C)	700-1000°C	500-700°C
Power density	>0.25 Wcm ⁻²	>1 Wcm ⁻²
Lifetime	>40000 h	> 2000 h
Degradation rates	< 1 μVh ⁻¹	< 10 μVh ⁻¹
Fuel utilization	>80%	>80%
Thermal cycles	>100	>5000
Heating rates	>1 Kmin ⁻¹	>100 Kmin ⁻¹
Fuel	Natural gas, fuel oil	Gasoline, diesel
Oxidant	Air	Air
System costs	<\$500 kW ⁻¹	<\$100 kW ⁻¹

1.3 State of the art SOFC materials

Functional layers in the single cell (i.e. electrolyte and electrodes) satisfy different requirements. Electrolyte must be gas tight and purely ionic conductor whereas electrodes have to be porous to allow inlet and outlet gas transport and electronic or mixed conductors. In the case of a pure electronic conductor electrode, electrochemical reactions are restricted to electrode-electrolyte-gas interface. Those active sites are also called *triple phase boundary* (TPB) referring to gas, electronic conductor and oxygen conductor phase meeting points. It is commonly accepted that electrodes with acceptable efficiency should be either composites with ionic and electronic conducting phases or mixed conductors to extend the TPB.



Electrical properties	Thermomechanical properties	Stability
Mixed conductivity $\sigma_{ion} + \sigma_{elec}$ Catalytic activity	Porosity TEC Adhesion	Stable in oxidant atmosphere
Ionic conductivity $\sigma_{ion} \gg \sigma_{elec}$	Gas-tightness Mechanical stability	Stable in dual atmosphere (oxidant and reducing)
Mixed conductivity $\sigma_{ion} + \sigma_{elec}$ Catalytic activity	Adhesion TEC Porosity	Stable in reducing atmosphere
Electronic conductivity $\sigma_{ion} \ll \sigma_{elec}$	Adhesion TEC Gas-tightness	Stable in dual atmosphere (oxidant and reducing)

Figure I - 6. Electrical, thermomechanical and stability requirements of the SOFC single cell components [1].

State of the art materials currently used in most IT-SOFC systems include yttria-stabilized zirconia (YSZ) electrolyte, LSCF-GDC composite cathode and Ni-YSZ cermet anode. In addition, ferritic stainless steels are used to interconnect neighbouring cells. In Figure I - 6 principal requirements for single cell constituents and interconnect, at stack level, are summarized. In addition, a review of the principal component materials is reported in this section.

1.3.1 Electrolytes

The basic requirements for a suitable SOFC electrolyte are [8]:

- *High ionic conductivity*
- *Electronic insulator*
- *Thermal stability*
- *Stability under reducing and oxidizing atmospheres*
- *Chemical stability to contacting neighbours*
- *Ease of manufacturing as a thin gas tight film*
- *Low cost and availability*

The most common electrolyte is yttria stabilized zirconia (YSZ) due to its high ionic conductivity and low electronic conductivity. However, other materials such as gadolinium doped ceria (GDC) and lanthanum strontium gallium magnesium oxide (LSGM) are becoming popular due to their higher ionic conductivity at lower temperatures (500-700°C) [9]. Bismuth oxide systems have high ionic conductivities at low temperatures but suffer from high chemical instability, low mechanical strength and instability in reducing atmospheres [10]. Main electrolyte materials are presented in Figure I - 7. Assuming that the electrolyte component should not contribute more

than $0.15 \Omega\text{cm}^2$ to the total area specific resistance (ASR) [11], for a $15 \mu\text{m}$ thin electrolyte, then the associated specific ionic conductivity (σ) should be at least 10^{-2} S/cm for $\sigma = L/\text{ASR}$ [11]. Ionic conductivity of YSZ is competitive above 700°C whereas for $\text{Ce}_{0.9}\text{Gd}_{0.1}\text{O}_{1.95}$ (CGO), the relevant temperature is 500°C [12]. If thinner electrolyte was used, operation temperature could be further decreased. However, at present, $10\text{-}15 \mu\text{m}$ film is the minimum thickness which guarantees dense and impermeable films by inexpensive ceramic processing routes. On the other hand, $150 \mu\text{m}$ self supporting $(\text{ZrO}_2)(\text{Y}_2\text{O}_3)_{0.1}$ electrolyte would necessitate 1000°C for an acceptable ionic conductivity. Therefore, the electrolyte material and thickness designates the operating temperature of the cell. This is not trivial as in contrast to other fuel-cell types, SOFC stacks can be, in principle, operated within a wide temperature range as previously mentioned ($500\text{-}1000^\circ\text{C}$).

The state of the art solid oxide electrolyte used in SOFCs is yttria-stabilized zirconia (YSZ). Y^{3+} is added to stabilize the conductive cubic fluorite phase of ZrO_2 , as well as to increase the concentration of oxygen vacancies and thus increase the ionic conductivity. Highest ionic conductivities for 8YSZ (ZrO_2 stabilized with 8 mol% Y_2O_3) are reported but 3YSZ (ZrO_2 stabilized with 3 mol% Y_2O_3), with significantly lower conductivity, is widely adopted due to its outstanding mechanical stability [13]. Although yttria is the most common dopant, calcium (CaSZ) but especially scandia-doped zirconia (ScSZ) is very attractive as exhibits higher ionic conductivity [14]. ScSZ superiority is attributed to the better matching of Zr^{4+} and Sc^{3+} ionic radius, as compared to that between Zr^{4+} and Y^{3+} , leading to a smaller energy for defect association and increased mobility [15-18]. Nevertheless, Sc cost, stability and poor availability has constrained its use.

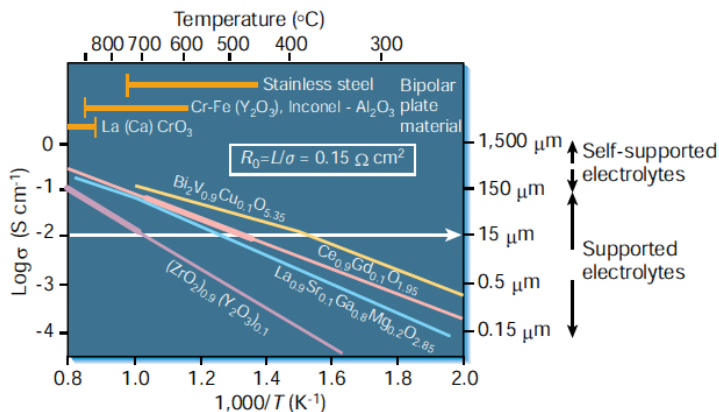


Figure 1 - 7. Specific conductivity versus reciprocal temperature for selected SOFC electrolytes [12].

Doped-CeO₂ with similar fluorite structure constitutes the most promising candidate to be used as electrolyte in SOFC at lower operating temperatures [19]. Gadolinia and samaria-doped CeO₂ (GDC and SDC) show high conductivity already at 500°C. However, at higher temperature, doped ceria becomes unstable under reducing atmosphere. Above 600°C, significant Ce⁴⁺ ions reduction to Ce³⁺ creates lattice expansion stresses and the electrolyte becomes a mixed conductor. The associated electronic conductivity produces an internal short circuit or leakage current. This lowers the OCV and additional fuel utilization even under OCV conditions takes place resulting in a decreased system efficiency [20]. This event limits doped-CeO₂ electrolytes use to the 500-600°C range.

The perovskite, LaGaO₃, can be doped with strontium and magnesium, La_{1-x}Sr_xGa_{1-y}Mg_yO₃ (LSGM), to produce a material with good ionic conductivity at low temperatures [21]. The conductivity of LSGM is higher than those of YSZ and ScSZ and in magnitude of that of GDC [22]. Though conductivity is slightly smaller than GDC at 500°C, its ionic domain is wider and it could be more appropriate to use this electrolyte at temperatures around 600°C, where the reduction of Ce⁴⁺ in GDC is becoming significant [11]. However, Ga-evaporation at reducing atmosphere results in long-term instability and LSGM reacts with Ni in the anode forming an insulating phase [21]. Moreover, the principal challenge for LSGM electrolytes is the development of cost-effective processes for fabricating the desired single-phase microstructure.

1.3.2 Anode

The main requirements for a SOFC anode are listed below [9]:

- *High electronic conductivity*
- *Catalytic activity for fuel oxidation/combustion*
- *High ionic conductivity*
- *Porous structure with mechanical resistance*
- *Stability over successive reducing and oxidizing (redox) cycles*
- *Thermal stability*
- *Chemical stability to contacting neighbours*
- *Matched thermal expansion coefficient (TEC)*
- *Capability to avoid coke deposition and tolerance to sulphur in fuels*
- *Low cost (especially when used as mechanical-support)*

In order to optimize fuel oxidation efficiency, high *triple phase boundaries* (TPB) concentration at the anode is necessary. This requires a fine microstructure with connected porosity for gas diffusion as well as an ionic/electronic conductor matrix that supplies oxygen and collects the liberated electrons. In the anode-supported design, mechanical robustness is also necessary. Obtaining a material with all these

properties is demanding, however composites and ceramic-metal catalyst cermets can produce a combination of all these properties.

The basic properties of nickel-zirconia cermets have been widely studied since the first patent was published in 1970 [19]. Nickel is an excellent catalyst for hydrogen oxidation as well as electronic conductor. The mixing of nickel with ionic conductor electrolyte material reduces TEC mismatch between anode and electrolyte and extends TPBs through the anode. Typically, Ni-cermets contain 30 vol% Ni at minimum to guarantee continuous electronic conduction (i.e. percolation threshold) and porosities in the 20-40% range. This cermet, however, is not stable under redox cycles and suffers from mechanical failure due to dimensional changes during Ni-NiO oxidation (i.e. 69.9% in solid volume) [23]. On the other hand, it is prone to carbon deposition, or coking, when fuel is internally reformed [24]. Low sulphur tolerance constitutes another hurdle to the use of natural gas with Ni-YSZ anodes [25]. Nevertheless, Ni-YSZ cermet anode is the most employed anode for IT-SOFCs working on hydrogen.

Ni-Fe alloys are more resistant against cooking and sulphur poisoning. However, the redox stability of these compounds is still called into question [9]. La-, Y- and Nb-doped SrTiO₃ perovskites (LST, YST and NbST) have received special attention thanks to their high electronic conductivity under reducing conditions [26-30]. Newly developed anode concept combines perovskites with good ionic conductors (YSZ or SDC) which are impregnated with nickel or other catalyst to improve the electrochemical performance. Thanks to the electrical properties those perovskites, little nickel is needed. This is essential to reduce anode expansion upon Ni-NiO oxidation and improve redox tolerance. Composite anodes such as Ni/NbST-YSZ [31] and Ni/YST-SDC [32] have provided with promising response to redox cycles. More recently, Ikebe et al. [33] have reported the high stability of 10 wt% Ni/YST-YSZ anode in five consecutive redox cycles.

1.3.3 Cathode

The essential requirements for the cathode material are [34]:

- *High electronic conductivity (preferably more than 100 S/cm under oxidizing atmosphere)*
- *Preferred mixed electronic-ionic conductivity*
- *High catalytic activity*
- *Matched thermal expansion coefficient (TEC)*
- *Chemical compatibility with electrolyte and interconnect material*
- *Adequate porosity*
- *Stability under oxidizing atmosphere*
- *Low cost*

Two cathode designs are adopted to increase the active sites (TPBs): (i) porous composite consisting of an electronic conducting cathode material and an appropriate amount of ionic conducting electrolyte material, or (ii) single-phase mixed ionic electronic conductor (MIEC) electrode permitting both oxide ion and electron mobility within the cathode material.

Perovskite oxides with the chemical formula ABO_3 are widely used as SOFC cathode materials. The ideal cubic-symmetry structure has the B cation in 6-fold coordination, surrounded by an octahedron of oxygen ions, and the A cation in 12-fold coordination. A-site cation is larger and total charge for A+B cations is +6. Normally, the A-site cation is a mixture of rare and alkaline earths cations (i.e. $A=Ln_{1-x}M_x$ where $Ln=La, Pr, Nd, Sm$ and $M=Ca, Sr, Ba$) and B-site cation is a reducible transition metal cation (i.e. Mn, Fe, Co, Ti, Cr, Ni). Therefore, in most cases, a redox catalytic mechanism is usually provided by B-site cations [35]. The octahedral symmetry around the transition metal cation often promotes a metal or semiconducting band structure at high temperatures, leading to high electronic conduction. On the other hand, substitution of A-site or B-site cations with lower valence cations is charge compensated by introducing vacancies at the oxygen lattice sites [36]. Thus, the large majority of perovskite oxides exhibiting oxide ion conduction are classified as mixed conductors, which show both ionic and electronic conduction.

For HT-SOFCs (800–1000°C) the preferred choice is the LSM-YSZ composite which combines pure electronic conducting Sr-doped $LaMnO_3$ perovskite (LSM) and electrolyte material (YSZ). The major inconvenient of this cathode material is the formation of $La_2Zr_2O_7$ and $SrZrO_3$ insulating phases due to the reactivity with YSZ at high sintering temperatures [37, 38]. However, the electrochemical properties of LSM perovskite are not sufficient for operation below 800°C. Performance of manganite perovskites is improved by La replacement with other rare earth elements (i.e. Pr) or by doping LSM with cations which promote the formation of oxygen vacancies. The most promising manganite perovskites for IT-SOFCs include $Pr_{1-x}Sr_xMnO_{3-\delta}$ (PSM) [39], $Pr_{0.7}Ca_{0.3}MnO_3$ (PCM) [40] and $La_{0.8}Sr_{0.2}Mn_{1-x}Sc_xO_{3-\delta}$ (LSMS) [41] structures.

Cobalt-based perovskites demonstrate higher ionic and electronic conductivity than other cathode materials, the most common being Sr-doped $LaCoO_3$ (LSC). However, huge TEC increase due to cobalt concentration constrains the compatibility with the electrolyte [42]. A decrease in the ASR and TEC is expected by La cation substitution with Gd and Pr. Alternative compositions include $Pr_{1-x}Sr_xCu_yCo_{1-y}O_{3-\delta}$ [43], $Pr_xSr_{1-x}CoO_{3-\delta}$, $La_{1-x}Sr_xCo_yMn_{1-y}O_{3-\delta}$ [44] and more popular $Sm_{1-x}Sr_xCoO_{3-\delta}$ (SSC) [45].

Thanks to the stable electronic configuration ($3d^5$) that Fe^{3+} exhibits, $LaFeO_3$ is expected to be more stable than $LaCoO_3$. Sr-doped $LaFeO_3$ (LSF) has shown promising power density and stability at intermediate temperatures [46, 47]. In fact, reactivity with YSZ is considerably reduced and TEC is very close to common

electrolyte materials (i.e. YSZ, GDC, LSGM) in the 10 - 12 ppmK⁻¹ range [34]. In the usual anode-supported configuration with Ni-YSZ anode and YSZ electrolyte, La_{0.8}Sr_{0.2}FeO₃ cathode showed power densities as high as 0.9–0.95 Wcm⁻² at 750 °C and 0.7 V [47]. Cu-doped LSF exhibited superior oxygen reduction kinetics and (La_{0.8}Sr_{0.2})_{0.98}Fe_{0.98}Cu_{0.02}O₃ cathode on an anode-supported YSZ cell have indicated power densities in the range of 1.35 -1.75 W cm⁻² at 750 °C and 0.7 V [48]. However, it still exhibits chemical reaction with YSZ above 950°C. The sole ferritic perovskite which has not shown reactivity with YSZ is the Ca-doped LaFeO₃ [49]. Usually, LSF type cathodes are used as composites with ceria based ionic conductors (GDC, SDC).

La_{1-x}Sr_xCo_yFe_{1-y}O₃₋₅ (LSCF) is the most popular cathode material at intermediate temperatures. The performance of LSCF perovskite is superior than LSF with similar A-site stoichiometry [50, 51]. However, it suffers from reactivity with zirconia-based electrolytes and forms the pyrochlore-phase La₂Zr₂O₇ and the perovskite SrZrO₃ in the cathode/electrolyte interface. This may be a limiting factor also for pure ferritic LSF perovskites. Therefore, a GDC barrier layer is frequently used to prevent the formation of low conducting compounds. The origin of higher degradation is found, however, in the strontium depletion out of the LSCF. In chapter III, intrinsic degradation mechanisms of ferritic perovskites as well as tolerance to chromium poisoning is discussed.

Iron-doped nickelate LaFe_{1-x}Ni_xO₃₋₅ exhibits an attractive combination of electronic transport properties, a moderate thermal expansion and phase stability in air. In addition, being free of nucleation agents (i.e. Mn and Sr) is less reactive with chromium species though it still deposits in the cathode/electrolyte interface [52]. Unfortunately, reactivity of LNF with ZrO₂-based electrolytes is higher than conventional LSM at temperatures of sintering [53].

Alternative materials with K₂NiF₄-type structure, usually formulated as A₂BO₄₊₅, have also attracted some attention to work as cathodes in a variety of solid oxide electrolyte devices. La_{2-δ}NiO_{4+δ} and Pr_{2-δ}NiO_{4+δ} are potential cathode candidates for SOFCs working below 700°C. However, perovskites maintain the supremacy and in Table I - 3 the principal properties of perovskite cathode materials are summarized.

Table I - 3. Perovskite-type oxide materials: coefficient of thermal expansion (TEC), electronic (σ_e) and ionic conductivity, (σ_i).

<i>Composition</i>	<i>TEC (ppmK⁻¹)</i>	<i>T (°C)</i>	<i>σ_e (S/cm)</i>	<i>σ_i (S/cm)</i>	<i>References</i>
La _{0.8} Sr _{0.2} MnO ₃	11.8	900	300	5.93x10 ⁻⁷	[54]
La _{0.6} Sr _{0.4} CoO ₃	20.5	800	1600	0.22	[55, 56]
La _{0.6} Sr _{0.4} FeO ₃	16.3	800	129	5.6x10 ⁻³	[55, 57]
La _{0.6} Sr _{0.4} Co _{0.2} Fe _{0.8} O ₃	15.3	600	330	8x10 ⁻³	[55, 58]
LaNi _{0.6} Fe _{0.4} O ₃	11.4	800	580	---	[59]

Note that TEC of electrolytes (YSZ, GDC, LSGM) are 10-12 ppmK⁻¹ [20].

It has been recognized that, as the operation temperature decreases, polarization losses in the cathode are limiting overall cell performance. Adding novel metal phases such as silver [60] or palladium [61], the catalytic activity for oxygen reduction is substantially increased.

1.3.4 Interconnector

The interconnect is one of the key components which provide the electrical connection between the individual cells in a series or parallel connections to make SOFC stacks. In the planar design, the interconnect is sometimes designated as bipolar plate, or separator, emphasizing the different polarities of anode and cathode which it connects. Interconnect materials for SOFC fall into two categories: conductive ceramic (perovskite) materials for operation at high temperature (900 to 1000 °C) and metal alloys for lower temperature operation. Though the shape of SOFC interconnects depends heavily on the cell and stack design, the materials choice is almost entirely determined by physical and chemical stability under operating conditions [62].

Ceramic interconnect materials used at high temperatures are LaCrO_3 based perovskites. These perovskites are unique in that they exhibit high electronic conductivity and resist reduction under exposure to syngas at high temperatures. Main compositions include LaCrO_3 doped with Sr or Ca on A-site or Mg on B-site, i.e., $\text{La}_{1-x}\text{Ca}_x\text{CrO}_{3-\delta}$, $\text{La}_{1-x}\text{Sr}_x\text{CrO}_{3-\delta}$ and $\text{LaCr}_{1-x}\text{Mg}_x\text{CrO}_{3-\delta}$. Siemens-Westinghouse, Mitsubishi Heavy Industries, and Rolls Royce are representative users of ceramic interconnects which are mostly applied in the tubular design, whereas Argonne and the former Dornier company use ceramic interconnects in the planar design.

In recent years, the tendency towards lower operation temperatures has made possible the use of cheaper metal alloys. Unlike ceramic processing, fabrication of complex-shaped metal interconnects is feasible and inexpensive. In addition, metals exhibit excellent thermal and electronic conductivity. An appropriate metal interconnector must satisfy the following criteria [63]:

- *Resistance to high-temperature and corrosion*
- *Stability in dual atmosphere (oxidizing and reducing)*
- *High electronic conductivity ($\text{ASR} < 0.1 \Omega\text{cm}^2$)*
- *Conductive and well adhered oxide layer in its surface*
- *Matching TEC with cell components*
- *Chemical compatibility with adjacent components*
- *Inexpensive*

Chromia and alumina forming alloys are the only commercially used high-temperature oxidation resistant alloys. However, alumina-scale insulates current collection conversely to chromia-scale, which exhibits good electronic conductivity.

On the other hand, ferritic stainless steels exhibit a compatible TEC ($10\text{-}12\text{ ppmK}^{-1}$) [20] with the cell in contrast to superalloys and austenitic stainless steels with higher TEC ($15\text{-}18\text{ ppmK}^{-1}$). Therefore, chromia forming ferritic stainless steels are favored as IT-SOFC interconnectors. Nevertheless, commercially available ferritic stainless steels are not exempt of some shortcomings. Poor oxidation behavior and oxide-scale properties are identified, especially in the air side. Relatively new ferritic stainless steels, some specifically developed for SOFC applications, have improved oxidation rate and scale adherence, for example, Crofer 22 APU, ZMG 232 and E-BRITE, and HP-441 (SECA) [64-69].

Metal interconnects have been widely adopted in the planar design [65]. Regarding the tubular design, IK4-Ikerlan proprietary MS-SOFC technology [70] had the exclusivity of using W-type ferritic stainless steel interconnects for cathode current collection in the bundle design [70]. In a recent report by TOTO [71], tubular stacks surrounded by metal frames are also mentioned. Alternative concepts include rolled Ag wire used by Acumentrics [4, 72].

1.4 SOFC designs

There are two basic SOFC designs that have been studied since 1960s: the planar and tubular design (Figure I - 8). In the planar design, the components are assembled in flat stacks, with air and fuel flowing through channels built into the interconnect. In the tubular design, components are assembled in the form of a hollow tube, with the cell constructed in layers around a tubular substrate. In the initial design, air flowed through the inside of the tube but at present, inverse designs are also used. The main characteristics of planar and tubular designs are compared in Table I - 4.

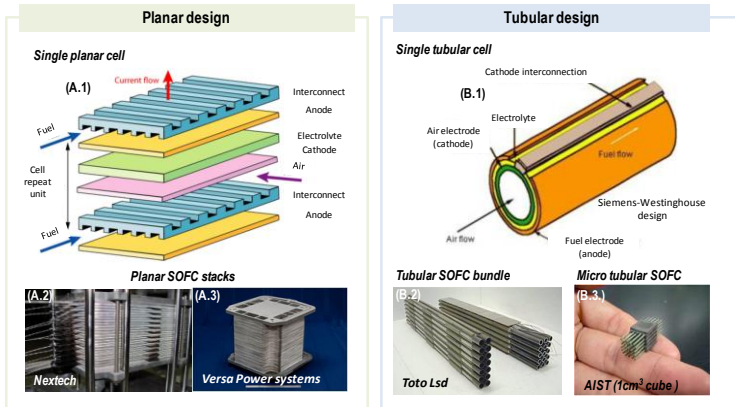


Figure I - 8. Schematic illustration of (A.1) planar [73] and (B.1) tubular SOFC design together with examples of commercially available SOFC stacks for both configurations. [73-76].

Table I - 4. Principal characteristics of planar and tubular design.

<i>Planar design</i>	<i>Tubular design</i>
High volumetric power density	Low volumetric power density
HT-sealing materials	LT-sealing materials*
Poor thermal cycling	Good thermal cycling
Ease of manufacturing	Higher manufacturing cost

*Depending on the design

A further design variation consists in downsizing of the cell to manufacture planar and micro-tubular SOFCs. This design offers high volumetric power density as well as rapid start-up times. Since its invention in the early nineties, growing interest has lead to a rapid progress on this field [77-81].

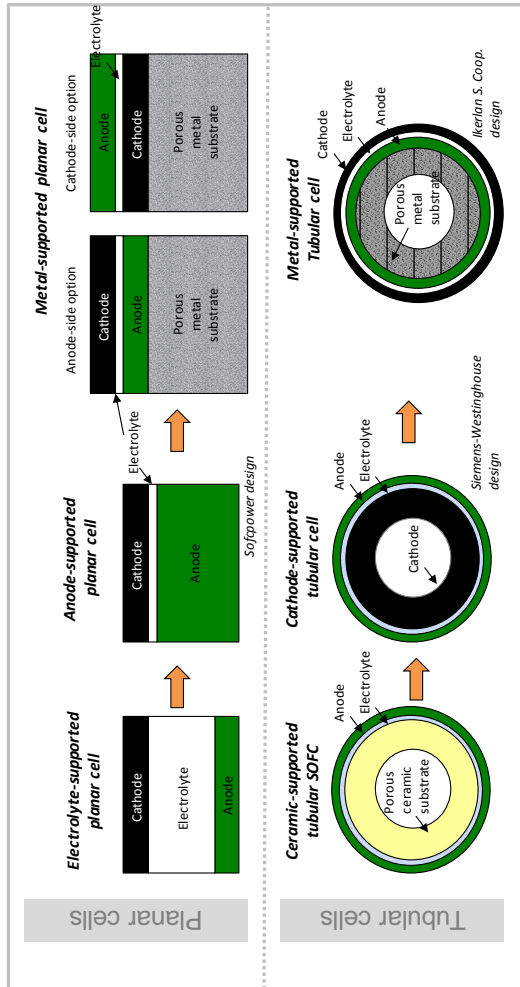


Figure I - 9. Cell generations for planar and tubular SOFC designs.

1.4.1 Planar design

As shown in Figure I - 9, a number of cell configurations exist, each classified according to the layer that mechanically supports the cell. The supporting element has a characteristic thickness $>150 \mu\text{m}$ whereas supported layers are only tens of microns [2]. The first generation of planar SOFCs was an electrolyte-supported cell. Thick YSZ electrolytes required for high operating temperatures (1000°C) and the

use of ceramic interconnects such as LaCrO_3 . A second generation of planar SOFCs consisted of thin electrolyte supported by the anode or the cathode. Much lower resistivity of this configuration permitted to lowering the operation temperature as well as introducing cheaper ferritic stainless steels as interconnect material. Generally, anode-supported SOFC configuration has been adopted by IT-SOFC industrial developers thanks to the lower polarization that this electrode exhibits compared to the cathode. More recently, a third generation of metal-supported cells has been considered and looks promising thanks to its excellent mechanical robustness. This innovative technology is introduced later on, in section 1.6.

Main advantages of planar SOFCs include high power density and ease of manufacturing. Furthermore, planar cells are easily integrated into stacks in a cell/interconnect sandwich geometry as shown in Figure I - 8. However, with planar cells, high temperature sealings have to be used to isolate air and fuel. An appropriate sealing must be electrically insulator with matching TEC to neighbouring elements, stable at high temperatures in both oxidizing and reducing atmospheres, tolerant to thermal cycles as well as inexpensive in terms of materials and manufacturing process [82]. Though a variety of sealings have been implemented (i.e. rigid, compliant and compressive seals) engineering a suitable sealing with high long-term stability is still a critical challenge that planar SOFC technology faces.

The principal industrial companies which develop planar SOFC concepts comprise Mitsubishi Heavy Industries and Tokyo Gas (Japan), Ceramic Fuel Cells Ltd. (Australia), Risoe-Topsoe (Denmark), H. C. Starck (Netherlands), Ceres Power and Rolls Royce (UK), VTT (Finland), BMW, H C Starck and Webasto (Germany), Hexis (Switzerland), HTCeramix/SOFCpower (Italy), SOFCo, Delphi Automotive Systems, GE, ZTek (USA) and Versa Power Systems (Canada) [83].

Figure I - 10 shows recently pursued planar SOFC approaches. The planar anode-supported SOFC with metal interconnects has benefited from support for fundamental science and stack development under DOE's SECA Program [74]. Sulzer Hexis built 1101 kW demonstration units based on its electrolyte-supported technology with superalloy interconnects that exhibited 1-2% degradation in 1000h [84]. Mitsubishi adopted an all-ceramic MOLB design (15 kW) that was stable for almost 10000 hours with degradation rates below 0.5% per 1000 h, but without thermal cycles [85].

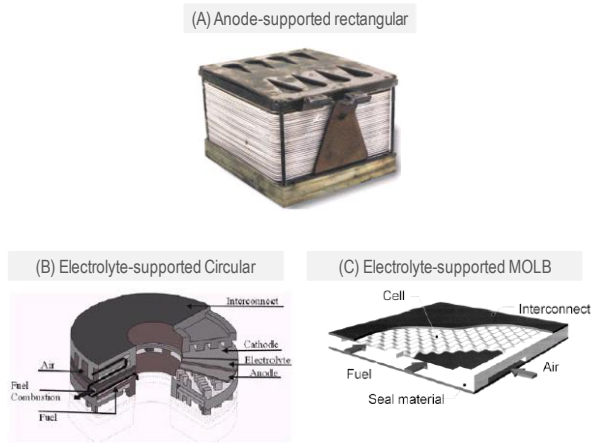


Figure 1 - 10. Overview of planar cell designs: (A) planar anode supported SOFC with metal interconnects developed in the SECA program [74] (B) electrolyte-supported planar SOFC technology with metal interconnects pursued by Hexis [84] and (C) electrolyte-supported design with “egg-crate” shape and ceramic interconnect by Mitsubishi [85].

1.4.2 Tubular design

The first tubular generation was introduced by Siemens Westinghouse Power Corporation (SWPC) in 1980. Originally, this HT-SOFC consisted on a porous CaO stabilized zirconia tube. However, it was rapidly substituted by a second generation of tubular cells fabricated on LSM substrates. Cells consisted of YSZ electrolyte and Ni-YSZ anode that were deposited by electrochemical vapour deposition (EVD) over cathode supports [11]. SWPC configuration was closed in one end tube. This cell worked at high temperature (1000°C) and used ceramic interconnect material (Figure 1 - 9).

Tubular cells exhibit low volumetric power density as compared to planar cells. The manufacturing cost is also higher, thus limiting the commercialization of higher diameter tubular cells. However, the main advantage of tubular cells is that they can be sealed at low temperatures. Generally, as the tube can be made longer than the furnace, the sealing at both ends can be done in the cold zone, eliminating constringent exigencies of high-temperature sealing materials. This has made the performance of tubular cell stack very stable as well as exhibiting good tolerance to rapid thermal cycles [86]. However, they represent a special geometric challenge to the stack designer when it comes to achieving high power density and short current paths.

At present, the leading group of tubular SOFC developers is integrated in USA by Siemens Westinghouse Power Corporation (SPWC) and Acumentrics, and by Kyocera, TOTO and Mitsubishi Heavy Industries in Japan [83].

The most advanced concept, developed by Siemens Westinghouse Power Corporation, is based on a porous cathode tube, manufactured by extrusion with an active area deposited by spray-sintering. The tube length is 1.5 m and outer diameter 22 mm. Cells are joined into bundles by nickel felts or using a modified concept with flattened tubes with internal ribs for reduced resistance [87, 88]. Toto, in Japan, follows an almost identical approach with cheaper manufacturing processes in shorter tubes of 0.5 m with an outer diameter of 16 mm [89]. Kyocera adopts the flattened tubes concept in an anode-supported design for small-scale CHP systems. In the micro-tubular field, the U.S. company Acumentrics is currently working on anode-supported cells which collect the current axially using various proprietary interconnect systems. In the outside, metallic parts (typically silver) are used to collect current from the cathode. A different tubular design is pursued by Mitsubishi Heavy Industries. The single cells are positioned on a central porous support tube and connected in series via ceramic interconnect rings, which leads to an increased voltage at the terminals of a single tube [90]. Fuel is supplied to the tube inside. In Figure I - 11, design concepts developed for stack interconnection and current collection in tubular cells are shown.

In Europe, IK4-Ikerlan S. Coop. (Spain) is a referent centre that develops metal-supported tubular SOFCs with industrially scalable colloidal processing routes for domestic CHP applications.

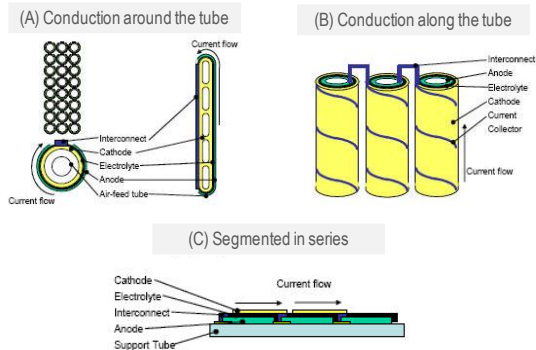


Figure I - 11. Tubular SOFC designs used by (A) Siemens-Westinghouse [88] (B) Acumentrics [72] and (C) Mitsubishi Heavy Industries [91].

1.5 Stability issues of IT-SOFCs

1.5.1 Degradation mechanisms of cell components

Demonstration of total stack durability is crucial for SOFCs commercialization. Unfortunately, operating conditions of SOFCs lead to a variety of degradation mechanisms and lifetime requirements have not been met yet. The main degradation mechanisms at cell and stack level (i.e. with interconnect) are the following for each component [92]:

- *Electrolyte*
 - o *decrease in the intrinsic electrical conductivity of YSZ electrolyte* [93]
 - o *Mechanical failure (i.e. cracking, delamination)* [23]
- *Anode*
 - o *Nickel coarsening* [94]
 - o *Carbon deposition* [95, 96]
 - o *Volumetric changes due to variations in the anode atmosphere* [23]
- *Cathode*
 - o *Chemical reactivity between cathode and YSZ electrolyte* [97]
 - o *Sr depletion from the perovskite and resistance increases in the cathode/electrolyte and cathode/current collector interfaces* [98, 99]
 - o *Poisoning by Cr species* [99, 100]
- *Metal interconnect*
 - o *Chemical interaction between glass-ceramic sealant and ferritic steel interconnects (in the planar design)* [101]
 - o *Oxidation of metal interconnect* [102]

In addition, the impact of various cycling conditions such as thermal, redox and load cycles and fuel utilization on the stability of SOFC constituents is critical [23, 103-105]. Quite recently, negative effect of impurities has been also reported in stack/system level after a long term-operation [106]. Among the investigated electrolyte materials, YSZ exhibits an excellent ionic conductivity as well as chemical stability [107] and degradation originates mainly at the electrodes. In the text which follows, main intrinsic and extrinsic degradation mechanisms which take place in the anode and cathode electrodes are described.

1.5.1.1 Anode degradation mechanisms

For common Ni-YSZ cermet anodes working on hydrogen, it is commonly accepted that the main degradation is caused due to morphological changes during operation. Sintering and coarsening of nickel particles play an important role on performance degradation [108]. Nickel agglomeration is a naturally occurring phenomenon as

thermodynamically driven force tends to decrease free energy by minimizing surface area. However, the sintering behaviour of Ni-YSZ cermet anodes is highly dependent on the wetting properties of Ni particles on YSZ. Under SOFC operating conditions, nickel agglomeration leads to a reduction of electrochemically active-sites (TPB) and the limitation of current paths [109]. It has been shown that tailoring Ni-YSZ processing parameters, long life anodes with a strong YSZ framework which prevents Ni agglomeration can be produced [110]. However, Ni is extremely unstable under redox cycles and Ni-YSZ anode suffers huge dimensional changes upon Ni oxidation. This anode stresses the electrolyte and mechanical failure occurs via crack proliferation and electrolyte delamination [23].

Other *deactivation* mechanisms include carbon deposition [95, 96] and sulphur poisoning [111] under operation with natural gas or coal gases. Those degradation mechanisms work blocking active sites or the pore network. In addition, impact of impurities by accumulation in the anode/electrolyte interface (i.e. Na_2O , SiO_2) is also reported [112].

1.5.1.2 Cathode degradation mechanism

Cathode overpotential is often the main factor limiting SOFC performance [113]. In addition, main degradation mechanisms in the cathode are [92]:

- *Decomposition of the cathode material*
- *Chemical reaction with the electrolyte and formation of insulating phases at the interfaces*
- *Cathode delamination*
- *Chromium poisoning*

All these effects are dependent on each other and may be influenced by cell operation conditions (i.e. temperature, current density, overvoltage, air flow and humidification). In order to discover the origin of degradation mechanisms, it is essential to look at the influence of operation parameters. This is also convenient for establishing “safe” operation conditions.

For conventional LSM cathode, one potential degradation mechanism is the chemical reaction with YSZ and $\text{La}_2\text{Zr}_2\text{O}_7$ and SrZrO_3 insulating phase formation at the interface between cathode and electrolyte [97]. Yokokawa et al. [92] assume that reaction between LSM and commercial 8YSZ does not occur under high temperature thermal treatment in non-operative conditions. However, Heneka and Ivers-Tiffée observed strong performance degradation attributed to $\text{La}_2\text{Zr}_2\text{O}_7$ formation and cathode spallation as a result of operation under several current cycles at overpotentials above 400 mV [114]. Posterior work demonstrated that degradation originated due to the high overpotentials. This is in agreement with findings reported by Hagen et al. [115] which found high voltage degradation at low temperature and high current densities ($>0.5 \text{ Acm}^{-2}$), that is, at high overpotential. In

the absence of metal interconnects, however, low degradation rates below 1% are reported for cells with LSM. Siemens-Westinghouse has demonstrated more than 70.000h operation for tubular cells based on such cathodes [116]. Therefore, intrinsic degradation mechanisms of LSM-based cathodes are insignificant as far as operation conditions are kept away from high overpotential and very low oxygen concentrations in the cathode side [92].

LSCF-based cathodes are more performing than LSM/YSZ composites but degradation rates are slightly higher [92]. In contrast to LSM-based cathodes, LSCF and YSZ react to undesirable phases like $\text{La}_2\text{Zr}_2\text{O}_7$ and SrZrO_3 already firing at 1210°C or 700°C for several hundred hours [117]. Even with the incorporation of a GDC diffusion barrier layer, Sr diffusion has been observed, especially during sintering [98, 117]. However, intrinsic degradation due to Sr migration out of the cathode is considered more important as it leads to strontium depletion in the LSCF perovskite. Sr segregation involves a deterioration of the perovskite conductive properties [58]. Tietz et al. [118] found Sr and to less extent La diffusion to the GDC grains surface by SIMS technique. In addition, Simner et al. [98] detected Sr enrichment on the cathode surface after operation.

In real IT-SOFC systems with metal interconnects, “extrinsic” mechanisms related to chromium poisoning dominate degradation at the cathode side. MIEC electrodes (i.e. LSF and LSCF) are probably more resistant against electrochemical deposition of Cr_2O_3 due to the extended electrochemically active area that is not restricted to the TPB. Still, there is no consensus on this subject; while Matsuzaki et al. [119] and Simner et al. [120] support this assumption, Konyshva et al. [121] observed similar degradation for LSM/YSZ and LSCF cathode compositions. Conversely, it is agreed that chemical reaction with Cr depends upon the cathode compositions. Whereas for LSM/YSZ cathodes, chromium reacts near the electrolyte partially forming $(\text{Mn,Cr})_3\text{O}_4$; for LSCF cathodes, SrCrO_4 is formed preferentially on the cathode surface [122].

In the SOFC operation framework, cathode is fed with ambient air. This air contains certain amounts of water vapour that can affect the cathode stability. However, the role of air humidification was considered only recently and it is still hardly understood.

1.5.2 Implications of IT-SOFC metal components

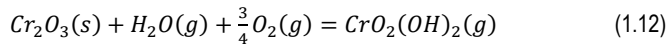
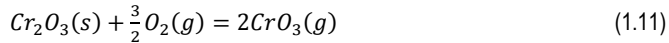
At intermediate temperatures, ferritic stainless steels are used as interconnect materials at the stack level but also as mechanical support in the newly developed metal-supported (MS-SOFC) concept. In the planar stack configuration, interconnect is placed between the anode and cathode electrodes to collect the current from cells in series arrangement. In this configuration, ferritic stainless steel must be stable in dual atmosphere (i.e. oxidizing and reducing). In contrast, in the metal-supported

SOFC configuration, ceramic functional layers (anode, electrolyte and cathode in such order) are deposited on a porous metal substrate which is fed with fuel. That is to say, metal support is only exposed to reducing atmosphere but can follow high temperature processing routes. In addition, high fuel utilization requirement (>80% in Table I - 2) involves a highly humidified anodic reducing conditions in both cases.

Chromium evaporation from ferritic stainless steel has been proved to be critical in both configurations. It is, thus, opportune to revise fundamental aspects about chromium evaporation and ambient influence in such a mechanism.

1.5.2.1 Chromium evaporation and poisoning under operation

Ferritic stainless steels contain high levels of Cr [64] which evaporate under SOFC operation and/or processing conditions. Chromia-rich scales which form in the surface of ferritic stainless steel react with water or oxygen molecules and form volatile chromium oxyhydroxide and/or Cr (VI) oxides at the high temperature (Figure I - 12). Evaporation increases in air and chromium poisoning mainly occurs in the cathode. Experimental data on the volatility of chromium from Cr(s) and Cr₂O₃(s) demonstrate that chromium is volatilized preferentially from the oxide scale and that it is enhanced in moist air over dry air [123, 124]. In dry air, CrO₃ evaporation is favored as described in Eq.(1.11) but at relatively low humidity levels (60% RH), CrO₂(OH)₂ oxyhydroxide evaporation in Eq.(1.12) is more stable [3].



On the other hand, chromium evaporation occurs at reducing atmospheres even with relatively low water vapour (96%H₂/3%H₂O) and it increases with temperature [125]. CrO(OH)₂, CrO(OH) and CrO(OH)₃ oxyhydroxides are the most stable chromium vapours in the pO₂ ≈ 10⁻¹⁰-10⁻²³ Pa range.

Cr-species evaporation does not significantly affect the chromia-scale oxidation rate below 1000°C but it can be detrimental in other ways to fuel cell performance [126]. Chromium-containing vapour species can be electrochemically or chemically reduced in the cathode. In the air side, chromium poisoning of the cathode drastically deteriorates cells performance and has been the subject of many research studies [99, 119, 121, 122, 127]. On the other hand, under reducing atmosphere, metal-supported cells suffer from massive chromium poisoning of the anode during the high temperature co-sintering required for full electrolyte densification [70, 128, 129]. Coatings which work as chromium barriers have been exclusively developed to work at oxidizing or reducing atmospheres and prevent Cr transport to the cathode or anode, respectively. A review on interconnect coatings used to protect the cathode side is reported below. Detailed description of barrier layers or coatings used in

metal-supported cells reducing conditions is reported in section 1.6, dedicated to MS-SOFC technology overview.

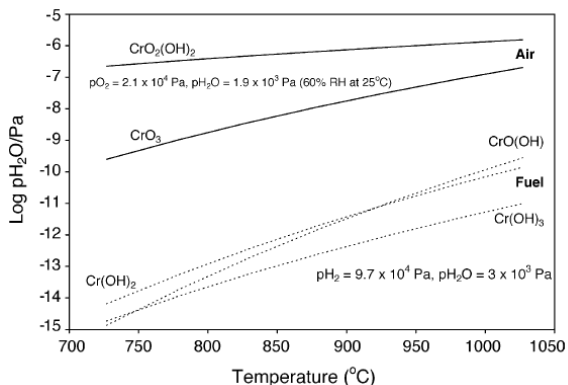


Figure I - 12. Cr(VI)-species vapour pressure in air and fuel conditions [65]. Calculations were made using thermodynamic data from Ebbinghaus [130] and assuming 60% RH at room temperature.

1.5.2.2 Metal coatings for oxidizing atmosphere

The coating material must be a good electronic conductor as well as stable in oxidizing atmosphere. Materials with low ionic conductivities are preferred to block oxygen transport to the metal interconnect. Main functions that metal interconnect coatings must fulfil are [63]:

- *Decrease oxide growth kinetics of interconnect*
- *Increase oxide scale conductivity*
- *Improve oxide scale adherence to the interconnect*
- *Inhibit chromium evaporation*
- *Sufficient electronic conductor and stable in oxidizing atmosphere*

Addition of small amount of reactive elements such as Y, La, Ce and Hf or their oxides (REOs) in the form of dispersed particles is effective to inhibit chromia-scale growth and improve its adherence. Perovskite oxides have similar effects as REO coatings and improve the oxidation resistance of the interconnect together with the contact resistance. Most common perovskite coatings include $\text{La}_{1-x}\text{Sr}_x\text{CrO}_3$, $\text{La}_{1-x}\text{Cr}_x\text{O}_3$, $\text{La}_{1-x}\text{Sr}_x\text{MnO}_3$, $\text{La}_{1-x}\text{Sr}_x\text{CoO}_3$ and $\text{La}_{1-x}\text{Sr}_x\text{FeO}_3$. In general, however, perovskite coatings do not inhibit Cr migration significantly due to the ionic conductive nature of most of them. Spinel such as $(\text{Co},\text{Mn})_3\text{O}_4$, Co_3O_4 and

$(\text{Cu,Mn})_3\text{O}_4$ show excellent capability for blocking outward diffusion of Cr as well as good electronic conductivity for appropriate compositions [63].

The techniques commonly used for the deposition of such materials on ferritic stainless steels include sol-gel techniques, chemical vapour deposition (CVD), pulsed laser deposition, plasma spraying, and screen printing.

1.6 Metal-supported SOFC overview

1.6.1 Technology and approach

Metal-supported cells date from the 1960s, when a cell including a presintered austenitic stainless steel substrate with flame-sprayed zirconia based electrolyte was first fabricated [131]. At that time, 115 mWcm^{-2} were recorded at 770°C and fuel flexibility demonstration, with cell operation in hydrogen, methanol and kerosene, broke down and opened the way for this new SOFC design rapid development. By the 1990s, power densities approached 1 Wcm^{-2} at 900°C with tubular presintered NiCrAlY [132] and planar $\text{CrFe}_5\text{Y}_2\text{O}_3$ [133] coated with plasma sprayed zirconia electrolytes. Cost reduction was considered priority and in the 2000s, colloidal and wet-chemistry methods, already used for anode-supported SOFC, were also implemented in metal-supported cells. Those inexpensive deposition techniques produced thinner electrolytes that lowered operation temperatures in favor of low-cost ferritic stainless steels. MS-SOFC concept was pioneered at Imperial College/spin-off Ceres Power for GDC electrolyte [134] and at LBNL for YSZ electrolyte [135].

Metal-supported SOFC is potentially distinguished from alternative anode and electrolyte-supported SOFC thanks to the excellent mechanical stability, lower cost, robustness under transient conditions and rapid start-up times. Interest in the field has rapidly increased during the last 20 years. Significant technical progresses have been achieved by Aerospace Research Center and Space Agency (DLR) and Plansee [128, 136], Ceres Power and Imperial College [137], Topsoe/Risoe [138], Lawrence Berkeley National Laboratory (LBNL) [135] and IK4-Ikerlan [70, 102, 105, 139].

In the intermediary operation temperature, around $500\text{-}800^\circ\text{C}$, High-Cr ferritic steels have been favoured as interconnect materials due to their low-cost, TEC match to common electrolyte materials, formation of conductive protective layers and adequate low oxidation rate. Those steels typically contain between 10.5 wt% Cr to form a continuous chromia scale and no more than 26 wt% Cr to avoid brittle sigma phase formation at higher Cr content. TEC in $10\text{-}12 \text{ ppmK}^{-1}$ range is compatible to conventional electrolytes (LSGM, YSZ and GDC) [140, 141]. Main ferritic-stainless steels employed comprise Crofer 22 APU [142] and ITM (Plansee) [143].

1.6.2 Ceria-based MS-SOFC

The low operating temperatures and chemical nature of ceria-based electrolytes (500-600°C) permit full electrolyte densification through constrained-sintering. This means that electrolyte is deposited on a prefabricated support that shrinks very little or nothing during processing for full-densification of electrolyte. It has been recognized that sintering aids improve GDC sintering at low temperature [144, 145]. For instance, with 3 mol% Li as dopant in $\text{Ce}_{0.9}\text{Gd}_{0.1}\text{O}_{1.95}$, sintering to 99% of full density at a record-low temperature of 800°C was achieved [146]. More recently, full-dense GCO electrolyte with iron-aids was reported by the implementation of wet-spraying and pressing with posterior sintering at 1050°C [147].

The first major industrial initiative on MS-SOFC came from Ceres Power based on the work conducted at Imperial College of London by Steele et al. with ceria-based electrolytes [148]. Maximum power densities of 350 mWcm⁻² were obtained at 600°C with perforated Ti-Nb-stabilized 17%Cr ferritic stainless-steel and fully dense 10-30 μm GCO electrolyte which was deposited by electrophoretic deposition and sintered below 1000°C [134]. Stability is also promising with 2.3% degradation over 1000 hours for >2500h galvanostatic operation and 5% degradation over the 20 thermal cycles (10°Cmin⁻¹ heating rates) which were reported in 2005 [149, 150]. Ceres Power has recently started MS-SOFC commercialization activities on a natural gas fed CHP (1kW) and public update on recent technical advances have not yet been provided.

1.6.3 YSZ-based MS-SOFC

YSZ offers some advantages over GCO and it is used by many MS-SOFC developers. The allowed operation range is favourable for internal reforming (i.e. >650°C), which reduces system complexity and eliminates the need of an external pre-reformer, generally required for cells based on GCO [134, 149]. Nevertheless, YSZ cannot be sintered to full density in a constrained geometry and therefore two distinct processing routes are adopted to overcome this limitation:

- i) Near-dense YSZ deposition on a preformed surface
- ii) Colloidal/wet YSZ deposition onto a green substrate followed by co-sintering to full density

1.6.3.1 Plasma-spray sintering

Near-dense films are deposited on a preformed substrate by techniques that include atmospheric plasma spray processing (APS) [151, 152], vacuum plasma spraying (VPS) [153-155], suspension plasma spraying (SPS) [156], pulsed laser deposition (PLD) [157] and electrophoretic deposition [149]. This is certainly advantageous for

the metal-support. First, lower thermal treatment required for full electrolyte densification protects ferritic stainless steel from excessive oxidation. Second, separated processing of ceramic layers permits metal substrate microstructure and porosity to be controlled more easily. However, restrictions related to this processing technique still exist. In order to guarantee a gas-tight electrolyte, lower thermal treatment demands thicker green YSZ layers (30-70 μm). The apparent ionic conductivity of plasma-sprayed electrolyte is also substantially lower than for sintered YSZ [158]. Therefore, acceptable efficiencies are restricted to operate above 800°C.

Plasma-sprayed concept for cell fabrication was introduced by the German Aerospace Center (DLR) in late 90s [128, 129, 133, 158, 159]. Basic cell concept includes ferritic stainless steel, $\text{La}_{0.6}\text{Sr}_{0.2}\text{Ca}_{0.2}\text{CrO}_3$ or $\text{La}_{1-x}\text{Sr}_x\text{MnO}_3$ diffusion barrier layer (DBL), Ni-YSZ anode, 35-50 μm YSZ electrolyte and LSM or LSCF cathode which are deposited by an integrated multistep plasma-spray process and do not need any post deposition sintering steps. As an exception, 2-3 μm thin $\text{La}_{1-x}\text{Sr}_x\text{MnO}_3$ DBL is deposited by physical vapour deposition (PVD). Performance of a single cell has achieved 609 mWcm^{-2} at 800°C [136, 158]. A proof-of-concept stack design for APU is now under development in a consortium with Plansee: performance of 384 mWcm^{-2} with 32% fuel utilization is the best result to date [136, 158].

1.6.3.2 Co-sintering

“Wet” or “colloidal” deposition techniques allow 10-20 μm thin gas-tight YSZ electrolytes to be produced and therefore a more efficient cell can operate at desirable 650-700°C for ferritic stainless steels. Colloidal techniques include dip-coating, screen printing, tape-casting, aerosol spray-coating, spin-coating and drip-coating. Deposition occurs at low temperatures and it produces a green porous YSZ layer. This is followed by a high-temperature sintering step to achieve full densification of the YSZ layer (typically 1200-1400°C).

Co-sintering was originally proposed and developed by LBNL [135], and it is pursued by IK4-Ikerlan [70, 102, 105, 139], Riso/Topsøe [138, 160-163] and Plansee [143, 164].

1.6.4 Key problems and degradation mechanisms in current MSC concepts

Independently of the fabrication process (sintering or plasma-spraying), the principal degradation mechanisms that are identified in the current MSC concepts are:

- (1) Metal-substrate corrosion
- (2) Ni, Cr and Fe interdiffusion between the metal-substrate and anode layer
- (3) Ni coarsening

The fabrication process, whether by sintering or plasma-spraying is closely related to those events. FeCr substrates have a limited corrosion resistance and any cell processing above 900°C requires a non-oxidizing atmosphere (inert or reducing) to prevent oxidation of the metal support. Nickel oxide is reduced *in-situ* during the co-sintering process leading to nickel coarsening. In addition, high temperatures promote element interdiffusion between the metal substrate and anode. Nevertheless, those degradation mechanisms still occur under SOFC operation conditions.

1.6.4.1 Metal-substrate corrosion

Earlier studies [165, 166] have demonstrated satisfactory long-term corrosion resistance of ferritic stainless steels with Cr-content >20 wt% and low manganese contents (0.02-0.05 wt%) under SOFC operation conditions. However, in the MS-SOFC field, the corrosion resistance of analogous porous metal substrates decreases significantly. This is attributed to the high surface to volume ratio of the ferritic steel support, compared to dense metal interconnects [128].

The formation of a protective Cr₂O₃ chromia scale is critical for longevity of a metal-supported SOFC. Chromia-scale protects metal substrate from corrosion but gradual growth by outward diffusion of chromium ions leads to spallation (i.e. cracking and delamination of the chromia scale), break-away oxidation and destruction of the cell after certain time of exposure [126]. Although the oxygen partial pressure is low on the anode side (10⁻²⁴-10⁻²⁶ Pa), it is high enough for Cr₂O₃ to be stable. Corrosion is accelerated at higher temperature, as the chromia growth rate increases. Spallation occurs more frequently for chromia layers above 3-5 μm and breakdown estimated above 3 μm serves to predict metal-substrates lifetime [167]. Oxidation rates are higher for ferritic stainless steels than for nickel-based alloys [65] and shows a strong dependence upon temperature. According to Tucker [20], both mobile and stationary applications require a limited growth of adherent scales below 3 μm. This imposes a relatively narrow operation window. Whilst mobile applications specifications (i.e. 5000 h) obliges operation at 800°C, for long lasting stationary applications, lifetime requisites (i.e. 50000 h) involve intermediate operation temperatures, in the 650-700°C range [20].

Fuel utilization and water vapour effect

During operation, especially at high fuel utilization, moisture affects FeCr substrate stability. Efficient SOFCs require high fuel utilization and metal-support must be resistant in atmospheres which contain high water concentrations, as iron becomes susceptible to corrosion around 50% of water in the ambient (section 4.4.3.1).

Experimental evidences exist which confirm the dissimilar influence of moisture in oxidizing and reducing atmospheres. Webber et al. found no differences in the oxidation rate of FeCr alloys in dry and moist air at 850-1050°C [168]. However, in a

more recent publication by Hänsel et al. [169], it was confirmed that the oxidation rate of Cr-base alloys change under the influence of water vapour, but only in atmospheres with low oxygen partial pressure. $p_{\text{H}_2\text{O}}/p_{\text{H}_2}$ ratio increase aggravates chromia scale-growth and forms sharp oxide blades. In addition, stainless steel scales formed in anodic conditions (850°C, moist hydrogen) display several times higher resistance than those formed in air [170, 171]. Conversely, one beneficial effect of water vapour is that it can improve chromia scale adherence by reducing the porosity in the alloy/scale interface [66, 172].

1.6.4.2 Ni, Cr and Fe interdiffusion between the metal substrate and anode layer

FeCr substrate/anode interdiffusion during co-sintering

At the high temperatures necessary for the full densification of the electrolyte, Ni, Fe and Cr interdiffusion occurs [70, 128, 129]. In one hand, diffusion of Fe and Cr into the Ni-containing anode can cause formation of insulating phases such as Cr_2O_3 , NiCr_2O_4 and FeO , etc. which affect the catalytic activity [20]. Besides, nickel incorporation within the ferritic stainless steel may cause austenitization. This involves inferior corrosion resistance of the metal-support together with a TEC increase. As a matter of fact, austenitic steels have a TEC between 18-20 ppmK^{-1} which is not compatible with 10-12 ppmK^{-1} of main electrolytes (YSZ, GDC, LSGM) [20]. Besides, element interdiffusion is not exclusive to co-sintering. It has been shown that regardless of electrolyte material and processing choice, interdiffusion can occur during operation of the cell [129]. Straight application of pre-oxidized FeCr substrates with self-grown Cr_2O_3 and Cr_2MnO_4 as diffusion barrier layers was evaluated but early results confirmed still the presence of Cr and Ni interdiffusion [173, 174]. Hence, a diffusion barrier layer (DBL) between Ni-based anodes and FeCr-alloys is highly recommended.

Diffusion barrier layer (DBL)

There are two possibilities to integrate a DBL between the metal substrate and anode layer [175]. A diffusion barrier layer can be coated or sintered. Coating techniques include plasma-spraying [136] and physical vapour deposition (PVD) [136, 143] and are more adequate to obtain a thin DBL with good properties. DBL deposition using colloidal techniques (i.e. screen printing or dip-coating) is combined with a co-firing process in which metal substrate, the DBL and the anode can be fabricated simultaneously [70, 176]. However, in both cases DBL should be relatively porous to permit fuel transport to the electrochemically active anode. Alternatively, a metal substrate enables the creation of a fine and dense particle coating by means of a pre-oxidation process. Self-grown CrO_3 and MnCr_2O_4 oxide-scales [173] were proposed but not successful suppression of Fe, Cr and Ni was obtained. Sr- and Ca-

doped LaCrO_3 type perovskites can also be plasma sprayed onto the substrate surface [129].

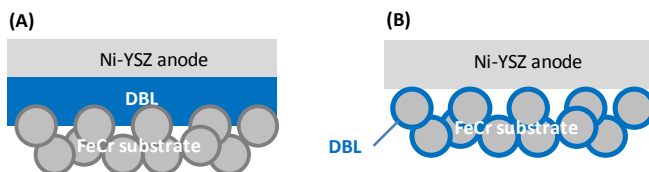


Figure 1 - 13. DBL intergration following to methods: (A) coating of the metal substrate surface with a porous DBL structure and (B) coating of the substrate particles by a dense and passivated oxide scale.

Independently of the structure, a DBL should satisfy the following requirements [129]:

- *Effective barrier against Fe, Cr and Ni diffusion*
- *Compatible TEC with adjacent components*
- *High electronic conductivity in reducing and humidified anode gas atmospheres (1-3 S/cm)*
- *Chemical compatibility with metal substrate and anode material*

Two main anode-barrier groups have been proposed in the literature: ceria-based and perovskite-based materials.

Ceria-based DBL

Ceria-based DBL (CeO_2 and $\text{Ce}_{0.8}\text{Gd}_{0.2}\text{O}_2$) demonstrated to be effective against interdiffusion [173, 174]. However, doping CeO_2 with gadolinium translate in oxygen vacancies being introduced in the fluorite and ionic conductivity increases. This is also related to Ce^{3+} decrease and a deterioration of electronic properties. Therefore, pure CeO_2 has been preferred to work as DBL, initially. Plansee has reported chemical stability at 800°C during 1000 h for a $4\ \mu\text{m}$ thick CeO_2 DBL and proposed to add a complementary Cu layer which successfully decreased contact resistance with FeCr-substrate [174].

In IK4-Ikerlan, ceria-based materials potential use as DBL has been also investigated. It is well known that Sm and Gd-doped CeO_2 (SDC, GDC) exhibit better electronic conductivities at intermediate temperatures. However, at IK4-Ikerlan's operation temperature (800°C), the effect of the doping element is not significant [177, 178] and low cost YDC was seen as an attractive candidate. Investigated materials included Sm-doped CeO_2 (SDC), Y-doped CeO_2 (YDC) and Zr-doped CeO_2 (ZDC). SDC showed poor chemical stability and a continuous $(\text{SmFe})\text{CrO}_3$ perovskite layer formed due to reactivity at 1350°C in the interface between metal substrate and SDC [179]. Moreover, not only dense $(\text{SmFe})\text{CrO}_3$ and SDC barrier

were blocking fuel transport, stresses due to (SmFe)CrO₃ formation and crack proliferation in the SDC barrier were also observed, leading to the mechanical failure of the cell. On the other hand, YDC and ZDC also reacted with the metal substrate and formed CeCrO₃. However, this phase formation is not considered detrimental as extensively studied CeO₂ protective coatings for ferritic interconnects do not indicate any resistance increase [180, 181]. Nevertheless, ZDC densification ability is considerable and metal-supported cells with Ni-ZDC cermet DBL showed diffusion problems and low performance. Finally, Ni-YDC cermet with incorporated nickel (<20% Ni) to improve electronic conductivity was adopted as DBL for a first generation of MS-SOFCs at IK4-Ikerlan [179].

Perovskite-based DBL

Franco and coworkers at DLR and Plansee consortium [128, 129, 143] have adopted the same perovskite-type DBL that they use in the air side to prevent Cr poisoning of the cathode. Selected perovskites are essentially lanthanum chromites with different dopants and stoichiometries (i.e. La_{0.6}Sr_{0.2}Ca_{0.2}CrO_{3-δ}, La_{0.7}Sr_{0.15}Ca_{0.15}CrO_{3-δ}, La_{0.7}Sr_{0.15}CrO_{3-δ}) and lanthanum manganites (La_{1-x}Sr_xMnO₃). Fundamentally, plasma-spray techniques which do not require a posterior thermal treatment have been used for DBL processing. More recently, thin La_{1-x}Sr_xMnO₃ deposited by physical vapour deposition (PVD) was integrated in the manufacturing process. To date, best results were attained by DLR and Plansee consortium with La_{0.6}Sr_{0.2}Ca_{0.2}CrO₃ (10-30 μm) and La_{1-x}Sr_xMnO₃ (2-3 μm) perovskite DBLs [158]. Robust MSC degraded 1%/kh when it was operated at 800°C during 2000 h. It was stable to withstand 20 full redox cycles with no OCV loss and less than 2.5% degradation in power density.

At IK4-Ikerlan, a second generation of MS-SOFCs includes a perovskite-type DBL. La and Y-doped SrTiO₃ perovskites (LST, YST) exhibit excellent electronic conductivity under reducing atmospheres [26-30]. However, LST is easier to fabricate and it was tested together with lanthanum chromate during an initial screening procedure. Selected stoichiometries were La_{0.7}Sr_{0.3}TiO_x and La_{0.7}Sr_{0.3}CrO_x. Reactivity proofs demonstrated that LSC reacted with the metal support as well as with Ni-YSZ anode leading to Sr₂CrO₄ and Ln₂NiO₄ phases formation, respectively [179]. Those phases are not necessarily harmful and Ln₂NiO₄ has been proposed in the literature as an alternative cathode material [182]. Nevertheless, most of literature data correspond to operation conditions in oxidizing atmosphere and are not representative for the anode side. On the other hand, reactivity of LST perovskite is practically inexistent with metal substrate and anode. As an exception, an unidentified phase which contains Mn-Cr-Ti-O was detected by XRD as a minor by-product of FeCr and LST reactivity at 1350°C [183]. Conductivity tests were carried out in reducing atmosphere with LST and LSC after a thermal treatment that reproduces the cell sintering step. In the 600-800°C temperature

range, LST perovskite exhibited electronic conductivity 1-2 orders of magnitude higher than LSC; 2-8 S/cm were recorded for LST and 0.03 - 0.08 S/cm for LSC [179]. Difference between LST and LSC is in agreement with findings in the literature but values are much lower for LST. While at reducing atmosphere 216 S/cm are reported for $\text{La}_{0.3}\text{Sr}_{0.7}\text{TiO}_{3-\delta}$ [184] at 800°C, conductivity for $\text{La}_{0.7}\text{Sr}_{0.3}\text{CrO}_x$ is 0.05-0.1 S/cm. As a matter of fact, most performing lanthanum chromites, $\text{La}_{0.6}\text{Sr}_{0.2}\text{Ca}_{0.2}\text{CrO}_{3-\delta}$ and $\text{La}_{0.7}\text{Sr}_{0.15}\text{Ca}_{0.15}\text{CrO}_{3-\delta}$ show 1.6 and 1.2 S/cm, respectively [175]. Lower conductivity of $\text{La}_{0.3}\text{Sr}_{0.7}\text{TiO}_{3-\delta}$ as measured in IK4-Ikerlan was attributed to variations in perovskite stoichiometry upon cell fabrication. Finally, $\text{La}_{0.3}\text{Sr}_{0.7}\text{TiO}_{3-\delta}$ perovskite was adopted as the DBL of second generation MS-SFCs in IK4-Ikerlan. LST perovskite demonstrated to be an excellent barrier towards Cr, Ni and Fe interdiffusion during sintering as it will be seen later on chapter IV.

1.6.4.3 Nickel coarsening

Co-sintering is implemented at high temperature in reducing atmospheres to protect the metal-support [128, 138, 185, 186]. However, nickel reduction at high temperature promotes sintering and vast agglomeration as NiO is reduced to Ni [187]. TPB and thus active area significantly decreases in the coarse Ni-YSZ final structure. In many cases, it inhibits electronic percolation through the electrode, significantly enhancing ohmic losses [167]. In addition, agglomerated nickel is more susceptible to redox cycles. Nickel particles suffer dramatic dimensional changes upon reoxidation (69.6% in volume) which stresses the electrolyte causing the mechanical failure of the electrolyte.

Infiltration

LBNL [186, 188] and more recently Risoe [138, 161, 162] adopted Ni-infiltration to avoid nickel agglomeration. For infiltration, the procedure is the following:

- (1) A porous YSZ anode structure is co-sintered with the metal support and electrolyte in the standard high temperature and reducing atmosphere.
- (2) Ni catalyst is subsequently infiltrated by the precursor method.

Resultant microstructure with nano-scaled Ni particles exhibits high performances together with better stability upon redox cycles. Though Ni-infiltration excellent initial performances (1Wcm^{-2} at 650°C) were registered, unfortunately, rapid degradation due to nickel agglomeration was observed [186]. Co-infiltration of ceria-based catalysts improves stability but still compromises the electronic conductivity [167]. Performance limitation can be addressed adding a further electronic conductive component in the anode backbone. Risoe-Topsoe has proposed metal stainless steel particles addition with promising results [160]. Cu

catalyst addition is another option as it has been shown by Ni replacement in the newly patented Cu-YSZ cermet anode [189].

Chapter II

EXPERIMENTAL TECHNIQUES

2.1 Electrochemical characterization

IV-curves and Electrochemical Impedance Spectroscopy (EIS) are powerful techniques widely used for SOFC electrochemical characterization. In this section, both techniques are introduced and experimental equipment in both, SOFCpower and IK4-Ikerlan laboratories are described.

2.1.1 Test furnaces

The electrochemical characterization of anode-supported cells (Chapter III) was carried out in Hobylland horizontal furnaces. Conversely, metal-supported cells (Chapter III) were tested in Carbolite VST 12/-/200 vertical furnaces.

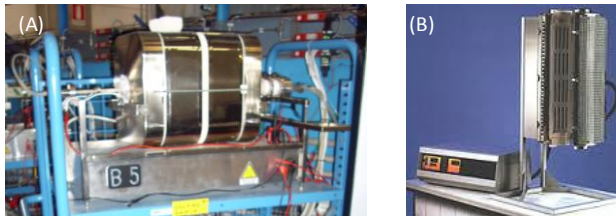


Figure II - 1. Testing furnaces: (A) Hobylland and (B) Carbolite VST 12/-/200.

2.1.2 Air humidification

Planar ASC air humidification

In the specific design of experiments used in Chapter III, dry air, 3 or 20% humidified air stream was used. Different humidification levels were attained by using a bubbler with distilled water. For 3% humidification, the bubbler was introduced in a bath at 25°C (Figure II - 2). For 60% humidification, it was put in a heating plate and air circuit to the furnace entry was thermally insulated to avoid water condensation.

Tubular MSC air humidification

MSCs work with ambient air and thus, air humidification depends upon ambient conditions in the laboratory.

2.1.3 Fuel humidification

Planar ASC fuel humidification

Fuel is 3% humidified by circulating the pure hydrogen fuel flow in a bubbler with distilled water which is maintained at 25°C in a bath. Stability tests are performed in the same way (Figure II - 2A).

Tubular MSC fuel humidification

For simple electrochemical characterization, the fuel is humidified with a bubbler with distilled water at ambient temperature. Thus, 2-3% fuel humidification is obtained (Figure II - 2A).

For *simulated* fuel utilization tests, fuel is highly humidified using a Controlled Evaporator Mixer (CEM, Bronkhorst) as illustrated in Figure II - 2B. Circuit to the cell is thermally insulated to avoid water condensation. In this work, 25-80% H₂O in the fuel was used for a specific analysis of the water vapor effect in the electrochemical performance. For generalized fuel utilization tests, 50% H₂O was used in the fuel stream.

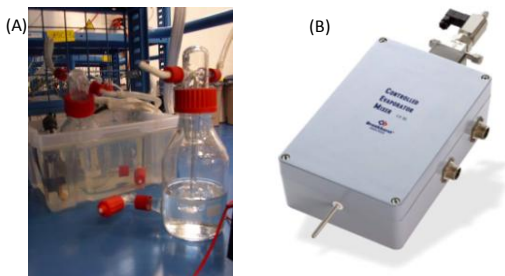


Figure II - 2. Humidification methods: (A) Bubbler with distilled water and (B) Bronkhorst Controlled Evaporator Mixer (CEM).

2.1.4 IV curves

IV curves, by the simple application of an electrical current and the analysis of the potential response, are used to study the cell electrochemical performance. The power density of cell at 0.7V is typically used to characterize performance at realistic operation conditions. However, IV curves also provide with useful information about specific irreversibilities and voltage losses. A detailed description is reported in section 1.2.2.

Planar ASC characterization

In SOFCpower, every test bench include an Agilent DC power supply with 4A and 50V limits, fuel and air mass flow controllers and a thermocouple. Current density and cell voltage, fuel flow and cell temperature are monitored and controlled with a PC which includes an integrated multichannel data acquisition system.

Tubular MSC characterization

IV curves were performed with a power source integrated to a data acquisition system developed at IK4-Ikerlan and controlled with a PC. This system allows the application of electrical current below 3.2 A and potential between 0 and 5V.

For long-term stability tests, a special system which permits the simultaneous measurement of 16 cells was used. This data acquisition system was developed at IK4-Ikerlan and allows applying 6 A maximum current. This system is also able to control the furnace temperature and the fuel mass flow in some cases. In addition, a UPS system protects the experimental system of the laboratory from eventual power cuts in the electrical grid.

2.1.5 Electrochemical Impedance Spectroscopy

Electrochemical impedance spectroscopy (EIS) is a powerful method for the characterization of electrode processes and complex interfaces. This sensitive technique was complemented with IV-curves to elucidate the interfacial processes and main contribution to electrochemical performance.

Electrochemical impedance is usually a potentiostatic measurement; applying an AC potential to an electrochemical cell and then measuring the current through it. Inversely, a galvanostatic measurement can be performed by applying an AC current and measuring the potential through the cell. In order to obtain a pseudo linear response of the cell, a small excitation signal is applied. In a linear (or pseudo-linear) system, the current response to a sinusoidal potential will be a sinusoid at the same frequency but shifted in phase.

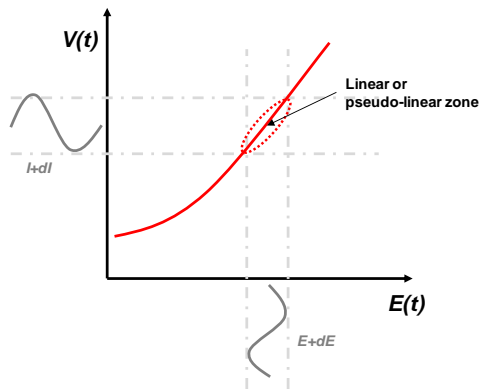


Figure II - 3. Relation between the applied potential, $E(t)$, and the current response, $I(t)$.

The excitation signal, expressed as a function of time, has the form

$$E(t) = E_0 \sin \omega t \quad (2.2)$$

where E is the potential at time t , E_0 is the amplitude of the signal, and ω is the radial frequency. In a linear system, the response signal, $I(t)$, is shifted in phase (φ) and has a different amplitude, I_0 .

$$I(t) = I_0 \sin(\omega t + \varphi) \quad (2.3)$$

Analogous to Ohm's Law, the impedance (Z) of the system is calculated as:

$$Z(t) = \frac{E(t)}{I(t)} = \frac{E_0 \sin wt}{I_0 \sin(wt+\varphi)} = Z_0 \frac{\sin wt}{\sin(wt+\varphi)} \quad (2.4)$$

The impedance is therefore expressed in terms of a magnitude, Z_0 , and a phase shift, φ . With Eulers relationship it is possible to explain the impedance as a complex function. The potential is expressed as,

$$E(t) = E_0 e^{j\omega t} = E_0(\cos \omega t + j \sin \omega t) \quad (2.5)$$

and the current response as,

$$I(t) = E_0 e^{j(\omega t - \varphi)} = E_0(\cos \omega t - \varphi) + j(\sin \omega t - \varphi) \quad (2.6)$$

Thus, the impedance expression as a complex number holds as

$$Z(\omega) = \frac{E_0 e^{j\omega t}}{I_0 e^{j(\omega t - \varphi)}} = Z_0 e^{j\varphi} = Z_0(\cos \varphi + j \sin \varphi) \quad (2.7)$$

Note that the impedance, Z , is a function of the radial frequency, ω , because the shift in phase, φ , changes with it ($\varphi(\omega)$).

The most popular impedance representations include the Nyquist and Bode plots. Whereas the Nyquist plot is a representation of the real and imaginary parts of the impedance; in the Bode plot, the phase shift, φ , and impedance module, Z_0 , are represented as a function of the frequency (f) (Figure II - 4). Through this work the Nyquist representation has been widely used to identify the electrochemical resistances; area specific resistance (ASR), ohmic resistance (R_o) and polarization resistance (R_p) as indicated in Figure II - 4.

- R_o is evaluated at high frequencies in the intersection point of impedance with the real axes.
- ASR is evaluated at low frequencies in the intersection of impedance with the real axes
- R_p is the difference between both intersections at high and low frequencies, thus, ASR- R_o

The meaning of the electrochemical values in the fuel cell context is explained in section 1.2.2.

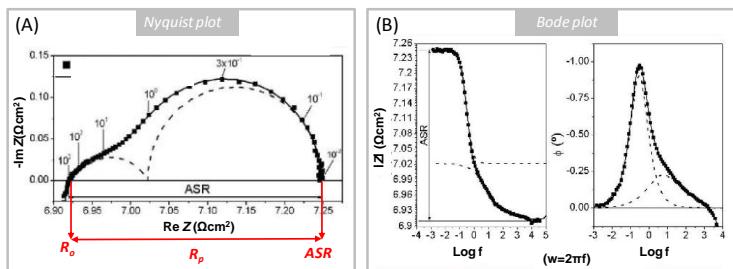


Figure II - 4. (A) Nyquist diagram and (B) Bode diagram of a SOFC [190].

The characteristic profile of the Nyquist diagram is a result of the superposition of ideal semicircles with a characteristic "time constant". Each semicircle corresponds to a specific resistive mechanism in the cell (i.e. electrolyte resistance, capacitance in the electrode/electrolyte interface, charge transfer, electrode polarization). Thus, EIS data can be also analyzed by fitting to an equivalent electrical circuit model using resistors, capacitors, and inductors. However, in this work, EIS technique was used to identify the electrochemical resistance values ASR, R_o and R_p . The EIS equipment and conditions used during measurement with ASC (Chapter III) and MSCs (Chapter IV) are reported in the text which follows.

2.1.5.1 ASC and MSC characterization

Impedance spectroscopy measurements were performed by using PGSTAT302N (Metrohm Autolab) high current potentiostat/galvanostat combined with the FR2A (Metrohm Autolab) frequency response analyzer module (Figure II - 5). Impedance was measured in potentiostatic (0.7 V) condition and frequency range was 10 kHz to 0.1 Hz with signal amplitude of 10 mV. The impedance data were normalized by the active contact area between the gold or Crofer mesh and LSC current collector. Impedance spectroscopy measurements were carried out at the beginning and at the end of the 500 h durability tests. Impedance spectroscopy measurements were recorded both at operation (Table III - 2) and standard conditions (150 ml/min cm^2 dry air and 750°C).

Two different equipments were used to perform the impedance measurements: Solartron 1286 electrochemical interface connected to Solartron 1266 frequency response analyzer module and Zanner Zennium electrochemical interface combined to a Zahner PP2241 (Figure II - 5). The standard electrochemical characterization of metal-supported cells was performed at 800°C with 3% humidified 200 ml min^{-1} H_2 in the anode side and ambient air in the cathode side. The impedance data were normalized to the active area (i.e. cathode area). Data were acquired at OCV conditions and at 0.7V operational voltage.



Figure II - 5. Electrochemical Impedance Spectroscopy equipment: (A) Autolab, (B) Solartron and (C) Zanner.

2.2 Microstructural characterization

Through this work, the microstructure analysis of anode-supported and metal-supported cells was carried out using Scanning Electron Microscopy, Energy Dispersive X-ray analysis and X-ray diffraction techniques. In this section, fundamental aspects and experimental procedure are reported.

2.2.1 Scanning Electron Microscopy (SEM) and Energy Dispersive X-ray analysis (EDS)

Planar ASC characterization

Scanning Electron Microscope (SEM) (JSM5500, Jeol - Japan) equipped with EDS (Energy Dispersion X-ray Spectroscopy) (EDS2000, IXRF System - USA) was used for microstructural analysis (Figure II - 6) of anode-supported cells. Samples were prepared by clean manual cracking of the anode-supported cells. Cross sections were cleaned-up with compressed air and metalized with Au in vacuum. For microstructural analysis of GDC barrier layers surface, chemical etching of the cathode was carried out by exposing cells to hydrochloric acid for 1 min and then to ultrasonic bath for 10 min.

Tubular MSC characterization

The microstructure of metal-supported cells was characterized by a FEI 200 Quanta FEG-SEM and EDS EDAX Genesis (Figure II - 6) at CIC-Energigune installations.

Samples were prepared following the standardized process at IK4-Ikerlan due to the complex nature of porous metal plus fine ceramic multilayered structure. Cells are embedded, cut and polished for transversal inspection in the microscope. Cells are embedded with an Epofix resin in vacuum (Epovac Chamber-Struers) to promote resin penetration in the porous metal substrate. The resin is mixed with hardener agent (Epofix Hardener) that produces solid samples in 24h. Embedded samples are cut by abrasion with a diamond disk that is refrigerated with an integrated water circuit (Secotom 10 - Struers). Next, transversal surface of cells is polished in two

phases in a Tegrapol 11 polisher (Struers). First, sample is polished with SiC sandpaper lowering grid sizes (i.e. P600, P800, P1200, P2400, P4000 in sequence) and using water as lubricant and refrigerator. In a second phase, samples are polished with diamond suspensions (9 μm , 3 μm , 1 μm in sequence). After polishing, samples are cleaned-up in an ultrasound machine with ethanol during 10 min. Finally, they are painted with carbon ink and scotch to guarantee an adequate current flow through the cell. Some cells were coated with carbon and gold thin films using a metallizer (Structure Probe Inc.). Equipment for sample preparation is shown in Figure II - 7.

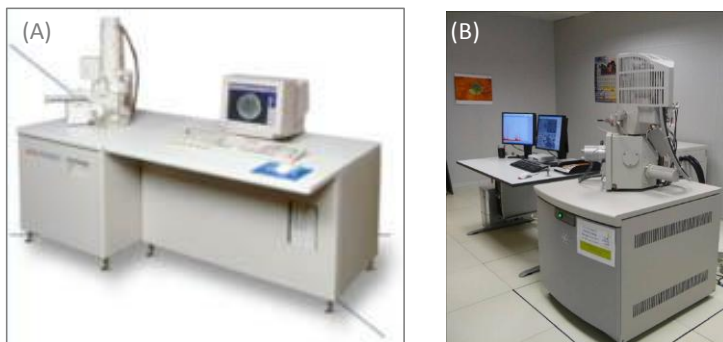


Figure II - 6. SEM equipment : (A) JSM5500, Jeol with EDS2000 and (B) FEI 200 Quanta FEG-SEM and EDS EDAX Genesis.

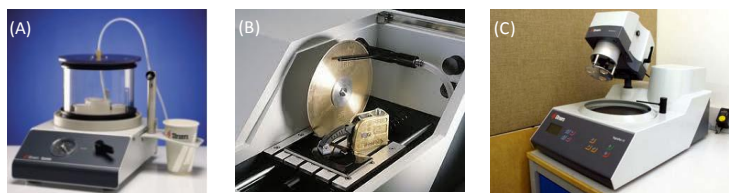


Figure II - 7. Sample preparation equipment: (A) Struers Epovac - vacuum impregnation, (B) Secotom-10 precision cut-off machine with diamond wheels (Struers, Inc.) and (C) polishing machine Struers TegraPol-11.

2.2.2 X-ray Diffraction

Planar ASC characterization - Surface analysis

Crystalline phases which form on the surface of anode-supported SOFCs during operation were analyzed in a Rigaku D-MAX III diffractometer with monochromatic CuK α radiation (Figure II - 8). In this configuration, incident X-rays diffract in the vertically mounted sample (i.e. cell surface) and the diffracted or reflected beam is focused into a diffracted beam monochromator. The sample holders can accommodate 30x30x10 cm in size and cells surfaces are cut to fit the required dimensions. The sample and detector are rotated with respect to the incident beam at 2θ angles. Data were collected in the Bragg-Brentano (reflection) geometry over a range of $10-90^\circ 2\theta$.

Tubular MSC characterization - Reactivity of LST and YSZ

X-ray diffraction technique was also used to analyze the reactivity of LST perovskite and YSZ fluorite at high temperatures under different atmospheres. Polycrystalline samples were prepared by crashing previously sintered LST+YSZ pellets in a mortar. Diffraction measurements were carried out in the Energy Research Institute (IER) in Albacete (Spain). X'PERT Pro XRD diffractometer with monochromatic CuK α 1 radiation, equipped with an ultra-fast X'Celerator detector was used (Figure II - 8). Data were collected in the Bragg-Brentano (reflection) geometry over a range of $10-90^\circ 2\theta$.

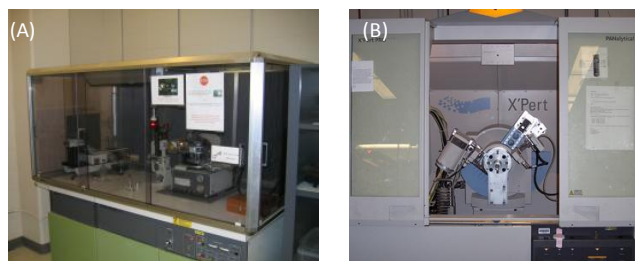


Figure II - 8. Images of used diffractometers: (A) Rigaku D-MAX III and (B) X'Pert PRO X-ray diffractometer coupled to an X'Celerator detector.

2.3 MSC fabrication and characterization

2.3.1 Processing techniques and equipment

2.3.1.1 Attrition

During cells processing, Attritor 01HD-CE (Figure II - 9) was used for anode and cathode powders preparation; that is, i.e. Ni-YSZ cermet anode and LSF40-SDC composite cathode. This technique serves to prepare powder mixtures but also for particle size reduction.

The functioning principle of this equipment consists in the stirring of powder and attrition balls in a tank with rotator blades. Rotation speed is sufficient to promote an irregular motion of powder and balls. Resulting wear stress and impact forces allow a gradual reduction of the particle size as well as an optimal dispersion.

This technique is highly efficient as the rotation energy is directly used in the milling process. Balls are typically small to multiply the effect and rotated at high speed. Typically, spheres between 1/8'' and 3/8'' in diameter include carbon steel, stainless steel, chromium steel and zirconia as composition. In this work, zirconia balls of 2 mm in diameter were used for anode and cathode processing.

Powders are placed in the middle of the milling media strategically to obtain a homogeneous mixture. First, half milling media, next, ceramic and metallic powders, and then, the other half of milling media are introduced in the tank. 250 ml of isopropanol are added at the end. After 3 and 0.5 h operating at 500 rpm for anode and cathode preparation, respectively, powder mixtures are separated from milling media and put drying below an infrared lamp. Once dried, powder blocks are sieved using a nylon mesh with 100 μm aperture. During this process, nickel particle size is reduced from 10 μm to 0.5 μm .

Table II - 1. Specifications for Ni-YSZ anode and LSF₄₀-SDC cathode powder preparation in the attritor.

Component	Material	Quantity (g)	Milling media quantity (g)	Milling time (h)	Velocity (rpm)
Ni-YSZ anode	NiO	197.1	1300	3	500
	YSZ	102.9			
LSF-SDC Cathode	LSF40	210	1000	0.5	500
	SDC	90			

*YSZ balls with 2mm diameter as milling media



Figure II - 9. 01HD-CE wet grinding attritor.

2.3.1.2 Slurries preparation

Milling and dispersion. Slurries are prepared in a Labmill 8000© (Figure II - 10) for dip-coating deposition. A cylindrical container with slurry and milling media inside rotates around the horizontal axis. Milling media (typically spheres or cylinders of alumina or zirconia) collision reduces particle size. However, this effect is, in general, secondary in comparison to the role in the dispersion of powder and eventual agents in the slurry.

Slow roll. Once that LST, NiO-YSZ and LSF40-SDC ceramic slurries are prepared, they are conserved rotating in a Mini Tube Roller 7622-30000 (Figure II - 10) at 2-3 rpm to avoid the decantation of ceramic powders.

Mixture and degasification. Before deposition, ceramic slurries are mixed during 1 min in a Thinky Mixer Awatori Rentaro AR-250 (Figure II - 10). This technique combines rotation and revolution of slurry container. This process guarantees an homogeneous mixture of components in the slurry and the elimination of bubbles that may generate during the slow roll stage. The centrifuge machine can work in two modes: mixing and defoaming. Mixing mode, with 1:2.5 rotation to revolution ratios (typically 800:2000 rpm), is used for homogeneous mixtures preparation. Defoaming mode, with 1:36 rotation to revolution ratios (usually 60:2200 rpm), is suitable for bubble elimination. In Table II - 2, treatment prior to dip-coating is summarized for each cell component.

Table II - 2. Centrifuge parameters of slurries prior to dip-coating.

Cell component	Composition	Action	Time (min)
DBL	LST	Mixing	1
Anode	NiO-YSZ	Defoaming	1
Cathode	LSF ₄₀ -SDC	Mixing+Defoaming	1+1

Ultrasound mixture. An ultrasound homogenizer Branson 450 Analog sonifier (Figure II - 10) was used to disperse the YSZ powder in isopropanol for electrolyte deposition. This equipment features a load meter, variable power control, 0-15 min timer and pulsing mode. Supplied with a converter and 1/2" diameter disrupter horn, it is designed to apply high-frequency ultrasonic energy to chemical processing and it is used to disperse or mix compounds.

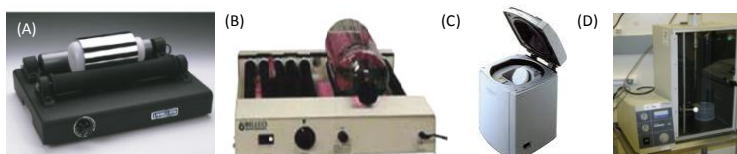


Figure II - 10. Equipment for ceramic slurry preparation: (A) Labmill 8000[®], (B) Mini Tube Roller 7622-30000, (C) Thinky Mixer Awatori Rentaro AR-250) and (D) Branson 450 Analog ultrasound homogenizer.

2.3.1.3 Deposition techniques

Dip-coating. The deposition of diffusion barrier, anode and cathode layers is carried out by dip-coating using a Diptech Automatic Dip Coating Unit (Figure II - 11). In this process, the substrate (i.e. porous tubular metal substrate) where layers are to be deposited, is submerged in a test tube which contains the slurry. The substrate is maintained submerged for a certain time and it is finally extracted in a controlled way. The excess liquid is drained and additives in the slurry evaporate creating a film in the substrate surface.

The thickness of layer is determined by the forces that interact in the process (i.e. viscosity of slurry, capillarity and gravity). While temperature of deposition and solid volume of slurry affect viscosity, immersion time and extraction speed allow the balance of different forces. In this way, thicker layers are obtained as immersion time and extraction rate increase. Repeated dip-coating combined with drying stages is an alternative way to produce thick layers. This technique is adapted for full covering

or deposition in selected zones. Dip-coating parameters for corresponding ceramic slurries are specified in Table II - 3.

Table II - 3. Dip-coating parameters for DBL, anode and cathode deposition.

<i>Ceramic slurry</i>	<i>Immersion rate (cm/s)</i>	<i>Immersion time (s)</i>	<i>Extraction rate (cm/s)</i>
LST	1.7	0	1
NiO-YSZ	0.45	10	0.3
LSF ₄₀ -SDC	0.45	10	0.3



Figure II - 11. Diptech Automatic Dip Coating Unit

Robot spray. The electrolyte is deposited using a PVA2000 spray robot (Figure II - 12) which sprays the YSZ powder dispersed in isopropanol. Spray deposition is customized for irregular surfaces and a variety of shapes. For spraying tubular half-cells, tubes rotate around their longitudinal axis while spray gun moves through its length. Thickness and quality of the deposited layer depend on the rheology of slurry, surface adherence, amount deposited and spray cycles.

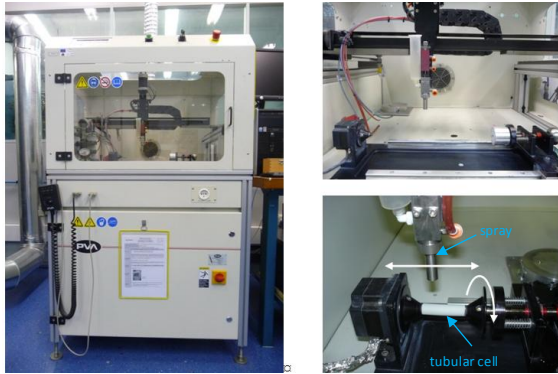


Figure II - 12. PVA2000 spray robot for electrolyte deposition.

2.3.1.4 Co-sintering

Cosintering was carried out on three Carbolite STF (16/-/610 or STF/-/610) tubular furnaces for cell production (Figure II - 13). The alumina cavity is sealed in both edges by combining O-rings and metallic pieces especially designed in IK4-Ikerlan.



Figure II - 13. Carbolite STF (16/-/610 or STF/-/610) cylindrical furnaces for tubular half-cells cosintering.

Co-sintering atmosphere.

The sintering atmosphere is critical in the reduction and shrinkage of cell components. Thus, a control of the atmosphere is needed and oxygen partial

pressure (pO_2) and dew point (T_d) are systematically measured. Dew point is the temperature where condensation begins, and thus, it is essentially a measure of the relative humidity. Concretely, it specifies the temperature at which relative humidity would be 100% if the gas was cooled.

In Figure II - 14, typical pO_2 and dew point profiles during co-sintering are illustrated. In the standard process, Argon ($pO_2=-4.21$ bar in the bottle) is introduced in the furnace at ambient temperature up to 1100°C . During this period, little oxygen which is present in the atmosphere is absorbed by the oxygen getter (FeCr) that is placed at the furnace entrance. However, this oxygen can also oxidize the metal substrate to some extent. Oxygen getter FeCr is activated around 700°C and it is indicated as T_{ox} in the figure.

However, some cells have shown an oxygen absorption peak at lower temperatures (T_{abs}) as indicated by the green profile in Figure II - 14. This is attributed to the eventual firing of binder residues.

At 1100°C , when gas is changed from inert (Ar) to reducing atmosphere ($10\%\text{H}_2 + \text{Ar}$ with $pO_2=-26.47$ bar in the bottle) this is reflected in additional lowering of the oxygen partial pressure from $pO_2'(\text{Ar})$ to $pO_2(10\%\text{H}_2 + \text{Ar})$. Simultaneously, an increase in the dew point due to the water production from the oxygen getters during reduction is accounted. At this point, low pO_2 is maintained but dew point gradually decreases up to the end of the thermal cycle.

Characteristic peaks which are observed at low temperatures in the T_d profile are water absorption/desorption mechanisms of the alumina tube [191-193].

When cells are sintered fully in Argon, $pO_2(\text{Ar}) \approx -20$ bar is maintained at high temperature but after a certain time, oxygen getter is saturated and porous metal substrate is oxidized. When further absorption in the oxygen getter and metal substrate is not possible, oxygen partial pressure increases at high temperatures matching again Argon bottle specifications ($pO_2=-4.21$ bar). After co-sintering, metal-support oxidation for cells which are sintered fully in Argon can be observed by visual inspection. However, sintering fully in Argon, water expulsion which occurs at high temperature (1100°C) in the Ar/ $10\%\text{H}_2+\text{Ar}$ gas change is eradicated.

When the sintering process is carried out without cells and getters, humidity in the furnace is in general lower and little oxygen in inert atmosphere (Ar) is absorbed by the furnace at high temperatures and eliminated during the cooling phase.

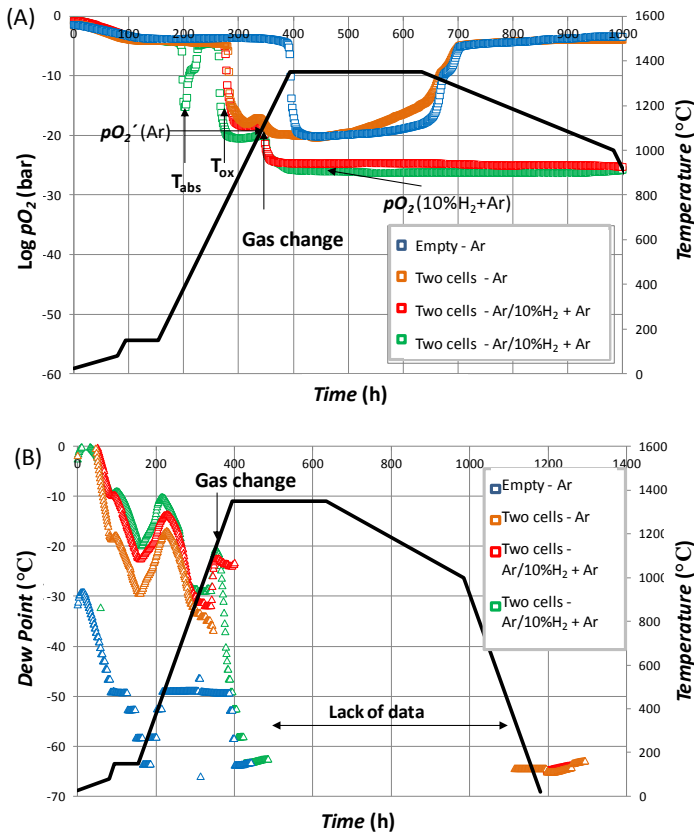


Figure II - 14. Characteristic evolution of the oxygen partial pressure, pO_2 , and dew point during the thermal cycle, in the presence and absence of G2 half-cells and inert or standard atmosphere (with gas change from inert to reducing atmosphere at 1100°C).

Equipment and humidity conversion

Metrotec GSM-V6 and Vaisala HMT337 with integrated Shaw humidity sensor are connected to the furnace gas stream exit to measure the oxygen partial pressure and relative humidity (RH), respectively. pO_2 monitoring is automatically registered in a PC. At the beginning, RH registration was manual and its evolution was only known up to ≈ 350 min of operation. However, data logger was recently integrated to

the Vaisala HMT337 system and currently; it allows the registration of the whole sintering process.

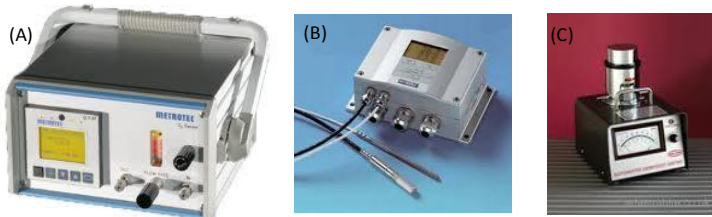


Figure II - 15. (A) Metrotec GSM-V6, (B) Vaisala HMT337 and (C) Shaw humidity sensor.

Collected values of relative humidity (RH) are converted to the Dew point temperature (T_d) using the following two expressions [194]:

$$RH = \frac{P_w}{P_{ws}} \times 100\% \quad (2.9)$$

$$T_d = \frac{T_n}{\left[\frac{m}{\log_{10}\left(\frac{P_w}{\lambda}\right)} - 1 \right]} \quad (2.10)$$

where P_w and P_{ws} are the actual and saturated water vapor pressure, T_n is the triple point temperature and a, m are constants ($a=6.1162$; $m=7.5892$).

2.3.2 Processing characterization and equipment

2.3.2.1 Slurries viscosity characterization

Rheological measurements of ceramic slurries serve as quality control prior to deposition by *dip-coating*. Viscosity measurements are performed in a Haake Rheo Win 3 (Figure II - 16) that allows performing viscosity measurements at different temperatures. Standard viscosities for ceramic slurries are summarized in Table II - 4.

Table II - 4. Rheology of ceramic slurries at 25°C.

Slurry	Viscosity (Pa s)
LST	0.025-0.05
NiO-YSZ	0.2-0.3
LSF40-SDC	0.05-0.1

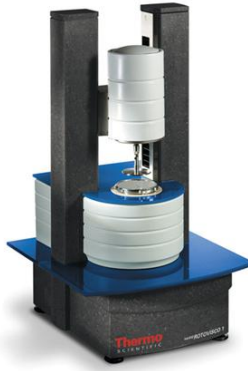


Figure II - 16. Haake RheoWin 3 rheometer.

2.3.2.2 Shrinkage and weight loss during co-sintering

Initially, presintered tubes are characterized by green density measurements in CEIT-1K4. In order to analyze shrinkage and weight loss of half-cells during co-sintering at reducing atmospheres, cells are characterized before and after thermal treatment. In practice, it is not possible to accomplish an accurate measurement of the external diameter without damaging the ceramic layers before sintering. Thus, weight and size (i.e. length, external and internal diameter) are measured in the metal tube before ceramic layers deposition. Similar calculus holds for the half-cell after co-sintering.

Even if weight loss (%*m*), longitudinal (%*H*), transversal shrinkage (either external, %*D_e*, or internal, %*D_i*), porosity and density after sintering were considered in the analysis of G2 cells through this work, transversal shrinkage of external diameter of half-cell during co-sintering was the only parameter which showed significant tendencies and it is expressed as:

$$\%D_e = -\frac{(D_e)_f - (D_e)_i}{(D_e)_f} \times 100 \quad (2.11)$$

where $(D_e)_i$ and $(D_e)_f$ hold for the external diameter before and after co-sintering, respectively. Porosity values of half-cells which are reported in chapter IV, were calculated as follows:

$$p(\%) = \frac{(7.7 - \rho_g)}{7.7} \times 100 \quad (2.12)$$

where 7.7 is the theoretical density of Crofer 22 APU [195] and ρ_g is the geometrical density.

Chapter III

CATHODE STABILITY IN ANODE-SUPPORTED CELLS

Part of this chapter has been published in:

Arregui A., Rodriguez-Martinez L.M., Modena S., Bertoldi M., van Herle J., Sglavo VM.,

“Stability of ferritic perovskite cathodes in anode-supported solid oxide fuel cells under different processing and operation parameters”,
Electrochimica Acta, 58 (2011);312-21.

Arregui A., Rodriguez-Martinez L.M., Modena S., Bertoldi M., van Herle J., Sglavo VM.,

“Influence of operational parameters on LSF and LSCF cathodes degradation”,
The American Ceramic Society’s Ceramic Engineering and Science Proceedings, 32 (2011);

Arregui A., Rodriguez-Martinez LM, Modena S., Bertoldi M., Sglavo VM.,

“Cathode degradation mechanisms by potassium/chromium poisoning and air humidification”,
Fuel Cells, accepted (2013).

3.1 SOFCpower ASC-Technology

3.1.1 Introduction

SOFCpower is an emerging Italian company devoted to SOFC production and development. First R&D activities in SOFCs started in 2002 within the Eurocoating - Turbocoating Group, a privately-held group active in the fields of coatings and processes for gas turbines, machinery and biotechnology. Short-time research activity in the SOFC field crystallized in 2006 and SOFCpower was founded. In early 2007, SOFCpower acquired 100% of HTceramix SA (Yverdon-les-Bains, Switzerland), a spin-off of the Swiss Federal Institute of Technology in Lausanne (EPFL). The Pilot Production Plant is located in Mezzolombardo (TN, Italy), where the R&D activities on material and process are also conducted in close collaboration

with the University of Trento. The system engineering group is located in Yverdon-les-Bains (Lausanne, Switzerland).

The assortment of commercialized products include cells, stacks (StackBox ®), integrated stacks (HoTbox™) and a microCHP system prototype (EnGen ®500) [196] (Figure III - 1). The vision of the company is to become a leading supplier of SOFC-based products. In the period between 2010 and 2011 more than 10.000 cells, 250 stacks and 30 HoTbox™ generators were produced in the pilot plant in Mezzolombardo [197]. SOFCpower-HTc focuses on the small size stationary market with two distinct products which are elaborated based on the same technology platform. The first product is a 1 kW class HoTbox™ generator that provides electricity and heat in a Combined Heat and Power (CHP) module running on natural gas. Efficiencies above 30% electric and 90% overall are deemed for this product segment. The second product is high efficiency co-generator (90%) providing electricity in the 50% plus efficiency class, at a 2.5 kW level. Those products seek to be part of the future heat appliance market.



Figure III - 1. SOFC-based products commercialized by SOFCpower [196].

SOFCpower is involved in several national and international programs. In the framework of Crisalide project, SOFCpower is currently implementing microCHP installations for pilot experimentation in Trentino-Alto Adige. This strategic project is a longterm investment supported by the province and European project Ene.field [198], which will deliver similar trials in 12 EU Member States. First installations fuelled with methane or LPG provided with 6 kW heat and 3 kW electricity and microCHP was connected and recognised by the Italian national grid. This project aims, however, to give preference to scenes where electricity is not exchanged with the network and the heat produced is used all year round through (i.e. swimming pool in Arco).

3.1.2 Anode-supported SOFC

Anode-supported SOFC planar cells are produced in SOFCpower by water-based cofiring of anode and electrolyte and screen-printing of barrier and cathode layers [197, 199]. This cell architecture, developed in 2005, is in permanent evolution and mechanical strength and electrode durability were extensively improved upon late years.

Anode-supported SOFC manufacturing process in SOFCpower is schematized in Figure III - 2. Half-cells are produced by co-casting and sintering Ni/YSZ cermet anode and 8YSZ electrolyte. Gadolinia doped ceria (GDC) is adopted as a barrier layer between cathode and electrolyte to prevent chemical reaction and resultant SrZrO_3 formation. GDC powder is screen printed on the electrolyte after dispersing the powder in a terpineol and ethyl cellulose solution and fired at 1350°C for 2h. Cathode layers are subsequently screen-printed and sintered. Commercially available compositions include state of the art LSM-YSZ and LSCF-GDC composite cathodes.

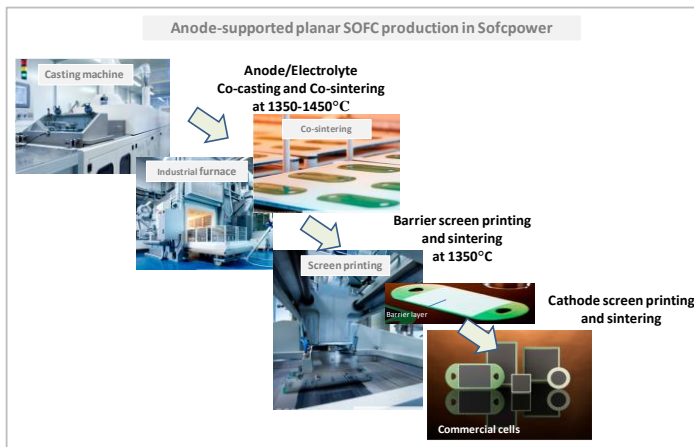


Figure III - 2. Industrially standardized ASC manufacturing process in SOFCpower [196].

LSCF-GDC cathode composition (ASC-700) can be used between 650°C and 800°C and present an ASR $< 0,3 \Omega\text{cm}^2$ at 750°C . Those cells have been tested in single cell and stack configurations demonstrating stable performance with insignificant degradation for at least 3000 h when polarized at 0.5Acm^{-2} [199].

3.2 Ferritic cathodes stability study

3.2.1 Introduction

In recent years, significant efforts have been done to lower the operation temperatures of SOFC. Operating at intermediate temperatures (600°C-800°C) offers the possibility to use cheaper ferritic stainless steels as interconnect material, simplifies heat distribution, limits thermal expansion mismatch and inhibits thermodynamically activated reactions within the stack. Perovskite-type $(\text{La,Sr})_{1-z}(\text{Co,Fe})\text{O}_{3-\delta}$ mixed ionic-electronic conductors (MIEC) figure amongst the most investigated cathode materials for IT-SOFC applications due to their excellent surface exchange and chemical diffusion coefficients [200]. Optimized L55SCF ($\text{La}_{0.55}\text{Sr}_{0.4}\text{Co}_{0.2}\text{Fe}_{0.8}\text{O}_{3-\delta}$) and L58SCF ($\text{La}_{0.58}\text{Sr}_{0.4}\text{Co}_{0.2}\text{Fe}_{0.8}\text{O}_{3-\delta}$) stoichiometries have demonstrated power densities nearly twice as high as conventional LSM-YSZ at 700-800°C in anode-supported single cells [51]. Nevertheless, LSCF and LSF cathodes have revealed intrinsic degradation mainly due to the perovskite instability and Sr depletion. In the cathode/electrolyte interface, Mai et al. [201] observed SrZrO_3 formation due to LSCF-YSZ reactivity already occurring during cathode sintering (at 1080°C), or even during prolonged operation at 800°C. LSCF-YSZ reaction occurs even in the presence of ceria-based (SDC, GDC) protective layers, mainly during sintering [98, 201, 202]. Besides, Sr-enrichment has been also identified in the LSCF cathode surface during testing.

Although a protective chromia layer prevents corrosion of metal interconnects at intermediate temperatures, in the absence of an effective barrier, chromium vapors can quickly lead to performance deterioration by blocking of active sites. Chromium vapors (CrO_3 or $\text{CrO}_2(\text{OH})_2$) pressure is higher in air [130] and chromium poisoning predominantly occurs in the cathode [127, 203-207]. LSCF and LSF mixed conductors are possibly more resistant against chromium poisoning than LSM-YSZ cathodes, due to the extended electrochemical active area that is not restricted to the TPBs.

Several researchers have recently shown growing interest in the investigation of the effect of humidified air in conventional cathode materials. As a matter of fact, water presence can not be excluded in real operation conditions. Encouraging results by Nielsen et al. [208] indicated tolerance during 100 h operation to 12.8% humidification in the air stream for cells with LSCF-GDC composite cathodes. Conversely, LSM-YSZ composite cathodes exhibited partially reversible performance degradation. Recent results by Bucher et al. [209, 210] confirm LSCF and LSC pellets susceptibility to wet atmospheres and consequent surface exchange activity deterioration. In the case of dry pellets, moderate degradation at 600°C is attributed to SrO and La_2O_3 insulating phase [211, 212] formation on the surface. In contrast, humidified pellets exhibited pronounced surface exchange activity deterioration that

was attributed to Si-poisoning. Based on this finding, Bucher et al. recommend the use of pre-dried air in the presence of Si-sources [209, 210].

Recently, degradation rate of stacks have been reduced to values around 0.5% (with LSM) and 3% (with LSCF) in 1000 h tests, this pointing out the necessity of studying the degradation mechanisms of single cells in more detail [213]. It is worth saying that the amount and nature of the degradation highly varies with the operation conditions; experts in the field, however, have not agreed upon a set of optimal operating parameters.

In the present work, a detailed comparison of the stability of intermediate temperature cathodes LSF-SDC and LSCF-GDC used at IK4-Ikerlan and SOFCpower manufacturing plants, respectively, is presented. SOFCpower uses a composite cathode which contains high performing cobaltite (LSCF). In IK4-Ikerlan, stability is prioritized and a pure ferritic perovskite (LSF) which is processed *in-situ* at low temperatures is used to avoid reactivity with the electrolyte (YSZ).

The influence of cathode processing parameters and operation conditions in performance stability is studied in 500 h durability tests with anode-supported cells (SOFCpower) through a specific experimental design, L₁₈ Taguchi matrix. Following this approach, single influence of each studied parameter is determined and most favourable conditions for prolonged service are identified. In addition, an accurate microstructural characterization carried out on the tested cells is presented, in a new approach aiming to connect microstructural changes with performance loss. Specific degradation mechanisms (chromium poisoning, humidification effect) are analyzed in detail. In a second part, stability studies in realistic operation conditions with coated metal interconnect meshes which are used for current collection in the air side are reported. The viability of two candidates as metal coating material is analyzed and discussed.

3.2.2 Experimental procedure

3.2.2.1 Cells fabrication

Commercially available anode-supported planar half-cells with circular design (diameter = 30 mm) produced by SOFCpower S.p.A. were used in this study. The long-term stability of two different composite cathodes (i) LSF-SDC and (ii) LSCF-GDC was investigated. Those compositions were prepared by dispersing the composite cathode powders (La_{0.6}Sr_{0.4})_{0.95}FeO_{3-δ}/ Sm_{0.2}Ce_{0.8}O₂ - 70:30 w/w - or (La_{0.6}Sr_{0.4})_{0.995}Co_{0.2}Fe_{0.8}O_{3-δ}/Gd_{0.1}Ce_{0.9}O₂ - 50:50 w/w - in terpeneol and ethyl cellulose and subsequently screen-printing on the GDC barrier layer. The cathode area of both types of cell was 1.96 cm². Two nominal electrode thicknesses were used, 30 μm and 50 μm. This yielded to slightly thicker electrode in the case of LSF-SDC composite powder. La_{0.5}Sr_{0.5}CoO₃ layer was screen-printed on both cathode types after sintering to facilitate current collection. Cells principal characteristics are

summarized in Table III – 1 and Figure III - 3 represents typical cells appearance and microstructure.

Table III - 1. Schematics of the anode-supported SOFC functional layers.

Functional layer	Composition	Stoichiometry	Fabrication route	Thickness (μm)
Anode-substrate	Ni-YSZ		Co-casting	220 \pm 20
Electrolyte	8YSZ	8 wt% Y_2O_3 – stabilized ZrO_2	Co-casting	8 \pm 2
Barrier	GDC	$\text{Gd}_{0.1}\text{Ce}_{0.9}\text{O}_2$	Screen printing	\approx 4
Cathode	LSF ₄₀ -SDC ₂₀	$(\text{La}_{0.8}\text{Sr}_{0.4})_{0.95}\text{FeO}_{3-\delta}$ / $\text{Sm}_{0.2}\text{Ce}_{0.8}\text{O}_2$ - 70:30 w/w	Screen printing	30/50*
	LS ₁₀ CF-GDC	$(\text{La}_{0.8}\text{Sr}_{0.4})_{0.995}\text{Co}_{0.2}\text{Fe}_{0.8}\text{O}_{3-\delta}$ / $\text{Gd}_{0.1}\text{Ce}_{0.9}\text{O}_2$ - 50:50 w/w	Screen printing	30/50*
Current collector	LSC	$\text{La}_{0.5}\text{Sr}_{0.5}\text{CoO}_3$	Screen printing	\approx 15

(*) Nominal thickness

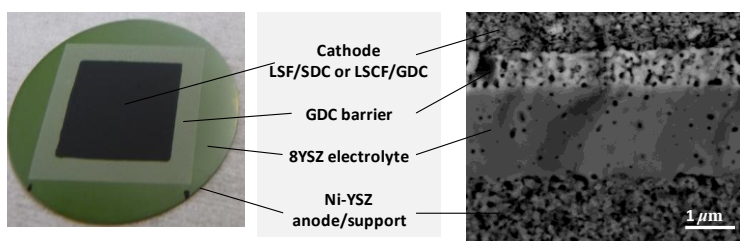


Figure III - 3. Circular anode-supported SOFC and microstructure used in these tests.

3.2.2.2 Electrochemical characterization

Experimental set-up

Cell characterization was performed through four-point resistivity measurements (Figure III - 4) using IV-curves and impedance measurements. Gold and nickel mesh in contact with the electrodes served as current-collector at the cathode and anode side, respectively. A load of 250 g/cm^2 was used to contact the current collectors by accommodating an alumina filter placed below the Au/Ni mesh. Two Au/Ni wires were welded to the corresponding Au/Ni meshes in the cathode and anode side, respectively.

In the experiments where chromium poisoning effect at the cathode was studied, sheets (14 mm x 14 mm x 0.5 mm) of commercial Crofer 22 APU steel were placed between the alumina filter and the mechanical support (refractory material) of the current collector. The surface of Crofer 22 APU steel was not pre-treated and was insulated from current collection in order to evaluate Cr-VI species diffusion to the cathode in 500 h tests. The cell was then fixed to the edge of an alumina cylinder using zirconia based Ultra-Temp 516 and magnesium oxide based Ceramabond 571 (Aremco Products Inc.) as sealants. The anode was reduced by a stepwise

replacement of N_2 by H_2 at $800^\circ C$, the latter being humidified at 3 mol % with a bubbler using standard SOFC test conditioning procedure.

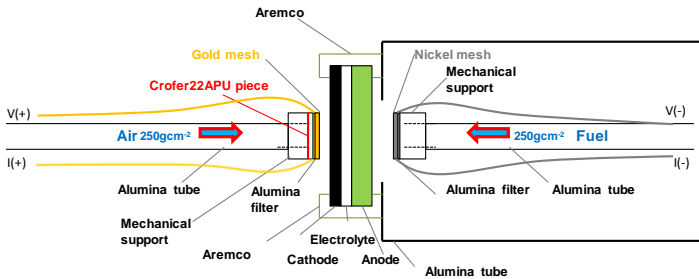


Figure III - 4. Experimental set-up.

IV curves and EIS measurements

Impedance spectroscopy measurements and IV curves were carried out at the beginning and at the end of the 500 h durability tests. Measurements were recorded both at operation (Taguchi matrix in Table III - 2) and standard conditions (150 ml/min cm² dry air and $750^\circ C$). The impedance data and IV curves were normalized by the active contact area between the gold mesh and LSC current collector. Experimental conditions and equipment are described in section 2.1.

Microstructural characterization

Cells microstructure was characterized by means of SEM, EDS and XRD. Experimental procedure is described in section 2.2.

3.2.3 Overview of cathode processing and operation parameters under analysis - Considerations on degradation

After revisiting the existing literature, eight parameters have been identified and ranked in terms of relevant influence in the long-term stability of ferritic cathodes were selected:

- 3 cathode processing parameters
 - o Composition
 - o Thickness
 - o Sintering temperature

- 5 operation parameters
 - Chromium presence
 - Air flow
 - Air humidification
 - Current density
 - Temperature of operation

The overall objective is to determine the main influential parameters that affect cathode stability under a wide representative range of conditions. The reliable comparison is made under the premises of efficient experimentation and impact of analysed factors on cells degradation. The factors analyzed and levels chosen are described below.

Factor A: Cathode composition

Levels: A₁= LSF-SDC, A₂=LSCF-GDC

The primary aim of the Taguchi matrix is to compare long-term stability of LSF-SDC and LSCF-GDC composite cathodes. Pure ferrites with the same A-site stoichiometry exhibit inferior performances than LSCF cathodes due to the lowered electronic and ionic conductivity when iron concentration in B-site is increased [56, 214, 215]. In addition, perovskite structures containing two different transition metal ions in the B site are catalytically more active towards oxygen reduction than those with one single transition metal ion [56]. Though La and Zr interdiffusion has been proved to occur at cathode/electrolyte interface in the case of pure ferrites [47, 49], it is assumed that (La,Sr)FeO_{3±δ} is thermodynamically more stable against Sr segregation [50]; accordingly, lower performance loss is expected in long-term operation for LSF cathodes.

Factor B: Presence of chromium source

Levels: B₁= presence of Cr, B₂= no Cr

Two mechanisms of chromium - induced degradation have been distinguished; the electrochemical reduction of Cr-VI species and chemical reaction [121]. The former competes with oxygen reduction; therefore, cell performance will be affected by blocking of active sites. It depends on cathode polarization and it is kinetically slow at low temperatures [122]. On the other hand, the decomposition of cathode by formation of chromium containing oxides is thermodynamically controlled without any influence of electrical potentials. For LSCF cathodes, experimental evidences of SrCrO₄ formation preferentially in the cathode surface and uniform chromia deposition in the cathode have been widely described [99, 119-121]. SrCrO₄ formation is thermodynamically favored for cathodes containing less stable tetravalent ions (Fe⁴⁺ and Co⁴⁺); it is kinetically rather fast but does not lead to rapid degradation [122].

Factor C: Air flow

Levels: $C_1=30$, $C_2=75$, $C_3=150 \text{ ml cm}^{-2}\text{min}^{-1}$

Air flow levels were selected in order to cover an extended region from commonly used air flow, $150 \text{ ml cm}^{-2}\text{min}^{-1}$, to rather static conditions, $30 \text{ ml cm}^{-2}\text{min}^{-1}$. When 0.75 A/cm^2 current density and 20 mol% H_2O on air are selected as control factor levels, oxygen utilization is maximum, stoichiometric air flow is $16 \text{ ml cm}^{-2} \text{ min}^{-1}$ and the oxidant utilization is 52%. The anode was fed with $75 \text{ ml cm}^{-2} \text{ min}^{-1} \text{ H}_2$ with 3 mol% H_2O in every experiment.

Factor D: Water vapor in cathode

Level: $D_1=0$, $D_2=3$, $D_3=20\% \text{ H}_2\text{O}$

Recently, detrimental effect was confirmed for LSM cathodes exposed to air humidification [208, 216]. Nielsen et al. [208] reported a partially reversible performance loss for Riso 2G LSM-YSZ composite cathodes. Degradation mechanism was attributed to microstructural changes in the cathode/electrolyte contact area. However, cells including LSCF-GDC composite cathodes deposited on GDC protection layer exhibited humidification tolerance even at 12.8 mol % H_2O .

Factor E: Current density

Levels: $E_1=0.25$, $E_2=0.5$, $E_3=0.75 \text{ Acm}^{-2}$

Factor F: Operation temperature

Levels: $F_1=700$, $F_2=750$, $F_3=800^\circ\text{C}$

Operation temperature differs with current due to additive contribution from cell constituents. Nickel coarsening is promoted in the anode as temperature increases [122], though it has not a relevant effect in comparison to performance losses caused by cathode degradation. The effect of operation temperature is described differently for different state of the art cathode materials [217]. In the case of LSM cathodes, zirconate formation caused by overpotential has been suggested to induce major degradation rates and thus, to stay away from low temperatures and high current loads is preferable. For these reasons it is recommended to operate the cell at intermediate temperature and at low polarization to avoid any significant cathode overpotential and further degradation [92, 218, 219]. Nevertheless, in the case of LSCF cathodes, Mai et al. [201] found that the degradation rates at 800°C are twice as high as for cells operated at 700°C but no clear influence of current density was identified. Under realistic operation conditions cell voltage is commonly maintained between $0.7 \text{ V} - 0.8\text{V}$, above the failure threshold that is established at 0.6V . Working with optimized LSF-SDC and LSCF-GDC cathodes at intermediary temperatures, $700^\circ\text{C} - 800^\circ\text{C}$, operation requirements are satisfied under the selected current density range, $0.25 - 0.75 \text{ Acm}^{-2}$. However, in the present study,

cathode processing parameters influence (composition, thickness and sintering temperature) was studied simultaneously and less performing cathodes failed to reach the cell working threshold. Nevertheless, more severe operation conditions were suitable to accelerate degradation processes in limited durability tests (500 h) of the actual characteristics, permitting a premature quantification of the degradation.

Factor G: Cathode thickness

Levels: $G_1=30, G_2=50 \mu m$

Oxygen flux through the mixed conductor is promoted when electrode thickness is reduced. Below a specific electrode thickness, surface exchange reactions become rate limiting. Bowmeester et al. [220] calculated L_c (characteristic thickness) values ranging between $20 \mu m$ - $3000 \mu m$, for ferrite and cobaltite perovskites, in a situation where oxygen potential gradient is controlled in a balanced manner by diffusion and surface exchange reaction. On the other hand, Adler et al. [221] suggested that oxygen reduction region extends few microns from the mixed conductor/electrolyte interface ($2-3 \mu m$ for $La_{0.6}Sr_{0.4}Co_{0.2}Fe_{0.8}O_{3-\delta}$) and the outer region is electrochemically inert and acts essentially as a current collector. Improved sheet resistance and lateral current distribution is expected, however, for thicker cells. The expected lower R_o for thicker cells was confirmed by impedance measurements in Figure III - 5.

Factor H: Cathode sintering temperature

Level: $H_1=950, H_2=1000, H_3=1050^\circ C$

The cathode sintering range selected includes the temperature of choice in both centres, SOFCpower and IK4-Ikerlan. Those companies employ different SOFC architectures; anode - supported planar cells developed by SOFCpower allow iron-perovskite cathodes to be optimized at higher sintering temperatures ($1050^\circ C$) whereas metal - supported tubular cells developed by IK4-Ikerlan demand lower cathode sintering temperatures ($950^\circ C$ or less) that allow only *in situ* processing without damaging the metal support.

3.2.4 Design of experiments and durability tests

3.2.4.1 DoE – Taguchi matrix

Ferritic perovskite cathodes stability was studied by a specific design of experiments (DoE). Table III – 2 summarizes the performed experiments which combined cathode processing parameters (composition, thickness and sintering temperature) and operation conditions (temperature, current density, air flow rate, air humidification and chromium presence) in 500 h durability tests. This table of experiments is, in reality, a L_{18} Taguchi matrix which combines 8 control factors in 18 experiments. The

property of orthogonality guarantees that the effect of each parameter is equilibrated and separated with respect to the considered parameters and are useful for fair comparison [222, 223]. Refer to Appendix III.A for detailed information about Taguchi method, L_{18} matrix and orthogonality.

Table III - 2. Design of experiments based on a L_{18} Taguchi matrix.

Exp#	Processing parameters				Operation conditions			
	Cathode	$t / \mu\text{m}$	$T_s / ^\circ\text{C}$	Cr	$\Phi_{\text{air}} / \text{ml cm}^{-2} \text{min}^{-1}$	$\text{H}_2\text{O} / \%$	$\text{J} / \text{A cm}^2$	$T / ^\circ\text{C}$
	A_i	B_i	C_i	D_i	E_i	F_i	G_i	H_i
1	LSF-SDC	30	950	Yes	30	No	0.25	700
2	LSF-SDC	50	1000	Yes	75	3	0.5	750
3	LSF-SDC	50	1050	Yes	150	20	0.75	800
4	LSF-SDC	50	1050	No	30	No	0.5	750
5	LSF-SDC	30	950	No	75	3	0.75	800
6	LSF-SDC	50	1000	No	150	20	0.25	700
7	LSF-SDC	50	1050	No	30	3	0.25	800
8	LSF-SDC	50	950	No	75	20	0.5	700
9	LSF-SDC	30	1000	No	150	No	0.75	750
10	LSCF-GDC	50	950	Yes	30	20	0.75	750
11	LSCF-GDC	50	1000	Yes	75	No	0.25	800
12	LSCF-GDC	30	1050	Yes	150	3	0.5	700
13	LSCF-GDC	50	1000	No	30	3	0.75	700
14	LSCF-GDC	30	1050	No	75	20	0.25	750
15	LSCF-GDC	50	950	No	150	No	0.5	800
16	LSCF-GDC	30	1000	No	30	20	0.5	800
17	LSCF-GDC	50	1050	No	75	No	0.75	700
18	LSCF-GDC	50	950	No	150	3	0.25	750

3.2.4.2 Analysis of results

a) Reproducibility of the measurements

Figure III - 5 reports the obtained results in terms of P (power density), R_o (ohmic resistance), R_p (polarization resistance) as calculated from impedance spectroscopy measurements at 0.7 V and 750°C for cell combinations designed by the Taguchi matrix (Table III – 2). Electrochemical values were corrected by using the effective cathode area from the contact between cathode and Au-mesh. Over the reported temperature range, data regarding power density fluctuate of 0.06 W/cm² at the highest except for 30 μm thick cathodes sintered at 950°C. This demonstrates the high reproducibility of the cells manufacturing process and the test bench set-up. Long-term reproducibility was further studied by the repetition of two of the durability tests that led to results in good agreement with each other.

b) Initial performance: influence of processing parameters

Combinations of cathode processing parameters specific to the Taguchi matrix (Table III – 2) are listed in Table III - 3. Note that not all possible combinations were used; LSF-SDC/30 μ m/1050°C and LSCF-GDC/30 μ m/950°C combinations are missing in the Taguchi matrix.

In agreement with the literature, better performance of LSCF-GDC cathode is experimentally confirmed in Figure III - 5(A). Power density increases for thick (50 μ m) cathodes in spite of the composition. In general, higher sintering temperatures are also beneficial. As an exception, lower power density is recorded for thin LSF-SDC cathode when sintering temperature is increased from 950°C to 1000°C.

Table III - 3. Cathode processing parameters combinations in the Taguchi matrix (Table III – 2).

Composition	Thickness (μm)	Ts (°C)
LSF-SDC	30	950
		1000
	50	950
		1000
LSCF-GDC	30	1050
		1000
	50	1050
		1000
		950
		1000
		1050

Impedance spectroscopy measurements revealed lower polarization and ohmic resistances for thicker cathodes, as shown in Figure III - 5 (B), (C). Despite of some scattering, the general trend was unaffected for cathodes with similar composition and sintering temperature. Experimental results can be fitted with the model proposed by Liu by using an equivalent circuit which describes the porous mixed ionic-electronic electrode behaviour [224]. In the cited work, it was proposed that an improvement of the MIEC/gas interface efficiency is accounted for an increase of electrodes thickness, when ionic transport is sufficiently fast.

From the results in Figure III - 5, one can observe that ohmic resistance decreases when sintering temperature increases. Improved ohmic resistance at higher cathode sintering temperatures is attributed to a contact enhancement at the cathode/barrier interface. Conversely, no correlation between sintering temperature and polarization resistance can be pointed out; the data show large scattering for different combinations of cathode composition and sintering temperature. Not all possible cell processing parameters have been used through the Taguchi matrix, this leading to additional difficulty in sintering temperature effect clarification.

Nevertheless, in the range between 1000°C and 1050°C, both LSF-SDC and LSCF-GDC cathodes display similar behaviour and R_p is lower when sintering at 1050°C.

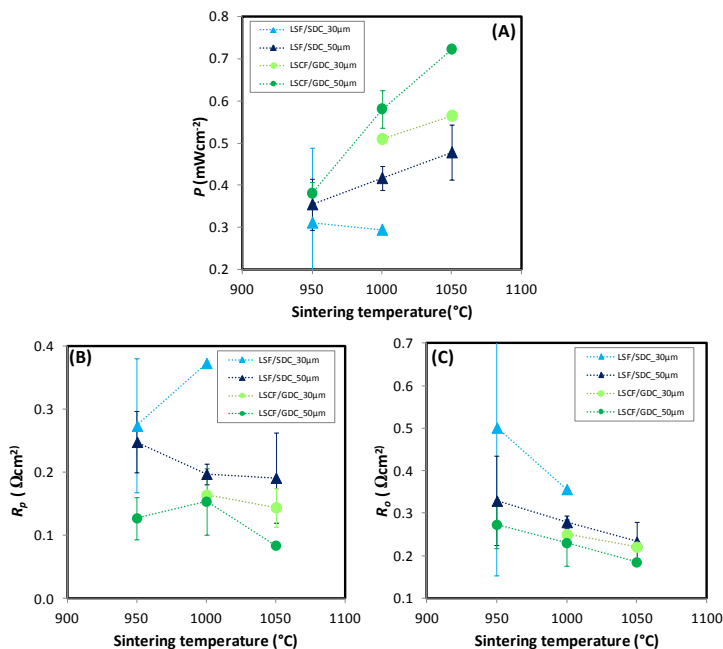


Figure III - 5. Performance at 750°C as a function of processing parameters: (A) power density, (B) polarization resistance and (C) ohmic resistance. Cells were fuelled with 150 ml $\text{cm}^{-2}\text{min}^{-1}$ air and 3% humidified 75 ml $\text{cm}^{-2}\text{min}^{-1}$ H_2 flux.

To sum up, the superior performance for the LSCF-GDC composition compared to LSF-SDC was confirmed; both R_o and R_p values are lower using LSCF-GDC cathode composition with analogous processing parameters. Better R_o for LSCF was expected as it exhibits better mixed ionic conductivity. Better R_p for LSCF is also in agreement with the superior catalytic activity for this perovskite. Thicker cathode ($\approx 50\ \mu\text{m}$) exhibits higher power density at 0.7 V, as a consequence of both ohmic and polarization resistance decrease. Moreover, cathodes sintered at higher temperatures demonstrate higher performances directly after sintering. Cathode/GDC barrier contact and R_o are systematically improved when sintering temperature increases from 950°C to 1050°C.

Microstructural analysis of the cathodes in the as-produced state revealed dissimilar behavior for LSF-SDC and LSCF-GDC cathodes with respect to the sintering temperature, as shown in Figure III - 6. In the case of LSF-SDC cathode, finer particles sinter already at 950°C and grain growth can be observed up to 1050°C. Interconnectivity increases with temperature but during the first 100 h of operation time considerable activation effect has been observed for cells sintered at 950°C. Conversely, for LSCF-GDC type cathodes, finer grains observed at 1050°C are expected to deliver higher active surface where electrochemical reaction occurs.

Experimental results reported here do not match with conclusions made by Bebelis et al. [225], who attributed the improved performance of $\text{La}_{0.78}\text{Sr}_{0.2}\text{Co}_{0.2}\text{Fe}_{0.8}\text{O}_{3-\delta}$ with respect to $\text{La}_{0.58}\text{Sr}_{0.2}\text{Co}_{0.2}\text{Fe}_{0.8}\text{O}_{3-\delta}$ to the decrease of sintering temperature from 1100°C to 1060°C. Nevertheless, it is worth saying that in the mentioned work, cathodes with different thicknesses (as estimated from SEM images) were considered, $\approx 40\ \mu\text{m}$ and $\approx 30\ \mu\text{m}$ for $\text{La}_{0.78}\text{Sr}_{0.2}\text{Co}_{0.2}\text{Fe}_{0.8}\text{O}_{3-\delta}$ and $\text{La}_{0.58}\text{Sr}_{0.2}\text{Co}_{0.2}\text{Fe}_{0.8}\text{O}_{3-\delta}$, respectively. Such difference was not discussed by Bebelis and can contribute to cell performance.

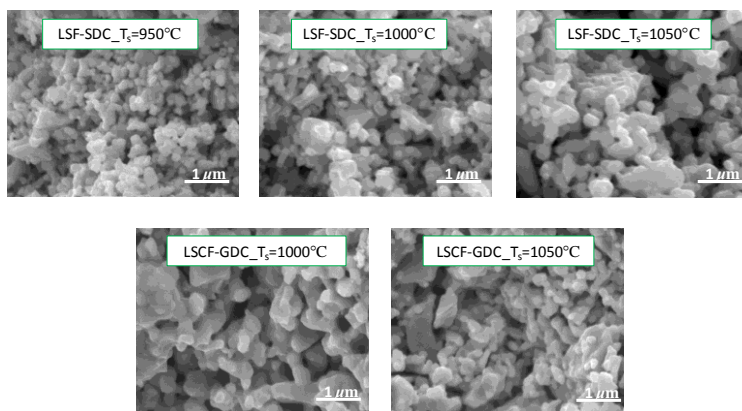


Figure III - 6. LSF-SDC and LSCF-GDC composites cathodes microstructure as a function of the sintering temperature.

c) Long-term activation/degradation analysis

Results from cell potential monitoring during long-term tests are presented in Table III - 4. Cell potential versus time was characterized here by evaluating cell potential at zero, activation and 500 h points, as illustrated for experiment #1 and #15 in Figure III - 7. Experiment #1 underwent appreciable activation during the first 200 h operation, followed by a period of constant voltage; afterward, gradual performance loss occurred. Degradation rate measurements using zero point as reference do not

distinguish however this degradation initiated at 200 h. In that sense, a second measurement from the maximal activation point is desirable to point out the degradation region that would otherwise be hidden in long-term tests of the actual characteristics.

Three measured potentials V_0 , V_a , V_f with the corresponding time t_0 , t_a , t_f characterizing initial, maximal activation and final instant are summarized for each experiment in Table III - 4. Note that not all experiments were performed up to 500 h and in experiment #13 t_0 is set up at 175 h when temperature was adjusted from 720°C to 700°C. In the first 175 h of operation at 720°C no activation/degradation phenomena was observed, thus experiment #13 performance evolution is fairly traduced in Table III - 4.

Table III - 4. 500h durability tests monitoring data. Eighteen experiments were performed under cathode processing and operation conditions specified in the Taguchi matrix (Table III – 2).

Exp#	<i>V(t) operation data</i>					
	t_0 (h)	V_0 (V)	t_a (h)	V_a (V)	t_f (h)	V_f (V)
1	0	0.396	200	0.676	500	0.588
2	0	0.797	12	0.822	499	0.480
3	0	0.757	5	0.770	190	0.626
4	0	0.802	83	0.816	478	0.795
5	0	0.696	90	0.710	500	0.551
6	0	0.917	30	0.926	500	0.917
7	0	0.924	53	0.930	500	0.922
8	0	0.530	200	0.539	500	0.525
9	0	0.672	48	0.672	481	0.580
10	0	0.660	280	0.660	504	0.228
11	0	0.913	50	0.926	500	0.712
12	0	0.678	50	0.729	500	0.515
13	175	0.491	400	0.501	400	0.501
14	0	0.945	0	0.945	504	0.904
15	0	0.858	500	0.869	500	0.869
16	0	0.867	84	0.900	378	0.775
17	0	0.627	500	0.672	500	0.672
18	0	0.949	0	0.949	478	0.938

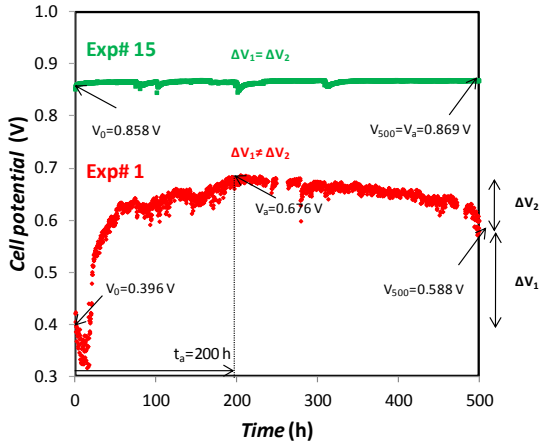


Figure III - 7. Degradation rates evaluation using initial, t_0 , and activation time, t_a , as reference. Experiment #1 and #15 in the Taguchi matrix are used to illustrate the advantage of the dual degradation measurement.

d) Effect of the processing/operation parameters on activation

Activation time and magnitude for each specific parameter combination in the Taguchi matrix (Table III – 2) are plotted as a function of the corresponding number of experiment in Figure III - 8. Cell performance stability extended up to 500 h operation time for experiments #5, #15 and #17. Experiments #8, #10 and #13 exhibited activation/stability regions in the range between 200 h – 300 h and the remaining started to lose performance before reaching 100 h of operation. The magnitude of performance activation does not coincide with its duration in time. The major performance enhancements during activation were registered for experiments #1, #5, #12, #16 and #17. The substantial improvement (≈ 275 mV) in experiment #1 was anticipated since the cell showed initial poor performance that originated the highly scattered ohmic resistance data for 30 μm thick LSF cathode in Figure III - 5. The large activation is essentially attributed to the contact enhancement between the LSC current collector and Au mesh. Activation in terms of potential increase was not further analyzed because highly dispersed data in experiment #1 could change tendencies.

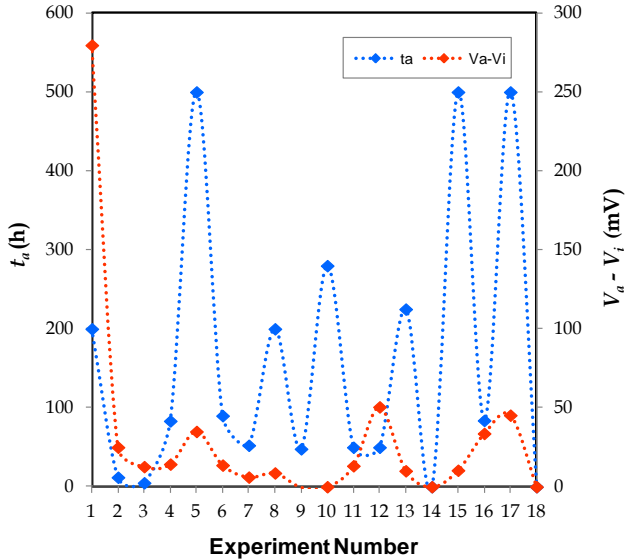


Figure III - 8. Activation time, t_a , and the activation voltage, $(V_a - V_i)$ values for the eighteen experiments in the Taguchi matrix (Table III - 2).

The activation time is analyzed by calculating the average for each level of the control factors and individual tendencies for each parameter are represented in the effect diagram (Figure III - 9). The maximum difference between the factor levels represents how relevant the factor is and it is useful to identify the relative importance of the factorial effects, as shown in Figure III - 10.

Current density and sintering temperature are classified as the most influencing parameters of the activation time (21%) in Figure III - 10. The average activation time for cells operated at 0.75 A cm^{-2} is ≈ 250 h, in contrast with the ≈ 70 h of activation measured for cells operated at 0.25 A cm^{-2} , as shown in Figure III - 9. The effect of the current density on the activation time is linear. When cathodes are sintered at 950°C , the activation region is prolonged to ≈ 280 h. On the other hand, cathodes sintered at 1000°C and 1050°C exhibit reduced stabilities, ≈ 85 h and ≈ 120 h, respectively. The non-linear relation between the cathode sintering temperature and activation time is attributed to the specific properties of each cathode composition. As a matter of fact, cathode microstructural analysis revealed dissimilar sintering behaviour for both LSF-SDC and LSCF-GDC composite cathodes (Figure III - 6).

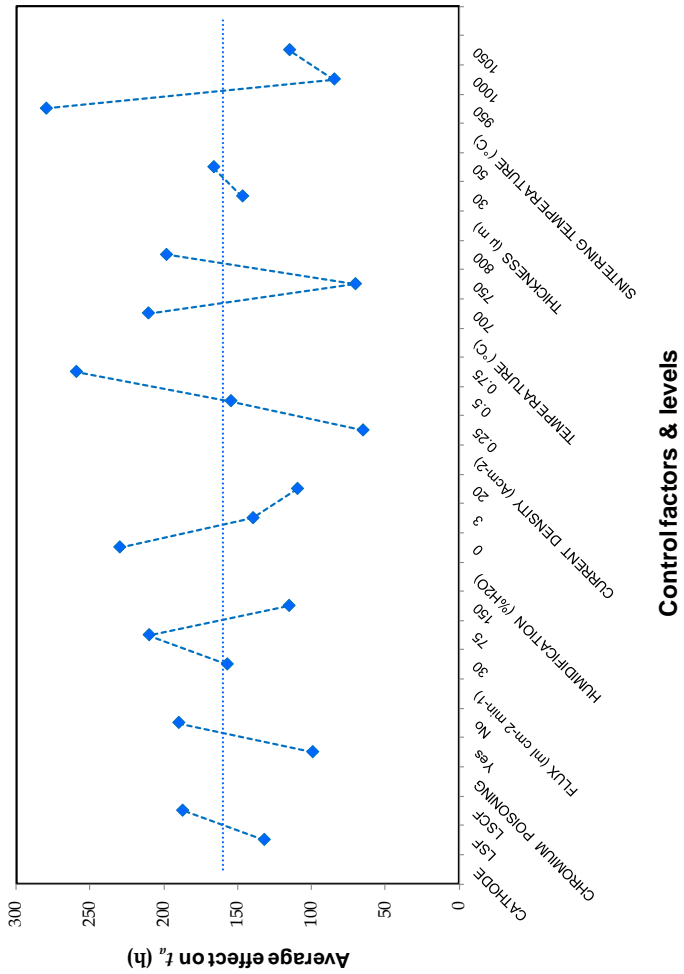


Figure III - 9. Individual effect of cathode processing and operation factors in the activation time, t_a . The average of activation for the sum of all experiments in the Taguchi matrix is represented by the dashed lines.

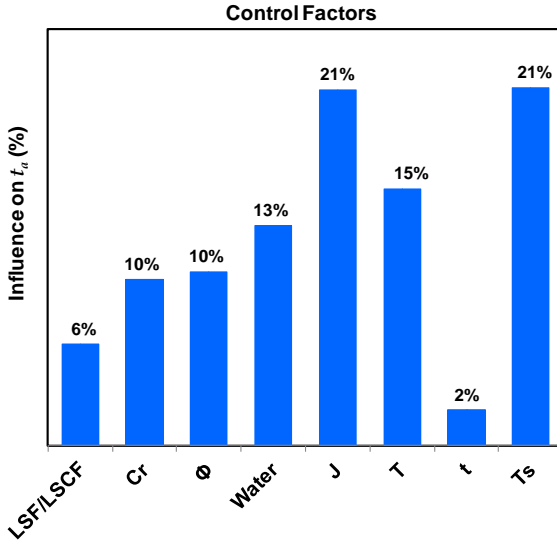


Figure III - 10. Cathode processing and operation factors influence on the activation time, t_a .

The operation temperature is classified as the third most relevant parameter of the activation in the ranking (15%), as shown in Figure III - 10. Non-linear peak-shape tendency with a substantially short stability region (≈ 70 h) for cells operated at 750°C can be observed. The trend is discussed as the sum of opposed activation/degradation mechanisms. In the initial time of cell operation, potential cathode sintering as well as contact enhancement between cathode/ceria barrier and current collector/cathode interface may lower the area specific resistance and improve performance. The effect of further cathode sintering and contact enhancement is reflected in a reduction in polarization and ohmic resistance, respectively. On the other hand, chromium partial pressure augments substantially in the range of temperatures under study causing premature degradation. The involvement of both phenomena may be reflected in the lower activation times observed at 750°C .

Air humidification has moderate influence on activation time (13%); the trend is rather linear and the stability/activation region is extended when dry air is used (≈ 230 h).

Chromium poisoning and air flow rate display slightly lower activation power (10%). Cells exposed to chromium vaporization show shorter stability/activation region and cells performance start to degrade around 100 h earlier. The air flow rate

trend is non-linear with a maximal activation time of ≈ 210 h when $75\text{ml cm}^{-2}\text{ min}^{-1}$ is introduced.

As far as cathode composition is concerned, prolonged activation region (≈ 50 h) is observed for LSCF cathodes.

Cathode thickness has no appreciable effect (2%) in activation.

e) Effect of the processing and operating parameters on degradation

Degradation rate, normalized to 500 h in order to guarantee fair comparison during data analysis, was calculated from experimental data by using as reference point time zero voltage, V_0 (Eq. 3.1) or the maximal activation time, V_a (Eq. 3.2), by the following expressions:

$$\Delta V_1/500h = (V_f - V_0)/(t_f - t_0) \quad (3.1)$$

$$\Delta V_2/500h = (V_f - V_a)/(t_f - t_a) \quad (3.2)$$

being t_a the maximal activation time and t_f , V_f the final time and potential. Final time is defined here to distinct final measurements that were carried out before reaching 500 h of operation. The aim of the dual measurement of degradation rates is to distinguish the activation phenomena that occur in the first hundred hours of operation due to cathode sintering and contact improvement between the cathode and current collector. Both activation phenomena can strongly affect tendencies in 500 h operation tests.

The degradation rate with the zero point as reference furnishes important information about the initial behavior of the cell, describing general contribution of simultaneous activation and deactivation processes; conversely, degradation rate calculated with respect to activation time focuses on long-term behavior even if 500 h tests are undersized to predict long-term stability. Over periods as long as 1000 h, the degradation rates are generally smaller than over the initial 100 h but the qualitative effect is expected to be similar. In order to confirm long-term trends, however, prolonged tests should be performed.

In Figure III - 11, individual degradation rates obtained are plotted as a function of the corresponding number of experiment in the Taguchi matrix (Table III - 2). The two minimum regions for experiments #1 - #3 and #10 - #12 correspond to LSF-SDC and LSCF-GDC electrodes, respectively, in contact with a chromium source. Also experiments #6 and #16 show considerable degradation rates, around 200 mV in 500 h, which are presumably due to air humidification. Degradation rate increases considerably in the case of experiments #1 and #10 when it is evaluated from the activation point instead of zero time. According to results in the previous region, the

extended stability/activation region for cells including cathodes sintered at 950°C and operated at the maximal current density (0.75 A/cm²) is understandable.

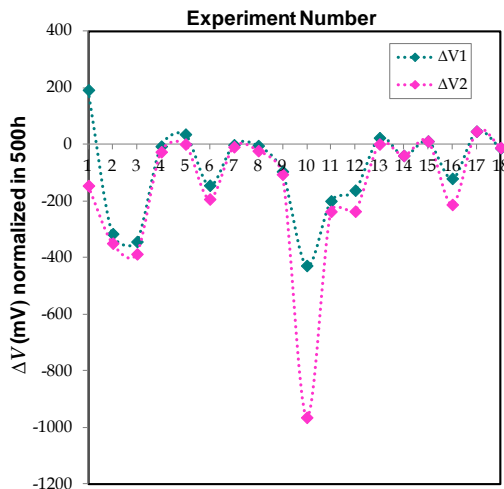


Figure III - 11. Degradation rates for the eighteen durability tests in the Taguchi matrix (Table III – 2). ΔV_1 and ΔV_2 are calculated by using time zero and maximal activation time as reference, respectively (Eq. 3.1 and 3.2).

The individual effect and relative influence of cathode processing parameters and operation conditions in performance degradation is represented Figure III - 12 and Figure III - 13, respectively.

The presence of chromium vapours is identified as the principal factor that triggers degradation of cell performance (ΔV_1 : 22 %; ΔV_2 : 31 %), as seen in Figure III - 13.

The second factor in the ranking is air humidification (ΔV_1 : 20% ; ΔV_2 : %21) and an average degradation rate as high as -300 mV/500h was evaluated from the maximum activation point for 20 mol% humidified air, as observed in Figure III - 12. This result does not match with experimental data reported by Nielsen et al. [208] who showed good tolerance for LSCF-GDC cathode with 12.8 mol% humidified air during 100 h. Two differences can be however pointed out between Nielsen experiments and the configuration used in the present work; stoichiometric LSCF perovskite was used instead of 0.5% A-site deficient LSCF perovskite used here. Nielsen also used LSCF as current collector whereas LSC current collector was used in the present work. A-site deficiency inhibits strontium segregation; accordingly, major stability is expected for cells tested here. On the other hand, at fixed Sr

concentrations, SrO activity is considerably high for LSC perovskites as a result of weaker valence stability of Co^{4+} with respect to Fe^{4+} , as reported in detailed thermodynamic analysis by Yokokawa et al. [50].

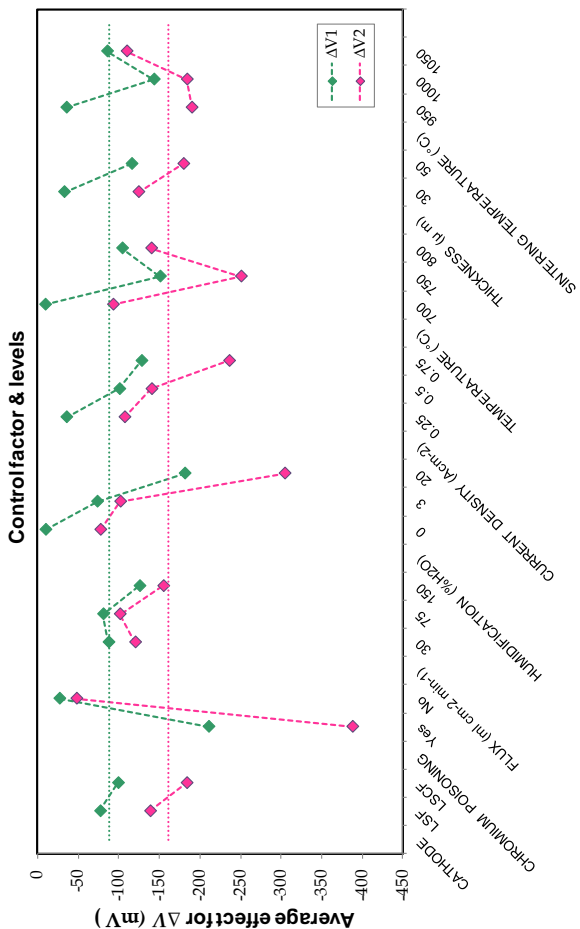


Figure III - 12. Cathode processing parameters and operation conditions effect in the degradation rates. ΔV_1 and ΔV_2 were calculated by using time zero and maximal activation time as reference, respectively (Eq. 3.1 and 3.2). The average of degradation for the sum of all experiments in the Taguchi matrix is represented by the dashed line.

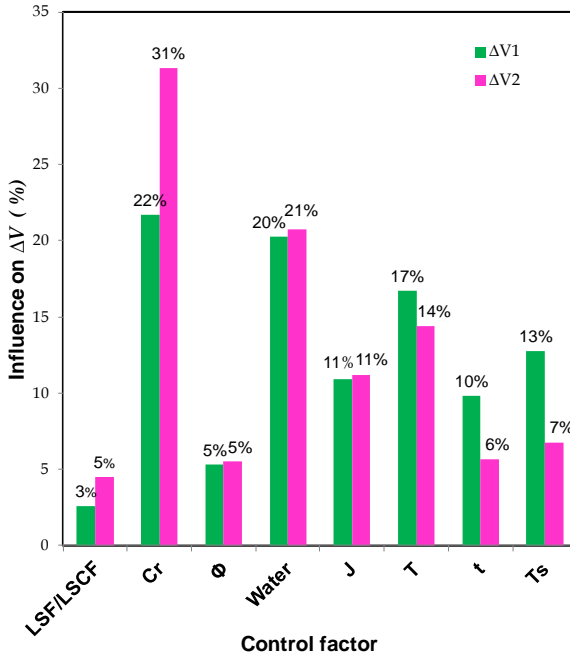


Figure III - 13. Cathode processing and operation conditions influence in degradation rates ΔV_1 and ΔV_2 . ΔV_1 and ΔV_2 are calculated by using time zero and maximal activation time as reference, respectively (Eq. 3.1 and 3.2).

Higher thermodynamic stability in reducing atmospheres is expected for LSCF perovskite in comparison to LSC current collector. Inversely to the acceptor doping mechanism in LSCF system, whose structural and electrical properties were widely studied by Tai et al. [58], when Sr segregation occurs, electroneutrality is compensated both electronically (electron hole elimination) and ionically (by oxygen vacancy suppression) with the proportion being temperature dependent. At the same time, the thermal expansion coefficient decreases and related thermal stresses induce the delamination of the current collector. Further analysis is required to determine air humidification influence for LSCF based cathodes.

The third most influent parameter is the operation temperature (ΔV_1 : 17 %; ΔV_2 : 14%). The maximum degradation was observed at 750°C as shown in Figure III - 12. This is probably the consequence of the overlay of two phenomena that show inverse trend with temperature; electrode polarization and chromium poisoning. The polarization resistance increases when temperature is lowered. However, chromium poisoning from the alloy is favoured at higher temperatures. Such simultaneous degradation mechanisms could cause the observed maximum of degradation at

750°C. However, the magnitude of the degradation rates estimated at 750°C remains surprisingly high.

Air flow rate has little influence on the degradation rates (ΔV_1 : 5%; ΔV_2 : %5). The minimum degradation was found for 75 mlcm⁻²min⁻¹. With regard to the current density, the optimal operation condition is 0.25 Acm⁻², the degradation tendency is rather linear and increases with the current load. In this case, results are in good agreement with previous results [92, 217, 218].

Cells sintered at 950°C are optimal if time 0 is taken as reference for degradation calculations but 1050°C becomes the most suitable sintering temperature from the activation point suggesting an enhanced stability in prolonged tests.

Influence of cell thickness, air flux and cathode composition on degradation is not substantial but stability should be improved when 30 μ m thick cells in combination with 75 mlcm⁻²min⁻¹ air through an LSF-SDC cathode are used.

3.2.4.3 Overall discussion and conclusions

Design of experiments demonstrated to be a powerful instrument for SOFC long-term operation analysis. Operational and processing parameters influence on long-term stability/degradation of ferritic composite cathodes was successfully evaluated through a Taguchi matrix in 500 h duration tests.

The superior performance of LSCF-GDC cathodes was experimentally confirmed. Thicker cathodes (50 μ m) were systematically higher performing than thin ones (\approx 30 μ m). Lower ohmic and polarization resistances were registered regardless the cathode composition and sintering temperature. As a general rule, cathode sintering temperature increase from 950°C to 1050°C improved the power density. Cathode contact with GDC barrier and ohmic resistance were systematically improved as the sintering temperature was raised. Microstructural analysis revealed that finer microstructure for LSF-SDC and LSCF-GDC cathodes at 950°C and 1050°C, respectively.

Current density and sintering temperature were classified as the most influencing parameters of the activation time. Also operation temperature was significant and activation time was substantially lowered at 750°C.

Chromium poisoning and air humidification were classified, in such order, as first and second most important parameter for cathode performance degradation. Temperature influence on degradation was also considerable and highest degradation rates were observed at 750°C. Further stability improvement was evaluated for low current loads, higher sintering temperatures and average air fluxes through the cathode. Modest influence of cathode composition was observed but LSF-SDC cathodes exhibited superior stability. Optimal parameters for minimum degradation in the investigated range can finally be classified in Table III - 5.

Table III - 5. Optimal cathode processing parameters and operation conditions for long-term stability of ferritic based composite cathodes.

Cathode	t / μm	T_s / °C	Cr	Φ_{air} / ml cm⁻² min⁻¹	H₂O / %	J / A cm⁻²	T / °C
LSF-SDC	30	1050	No	75	0	0.25	700

3.2.5 Degradation mechanisms

3.2.5.1 Introduction

In this section, degradation mechanisms inherent to ferritic perovskite cathodes are studied by the post-mortem analysis of cells which suffered the most significant degradation in the Taguchi matrix. Selected cells coincide with the stability tests which were performed in contact with a chromium-source or otherwise, in the presence of 20% humidified air. In fact, as described earlier, the essential role of chromium-sources and air humidification in the premature degradation of ferritic cathodes performance was confirmed. Though chromium poisoning has been extensively studied, this analysis provides with experimental evidences of a specific chromium-assisted degradation mechanism which was not reported in the literature until now. Regarding the scarcely studied humidification effect, cells post-mortem analysis identifies a degradation mechanism that could be directly associated to air humidification.

3.2.5.2 Chromium poisoning

Electrochemical characterization

Samples corresponding to experiments #1-3 (LSF-SDC) and #10-12 (LSCF-GDC) in the Taguchi matrix (Table III – 2) were exposed to chromium vapours from Crofer 22 APU sheets in 500 h tests as illustrated in the experimental set-up (Figure III - 4). Potential evolution of those experiments is shown in Figure III - 14. Additional electrochemical Impedance spectroscopy (EIS) measurements at the beginning (t_i) and the end (t_f) of the durability tests allowed to separate ohmic and polarization contributions. EIS measurements recorded at realistic operation conditions (0.7V) are summarized in Table III – 6.

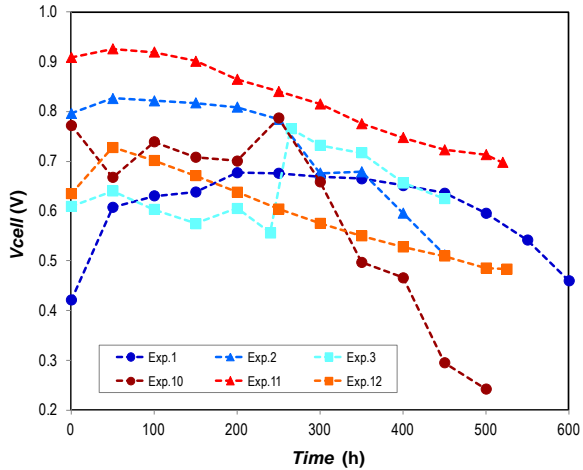


Figure III - 14. Potential evolution for 500h durability experiments in contact with a chromium source in the Taguchi matrix. In experiments #1-3 and #10-12, LSF-SDC and LSCF-GDC cathodes were tested, respectively. Specific processing and operation conditions for each experiment are summarized in Table III – 2.

The initial impedances of experiment #1 correspond to recordings at $t_i = 74$ h and final ones to $t_f = 570$ h. Cell #1 activation during the first 100 h operation was ≈ 250 mV but after 200 h gradual performance loss occurred. During the initial activation, polarization but especially ohmic resistance decreased substantially due to load accommodation and better cathode/Au-mesh contact, as already mentioned. This trend is out of the range for initial activation mechanisms and it affects chromium vapours effects evaluation. Therefore, experiment #1 was shifted of 70 h. Still, polarization and, in particular, ohmic resistance are high at 74 h. On the other hand, experiment #3 (20% H₂O) underwent an abrupt potential improvement at ≈ 250 h; after that, a more pronounced degradation occurred. According to this, impedance measurements were recorded directly after the activation and are included in Table III - 6. The degradation evolution was evaluated in the second part of the experiment.

Table III - 6. EIS measurements for experiments in contact with chromium vapors; impedances are recorded at 0.7V at the specific operation conditions for each experiment in Table III – 2.

Exp#	$t_i(h)$	X_i				$t_f(h)$	X_f			
		ASR (Ωcm^2)	R_p (Ωcm^2)	R_o (Ωcm^2)	P (Wcm^{-2})		ASR (Ωcm^2)	R_p (Ωcm^2)	R_o (Ωcm^2)	P (Wcm^{-2})
1	74	1.36	0.50	0.87	0.15	570	1.73	0.72	1.01	0.11
2	0	0.49	0.19	0.30	0.41	500	1.14	0.38	0.76	0.20
3	0	0.92	0.77	0.14	0.45	455	0.49	0.24	0.25	0.37
	282	0.35	0.16	0.19	0.56					
10	0	0.49	0.19	0.30	0.43	505	1.05	0.55	0.50	0.19
11	0	0.38	0.20	0.18	0.54	520	1.23	0.73	0.50	0.11
12	0	0.66	0.23	0.43	0.31	570	0.96	0.45	0.52	0.20

Electrochemical resistance evolution after 500 h was assessed by data conversion from Table III – 6 by the following expression:

$$\Delta X(\%) = \frac{(X_f - X_i)}{X_i} \frac{500h}{(t_f - t_i)} \times 100 \quad (3.3)$$

where X holds for ASR, R_p and R_o and X_i and X_f correspond to the resistance measurements at the beginning, and at the end of 500 h tests, respectively. The three resistances evolution is represented in Figure III - 15 for the six experiments in contact with a chromium source.

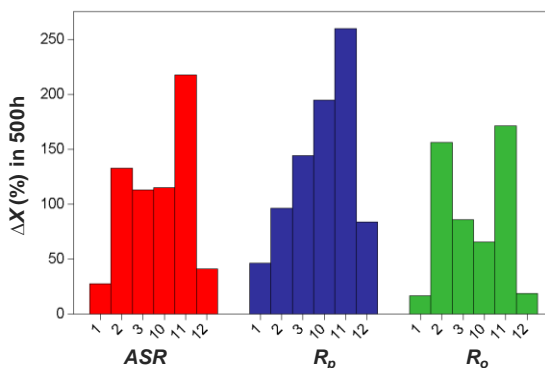


Figure III - 15. Resistance percentual increase for experiments #1-3 (LSF-SDC) and #10-12 (LSCF-GDC) in contact with a chromium source (Table III – 2). ΔASR , ΔR_p and ΔR_o in 500h are measured at 0.7V, through transformation of impedance data-

The electrochemical reduction of chromium vapors and TPB blockage in the cathode surface limits the charge transfer reaction in the cathode. This is therefore reflected

in a gradual increase in the activation polarization. If results in Figure III - 15 are analyzed separately for each cathode composition, for the experiments including LSF-SDC cathodes, polarization resistances increase significantly from experiment #1 to #3 at operation conditions (Table III - 2). Referring to previous results, this tendency can be explained as the simultaneous effect of increasing operation temperature (from 700°C to 800°C), air humidification (from 0% to 20%) and current density (from 0.25 A/cm² to 0.75 A/cm²). However, in the case of LSCF-GDC cathodes, control factor combinations do not follow a parallel trend and the highest ΔR_p (around 260%) is estimated for experiment #11 (dry air, 800°C and 0.25 A/cm²) followed by experiment #10 (20% humidified air, 750°C, 0.75A/cm²). On the other hand, moderate ΔR_p is observed at 700°C for both experiments #1 and #12. It is worth mentioning that in those experiments performed at 700°C, LSF-SDC sintered at 950°C and LSCF-GDC 1050°C exhibit fines microstructures (Figure III - 6). All summed up, it seems that the main factor that affects ΔR_p and associated chromium deposition is the operation temperature. This is reasonable as the partial pressure of the principal Cr-species at oxidizing atmosphere, CrO₃ and CrO₂(OH)₂, increases with temperature [125]. This effect is better illustrated in Figure III - 16, where the polarization resistance percentual increase, ΔR_p , in 500 h is represented as a function of operating temperature for both cathode compositions. In particular, LSCF-GDC cathodes exhibit higher ΔR_p with stronger dependency on temperature. This trend with temperature is visible despite the processing and operating conditions specific to each experiment. This is significant as the essential role of temperature in chromium poisoning is confirmed above certain parameters such as current density, cathode microstructure or humidification. However, cathode composition is important and LSCF-GDC cathodes show major susceptibility to chromium vapors compared to LSF-SDC cathodes which were used in this work.

On the other hand, experiments #2 and #11 exhibited outstanding increment in the ohmic resistance with $\Delta R_o > 150\%$ in 500h (Figure III - 15). For experiment #11, maximum ΔR_o and ΔR_p account for the particularly elevated ΔASR above 200%.

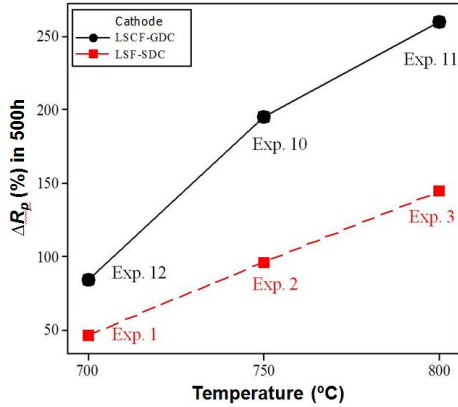


Figure III - 16. Polarization resistance percentual increase, ΔR_p (%), in 500h as a function of the operating temperature for experiments #1-3 (LSF-SDC) and #10-12 (LSCF-GDC) in contact with a chromium source (Table III – 2).

Microstructural characterization

In most cases, chromium was found homogeneously distributed through the cathode; but in experiments #2 and #11, localized high Cr concentrations were identified at the cathode/GDC barrier interface. In Figure III - 17, the elemental mapping of cell #11 indicates the coexistence of chromium, potassium and strontium on the surface of GDC barrier layer. As a matter of fact, Ceramabond 571, used for sealing, contains significant amounts of potassium as observed by Ingram et al. [226].

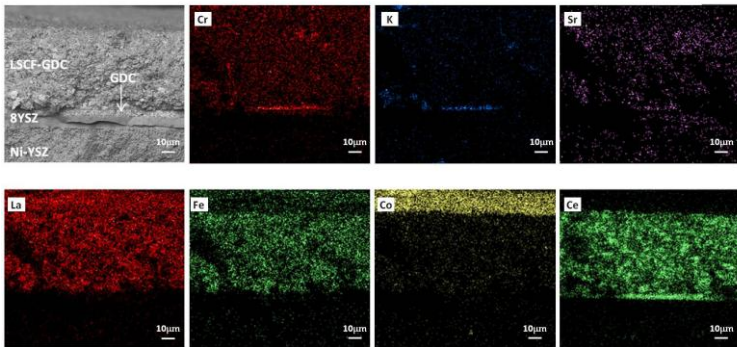


Figure III - 17. Maps of the chemical elements on the cross section of cell #11. Illustration of Cr, K and Sr deposition in the cathode/GDC barrier interface.

Further analysis was carried out at higher magnification at the cathode/barrier interface for both cells #2 and #11, as illustrated in Figure III - 18. Line scans were recorded orthogonally through the interface and Cr, K and Sr concentration zones could be detected. Cell #1 cross-section is also shown in Figure III - 18 for comparison. In the case of cell #2, cathode delamination was observed and Cr, K and Sr directly diffused to the ceria barrier partially blocking its porosity. On the other hand, in the case of cell #11, Cr, K and Sr elements crystallized preferentially at the cathode/GDC barrier interface. Perovskite instability can be also accounted for by strontium depletion to the surface of the current collector.

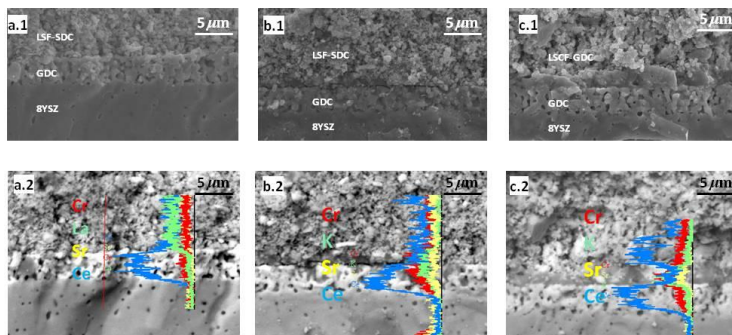


Figure III - 18. GDC barrier SEI (x.1) and BS (x.2) micrographs with line-scan elemental analysis for cell a) # 1 with standard microstructure and b) # 2 and c) # 11 with Cr, K and Sr element poisoning in the barrier.

Figure III - 19 shows the surface of cells #1-3 and #10-12 directly after testing. In the case of experiment #1, EDS analysis revealed the presence of strontium and cobalt oxides on the surface of LSC current collector. According to the literature [209, 210, 227], SrO ($\sigma \approx 10^{-5}$ S/cm at 800°C [211]) and Co₂O₃ ($\sigma \approx 3.35 \times 10$ S/cm at 800°C [228]) secondary phases were identified. These oxides are white and blue, respectively, and they form in free spaces where the current collector is not in direct contact with the gold mesh, giving a characteristic spotted pattern to the cell surface. In cells #3 and #10, combined white and blue spotted pattern is equally identified even if strontium oxide formation predominates. During cells cross-section analysis, strontium diffusion was identified though there was no evidence of cobalt migration. Cobalt concentration is especially high in LSC, the cathode contact layer and concentration inhomogeneities might be limited to the near surface in LSC surface [209, 210].

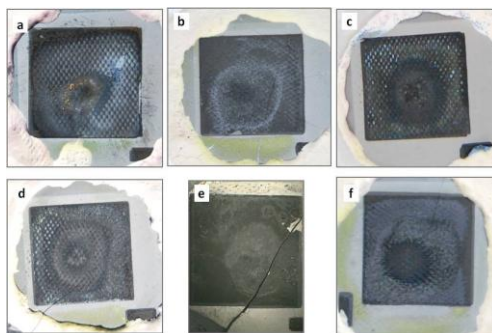


Figure III - 19. Surface image of cells after chromium evaporation experiments. Images correspond to cell a) #1 b) #2 c) #3 d) #10 e) #11 and f) #12.

Regions containing Cr, K and Sr are detected on the surface of cells # 2, # 11 and # 12. For cells #2 and #12 surface features are similar. Two specific regions are distinguished in Figure III - 19: a dark-blue core and a clearer grayish external zone. In the core, air stream is introduced and high Cr and K concentrations are detected (Figure III - 20). Strontium is also present in the inner zone, but preferentially crystallizes in the adjacent area in the form of SrCrO_4 . In the case of cells #2 and #12, massive chemical reaction occurring on the surface accounts for the formation of $\text{K}_2\text{Cr}_2\text{O}_7$ triclinic phase as detected by XRD in agreement with those results reported by Weakley et al. [229]. In the case of cell #11, the surface appearance is completely different (Figure III - 19); black background is partially covered by a grayish zone and yellowish deposits are evenly distributed through the electrode. However, EDS characterization revealed Cr, K and Sr deposits also on its surface.

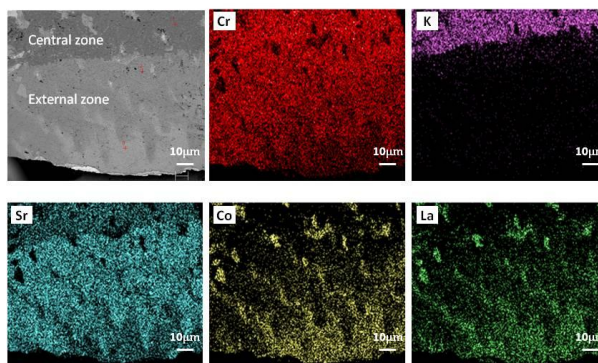


Figure III - 20. Element distribution in the surface of cell #12; K and Cr in the core and Sr and Cr in the external zone.

3.2.5.3 Humidification effect

The six experiments carried out in contact with chromium registered considerable degradation in comparison to the rather stable performances of chromium free cells (Figure III - 11). As an exception, experiments #6 and #16 showed high degradation rates even in the absence of chromium and are matter of study in this section. In both experiments, high humidification (20% H₂O) was introduced in the air stream which is presumably in the origin of the registered instability during operation. Voltage evolution for those cells is presented in Figure III - 21 for the specific cathode processing parameters and operation conditions in Table III – 2. Note that LSF-SDC and LSCF-GDC composite cathodes were used in experiment # 6 and # 16, respectively. After the first 50 h of operation, both cells followed relatively constant voltage degradation but experiment #16 suffered a drastic voltage loss at ≈ 380 h. After operation, the surface of cell #6 did not show any specific feature whereas cell #16 was covered with the characteristic white-blue spotted pattern and a partially peeled off cathode. In addition, anode was oxidized for cell #16. White and blue zones associated with SrO and Co₂O₃ phases, respectively, are not related to air humidification as Bucher et al. [18,19] confirmed in a recent study with LSCF and LSF pellets. Besides, in the mentioned work, it was stated that strontium and cobalt (III) oxide insulating phases do not substantially alter cells stability. This is experimentally corroborated here, as the characteristic blue-white pattern was also identified after operation in dry air for cells with stable performance (i.e. exp # 5).

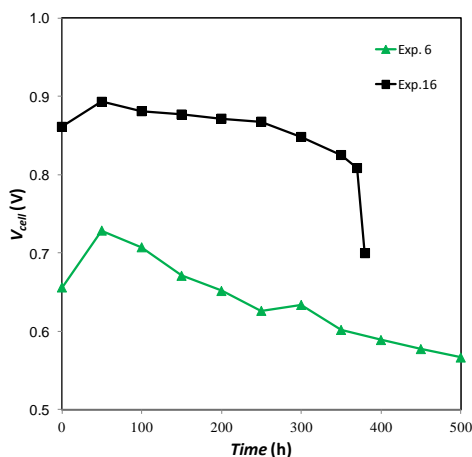


Figure III - 21. 500h durability tests for experiments #6 and #16 with 20% H₂O concentration in the air stream and specific cathode processing parameters and operation conditions in the Taguchi matrix (Table III – 2).

During sample preparation for SEM analysis, even limited bending caused immediate cathode delamination in cells #6 and #16, as illustrated in Figure III - 22. GDC barrier layer appeared brown/reddish below the peeled region but EDS could not detect the migration of any impurities to this zone. Cathode elimination by chemical etching confirmed, however, morphological transformations in the GDC barrier surface. A complete barrier analysis was carried out by chemical etching of cells at time 0 and after testing. GDC barriers microstructure was essentially the same before and after operation and characteristic GDC morphology is shown in Figure III - 23a. As an exception, crack propagation in the GDC barrier surface was confirmed in cells #6 and #16. Crack propagation through the barrier could be the starting point of a catastrophic failure in experiment #16. As a matter of fact, cross-section analysis confirmed crack proliferation through the electrolyte (Figure III - 24) and this could end by oxidizing the anode.

Overall, 6 experiments were carried out in the presence of 20% humidified air in the Taguchi matrix (Table III – 2). Two of them, experiments #3 and #10, were put in contact with Crofer 22 APU pieces and underwent substantial degradation mainly due to chromium poisoning (Figure III - 11). Other two, experiment #6 and #16, tested in Cr-free air atmospheres, suffered high degradation. Brittleness and cathode delamination as well as crack propagation in the GDC barrier and electrolyte were observed. In contrast, experiments #8 and #14, also tested in Cr-free air with 20% water concentration, were rather stable after 500h.

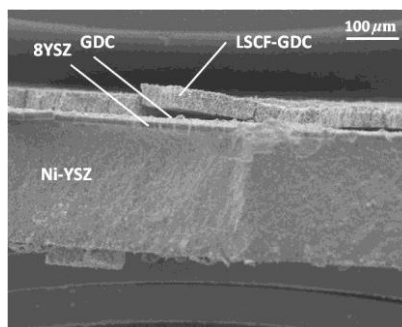


Figure III - 22. Illustration of LSCF-GDC composite cathode delamination in cell #16, operated with 20% humidified air during 500h and specific cathode processing parameters and operation conditions in the Taguchi matrix (Table III – 2).

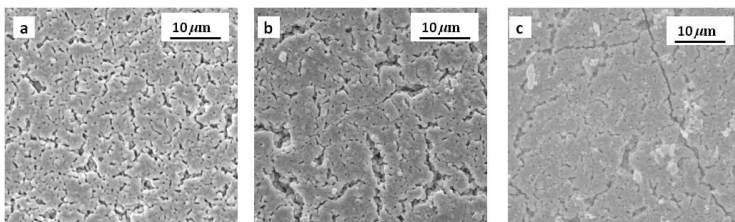


Figure III - 23. GDC surface with a) standard microstructure for as-produced cell and crack propagation in the cells b) #6 and c) #16 after 500h durability test in 20% humidified air ambient and cathode specific processing and operation conditions in the Taguchi matrix (Table III – 2).

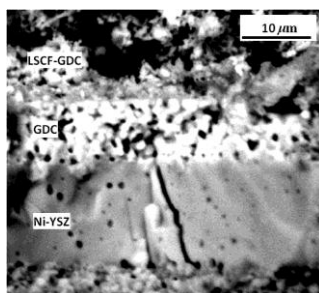


Figure III - 24. Cell #16 SEM cross-section micrograph with crack propagation through the 8YSZ anode after operation in 20% humidified air and specific cathode processing parameters and operation conditions in the Taguchi matrix (Table III – 2).

3.2.5.4 Overall discussion and conclusions

Sr massive diffusion occurs from LSF-SDC and LSCF-GDC composite cathodes to the LSC current collector surface during cells operation. In fact, Sr segregation is already reported in the literature [230, 231]. SrO and Co₃O₄ insulating phases have been observed on the surface of the LSC current collector regardless of dry/wet air and chromium vapors presence during operation. However, Sr segregation and SrO and Co₃O₄ phases are confirmed to be minor degradation mechanisms. This is in agreement with findings by Bucher et al. [209, 210].

Chromium poisoning

When cells were subjected to chromium vapors from Crofer 22 APU pieces, SrCrO₄ deposits were identified on the surface of LSC current collector. For the rest, chromium homogeneous deposition occurred through LSF-SDC and LSCF-GDC composite cathodes. Blocking of active sites with chromia deposition was more

severe at higher temperature and ΔR_p during operation gradually increased as the operating temperature increased. Those observations are already documented for ferritic perovskites in the literature [99, 119-121]. Nevertheless, polarization resistance increase was more pronounced in the case of LSCF-GDC composite cathodes, this suggesting a major susceptibility of LSCF-GDC cathodes to the electrochemical reduction of chromium vapors.

Potassium assisted Cr poisoning

Thermodynamic equilibrium calculations by Sakai et al. [232] have predicted high reactivity of chromium components in lanthanum chromite or oxide scales (Cr_2O_3 , $(\text{MnCr})_3\text{O}_4$) of alloys with alkaline metal components such as potassium or sodium, with the formation of K_2CrO_4 and Na_2CrO_4 under oxidizing atmosphere. In a work by Ingram et al. [226], drastic increase in degradation rates was observed in a single cell with LSM cathode when a potassium source was present. Such degradation was attributed to the electrochemical reduction of highly volatile K_2CrO_4 [233] and no evidence of potassium deposits were found in the cathode. Furthermore, Ceramabond 571 used also here was identified as the potassium source.

Whereas Ingram et al. [22] suggested potassium assisted chromium evaporation (K_2CrO_4) with no K deposits on LSM cathodes, here, $\text{K}_2\text{Cr}_2\text{O}_7$ is detected on the surface of LSC current collector and on the interface of LSF-SDC and LSCF-GDC composite cathodes with GDC barrier layer. The presence of strontium in $\text{K}_2\text{Cr}_2\text{O}_7$ containing sites stimulates the hypothesis of the role of strontium as nucleation agent for $\text{K}_2\text{Cr}_2\text{O}_7$ crystallization. In cells where $\text{K}_2\text{Cr}_2\text{O}_7$ crystallized at the cathode/GDC barrier interface, maximum degradation rates were observed (%ASR). $\text{K}_2\text{Cr}_2\text{O}_7$ insulating phase formation at the cathode/barrier interface was correlated to huge ohmic resistance increases.

Humidification effect

In the previous section, air humidification was classified as the second most important parameter of degradation behind chromium poisoning. Humidification influence on the potential degradation was 21%, high as compared to other factors such as cathode composition, thickness or air flux, which influence in degradation was well below 10%. The effect was evaluated in average through the 18 experiments thanks to the specific Taguchi design based on an orthogonal matrix. However, when experiments were analyzed independently, opposite effects under high air humidification were confirmed. Whereas experiments #6 and #16 suffered severe degradation, experiments #8 and #14 were stable with similar 20% water concentration in the air stream. Though the influence of cathode processing

parameters and operation parameters is not excluded, interaction with humidification could not be identified.

Microstructural analysis reported here suggests a correlation with degradation mechanisms in the cathode/GDC interface. Two of the cells that were 20% humidified exhibited high degradation rates. This was connected to cracks propagation on the surface of GDC barrier layers. Cathode delamination and characteristic brown color of the barrier below the cathode suggest a possible impurity diffusion that could not be identified. One of the cells exhibited crack proliferation also in the electrolyte and anode was completely oxidized. Hence, degradation mechanisms related to air humidification are most probably generated in the cathode/GDC interface. This is in agreement with Nielsen et al. [208] investigations in a 2G cell (LSM:YSZ cathode) which suffered substantial degradation even under low air humidification. Microstructural analysis revealed accelerated cathode interface degradation and nano-sized impurities (Si, S, Ca, Mn) in the electrolyte/cathode interface. However, similar cell with LSCF:GDC cathode, 2.5 G, was stable under high 12.8% air humidification. Si-impurity diffusion in wet atmosphere was also reported by Bucher et al. [209, 210]. In this work, no impurities are detected by EDS in the GDC barrier surface of cells #6 and #16. The precise effect of air humidification is still uncertain and further specific investigations remain necessary.

3.3 Metal interconnect coatings against chromium poisoning

3.3.1 Introduction

At intermediate temperatures, ferritic interconnects used at stack level require coatings to protect the metal substrate from corrosion but also to work as a barrier and suppress chromium poisoning of the cathode. In fact, stability studies in the first part of this chapter demonstrated the harmful effect of chromium evaporation sources in the cathode performance.

With this aim, a variety of oxide coatings have been developed. However, material requirements are demanding. A good coating should enhance electric connection between the interconnect and cathode contact paste, decrease oxide growth kinetics of the interconnect and retard Cr volatilization. Perovskite and spinel materials have been extensively explored for such applications [234-236].

Among the perovskites, pure electronic conductors such as $(\text{La,Sr})\text{MnO}_3$ and $(\text{La,Sr})\text{CrO}_3$ offer relatively low conductivity, with required 50 S/cm that are reached at high 800°C or above. MIEC perovskites such as $(\text{La,Sr})\text{FeO}_3$, and $(\text{La,Sr})\text{CoO}_3$ exhibit excellent conductivities and low initial contact resistance. However, the resistance of such coated materials increases rapidly, due to chromia scale growth in

the metal surface and reactivity with the coating [237]. Although compatibility between the coating and the cathode material is advantageous, it is difficult to obtain a dense coating and these materials require the use of specialized deposition technologies including sputtering, PVD and pulsed laser deposition. Therefore, the use of highly conductive perovskite materials is somewhat limited [238].

More recently, spinel coatings such as $Mn_{1.5}Co_{1.5}O_4$ (MCO) and $MnCo_{1.9}Fe_{0.1}O_4$ (MCF) demonstrated efficacy on retarding oxidation and inhibiting chromia vaporization for ferritic steels [235, 239, 240]. Unfortunately, the low bulk conductivity of spinels demands coating application by redox firing. TEC matching with cell components is also somewhat compromised.

In this section, the effectiveness of two coatings developed by Nextech Materials for Crofer 22 APU ferritic mesh interconnects was studied. The first material was a spinel with $Mn_{1.5}Co_{1.5}O_4$ (MCO) composition. The second was a novel perovskite material with $LaNi_{0.6}Co_{0.4}O_3$ (LNC) composition and promising physical properties. This perovskite is n-type conductor which exhibits high electronic conductivity (>500 S/cm at 800°C) and TEC of 14.3 ppmK⁻¹. Unlike the conventional alkaline earth doped perovskites, LNC has few oxygen vacancies in the crystal lattice, thus, reducing oxygen diffusion to the metal/oxide interface. In this work, stability of the two candidate materials for interconnect coating is reported in 500 h durability tests performed in anode-supported cells. Crofer 22 APU mesh coated with such materials is used as current collector in the cathode side to reproduce stack operation conditions. Nextech Materials has kindly sent their coated and uncoated Crofer 22 APU meshes for their evaluation as cathode metal interconnect.

With this commitment, the specific set-up used for electrochemical characterization of ASCs in SOFCpower (Figure III - 4) was transferred to IK4-Ikerlan. Set-up used for tubular MSCs at IK4-Ikerlan has a different configuration which is not compatible for planar ASCs characterization. Based on the *know-how* of SOFCpower, an ASC testing bench was designed and built in a horizontal furnace especially acquired for planar ASCs electrochemical characterization. In order to optimize testing capability, a 4 cell testing design was integrated in this furnace (Figure III - 25).

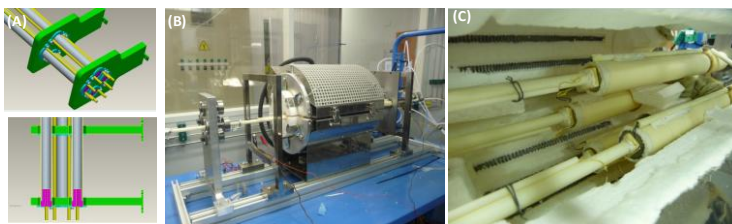


Figure III - 25. Illustration of IK4-Ikerlan set-up for planar ASC characterization: (A) four cell testing design, (B) test-bench furnace and (C) four cell montage in the furnace cavity.

3.3.2 Experimental procedure

In this study, experimental results reported in the *Ferritic Cathodes Stability Study* (section 3.2) were used; cathode processing parameters and operation conditions were selected to optimize the stability and operate at “safe” conditions.

- 30 μm thick LSF-SDC and LSCF-GDC composite cathodes were sintered at 1050°C
- 500 h durability tests were performed at 700°C; 75ml/cm² dry air; 75ml/cm² H₂ (3% H₂O) ; 0.25 A/cm²

Anode-supported cells manufactured at SOFCpower were similar to the used in the previous section (Table III - 1); Ni-YSZ supported cells with YSZ electrolyte included either LSF-SDC or LSCF-GDC composite cathodes with a GDC barrier and thin LSC layer for current collection. 500 h durability tests were carried out with three different interconnect configurations (Table III - 7); Crofer 22 APU mesh was used uncoated and coated with LNC and MCO. Analogue tests were performed using Au mesh and served for comparison of the electrochemical performance at initial time.

Table III - 7. 500h durability tests as a function of cathode composition and metal interconnect coatings.

Cathode	Contact paste	Mesh	Mesh-Coating
LSF/SDC	LSC	Crofer 22 APU	Uncoated LNC MCO
LSCF/GDC	LSC	Crofer 22 APU	Uncoated LNC MCO

The experimental set-up was essentially the same as the one described in Figure III - 4. The only difference was the Crofer 22 APU which was used as current collector instead of gold (Figure III - 26).

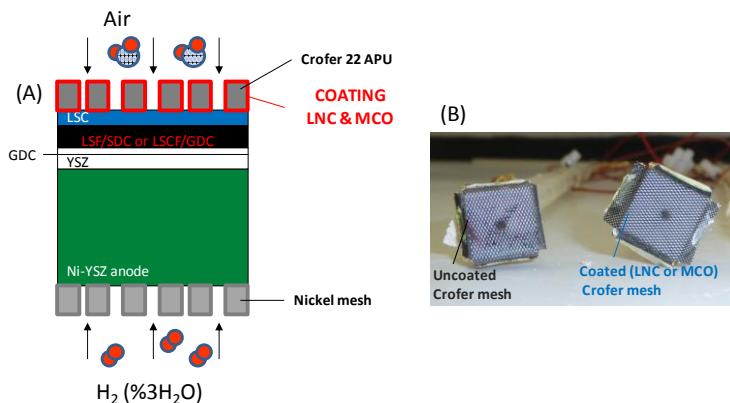


Figure III - 26. (A) Illustration of cell configuration and (B) cathode side current collectors with uncoated and coated (LNC or MCO) Crofer 22 APU meshes from Nextech Materials.

3.3.3 Analysis of results

Initial performance

IV curves revealed excellent OCVs above 1.09 V and quite similar trends for both cathode compositions (Figure III - 27). In general, contact between metal and contact paste (LSC) enhanced and performance increased significantly when Crofer mesh was coated. Best performance was attained for LNC coating. A detailed characterization in the 700-800°C range provided with exceptional power densities at high temperatures; at least 1640 mW/cm² were recorded at 800°C for LSCF-GDC cathode when LNC-coated Crofer mesh was used as current collector (Figure III - 28). This is a remarkable result. Performance was also high when MCO coating was used and 1310 mW/cm² were recorded with LSCF-GDC cathode composition. Lower performing LSF-SDC cathode also exhibited high 1260 mW/cm² at 800°C with LNC coating. Performance with uncoated Crofer was especially low when it was combined with LSF-SDC cathode composition and it improved using gold mesh. Tendencies were similar regardless the operation temperature (Figure III - 28). At low temperature selected for stability tests (700°C), for LSCF-GDC cathode, power densities above 750 and 700 mW/cm² were recorded for LNC and MCO coatings,

respectively. In the configuration with LSF-SDC cathode, power densities above 590 mW/cm² for LNC and 396 mW/cm² for MCO coatings were registered.

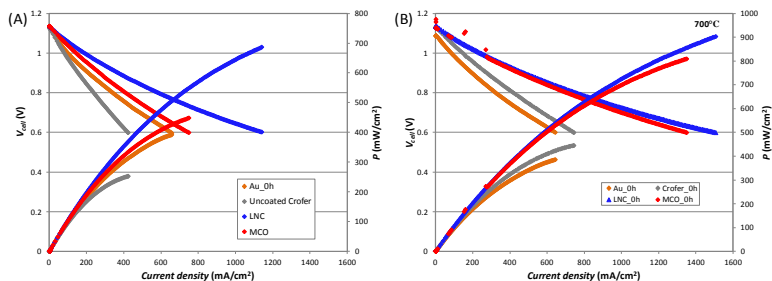


Figure III - 27. IV curves at 700°C at the initial time for (A) LSF-SDC and (B) LSCF-GDC composite cathode as a function of the current collector (Au, Crofer) and coating material for Crofer (MCO or LNC).

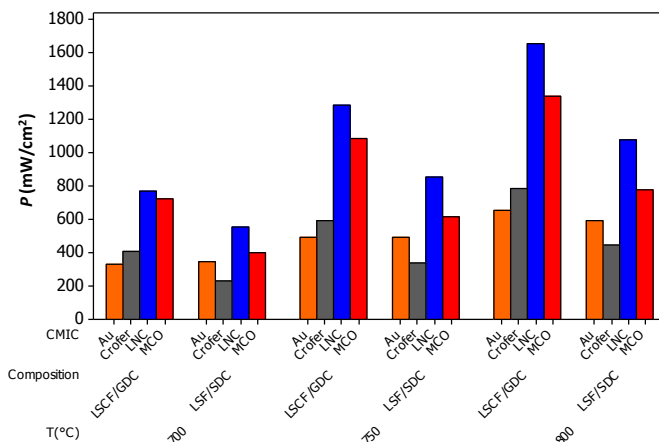


Figure III - 28. Power density at the initial time as a function of temperature (700°C, 750°C and 800°C), cathode composition (LSF-SDC or LSCF-GDC), current collector (Au or uncoated Crofer) and coating material for Crofer (MCO or LNC).

During Impedance Spectroscopy measurements, LNC coated Crofer mesh showed lowest ohmic resistance (Figure III - 29); R_o was lower than using Au mesh regardless the cathode composition. When MCO spinel was used as interconnect coating, trend was different depending on the cathode composition; as compared to

results with Au mesh, higher and lower R_o depending on the LSF-SDC and LSCF-GDC cathodes was measured, respectively. R_p was also higher for LSF-SDC cathode. Regarding the uncoated Crofer mesh, Nyquist diagram in Figure III - 29 further demonstrates the substantially scattered impedance for LSF-SDC cathode composition. This is most probably related to poor contact and problems in air diffusion.

Overall, Crofer mesh exhibits excellent contact with LSC contact paste in the cathode surface when it is coated with LNC perovskite.

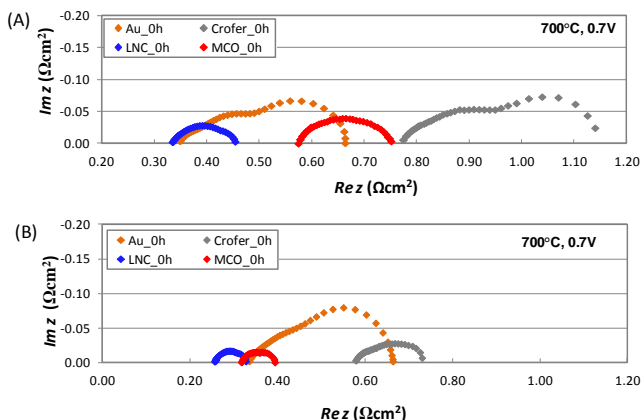


Figure III - 29. EIS measurements at 700°C and 0.7V at the initial time for (A) LSF-SDC and (B) LSCF-GDC composite cathode as a function of the current collector (Au or uncoated Crofer) and coating material of Crofer 22 APU (MCO or LNC).

Table III - 8. EIS measurements at 700°C and 0.7V as a function of cathode, current collector and coating material.

Cathode	Contact paste	Mesh	Mesh-Coating	R_o (Ωcm^2)	R_p (Ωcm^2)	ASR (Ωcm^2)
LSF/SDC	LSC	Au	Uncoated	0.35	0.32	0.66
			Crofer 22 APU	Uncoated	0.77	0.37
		Crofer 22 APU	LNC	0.33	0.12	0.45
			MCO	0.57	0.18	0.75
LSCF/GDC	LSC	Au	Uncoated	0.33	0.33	0.66
			Crofer 22 APU	Uncoated	0.58	0.15
		Crofer 22 APU	LNC	0.25	0.05	0.33
			MCO	0.32	0.07	0.39

Durability tests (500 h) were performed at 700°C and thus, EIS measurements are reported at such temperature in Table III - 8. However, it is worth to mention that ASR of cell was in the 0.15 - 0.2 Ωcm^2 range for LNC coating and 0.32 - 0.35 Ωcm^2 range for MCO coating at 800°C and 0.7V.

Performance under steady state operation

During the 500 h durability tests, cells with uncoated Crofer mesh underwent rapid voltage degradation decrease (Figure III - 30). Degradation was particularly high for the cell with LSF-SDC cathode composition and it broke before reaching 200 h of operation. Cells performance with LNC or MCO coatings were stable as compared to experiments performed with uncoated Crofer mesh. However, an abrupt voltage loss was observed simultaneously at 300 h for cells with LSF-SDC/LNC and LSCF-GDC/MCO cathode and coating combinations. Those cells were tested together and this loss is attributed to problems in the data acquisition system (i.e. eventual contact in the circuit). In fact, after a certain time voltage was recovered and performance was once again stable.

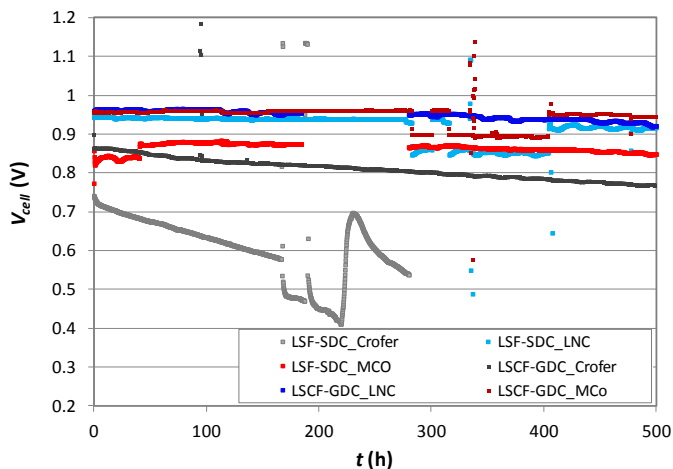


Figure III - 30. Voltage evolution during the 500 h durability tests as a function of cathode composition (LSF-SDC or LSCF-GDC) and uncoated or coated (LNC or MCO) Crofer 22 APU current collector. (Operation at 700°C and 0.25 A/cm²; 75ml/mincm² H₂ (%3 H₂O); 75ml/mincm² air).

At the end of the durability tests (~ 500 h), cells were again electrochemically characterized. However, IV-curves demonstrated that cells which use LNC and MCO coatings also degrade to some extent (Figure III - 31).

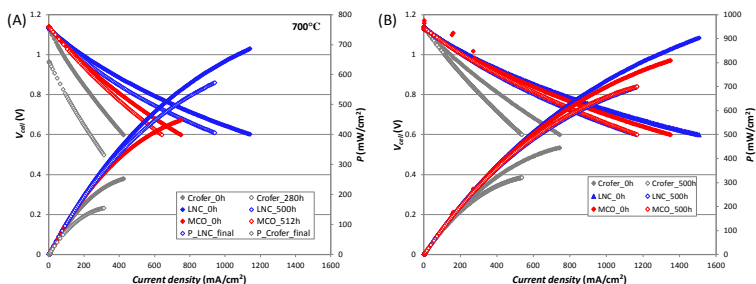


Figure III - 31. IV curves at 700°C at the initial and final time of 500h durability tests tests for (A) LSF-SDC and (B) LSCF-GDC composite cathode as a function of uncoated (indicated as Crofer) or coated (LNC or MCO) Crofer 22 APU current collector.

EIS measurements revealed that main degradation is caused by different mechanisms for the uncoated and coated (i.e. LNC or MCO) Crofer meshes (Figure III - 32). While degradation of cells with uncoated Crofer mesh is mainly reflected in an R_p increase, for cells tested with coated mesh (i.e. LNC or MCO), it is mostly related to R_o increase. In the first case, huge R_p increase when Crofer mesh is uncoated is reasonably related to chromium poisoning and deposition in the cathode. In contrast, for coated Crofer meshes, major R_o degradation could be related to coating reactivity with interconnect (Crofer) or contact paste (LSC). This should be, however, confirmed by microstructural analysis. As an exception, when MCO coating was used combined with LSCF-GDC cathode composition, R_o increase was very low $\approx 0.03 \Omega\text{cm}^2$ in 500 h. In fact, for this configuration, the lowest ASR increase $\approx 0.07 \Omega\text{cm}^2$ in 500 h is reported.

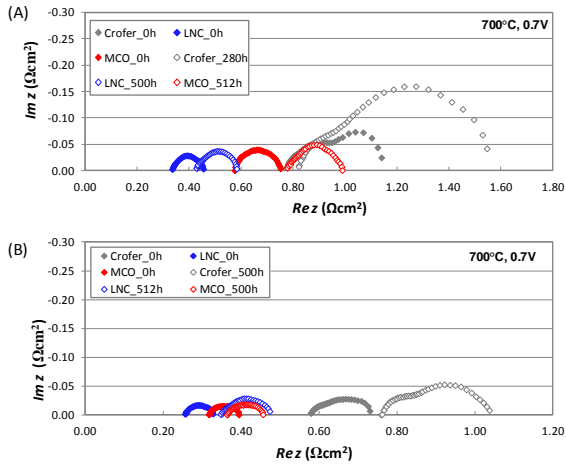


Figure III - 32. EIS measurements at 700°C and 0.7V at the initial and final time of 500 h durability tests (700°C; 0.25 A/cm²) for (A) LSF-SDC and (B) LSCF-GDC composite cathode as a function of uncoated (indicated as Crofer) or coated (LNC or MCO) Crofer 22 APU current collector.

Table III - 9. R_o , R_p and ASR increase in the 500 h durability tests as a function of cathode, current collector and coating material. (EIS measurements at 700°C and 0.7V)

Cathode	Contact paste	Mesh	Mesh-Coating	Δt	ΔR_o (Ωcm^2)	ΔR_p (Ωcm^2)	ΔASR (Ωcm^2)
LSF/SDC	LSC	Crofer 22 APU	Uncoated	280	0.05	0.37	0.42
			LNC	500	0.10	0.03	0.13
			MCO	512	0.21	0.03	0.24
LSCF/GDC	LSC	Crofer 22 APU	Uncoated	500	0.18	0.13	0.31
			LNC	512	0.10	0.07	0.14
			MCO	500	0.04	0.03	0.07

Voltage degradation as measured from the maximal activation point during operation, ΔV_2 , shows rather similar stability for LNC and MCO coatings regardless the cathode composition; 5-10% kh⁻¹ for LNC and 3-10% kh⁻¹ for MCO coatings. However, lowest degradation of 3%kh⁻¹ was registered when MCO coating was combined with LSCF-GDC composite cathode.

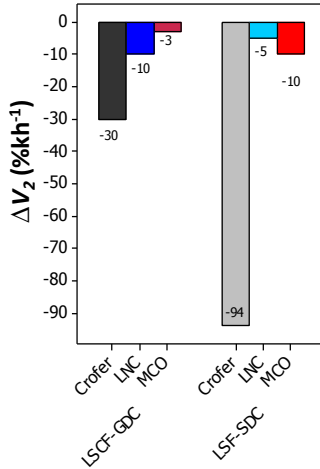


Figure III - 33. Degradation rates during the 500 h durability tests. ΔV_2 is calculated by using maximal activation time as reference and degradation rates are normalized in 1000 h using analogous equation to Eq. (3.2).

3.3.4 Overall discussion and conclusions

In this section, the performance and stability of candidates for metal interconnect coatings, novel LNC perovskite and MCO spinel, have been tested. Nextech Materials provided with Crofer 22 APU meshes coated or uncoated with such materials and they were used as current collector in the air side of anode supported cells, thus, reproducing the real operation conditions with metal interconnect.

Initial characterization of cells showed extensively improved electrochemical performance when Crofer mesh was coated with LNC or MCO materials. Power density was especially high for LNC coating and exceptional 1640 mW/cm² were recorded at 800°C when LSCF-GDC cathode was used. This is attributed to the high electronic conductivity of LNC but also to the excellent contact properties that it exhibits.

Additionally, performance stability improved significantly during 500 h tests when Crofer mesh current collector was coated with LNC or MCO. Tests which were performed using uncoated Crofer mesh showed high R_p increase due to chromium poisoning at the cathode. In contrast, when LNC or MCO coated Crofer mesh was used as current collector, cell was rather stable but little degradation mainly related to ohmic resistive effects were still detected. The variation of polarization resistance are below 0.07 Ωcm^2 for all coated meshes, showing the effectiveness and quality of coating against chromium poisoning. R_o increase might be related to chemical

reaction between coating material and neighbouring components, however, this assumption should be verified by SEM inspection. MCO coating combined with LSCF-SDC cathode exhibited the lowest degradation of $3\% \text{kh}^{-1}$. However, combinations with different cathode compositions lead to degradation rates between $3\text{-}10\% \text{kh}^{-1}$ for MCO and $5\text{-}10\% \text{kh}^{-1}$ for LNC. Therefore, it seems that stability and effectiveness for MCO spinel and LNC perovskite interconnect coatings is comparable. However, high performance and extremely low contact resistance that LNC coating exhibits makes this material a suitable candidate for interconnect coating.

As a matter of fact, while this experimental work with LNC and MCO coatings was ongoing, Nextech Materials decided to patent the LNC coating and processing techniques for its use as protective layer in metal alloys [241].

3.4 Appendix III

Taguchi matrix

Taguchi methodology is a widely used approach for systematic analysis of impact factors in a cost and time efficient way. It is widely applied in industrial processes and its applicability has been evaluated in this work.

The original L_{18} orthogonal matrix which was used in the cathodes stability study (section 3.1.2) consists of one control factor at two levels and seven control factors at three levels. Two of the control factors at three levels were downgraded to two levels preserving the orthogonality of the matrix. Taguchi matrix in coded variables is presented in Table III - A.

Table III - A. L_{18} Taguchi matrix in coded variables with Dummy treatment in two variables which are downgraded from three to two levels.

Exp#	a_i	b_i	c_i	d_i	e_i	f_i	g_i	h_i
1	-1	-1	-1	-1	-0.50	-1.0	-1	-1
2	-1	0.5	0	-1	0.13	-0.7	0	0
3	-1	0.5	1	-1	0.50	1.0	1	1
4	-1	0.5	1	0.5	-0.50	-1.0	0	0
5	-1	-1	-1	0.5	0.13	-0.7	1	1
6	-1	0.5	0	0.5	0.50	1.0	-1	-1
7	-1	0.5	1	0.5	-0.50	-0.7	-1	1
8	-1	0.5	-1	0.5	0.13	1.0	0	-1
9	-1	-1	0	0.5	0.50	-1.0	1	0
10	1	0.5	-1	-1	-0.50	1.0	1	0
11	1	0.5	0	-1	0.13	-1.0	-1	1
12	1	-1	1	-1	0.50	-0.7	0	-1
13	1	0.5	0	0.5	-0.50	-0.7	1	-1
14	1	-1	1	0.5	0.13	1.0	-1	0
15	1	0.5	-1	0.5	0.50	-1.0	0	1
16	1	-1	0	0.5	-0.50	1.0	0	1
17	1	0.5	1	0.5	0.13	-1.0	1	-1
18	1	0.5	-1	0.5	0.50	-0.7	-1	0

L_{18} can be converted to coded variables u_j , instead of the natural variables used in the experimental design U_j (Table III - 2), by the following transformation:

$$u_j = \frac{[U_j - U_j(0)]}{\Delta U} \quad (3.3)$$

being $U_j(0)$, the center of the interval of the natural variable and ΔU the half of the natural interval. In the case of control factors with Dummy treatment the duplicated

levels natural value is half weighted. Orthogonality can be expressed in coded variables as follows:

$$\sum_{i=1}^{18} \mathbf{u}_{ij} \mathbf{u}_{ik} = \mathbf{0} ; \sum_{j=1}^{18} \mathbf{u}_{ij} \mathbf{u}_{kj} = \mathbf{0} \quad (3.4)$$

These standardized variables allow to work with variables centered at zero and varying in the interval [-1, 1]. Columns (rows) are linearly independent; the scalar product is equal to zero for any combination of columns (rows). One can observe that for the experiments where *a* factor is at the level $a_1=-1$, the levels of *g* factor (g_1 , g_2 and g_3) appear three times and the same holds for level $a_2=1$, for which the levels of *g* factor appear again balanced.

Therefore, to build an experimental design on the basis of a coded Taguchi matrix (L₁₈ in Table III – A in this case), variables for analysis are first selected (i.e. cathode processing parameters and operation conditions in this work) and they are assigned to columns in the Taguchi matrix. Then, levels for each variable are set. For instance, for coded variable *a* with two levels ($a_i=1$ or -1), cathode composition (A) was assigned in natural variables with levels for A are $A_1=LSF-SDC$ and $A_2=LSCF-GDC$.

Chapter IV

METAL-SUPPORTED CELL FABRICATION AND OPERATION

Part of this chapter has been published in:

Lide M. Rodriguez-Martinez, Laida Otaegui, Amaia Arregui, Mario A. Alvarez, Igor Villarreal

“Tubular metal supported solid oxide fuel cell resistant to high fuel utilization”,
10th European SOFC Forum, A0905 (2012) 1-10.

Amaia Arregui, Laida Otaegui and Lide M. Rodriguez-Martinez

“Stability under severe operation of tubular metal supported SOFCs”,
In preparation.

4.1 IK4-Ikerlan MSC-Technology

4.1.1 Introduction

In the early 2000, IK4-Ikerlan S. Coop commenced the research and development of low cost tubular metal-supported SOFC in close cooperation with Lawrence Berkeley National Laboratory (LBNL), from which a pioneering metal-supported cell design was transferred [135, 242]. The know-how acquired under planar configuration in LBNL and new further developments were used to produce tubular MS-SOFCs at IK4-Ikerlan. The ultimate application pursued for those fuel cells was a small domestic gas fired Combined Heat and Power Unit (CHP) below 2.5 kW. Commercialization of this product was set in 2001 within the strategic plan of Mondragon, Fagor, Copreci and MCC Components, four partners involved in the production and innovation of home appliances.

Market introduction of this technology implies advances in different knowledge areas and IK4-Ikerlan has largely invested in system components, power electronics, control system, fuel processing, stack and CHP system design for the tubular MSC

application. Nevertheless, materials development is the key factor to obtain viable cells with good efficiency and stability. In this field, IK4-Ikerlan S. Coop. has worked in continuous collaboration with Materials Science reference research centres and universities (CEIT-IK4, Nextech Materials, Polymer Innovations, Fraunhofer IKTS, Forschungszentrum Jülich, ICMA, ULL, UPV/EHU, CIC-Energigune). Tubular MSC production was addressed in partnership with CEIT-IK4.

In collaboration with LBNL, an attempt to incorporate catalyst infiltration technique in the manufacturing process was made also at IK4-Ikerlan. The configuration was essentially the same as that described by Tucker et al. [188]. Five layer configuration consisting of porous metal-support/porous YSZ/dense YSZ electrolyte film/porous YSZ interlayer/porous metal current collector was fabricated. After co-sintering of the cell framework, Ni and LSM catalysts were infiltrated in the anode and cathode, respectively. However, complexity added in the fabrication together with poor preliminary results persuaded as to continue with this route.

First generation tubular MSC developed at IK4-Ikerlan with own *know-how* includes a yttrium doped ceria and nickel cermet DBL, Ni-YDC, to prevent the interdiffusion of Ni, Cr and Fe that takes place during the high co-sintering temperatures necessary for the densification of the electrolyte.

Early experience with first generation cells (G1) includes an extensive optimization process with the metal tube and analysis of metal raw materials in cell performance [179]. FeCr-support porosity, surface roughness and shrinkage during co-sintering result key parameters that affect the final electrochemical performance. Those control factors strongly depend on processing parameters such as FeCr particle size and morphology and they have been studied in detail [179]. A variety of crofer batches (Crofer 2, 3+, 4, 6, 6') which were combined with different flake fractions, produced G1 cells with an assortment of shrinkage (7 to 17%), porosity (25 - 60%) and power densities (150 – 450 mW/cm²) [105].

In a first approach, robustness of first generation cells was successfully proved under low fuel utilization conditions. G1 tubular MSCs demonstrated good efficiencies as well as robustness under steady current load and thermal cycling. G1 cells were stable under constant current load during 2000 h and more than 500 thermal cycles under 4% and 5% hydrogen utilization, respectively [102]. However, these values are far below the initial aim to reach 70% fuel utilization. Subsequent stability tests with slightly higher fuel utilizations (9-17% FU) caused the drastic failure of cell performance in few hours (Figure IV - 1).

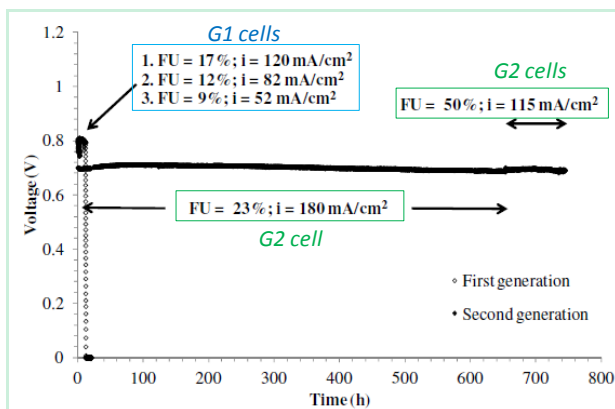


Figure IV - 1. Illustration of the stability of first and second generation cells as a function of the fuel utilization. (Reproduced under permission of Laida Otaegui [102]).

This failure is related to the catastrophic corrosion of the metal-support as illustrated in Figure IV - 2. Post-mortem analysis revealed that poor stability of first generation cells even at low fuel utilization (9 to 17% H₂O) is directly connected to element interdiffusion during co-sintering [102]. In one hand, chromium, manganese and iron released in the Crofer 22 APU stainless steel diffuse to the anode. These invasive elements preferentially crystallize on the surface of nickel particles affecting their catalytic activity. On the other hand, nickel present in the barrier layer and anode migrates to the metal-support. Nickel incorporates into the ferritic stainless steel causing the austenitic transformation. This phase is more susceptible to corrosion and when G1 cells are subjected to even low fuel utilization, water resulting from fuel electrochemical oxidation causes the immediate catastrophic corrosion of the metal support. It is worth to mention that detailed analysis with ceria-based DBL in first generation SOFC carried out at IK4-Ikerlan demonstrated that, element interdiffusion still occurs during operation at 800°C [102].

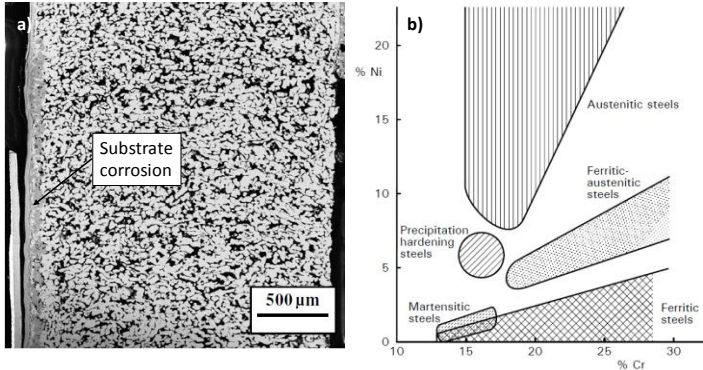


Figure IV - 2. a) Oxidized-support of G1 cell after 9 to 17% FU during 12 h operation shown in Figure IV - 1. Illustration of the stability of first and second generation cells as a function of the fuel utilization. (Reproduced under permission of Laida Otaegui [102]). (Reproduced under L. Otaegui permission [102]) and **b)** classification of stainless steels according to chromium and nickel content (Reproduced from The European Stainless Steel Development Association manual).

Phase diagram in Figure IV - 2b shows the austenitization of ferritic stainless steel that takes place above certain nickel concentration. This transformation occurs for lower nickel concentrations when chromium concentration is also lower in the steel. Hence, chromium migration and nickel incorporation which occur during co-sintering, promote ferritic stainless steel austenitization above a certain value.

Recently, preliminary tests with a second generation of MSCs provided with promising results under realistic operation conditions of fuel utilization [102]. Second generation cells (G2) differ from G1 cells basically in the perovskite-based DBL used and they have been specifically selected to prevent element interdiffusion during co-sintering. This perovskite is a La-doped SrTiO_3 ($\text{La}_{0.3}\text{Sr}_{0.7}\text{TiO}_{3-\delta}$) which exhibits excellent electronic conductivity under reducing atmospheres [184]. In contrast to G1 cells, the LST DBL is nickel free and Ni-YSZ cermet anode is the only Ni diffusion source during co-sintering. First stability tests with G2 cells showed a rather stable performance during at least 700 h at more realistic 25 to 50% fuel utilization conditions (Figure IV - 1). This is already a very encouraging starting point for second generation cell development.

The second part of this thesis focuses in the development of a second generation of MSC technology, related to manufacturability, performance optimization and detailed analysis of cell robustness under severe operation conditions. The following research activities have been carried out during this thesis:

- *Basic processing parameters optimization (i.e. particle fraction of the metal substrate and sintering temperature)*
- *Influence of LST-DBL thickness in characteristic features (i.e. spots or stains in the electrolyte surface) after co-sintering and electrochemical performance of cells*
- *Influence of electrodes thickness (i.e. anode and cathode) in the electrochemical response of MSCs*
- *Analysis of degradation during fabrication*
- *Analysis of degradation during operation*

During the optimization phase of G2 cells, the standardized manufacturing process demonstrated significant variability under an uncontrolled factor during the co-sintering process. This variability was reflected in dark stains which were frequently observed in the electrolyte surface after co-sintering. Therefore, in a second part, degradation mechanisms that occur during the manufacturing process of G2 cells (i.e. half-cell co-sintering at high temperatures) have been investigated. Despite the interdiffusion mechanism already recognized for G1 cells [179], G2 cells present an inherent degradation mechanism related to subtle variations in the co-sintering atmosphere. This degradation is related to the titanium segregation in the LST diffusion barrier layer and migration to the anode and electrolyte. Titanium diffusion is related to stains in the electrolyte surface and it is easily recognized after co-sintering. This phenomenon turns out to be critical in the electrochemical performance and stability of G2 cells. However, titanium diffusion is a variable mechanism that deteriorates G2 cells during co-sintering only when it is activated. Therefore, the main challenge of this work was to understand the factor that activates titanium diffusion during co-sintering.

In the final part of this work, G2 cells ageing and degradation under operation were investigated. Accelerated ageing techniques which include redox and thermal cycles were used to study G2 cells degradation in prolonged service. In addition, particular emphasis was put in the analysis of G2 cells stability under fuel utilization.

4.1.2 Fabrication of tubular metal-supported SOFC

Fabrication of IK4-Ikerlan proprietary tubular MS-SOFCs is divided in two phases: metal-support fabrication at CEIT-IK4 and ceramic coatings, cell processing and characterization at IK4-Ikerlan (Figure IV - 3).

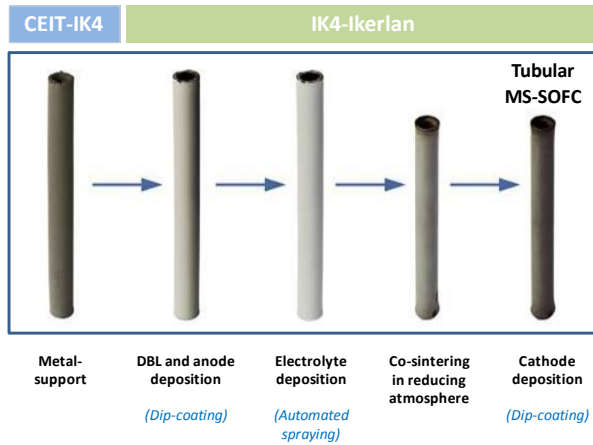


Figure IV - 3. Manufacturing process of tubular metal-supported SOFCs in IK4-Ikerlan.

Porous metallic tubes are produced with Crofer 22 APU, a ferritic stainless steel, at CEIT-IK4 by an innovative processing technique which is called *free-fall powder*. Presintered tubes are transferred to IK4-Ikerlan for cell fabrication. Functional ceramic layers are deposited by low cost industrial scalable routes that can be classified as “wet” or “colloidal” deposition techniques and include dip-coating and spray-coating. First, a diffusion barrier layer (DBL) is deposited by dip-coating to prevent Cr, Fe and Ni interdiffusion which occurs between the FeCr metal support and anode during co-sintering. Second, Ni-YSZ cermet anode is deposited by dip-coating. At this point, organic additives of ceramic slurries are burnt at 400°C. Third, 8YSZ electrolyte is deposited by automated spray. This is followed by co-sintering at high temperatures in reducing atmosphere to attain the full densification of the electrolyte (Figure IV - 3). Finally, LSF-SDC composite cathode is deposited by dip-coating and sintered *in-situ* at 950°C to avoid the reactivity of LSF and YSZ at higher sintering temperatures. Tubular cell configuration and microstructure followed by the processing route and layers thickness are summarized in Figure IV - 4 and Table IV - 1.

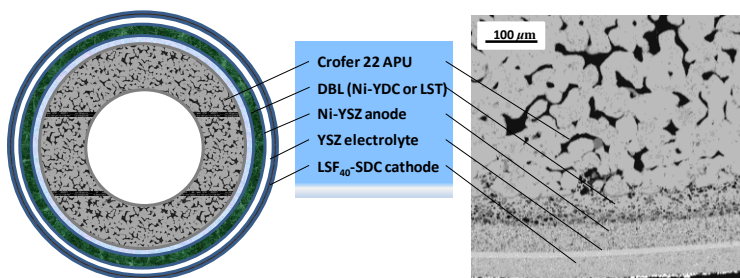


Figure IV - 4. Basic tubular metal-supported SOFC configuration and SEM cross section.

Table IV - 1. Summary of the functional layers of the MS-SOFC and their fabrication route.

<i>Functional layer</i>	<i>Composition</i>	<i>Fabrication route</i>	<i>Thickness (μm)</i>
Substrate	Crofer 22 APU	Free Powder	4200-4300
G1-DBL	Ni-YDC	Dip coating	0-30
G2-DBL	$\text{La}_{0.3}\text{Sr}_{0.7}\text{TiO}_x$	Dip-coating	60-80
Anode	NiO-YSZ (%50 vol. Ni)	Dip-coating	40-50
Electrolyte	8mol% YSZ	Automated spraying	10-15
Cathode	$\text{LSF}_{40}\text{-SDC}_{20}$	Dip-coating	15-30

In the following sections, a detailed description of tubular metal substrates production (CEIT-IK4) and cell processing (IK4-Ikerlan) is provided.

4.1.2.1 Metal support manufacturing at CEIT-IK4

Crofer 22 APU, a ferritic chromium-based stainless steel especially developed for SOFC applications by Forschungszentrum Jülich, is used to produce porous metal supports using atomized powders manufactured by HcStarck/IKTS (several batches). This alloy contains 20-24 wt.% Cr, 0.3-0.8 wt.% Mn, 0.5 wt.% Si, 0.02 wt.% S (max), 0.05 wt.% P, 0.03 wt.% C, 0.03-0.02 wt.% Ti, 0.04-0.2wt.% La [243]. At temperatures up to 900°C, a chromium-manganese mixed oxide layer - Cr_2O_3 and Cr_2MnO_4 - is formed on the surface of Crofer 22 APU, which is thermodynamically stable and possesses high electrical conductivity [171]. This alloy contains relatively low level of impurities and Ti and La as reactive elements; La improves scale adhesion and reduce oxidation rate and Ti forms internal oxides which results in strengthening of near surface alloy region [244]. A TEC of 12 ppmk^{-1} is compatible with adjacent ceramic components. At IK4-Ikerlan, cells based on Crofer 22 APU substrates with final porosities between 25-40% stability have been proved under operation at 800°C for more than 4500 h in 50% humidified hydrogen [245]. In the present study, a single batch of Crofer 22 APU, the so called Crofer3+ has been used for cell fabrication [179].

Tubular metal support is fabricated by an innovative technique called *free-fall powder* in CEIT. First, Crofer 22 APU is agglomerated at 1050°C for 1h in a reductive atmosphere in a Jones hydrogen furnace. Agglomerated bars are crashed and subsequently characterized via particle size distribution and C/O₂ concentration determination. Desired FeCr particle fraction is sieved for tube preparation. In a second step, metallic tubes are presintered. Alumina molds with tube shape are filled with the selected powder fraction. Standardized vibration protocol during powder filling guarantees a homogeneously distributed powder within the mold. Alumina tubes are then introduced in hydrogen furnace at 1100-1150°C for 1h. Final characterization of presintered tubes in terms of green density and porosity is listed in Table IV - 2 for selected FeCr particle fractions <45 μm, <53 μm and <80 μm. Finest FeCr fraction (<45 μm) was the optimal for G2 cells and has been used in the production of standard tubular metal-supports all through this work. Micrograph in Figure IV - 5 illustrates the typical microstructure of a standard presintered tubes (FeCr<45 μm).

Table IV - 2. Characteristics of presintered C3+ tubular supports. (SE holds for the standard error).

FeCr particle fraction (μm)	Green density		Green porosity	
	ρ (gcm ⁻³)	SE	p (%)	SE
<45	3.09	0.01	59.9	0.1
<53	3.04	0	60.5	0
<80	2.32	0.01	69.9	0.1

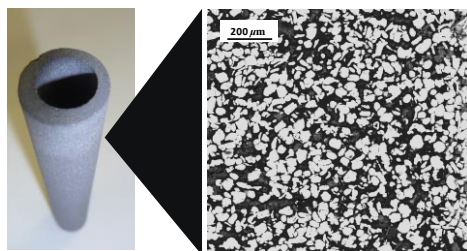


Figure IV - 5. Microstructure of the standard presintered C3+ tube cross section with fine (<45 μm) FeCr particle fraction.

4.1.2.2 SOFC fabrication in IK4-Ikerlan

In this work, the second phase of the manufacturing process was carried out in IK4-Ikerlan by the author to produce second generation (G2) cells. Every stage of the manufacturing process is described in this section.

Metal tube preparation and labelling

The first step is to cut and label the tubes (Figure IV - 6). Presintered tubes (≈ 10 cm) are transferred in batches from CEIT-IK4 (batch 202 in Figure IV - 6). Every tube in the batch is enumerated based on the mould that was used during the *free-fall powder* sintering and it has its own green density. We select tube 12 with 3.12g/cm^3 green density in Figure IV - 6. Depending on the desired dimensions, the tube is directly used or cut in several pieces. This is also specified in the label with an up to down enumeration of pieces. Thus, cell label gives information about batch, processing technique, mould and tube segment. Tube dimensions (i.e. length, internal and external diameter) and weight are registered to analyze shrinkage and weight loss after co-sintering (section 2.3.2.2). Finally, metal tube surfaces are cleaned-up with compressed air before ceramic layers deposition.

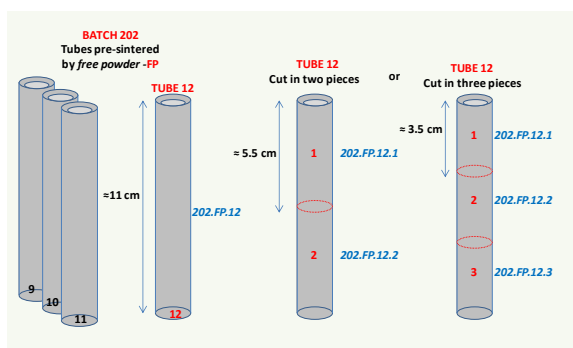


Figure IV - 6. Tube classification and cell labelling.

Ceramic layers processing

Ceramic slurries are water based environmentally friendly suspensions and contain, in addition to the ceramic powder, binder, plasticizer, pore-former (if porosity is desired), and other organic additives necessary for the fabrication process. Whilst first generation cells include a ceria-based Ni-YDC cermet as barrier layer (G1-DBL), second generation cells use a perovskite-type $\text{La}_{0.3}\text{Sr}_{0.7}\text{TiO}_x$ (LST) barrier (G2-DBL). Anode material is the conventional Ni-YSZ cermet with 8% mol Y_2O_3 stabilized zirconia (8YSZ) and 50 vol% Ni after processing. Electrolyte material is also the widely used 8% mol Y_2O_3 stabilized zirconia (8YSZ), a pure ionic conductor with excellent stability. Finally, cathode contains $(\text{La}_{0.6}\text{Sr}_{0.4})_{0.95}\text{FeO}_{3-x}$ ferritic perovskite combined with 30 wt% $\text{Ce}_{0.8}\text{Sm}_{0.2}\text{O}_2$.

Characteristic of commercial powders

Particle size (d_{50}) and specific surface area (SSA) of powders is strategically selected to fulfill the specific requirements for each cell component (Table IV - 3). Similar 8YSZ composition used for electrolyte and anode processing differ substantially in the SSA. While SSA is 6 m²/g for 8YSZ used in the anode, it is 13 m²/g for 8YSZ used in the electrolyte to promote full densification during co-sintering. As LSF₄₀-SDC cathode is sintered *in-situ* at low temperatures (950°C), morphological characteristics are adjusted to meet this criteria and small 0.32 μm LSF₄₀ and 0.37 μm SDC particles are used with 8.7 and 10.8 m²/g SSA, correspondingly. However, some powders do not exhibit adequate morphological characteristics. In particular, SSA for commercial La_{0.3}Sr_{0.7}TiO_x (LST) perovskite is very high (29 m²/g) and 10 μm NiO particles are too large. Hence, those powders are pre-treated before slurry preparation.

Table IV - 3. Commercial supplier, stoichiometry, particle size (d_{50}) and surface specific area (SSA) of commercial powders.

Component	Material	Stoichiometry	Commercial supplier	d_{50} (μm)	SSA (m ² g ⁻¹)
LST-DBL	LST	La _{0.3} Sr _{0.7} TiO _x	AGC SEIMI CHEMICAL	0.26	29
Ni-YSZ	NiO	NiO	Sigma Aldrich/Panreac	10	90
Anode	YSZ (TZ-8YS)	8%Y ₂ O ₃ stabilized ZrO ₂	TOSOH	0.5	6
YSZ Electrolyte	YSZ (TZ-8Y)	8%Y ₂ O ₃ stabilized ZrO ₂	TOSOH	0.5	13
LSF-SDC Cathode	LSF40	(La _{0.6} Sr _{0.4}) _{0.95} FeO _{3-x}	Nextech Materials	0.32	8.7
	SDC	Sm _{0.2} Ce _{0.8} O _{2-x}	Nextech Materials	0.37	10.8

Adaptation of powder properties

Commercial powders are modified by means of mechanical and thermal treatments to adjust their properties. In this section, specific treatment for each cell component is described.

Diffusion barrier layer - LST

Commercial LST powder is agglomerated to reduce high SSA (29 m²/g) which promotes barrier densification during co-sintering. In fact, barrier layer must be porous to allow fuel diffusion to the anode. In this commitment, 50g of LST powder are introduced in an alumina pot and are fired at 1150°C in air during 2h. Agglomerated powder is subsequently sieved using a nylon mesh with 120 μm

orifice. As a result of the thermal treatment particle size grows to 0.6 μm and specific surface area is reduced to 5 m^2/g .

Ni-YSZ cermet anode and LSF₄₀-SDC composite cathode

Before the preparation of slurries, Ni-YSZ cermet anode and LSF₄₀-SDC composite cathode mixtures are prepared in an attritor (Attritor 01HD-CR) that reduces particle size distribution at 500 rpm for 3h and 0.5h, respectively (section 2.3.1.1). Powder mixtures give NiO-YSZ cermet anode with 50 vol% Ni cermet anode after reduction; LSF-SDC composite cathode is 30 wt% SDC.

YSZ electrolyte

YSZ (TZ-8Y) powder used for electrolyte processing does not require any treatment prior to slurry preparation.

DBL and electrodes slurry preparation and deposition by dip-coating

LST diffusion barrier layer, Ni-YSZ cermet anode and LSF₄₀-SDC composite cathode are deposited by dip-coating using the Diptech Automatic Dip coating unit. This technique consists in the immersion of the substrate surface in liquid slurry which contains the material for deposition. This simple and fast deposition technique is cost effective and industrially scalable. However, it is limited to produce very thin coatings (<10-15 μm). In this work, uniform coatings were attained following a proper control of slurries viscosity and dip-coating parameters (i.e. immersion rate, dwell and extraction rate).

Ceramic slurries preparation

Barrier layer (LST), anode (Ni-YSZ) and cathode (LSF₄₀-SDC) slurries are water based solutions with organic additives (i.e. binder, plasticizer, pore-former). Those additives permit a better powder dispersion in the solution; they eliminate bubbles that might cause imperfections as well as providing with porosity when required. Standard formulations were optimized by Polymer Innovations for IK4-Ikerlan and they figure in Table IV - 4.

Slurries preparation is carried out in two phases. In the first phase, solvent, powder and additives are mixed (Table IV - 4) and mixtures are milled at 92 rpm during 16h in milling machine (Labmill 8000©) with 350g of YSZ cylinders (3/8"). In the second stage, some organic additives are newly introduced (indicated in brackets in Table IV - 4) and ceramic slurry is milled at 92 rpm during additional 4h. Finally, cylinders are removed and slurries are maintained fresh by rolling at 2-3 rpm in a Mini Tube Roller 7622-30000. Before deposition on the tube surface, slurries are mixed in a centrifugator (Awataori Rentaro AR-250) to guarantee homogeneous mixture and eliminate bubbles which may form during the slow roll. At this point, the

ceramic slurries viscosity is characterized at 25°C using a rheometer (Haake RheoWin 3). Viscosity measurements serve for *quality control* of the ceramic slurries (section 2.3.2.1).

Table IV - 4. Standard formulation of LST barrier, NiO-YSZ anode and LSF-SDC cathode.

Components	LST	NiO-YSZ	LSF-SDC
Powder			
	50.82 LST	61.4 NiO-YSZ	72 LSF-SDC
Solvent			
DI water	25.77	38.6	26
Additives			
WB4101	6.18 (7.23)	9 (15.34)	10(9.14)
D-3005		1.52	
DF002	0.18(0.09)	0.27(0.27)	0.15(0.15)
PL005	0.51	1.2	
NH ₄ OH			0.1
PF002	(3.09)		
PF007	(6.18)		

Second stage additives are indicated in brackets ().

Pre-sintered tubes cut into the desired dimensions are fixed into metallic pieces for dip-coating. Tube edges are covered with teflon to avoid slurry penetration on the inner face of the tube. Diffusion barrier layer and anode are deposited through the entire surface whereas cathode is deposited in a smaller central zone. This limits the electrochemically active area to the zone where cathode is deposited. This is advantageous, as cathode can be tactically placed in electrolyte areas with good quality (i.e. without defects, stains, cracks). Little cathode area facilitates current collection but introduces a higher error in the electrochemical measurements. According to this, optimal cathode area is set up in the 3-4 cm² range. As an exception, cells for fuel utilization tests are strategically prepared with larger efficient areas; 7-8 cm² cathodes. This approach is adopted to obtain high fuel utilizations with a flow-system with lack of precision under 30 ml min⁻¹ fuel flow.

Ceramic slurries are deposited by dip-coating (Diptech Automatic Dip Coating unit). In the process, the metal porous tube is introduced in a test tube with 50 ml capacity which contains about 35-40 ml of ceramic slurry. This slurry volume guarantees the complete immersion of tube and invariance in the immersion time. Find dip-coating parameters for ceramic slurries and equipment in section 2.3.1.3.

Removal of organic components

Before electrolyte deposition, the organic additives that DBL and anode contain are burnt at 400°C during 1h in air. The heating ramp pursued is 1°C/min⁻¹ to attain a gradual burning and avoid the defects that could arise from a sudden heating profile.

Electrolyte deposition by automatic spraying

YSZ deposition is carried out by automated spray (PVA spray robot). Finest YSZ particles are selected by dispersing 2.5g of YSZ in 350 ml of isopropanol in an ultrasound machine (Branson Sonifier 450) and collecting 220 ml after 24h of decantation.

The electrolyte thickness is controlled with the deposited volume. In a standardized YSZ spraying process, 10 μm thick YSZ electrolyte is obtained after co-sinterization for 10 ml of YSZ slurry which are deposited in 2.5 cm length tube. Thus, for typically 5.5 cm long tubes, 20 ml of YSZ slurry are deposited. Find spray robot working principle in section 2.3.1.3.

Half-cells co-sintering

FeCr/LST/Ni-YSZ/YSZ half-cells are co-sintered in a Carbolite STF furnace which contains in its core a long alumina tube as device. Half-cells lie down in parallel in an alumina bed and are sintered two by two in the central zone, with minimal temperature gradients (15 cm long space).

The standardized co-sintering process of half-cells is carried out between 1330-1370°C depending on the type of cell, G1 or G2 (Figure IV - 7). A non-oxidizing atmosphere is employed to prevent the oxidation of the metal support. The heating ramp is conducted in 200 ml min⁻¹ Ar inert atmosphere before reaching 1100°C. At this point, 10% H₂ + Ar reductive atmosphere is introduced maintaining the gas flow rate. This procedure prevents nickel reduction previous to the shrinkage of the metal-support that starts at 1100°C (bare metal substrate is presintered at 1100°C in reducing atmosphere to provide sufficient strength for handling). Therefore, gas change at this temperature promotes the simultaneous shrinkage of metal substrate and ceramic layers.

For first generation cells, the incorporation of a FeCr-getter in the furnace entrance demonstrated to be effective against cell bending during the sintering process. Also with G2 cells, a device with FeCr oxygen getter is incorporated to protect the metal-support from eventual oxygen impurities.

After the co-sintering process, half-cells dimensions (i.e. length, internal and external diameter) and weight are measured to analyze shrinkage and weight loss after co-sintering (section 2.3.2.2). In addition, half-cell photos are systematically registered.

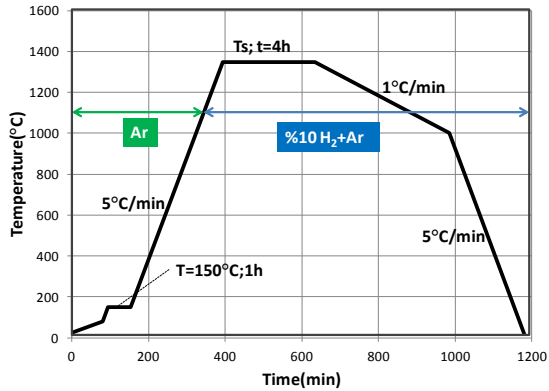


Figure IV - 7. Standardized co-sintering cycle of FeCr/DBL/Ni-YSZ/YSZ tubular half-cells.

4.1.3 Differences between G1 and G2 cells

Enhanced electrochemical efficiency is expected in practice for cells with perovskite-type LST DBL as the electronic conductivity is two orders of magnitude higher (Table IV - 5). In addition, TEC matches better with Crofer (11.9 ppmK^{-1} [195]) and YSZ (10.5 K^{-1} [140]) adjacent components.

Table IV - 5. Main characteristics for ceria and perovskite-based DBLs used in G1 and G2 cells, respectively. Conductivities are measured at 800°C under reducing atmosphere. (*) refers to manufacturers data and (**) are experimental data obtained at IK4-Ikerlan.

Composition	Thickness (μm)	Conductivity (S/cm)	TEC(ppmK ⁻¹)
G1-DBL	Ni-YDC	0-30	YDC: 1*
			Ni: 20000 [247]
			Ni-YDC: 2**
G2-DBL	$\text{La}_{0.3}\text{Sr}_{0.7}\text{TiO}_x$	60-80	216 [184]
			11-12 [26]

Shrinkage and electrochemical characteristics of G1 and G2 cells are summarized in Figure IV - 8. G2 cells are compared to corresponding G1 cells with Crofer C3+ metal-support with similar green densities in the $2.8\text{-}2.9 \text{ g/cm}^3$ range. Despite the promising stability during long-term operation with fuel utilization,

electrochemical performance of G2 cells was worse than expected. Power densities below 100 mW/cm² obtained for G2 cells are in contrast with the average 250 mW/cm² obtained with G1 cells. This was attributed to higher R_o and R_p . Higher shrinkage of G2 cells during co-sintering leads to a final porosity of 32%. This is low in comparison to G1 cells with 46% in average. However, electrochemical characterization (IV-curves) demonstrated that fuel diffusion is not affected in G2 cells. In fact, G2 cells OCV values above 1.09 V were recorded at 800°C. YSZ electrolyte densification is favored at higher shrinkage and better gas tightness of G2 cells was confirmed.

Shrinkage of FeCr/DBL/Ni-YSZ/YSZ configuration was also studied by dilatometry in FeCr pins with comparable green densities of presintered tubes. Experimental results are summarized in Figure IV - 9. FeCr pin alone shrinks 25%. First deposition of DBLs inhibits FeCr pin shrinkage during co-sintering. Little difference is observed with LST barrier ($\Delta L/L_o \approx 22\text{-}23\%$) but shrinkage with Ni-YDC is much lower ($\Delta L/L_o \approx 12\%$). When Ni-YSZ layer is first deposited there is no practical difference. Overall, cell shrinkage during co-sintering is mostly driven by the composition of the barrier layer. Therefore, there is no substantial difference between FeCr/DBL, FeCr/DBL/Ni-YSZ and FeCr/DBL/Ni-YSZ/YSZ configurations.

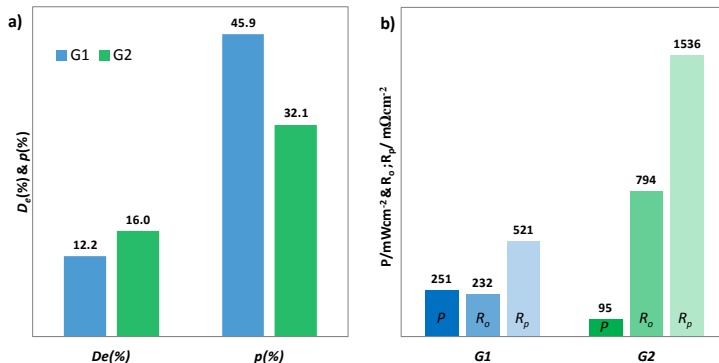


Figure IV - 8. Comparison of principal characteristics of G1 and G2 cells: a) transversal shrinkage ($\%D_e$) during co-sintering and b) electrochemical performance at 800°C and 0.7V. (G1 data analyzed from Laida Otaegui thesis work [179]).

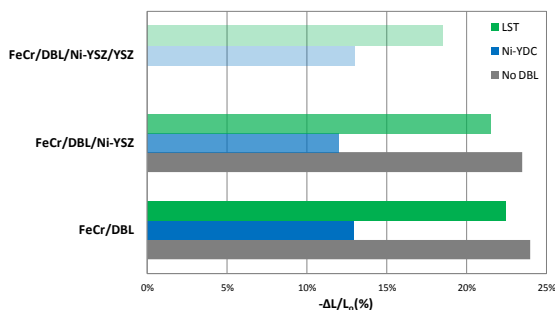


Figure IV - 9. Shrinkage of Crofer 22 APU pins and functional ceramic layers after standard cell sintering procedure. (Data analyzed from Laida Otaegui thesis work [179]).

Shrinkage is directly related to final thickness and microstructure of functional layers. Nominal thickness of G2 cells has been systematically measured by SEM, however, scarce information of specific G1-C3+ cells exist (Table IV - 6). First generation DBL, Ni-YDC, is much thinner than the second generation initial LST layer. Little data with G1-C3+ cells is available but Ni-YSZ cermet anode is also thinner. Thinner DBL and anode explain more probably the superior electrochemical performance of G1 cells.

During this work, an attempt to improve the electrochemical performance of G2 cells through the reduction of DBL and anode thickness was carried out. Results are discussed in section 4.2.

Table IV - 6. Functional layer thicknesses in G1 and G2 cells.

<i>MSC cell</i>	<i>Functional layer</i>	<i>Thickness (μm)</i>
G1	Ni-YDC barrier	5-30
	Ni-YSZ anode	≈ 30
	YSZ electrolyte	10-15
G2	$\text{La}_{0.3}\text{Sr}_{0.7}\text{TiO}_x$ barrier	70-90
	Ni-YSZ anode	40-50
	YSZ electrolyte	10-15

4.2 Second generation cells optimization

4.2.1 Introduction

In this section, optimization studies with G2 cells are presented. Some of the processing parameters which were studied are directly related to the shrinkage of half-cells during co-sintering and decide the final microstructure of half-cells. The microstructure is, in turn, directly related to the electrochemical performance. These processing parameters include the particle fraction of FeCr metal substrate, co-sintering temperature and DBL thickness. Other processing parameters (i.e. anode and cathode thicknesses), do not have an effect on the shrinkage but have a straightforward influence on the electrochemical performance.

Through this work, the influence of these processing parameters was characterized by means of shrinkage measurements during co-sintering (section 2.3.2.2), electrochemical characterization (section 2.1) and post-mortem analysis of cell microstructure (section 2.2). The experimental set-up used for the electrochemical characterization of is described in the next section.

4.2.2 Experimental set-up

The experimental set-up is shown in Figure IV - 10. SOFC cell is attached in the top of an alumina cylinder which is fed with fuel from in the inside part. In the exterior, the oxygen for cathode reaction is provided from the ambient air. Before mounting the assembly, nickel mesh in contact with two nickel wires is welded to the metal support to collect current in the anode side. Cell is subsequently sealed to the alumina cylinder using Ultra-Temp 516 (Aremco). This sealant is also used to cover the superior edge with a little alumina piece which gives a mushroom shape to the cell. Finally, platinum mesh in contact with two platinum wires is stack with platinum paste to the cathode surface to facilitate the current collection.

For standard electrochemical characterization, cells are fed with 200 ml H₂ and 3% humidified using a bubbler which is maintained at 25°C. Fuel flow will be lower for fuel utilization experiments. This set-up has been used for the electrochemical characterization and stability studies of cells carried out all through this work. As an exception, a more robust montage containing metallic parts was used for the thermal cycling experiment as described in section 4.4.1.

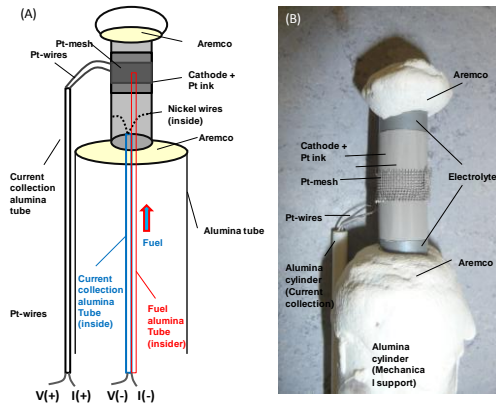


Figure IV - 10. Experimental set-up: (A) schematic design and (B) image.

4.2.3 Effect of sintering temperature and metal powder particle fraction

4.2.3.1 Introduction

During sintering, the electrolyte typically shrinks as much as 10-25%, depending on the green density reached after deposition [20]. Shrinkage of the metal support must be compatible to that of the electrolyte; otherwise, the electrolyte layer is stressed during co-sintering causing mechanical failure or in the opposing situation, it rests insufficiently densified. YSZ co-sintering approach demands a metal-support that matches shrinkage constraints as well as retaining adequate porosity after sintering. This largely depends on the metal composition, particle size, surface roughness, initial packing density and processing atmosphere and temperature [248].

For the ferritic stainless steel adopted as metal-support, Crofer 22 APU, those parameters were largely optimized for first generation cells leading to gas-tight electrolytes and porous FeCr substrates with good electrochemical characteristics [102, 105]. At the beginning of second generation cell development, optimized processing parameters from G1 cells were adopted. However, first trials with perovskite-type DBL showed largely superior shrinkage and poor electrochemical properties, as shown earlier in Figure IV - 8.

In this section, the effect of critical processing factors (sintering temperature and metal powder fraction) is analyzed in G2 cells shrinkage, microstructure and electrochemical performance.

4.2.3.2 Experimental procedure

Cells manufactured for experimentation combined two FeCr particle fractions: fine <45 μm and coarse <53 μm . FeCr/LST/Ni-YSZ/YSZ half-cells were sintered at 1330°C, 1350°C and 1370°C as it is shown in Table IV - 7. Two cells with the same configuration were processed from the same presintered tube. (Find detailed information about cells labelling in section 4.1.2.2).

Table IV - 7. Experiments table with Crofer 22 APU powder fraction and sintering temperature combinations together with the main characteristics. (OCV is measured at 800°C; find electrolyte surface appearance classification in Figure IV - 39).

Particle fraction (μm)	Sintering temperature ($^{\circ}\text{C}$)	Cell #	Surface appearance	OCV(V)
<45	1330	202.FP.2.1	Plain	1.113
		202.FP.2.2	Plain	1.111
	1350	202.FP.14.1	Plain	1.111
		202.FP.14.2	Plain	1.111
	1370	202.FP.22.1	Stains	1.077
		202.FP.22.2	Stains	
<53	1350	203.FP.2.1	Crack	1.067
		203.FP.2.2	Crack	1.1

4.2.3.3 Analysis of results

Shrinkage and physical appearance

Cells surface appearance was different after the sintering process and it is compared here with the OCV because it is an excellent indicator for gas tightness and works as a reliable quality control factor. Cells with fine fraction (<45 μm) sintered at 1330°C and 1350°C exhibited a plain electrolyte surface and optimal OCV. In contrast, cells sintered at 1370°C appeared covered with dark spots and OCV was lower for the single cell that could be tested. On the other hand, cells with coarse FeCr fraction presented some cracks propagating within the surface. Shrinkage during co-sintering varied with FeCr particle fraction and sintering temperature as expected. In Figure IV - 11, finer fraction sintered at 1330°C and 1350°C presented similar shrinkage ($D_e \approx 16\text{-}17\%$) and final porosity ($\rho = 29\text{-}32\%$). Shrinkage increased ($D_e \approx 17\text{-}18\%$) for cells sintered at 1370°C and final porosity was significantly lower ($\rho = 25\text{-}27\%$). When coarse fraction was used, which was sintered only at 1350°C, shrinkage was low ($D_e \approx 14\%$) and final porosity very high ($\rho = 38\text{-}41\%$) in comparison to analogous cells with fine fraction sintered at the same temperature.

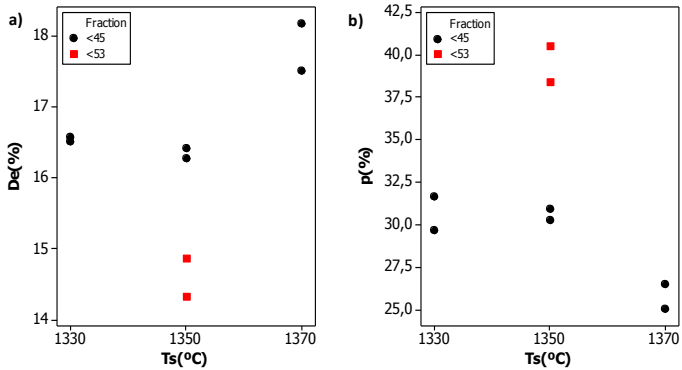


Figure IV - 11. Half-cells a) transversal shrinkage, $D_e(\%)$, and b) porosity, $p(\%)$, as a function of the sintering temperature, T_s , and FeCr particle fraction.

Electrochemical characterization

Most representative data from IV-curves and EIS measurements are shown in Figure IV - 12. Highest power densities (110-120mW/cm²) were recorded for cells with fine fraction sintered at 1350°C. Ohmic resistance was lower as sintering temperature increased and similar regardless the fine/coarse fraction used. In the third diagram (C), polarization resistance shows a minimum ($\approx 0.7 \Omega/\text{cm}^2$) at 1350°C with fine fraction but it increased substantially with coarser FeCr fraction.

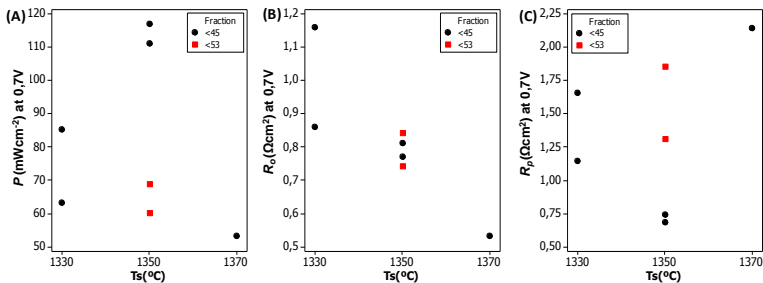


Figure IV - 12. (A) Power density, (B) ohmic resistance and (C) polarization resistance as a function of sintering temperature and Crofer 22 APU fraction used. (Measurement at 800°C and 0.7V. Anode fed with 3% humidified 200 ml min⁻¹ H₂ and cathode with atmospheric air)

Microstructural analysis

SEM analysis presents FeCr-supports with clearly differentiated porosities in Figure IV - 13 . Coarser FeCr fraction exhibits most porous microstructure. It is followed by cells with fine fraction sintered at 1330°C and 1350°C. Those sintered at 1370°C are denser, especially in the DBL boundary zone. Previous porosity estimations by simple cell size and weight measurements (Figure IV - 11) can be compared to tendencies observed in the metal support. Provided that metal substrate constitutes 96-97% of the cell cross-section, preceding porosity estimations are expected to be directly correlated to p_s , the metal-support porosity. SEM observations confirm previous tendencies and are summarized as follows:

- $p_s (<45 \mu\text{m}) < p_s (<53 \mu\text{m})$ when $T_s=1350^\circ\text{C}$
- $p_s (1330^\circ\text{C}) \approx p_s (1350^\circ\text{C}) > p_s (1370^\circ\text{C})$

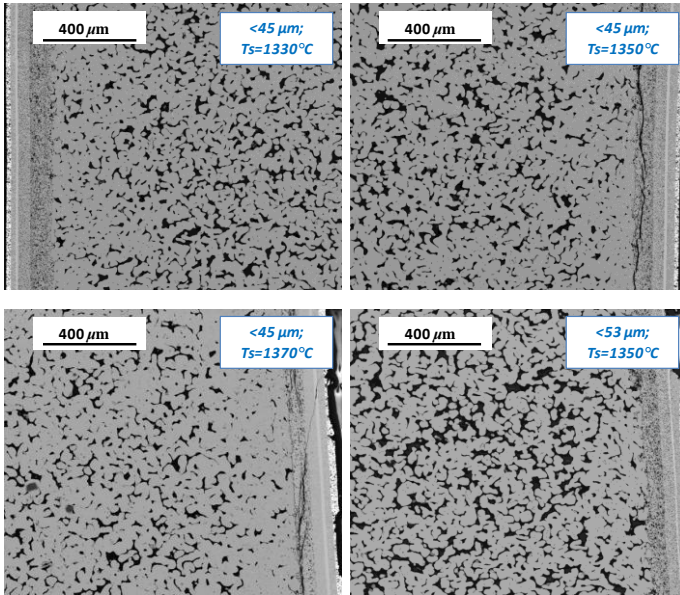


Figure IV - 13. Metal support micrographs combining different sintering temperatures (1330°C, 1350°C and 1370°C) and Crofer 22 APU particle fractions (<45 μm, <53 μm).

Functional layers were also analyzed with SEM. In Figure IV - 14, thickness of LST barrier, Ni-YSZ anode and YSZ electrolyte which are directly influenced by shrinkage during co-sintering are listed. LST barrier becomes thinner as the sintering temperature increases. The trend is rather linear and, with finer fraction, LST is

reduced $\approx 40 \mu\text{m}$ when sintering temperature increases from 1330°C to 1370°C . Ni-YSZ cermet anode thickness remains stable around $55 \mu\text{m}$ when sintered at 1330°C and 1350°C , but it is slightly thinner at higher sintering temperature. Electrolyte thickness is stable around $13 \mu\text{m}$ and it is not influenced by the sintering temperature.

When coarser FeCr fraction ($<53 \mu\text{m}$) is used, every functional layer (LST, anode and electrolyte) thickness reduces to some extent compared to the analogue with fine fraction sintered at 1350°C . Difference is more apparent for the LST barrier which is $\approx 10 \mu\text{m}$ thinner with coarser FeCr fraction.

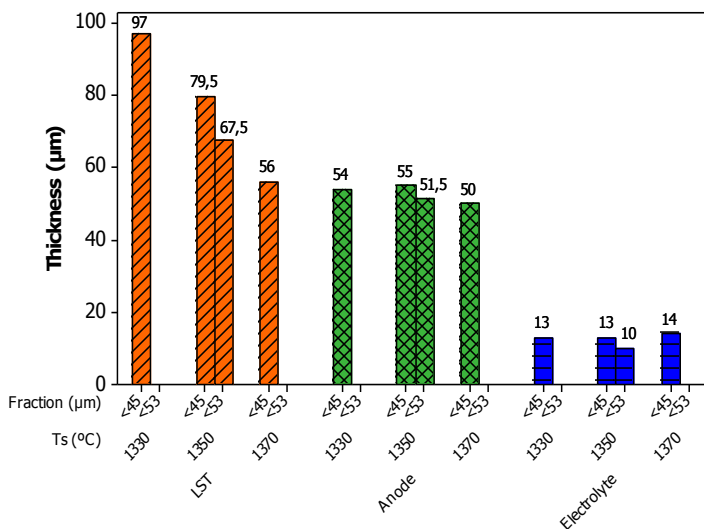


Figure IV - 14. Thickness of LST diffusion barrier layer, Ni-YSZ anode and 8YSZ electrolyte for different sintering temperature and Crofer 22 APU particle fractions as measured from SEM observations.

LST barrier and Ni-YSZ anode porosity decreases gradually as the sintering temperature increases (Figure IV - 15). In particular, an abrupt densification of LST barrier and anode is observed when cells are sintered at 1370°C . Elimination of characteristic closed porosity also confirms further densification of the electrolyte at high sintering temperatures (Figure IV - 16). This is comprehensible as shrinkage is higher at 1370°C . In addition, DBL/anode delaminating is observed for cells sintered at 1370°C . This is better appreciated in Figure IV - 15, where cracks propagate along the DBL concentric to the tube perimeter. However, delaminating is also observed for fine fraction cells sintered at lower 1350°C . Crack origin is not completely clear but experimental observations point toward its formation during

samples polishing prior to SEM analysis. Thus, it is not considered as a potential source of mechanical failure in G2 cells. Ohmic resistance values of these cells are too low for the cracks to be present during operation, supporting the idea of sample handling issues prior to SEM observations.

Ceramic layers (DBL, anode and electrolyte) microstructure does not exhibit major differences depending on the fine/coarse FeCr fraction used during the sintering at 1350°C (Figure IV - 15). LST barrier and Ni-YSZ anode are thinner (Figure IV - 14) but porosity and nickel particles size are very similar. Note that inhomogeneous anode microstructure is observed regardless the fine/coarse FeCr fraction for cells sintered at 1350°C; anode is denser in the DBL vicinity and more porous near the electrolyte. This in-homogeneity is further observed in Figure IV - 16, where micrographs illustrate anode and electrolyte at higher magnifications.

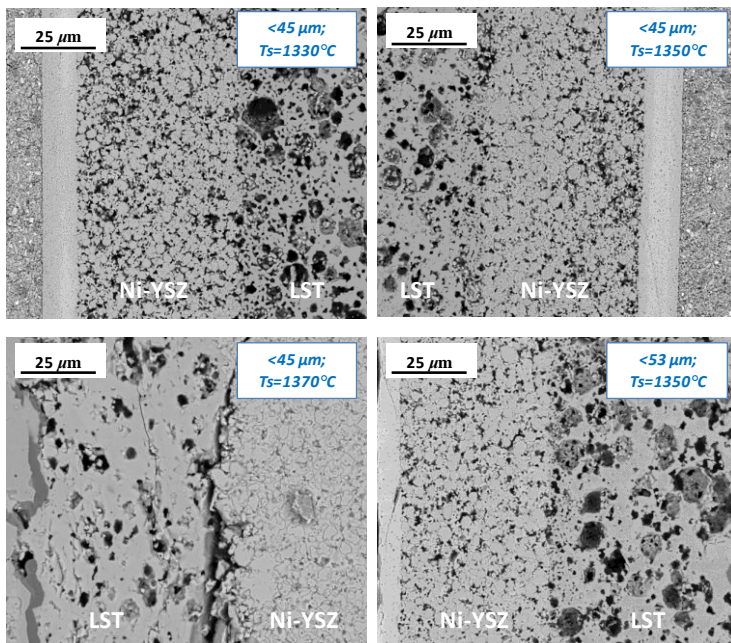


Figure IV - 15. Micrographs illustrating LST barrier and Ni-YSZ anode microstructure for cells combining different sintering temperatures (1330°C, 1350°C and 1370°C) and Crofer 22 APU particle fraction (<45 μm, <53 μm).

Ni particles agglomeration increases together with sintering temperature (Figure IV - 16). At 1350°C particles are larger, more regular and round. At 1370°C, even if having irregular morphologies, nickel particles are immense. Nickel agglomeration is prominent but the most distinguishing attribute is the outstanding densification that

YSZ microstructure experiences. In addition, dark points on the surface of nickel particles are essentially chromium oxides but little amounts of manganese and iron are also detected.

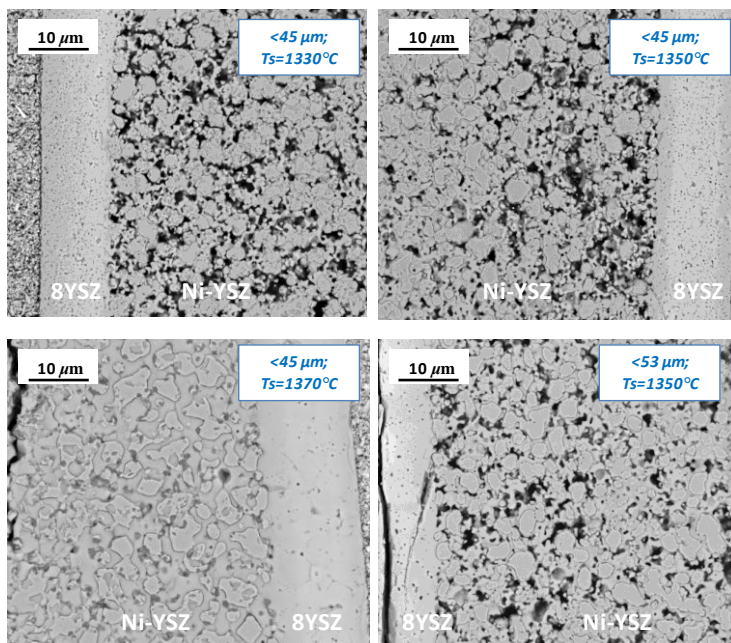


Figure IV - 16. Micrographs Ni-YSZ anode and 8YSZ electrolyte microstructure for cells combining different sintering temperatures (1330°C, 1350°C and 1370°C) and Crofer 22 APU particle fractions (<45 μm, <53 μm).

4.2.3.4 Overall discussion and conclusions

The influence of the sintering temperature has been analyzed in the range between 1330-1370°C for cells consisting of a fine FeCr fraction (<45 μm). Tendency with G2 cells is not linear in that range. Half-cells shrinkage is constant between 1330-1350°C (16-17%) and final microstructure of the metal-support is very similar. However, at 1370°C, shrinkage increases (17-18%) and this is reflected in a denser metal-support. On the other hand, when coarse FeCr fraction is used final porosity of the metal-support increases significantly.

Electrochemical characterization of those cells revealed that R_o decreases with the sintering temperature but remains similar regardless the FeCr fraction used. Fine and coarse FeCr substrates sintered at 1350°C, with final porosities around 24-26%

and 30-32% respectively, exhibit similar R_o . This demonstrates that in this range, current collection is not affected by the metal-support shrinkage and final porosity.

Best electrochemical results around 110 - 120 mW/cm² are reported for cells with fine fraction (<45 μm) sintered at intermediate temperatures (1350°C). Within the fine fraction cells, R_o decreases conversely to the sintering temperature. This is primarily attributed to thinner and denser functional layers that enhance current collection as sintering temperature increases. However, there is a minimum in the R_p at 1350°C that accounts for the optimal performance. As sintering temperature increases between 1330-1350°C, YSZ and Ni phases interconnectivity within the anode is favored and TPB efficiency is better. However, at 1370°C, R_p drastically increases. LST barrier and Ni-YSZ anode overdensification blocks fuel transport and reduces active-sites (i.e. TPB length) available for fuel oxidation in this case.

For coarser FeCr fraction, power density is reduced to half (60-70 mW/cm²). R_o is similar but R_p is high in comparison to the analogue with fine fraction sintered at 1350°C. According to microstructural observations, metal-substrate is more porous for coarser FeCr. However, equivalent R_o with both FeCr fractions indicates that current collection is not affected by the support. Comparable ceramic layers are thinner with coarser FeCr fraction, especially the LST barrier. To be precise, no physical evidence is found that explains the better performance with fine FeCr fraction. Only, one expects better surface roughness that affects the quality of the layers deposited on top of metal substrates.

To conclude, FeCr particle fraction and sintering temperature have successfully been optimized. Going forward, fine FeCr fraction (<45 μm) combined with 1350°C sintering temperature have been used as processing parameters for second generation cells.

4.2.4 Diffusion barrier layer thickness

4.2.4.1 Introduction

As its own name indicates, the scope of the DBL is to stop the element diffusion that occurs during co-sintering and operation between the anode and the metal support. An efficient DBL must be porous to allow fuel diffusion to the anode, must have a TEC that matches with adjacent components and a good electronic conductivity under reducing atmosphere. In practice, a DBL as thin as possible to minimize the overvoltage is demanded; 4 μm thin CeO₂ [174], 10-30 μm La_{0.6}Sr_{0.2}Ca_{0.2}CrO₃ and 2-3 μm La_{1-x}Sr_xMnO₃ [158] DBLs are reported in the literature with that purpose. Initial poor performance of G2 cells is partially associated to the 70-90 μm LST barrier, which is very thick in comparison to first generation 5-30 μm Ni-YDC DBL (Table IV - 6). Thus, once that sintering temperature and crofer particle fraction were optimized, the second objective was to optimize perovskite-based DBL thickness. This is pursued in two ways. In a first attempt, the original LST barrier formulation (Table IV

- 4) was diluted in 3 successive formulations. In a second attempt, two LST formulations were analyzed taking into account reproducibility aspects of cell fabrication and characterization.

4.2.4.2 1st attempt: Gradual dilution of the original LST barrier formulation

4.2.4.2.1 Experimental procedure

Thinner LST barrier are expected by the systematic dip-coating of LST slurries with lower viscosities. Thus, original LST formulation, F1, associated with a 70-90 μm DBL, which contains specific amounts of LST powder, binder, plastizier, defoaming and water content (Table IV - 4), was diluted in three successive formulations (F2, F3 and F4) by simply adding 2g more of water each time. Presintered tubes were cut in two pieces which were dip-coated with the same LST slurry. After anode and electrolyte standard deposition both FeCr/LST-F_x/Ni-YSZ/YSZ half-cells (x=1-4) were sintered together at 1350°C in the same furnace. Table IV - 8 illustrates cells initial characteristics together with the appearance after co-sintering and OCV at 800°C. LSF₄₀-SDC composite cathode was subsequently dip-coated over lengths of 2 cm of the tubular cell, which corresponds to an efficient area of $\approx 7.5 \text{ cm}^2$ except for 204.FP.37.2, which efficient area was 3.8 cm^2 . For simplicity in terminology, cells from standard F1 to most diluted F4 formulations are named LST-F1 and LST-F4, respectively. (Find detailed information about cells labelling in section 4.1.2.2).

Table IV - 8. Table of experiments related to dilution of the LST barrier layer formulation. (OCV is measured at 800°C; find electrolyte surface appearance classification in Figure IV - 39)

FeCr Fraction (μm)	Sintering temperature (°C)	LST slurry			Cell #	Electrolyte surface appearance	OCV(V)	Efficient area (cm^2)
		LST-F _x	H ₂ O (%)	H (Pa s)				
<45	1350	F1	25.8	0.164	204.FP.32.1	Plain	1.111	7.38
					204.FP.32.2	Plain	1.11	7.45
		F2	27.2	0.118	204.FP.37.1	Few stains	1.111	7.60
					204.FP.37.2	Few stains	1.108	3.81
		F3	28.6	0.084	204.FP.38.1	Stains	1.097	7.62
					204.FP.38.2	Stains	1.106	7.47
		F4	30.0	0.060	204.FP.53.1	Many stains	1.102	7.47
					204.FP.53.2	Many stains	1.102	7.25

4.2.4.2.2 Analysis of results

Shrinkage and physical appearance

The physical appearance of cells after sintering was not homogeneous. Spots or stains over the surface of the electrolyte started to become visible as LST

formulation, was diluted in water with F2 formulation but they became more obvious for F3 and specially F4 formulations. No explicit images of electrolyte surface after co-sintering exist for this batch. However, in Figure IV - 17, cells after LSF₄₀-SDC/Pt paste deposition illustrate the electrolyte appearance to some extent. Note that most diluted LST-F4 cell is covered with dark spots in the lower zone. OCV was optimal above 1.09V for every cell.

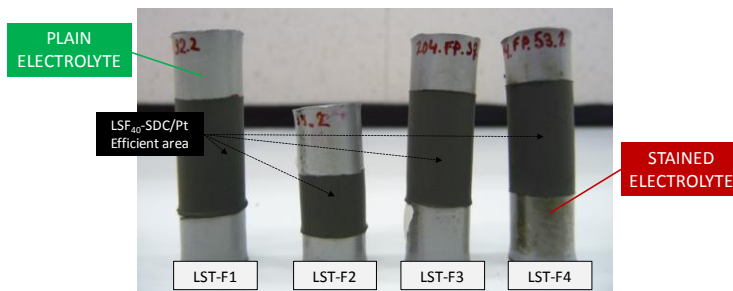


Figure IV - 17. Image of cells prepared with LST barrier formulations at different dilution levels.

Shrinkage during co-sintering increased in average with dilution (Figure IV - 18). Values for standard cells ($D_e \approx 15-16.5\%$) are comparable to previous results with equivalent cells (Figure IV - 11). Note that variability increased considerably as LST formulation was diluted from F1 to F4. Inversely to shrinkages, average final porosity decreases from $p \approx 36\%$ with LST-F1 cells to $p \approx 30\%$ with LST-F4 ones. However, variability was high and for each LST formulation there was a high and a low porosity cell.

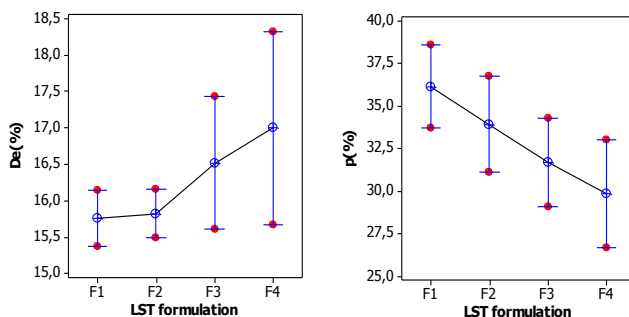


Figure IV - 18. Cell transversal shrinkage, %D_e, and final porosity as a function of the dilution of LST formulation.

Electrochemical characterization

IV-curves at 800°C did not confirm the expected enhanced performances for more diluted LST formulations (Figure IV - 19). As LST formulation was diluted from F1 (in yellow) to F2 (in violet), performance decreased. At this point, variability increased considerably for LST-F3 cells (in green). LST-F4 cells followed a similar trend and variability further increased; concretely, best (190mW/cm²) but also worst (63mW/cm²) power densities were recorded with most diluted LST slurry. This is better appreciated in Figure IV - 20, where power density is represented together with ohmic and polarization resistance as a function of LST formulation. Comparable R_o with LST-F1 and LST-F2 cells decreases for LST-F3 and LST-F4. In effect, thinner LST barrier expected for more diluted formulations should reduce ohmic resistance and facilitate current collection. Nevertheless, R_o variability gradually increases with F3 and F4 formulations. On the other hand, R_p trend is not clear from the diagram but cells with F4 formulation exhibit highly scattered R_p ($\sigma \approx 0.93 \Omega\text{cm}^2$) compared to the R_o variability ($\sigma \approx 0.22 \Omega\text{cm}^2$). In fact, direct correlation between power density and polarization resistance is confirmed in Figure IV - 21. R_p vs p is comparable with ASR vs p diagram; rather linear relation observed in ASR vs p diagram is more curved in the R_p vs p . In $R_p < 1 \Omega\text{cm}^2$ region, power density rapidly increases when R_p is reduced. In contrast, when $R_p > 1 \Omega\text{cm}^2$, power density is vaguely altered in equivalent R_p intervals. Conversely, power density does not present a direct relation with the ohmic resistance; resistances in the 0.5-0.8 Ωcm^2 region have been observed with the exception of cell 204.FP.53.1 with F4 formulation with $R_o = 0.32 \Omega\text{cm}^2$.

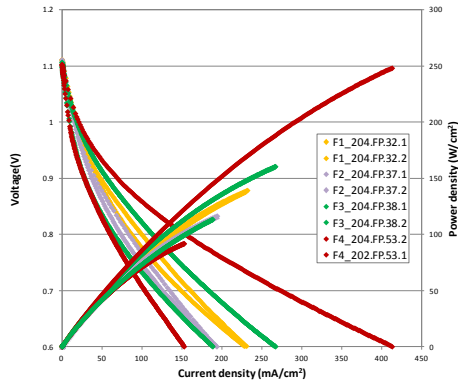


Figure IV - 19. IV-curves for cells with F1-F4 LST formulations. (Measurement at 800°C and 0.7V. Anode fed with 3% humidified 200 ml min⁻¹ H₂ and cathode with atmospheric air)

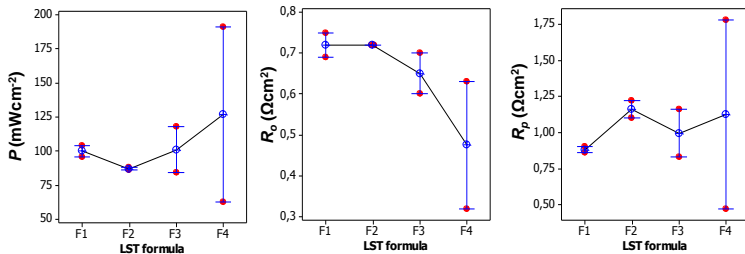


Figure IV - 20. a) Power density, b) ohmic resistance and c) polarization resistance as function of the LST formulation. (Measurement at 800°C and 0.7V. Anode fed with 3% humidified 200 ml min⁻¹ H₂ and cathode with atmospheric air)

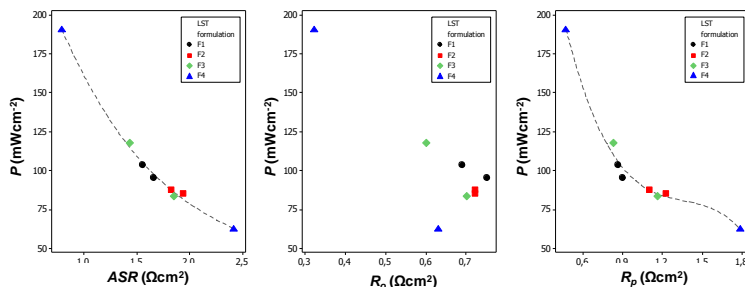


Figure IV - 21. Power density as a function of ASR, R_o and R_p . (Measurement recorded at 800°C and 0.7V. Anode fed with 3% humidified 200 ml min⁻¹ H₂ and cathode with atmospheric air) (Lines are guides to the eye)

Microstructural characterization

Given the high variability observed for LST-F3 and LST-F4 cells, no conclusions can be extracted from a simple data analysis. That is why in order to investigate LST formulation dilution effect more deeply, cells with lowest porosity were selected from each LST formulation (Figure IV - 18); 204.FP.32.1, 204.FP.37.1, 204.FP.38.2 and 204.FP.53.2 were analyzed by SEM equipment. In parallel, LST-F4 cells, 204.FP.53.1 and 204.FP.53.2, were compared to clarify the basis of the observed highly scattered results.

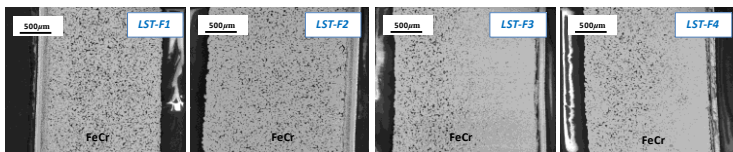
In Figure IV - 22, SEM observations reveal that LST-F3 and LST-F4 cells with lowest porosity are dense in the middle exterior part of the diameter whereas porosity in the support core is similar to LST-F1 and LST-F2 cells. Porosity

estimations, by means of mass and volume calculations for a homogeneous tube, predicted porosities higher than %30 for LST-F1 and LST-F2 whereas it was lower than 30% for LST-F3 and LST-F4. Post-mortem analysis demonstrates, however, that metal support porosity is not homogeneous for LST-F3 and LST-F4 cells.

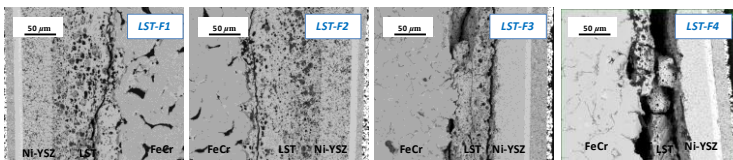
In line with the diffusion barrier layer, in the second row of Figure IV - 22, porous microstructure for specific 3 μm and 7 μm pore formers in the LST slurry is observed with standard LST-F1 cell. LST-F2 DBL is denser in the vicinity of the FeCr substrate and porous in the anode nearby region. Crack that propagates in the FeCr/DBL interface during sample polishing is again observed in both cells. On the other hand, for most diluted F3 and F4 formulations, LST barrier is completely delaminated and suspended from both sides. In this case, barrier deterioration was not attributed to damage caused during sample polishing. Thickness measurements (Figure IV - 23) demonstrate that LST barrier becomes thinner as LST is diluted from F1 to F4 formulation. Unexpected 124 μm thick layer estimated for F2 is probably due to drops that are from time to time stack in cells surface during dip-coating.

In the third row of Figure IV - 22, anode microstructure follows a similar trend to the DBL; whilst it is porous for cells with F1 and F2 formulation it appears extremely dense for LST-F4 and LST-F3. Despite the different microstructures, anode thickness is stable $\approx 49 \mu\text{m}$ regardless the LST formulation. On the other hand, characteristic closed pores in the electrolyte, are present in 12-14 μm thick LST-F1 and LST-F2 cells while they disappear for slightly thinner 10 μm thick LST-F3 and LST-F4 electrolytes. Even if preferentially dense electrolyte with no pores is looked for in SOFC technology, electrolyte with closed pores is already optimized since it has demonstrated gas tightness and typical OCV higher than 1.1V. The same holds here and OCVs higher than 1.1V were registered for every cell.

Metal-support



Functional layers



Anode and electrolyte

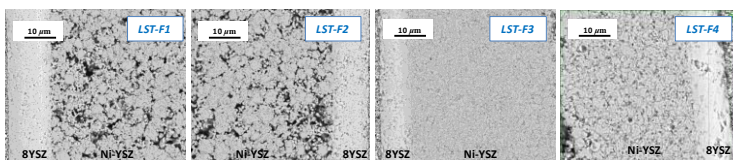


Figure IV - 22. Micrographs of cells with lowest porosity within the couple of samples processed for each LST formulation; 1st row) metal supports, 2nd row) functional layers and 3rd row) anode and electrolyte comparison.

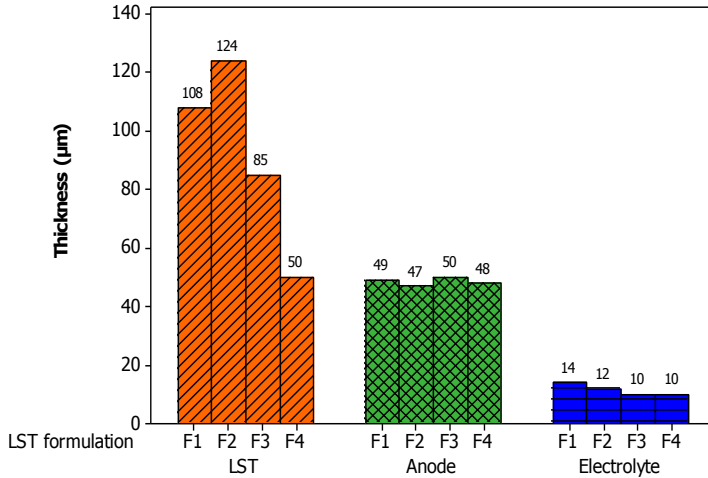


Figure IV - 23. Thickness of LST diffusion barrier layer, Ni-YSZ anode and 8YSZ electrolyte as a function of the dilution of LST formulation as measured from SEM observations.

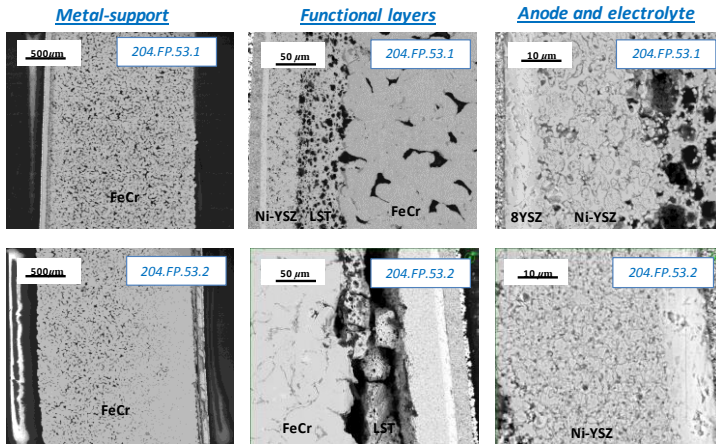


Figure IV - 24. SEM micrographs of two cells with diluted F4 formulation. Left) metal support, centre) LST barrier and anode and right) anode and electrolyte.

Table IV - 9. Functional layer thickness and electrochemical characteristics at 800°C and 0.7V. (Anode is fed with 3% humidified 200 ml min⁻¹ H₂ and cathode with ambient air)

<i>LST</i>	<i>Cell #</i>	<i>OCV</i> (V)	<i>LST</i> (μm)	<i>Ni-YSZ</i> (μm)	<i>8YSZ</i> (μm)	<i>R_o</i> (Ωcm^2)	<i>R_p</i> (Ωcm^2)	<i>ASR</i> (Ωcm^2)	<i>P</i> (mW/cm^2)
F4	204.FP.53.1	1.092	58	40	9	0.32	0.47	0.79	191
	204.FP.53.2	1.102	50	48	10	0.63	1.78	2.41	63

The electrochemical values for two cells with most diluted formulation (LST-F4) differ significantly. Actually, best 191 mW/cm² but also worst 63 mW/cm² efficiencies were recorded with F4 formulation. This difference was mainly attributed to R_p divergences even if R_o varied at some extent (Table IV - 9). Similar FeCr/LST-F4/Ni-YSZ/YSZ configurations, in theory, appear very different in practice. Post-mortem analysis of both cells has revealed, however, a completely different microstructure (Figure IV - 24). While the high performing cell (204.FP.53.2) exhibits a suitable porous support and LST diffusion barrier layer, the low performing cell (204.FP.53.1) presents a metal support largely densified in the external zone. Thinner LST layer is also dense for 204.FP.53.2 cell and it is completely separated from both the support and anode side. Anode is dense for both cells even if thinner for 204.FP.53.1. Anode microstructure resembles that observed for cells sintered at 1370°C in the previous section (Figure IV - 16). Nickel agglomeration and most remarkable YSZ sinterization are observed. Anode is poisoned fundamentally with chromium but little amounts of manganese and iron also crystallize in form of oxides in the nickel particles surface.

The immense variability found for both cells with identical processing parameters evidences the existence of an uncontrolled factor in G2 cells manufacturing process.

4.2.4.3 2nd attempt: Reproducibility of cells with F1 and F4 LST formulation

4.2.4.3.1 Experimental procedure

Previous experiments failed in proving the electrochemical superiority of thinner LST DBL. Even if thinner LST barriers were systematically obtained with more diluted F3 and F4 formulations, electrochemical performance was subjected to a large variability. Thus, a new set of experiments was designed combining two unique LST formulations; F1 and F4. In order to eradicate the potential variability from presintered tube and sintering furnace, a couple of cells with F1 and F4 formulations respectively, were manufactured from a single presintered tube and they were sintered together in the same furnace. This process was repeated six times with six different presintered tubes from 209 and 213 tube batches. After that, LSF-SDC composite cathode and Pt paste were deposited in a 2 cm high central diameter, leading to ≈ 7.3 cm² efficient areas. In Table IV - 10, tested cells are summarized

with the corresponding processing parameters. Cell 209.FP.6.1, with divided stained/plain electrolyte surface, was taken apart to carry out a specific dual measurement to understand stain formation. This analysis is presented in section 4.3.2. Cell 213.FP.3.2 could not be tested electrochemically. (Find detailed information about cells labelling in section 4.1.2.2).

Table IV - 10. LST-F1 and LST-F4 departure characteristics. (OCV is measured at 800°C; anode is fed with 3% humidified 200 ml min⁻¹ H₂ and cathode with ambient air; find surface appearance images in Figure IV - 39)

Fraction (μm)	Ts (°C)	Tube Batch	LST slurry		Cell #	Electrolyte surface appearance	OCV(V)	Efficient area (cm ²)
			LST- Fx	H ₂ O (%)				
<45	1350	209	F1	25.8	209.FP.5.1	Stains	1.107	7.42
			F4	30.0	209.FP.5.2	Stains	1.107	7.44
			F1	25.8	209.FP.6.1	Stains		*
			F4	30.0	209.FP.6.2	Stains	1.098	7.49
		213	F1	25.8	213.FP.2.1	Plain	1.097	7.38
			F4	30.0	213.FP.2.2	Stains	1.097	7.24
			F1	25.8	213.FP.3.1	Stains	1.044	6.51
			F4	30.0	213.FP.3.2	Stains		*
			F1	25.8	213.FP.4.1	Plain	1.102	7.46
			F4	30.0	213.FP.4.2	Stains	1.099	7.33
			F1	25.8	213.FP.5.1	Plain	1.06	7.46
			F4	30.0	213.FP.5.2	Stains	0.983	7.33

4.2.4.3.2 Analysis of results

Shrinkage and physical appearance

LST-F4 cells in batch 209 exhibit substantially lower transversal shrinkage (%D_e) than cells from batch 213 (Figure IV - 25). Main observations are divided as follows:

- %D_e (209) < %D_e (213) for LST-F4

Cells with 209 and 213 batches were prepared with two months of difference, in September and November of 2011. Apart from variability between presintered tubes, variability among batches and the influence of environmental conditions during tube processing (CEIT-IK4) and posterior cells manufacturing/sintering (IK4-Ikerlan) has to be considered.

Further divergences exist between 209 and 213 tube batches during sintering (Figure IV - 25). In the case of batch 209, transversal shrinkage (%D_e) is lower with LST-F4 cells, and every cell is covered with dark stains after sintering regardless the LST formulation. Cell images, including front and rear views of each cell are shown in Figure IV - 26.

- *Batch 209:*
 - i. $\%D_e$ (LST-F1) > $\%D_e$ (LST-F4)
 - ii. Stains in every cell.

In contrast, for batch 213, the majority of LST-F4 cells underwent higher transversal shrinkage than their LST-F1 couple (Figure IV - 25). Plain LST-F1 and spotted LST-F4 pairs were observed. As an exception, couple 213.FP.3.1 and 213.FP.3.2 experienced a similar transversal shrinkage in spite of the LST formulation but both cells were covered with stains.

- *Batch 213:*
 - iii. Three couples with plain LST-F1 and stained LST-F4 pairs:
 $\%D_e$ (LST-F1) < $\%D_e$ (LST-F4)
 - iv. One couple with stained surface for both LST formulations:
 $\%D_e$ (LST-F1) \approx $\%D_e$ (LST-F4)

The experimental result with cells from batch 213 suggests a possible connection between a higher transversal shrinkage during co-sintering and spots in the surface of the electrolyte.

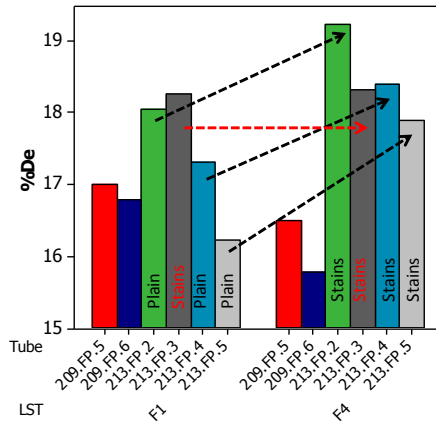


Figure IV - 25. Transversal shrinkage ($\%D_e$) of LST-F1 and LST-F4 cells in which tubes were made out of the same tube from batch 209 and 213. Plain and stain refers to the electrolyte surface appearance after co-sintering, as it is shown in Figure IV - 26.

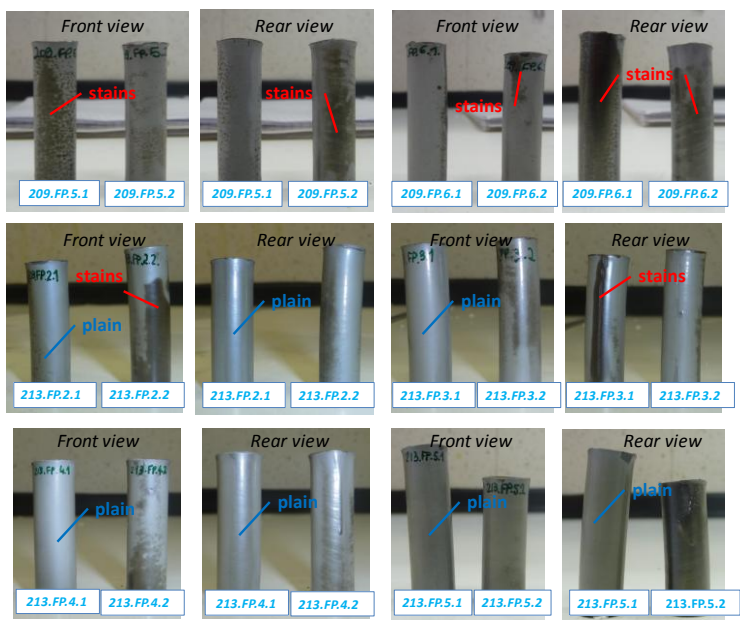


Figure IV - 26. Cells appearance after co-sintering. (Front and rear view of each cell)

Electrochemical characterization

Better performances for cells with LST-F1 formulation were obtained (Figure IV - 27). LST-F1 cells showed higher electrochemical performance regardless the batch used and their superiority was reproduced with every comparable pair of cells (i.e. same original tube and sintered together). Highest power densities ($\geq 180\text{mW/cm}^2$) were registered for cells exhibiting a plain electrolyte surface; 213.FP.2.1, 213.FP.4.1 and 213.FP.5.1. The remaining cells were covered with stains after sintering. The overall withdrawn tendencies are summarized as follows:

- $P(\text{LST-F1}) > P(\text{LST-F4})$ for every comparable cell couple
- Plain surface $\geq 180\text{mW/cm}^2 >$ Stained surface

Cells in batch 213 exhibited better electrochemical results than cells in batch 209 for both LST-F1 and LST-F4 cells.

- $P(209) < P(213)$;

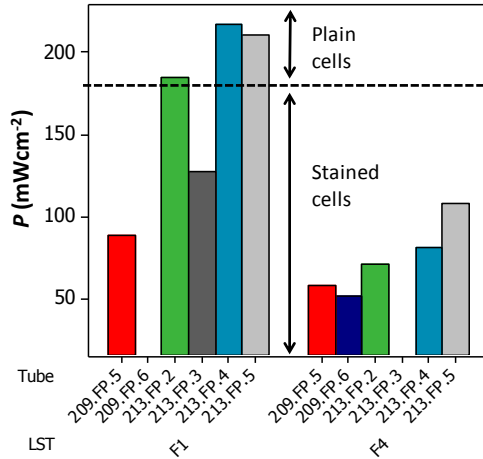


Figure IV - 27. Power density for LST-F1 and LST-F4 cells as measured at 800°C and realistic operation conditions (0.7V). (Anode fed with 3% humidified 200 ml min⁻¹ H₂ and cathode with atmospheric air)

EIS measurements demonstrated the lower ohmic resistance of LST-F1 cells ($0.39 \pm 0.02 \Omega\text{cm}^2$ in average) with respect to LST-F4 cells ($0.54 \pm 0.06 \Omega\text{cm}^2$ in average). This difference was independently reproduced in every comparable pair of cells (Figure IV - 28). Cells with plain surface exhibited lowest ohmic resistance ($\leq 0.42 \Omega\text{cm}^2$). Polarization resistance followed a similar trend but R_p was remarkably higher for LST-F4 cells ($1.44 \pm 0.21 \Omega\text{cm}^2$ in average) in comparison to LST-F1 cells ($0.51 \pm 0.06 \Omega\text{cm}^2$ in average). Uncertainty was also higher and R_p emerged widely distributed for LST-F4 cells. Cells with plain surface exhibited lowest polarization resistances ($\leq 0.61 \text{ m}\Omega\text{cm}^2$). General trends are summarized as follows:

- $R_o(LST-F1) < R_o(LST-F4)$; $\sigma_{R_o}(LST-F1) < \sigma_{R_o}(LST-F4)$
- Plain surface $\leq R_o = 0.42 \Omega\text{cm}^2 < Stained\ surface$
- $R_p(LST-F1) < R_p(LST-F4)$; $\sigma_{R_p}(LST-F1) < \sigma_{R_p}(LST-F4)$
- Plain surface $\leq R_p = 0.61 \Omega\text{cm}^2 < Stained\ surface$

Better electrochemical property of cells in batch 213 was a sum of both reduced ohmic and polarization resistance.

- $R_o(209) > R_o(213)$; $R_p(209) > R_p(213)$

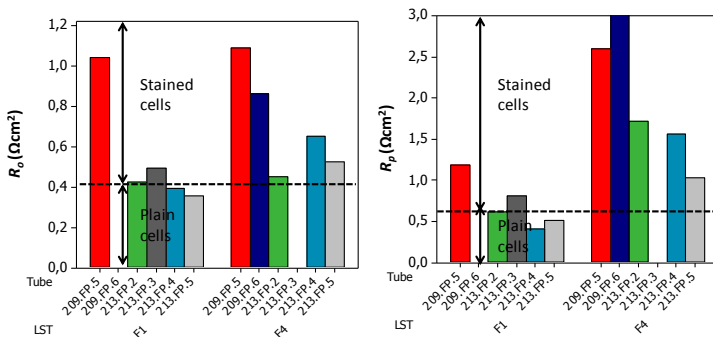


Figure IV - 28. Ohmic and polarization resistance for LST-F1 and LST-F4 cells as measured at 800°C and realistic operation conditions (0.7V). (Anode fed with 3% humidified 200 ml min⁻¹ H₂ and cathode with ambient air)

In Figure IV - 29, power density as a function of the polarization and ohmic resistance is presented for both LST-F1 and LST-F4 cells. This representation makes obvious the direct relation of power density with R_p ; it has certainly more influence in the power density. LST-F1 cell values fall in the region where power density rapidly increases with R_p reduction. LST-F4 cells values fall in the relaxation region where analogous R_p reduction translates in slight improvements in power densities. On the other hand, when power density is plotted as a function of R_o , general trend is similar but ohmic contribution to resistance is much lower. Note that whereas R_p values extend from 0.4 to 10 Ωcm^2 , R_o is less distributed from 0.3 to 1.1 Ωcm^2 .

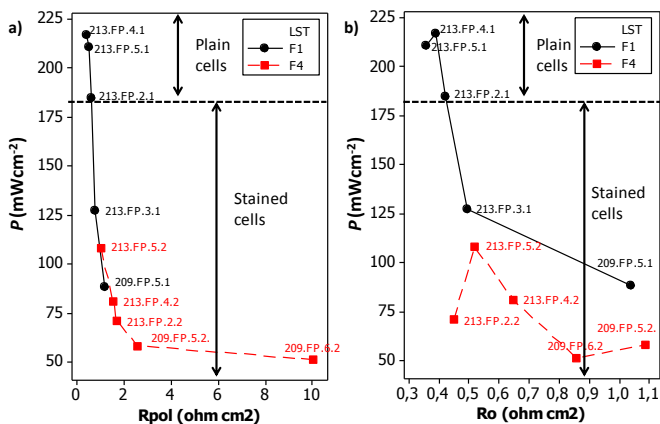


Figure IV - 29. Power density as a function of the polarization and ohmic resistance at realistic operation conditions (0.7V) and 800°C. (Anode fed with 3% humidified 200 ml min⁻¹ H₂ and cathode with ambient air)

4.2.4.4 Overall discussion and conclusions

In a first attempt, LST DBL thickness was effectively reduced by the LST slurry gradual dilution. However, variability increased as LST thickness decreased and FeCr/LST-F4/Ni-YSZ/YSZ configurations, similar in theory, exhibited highly scattered power densities. SEM analysis revealed that whereas best performing LST-F4 cell contained a porous metal-support and DBL, for the poor performing LST-F4, metal-support was extremely dense in the external zone and DBL was delaminated from both sides. High R_p for poor performing LST-F4 is almost certainly associated to the dense support and functional layers. In addition, moderate R_o increase due to the DBL delamination is also reasonable. Therefore, better performance of cells with thinner DBL could not be demonstrated due to variability in the microstructure.

In a second attempt, a statistically more reliable analysis was accomplished with 6 pairs of LST-F1 and LST-F4 cells with similar processing parameters (i.e. presintered tube and sintering batch). Contrary to expectations, LST-F1 cells demonstrated better electrochemical performance than LST-F4 cells. However, best performances were related to cells with stainless electrolytes. Even if the origin of those stains is not well understood, yet, experimental data suggest a negative effect of stains in the electrochemical performance. Lower power densities were systematically registered for cells with spots. Uncertainty was also higher. In addition, it seems that thicker LST barrier is more stable during co-sintering with no spots or stains formation. Experimental evidences further exist to suspect a connection between higher transversal shrinkage and spots or stains formation.

In conclusion, stains formation during co-sintering is a catastrophic event that deteriorates cells performance and it is necessary to investigate the mechanism that triggers this phenomenon. As far as the origin of stains is not well understood second generation cells viability is uncertain.

4.2.5 Optimization of electrochemically active electrodes

4.2.5.1 Introduction

MS-SOFC design permits to make use of functional ceramic layers as thin as necessary to provide the maximal electrochemical performance. 8YSZ electrolyte developed for G1 and G2 cells is $(12,6 \pm 1,7) \mu\text{m}$ thick and it contains closed pores and high OCV values guarantee gas tightness.

Nevertheless, it has been recognized that an electrochemically active layer, δ , exists in SOFC electrodes where electronic conductivity is typically orders of magnitude higher than ionic conductivity. Electrons are rapidly delivered in comparison to the oxygen ions and therefore TPBs close to the electrolyte are the preferred reaction sites. This is particularly true for Ni-YSZ cermet anodes, as a result of the high difference between electronic and ionic conductivity.

Determination of the electrochemically active layer thickness, δ , is necessary in designing a cell with optimum cell performance but δ estimations reported in the literature differ substantially. Regarding the anode, Moon and coworkers [249] estimated 20 μm thick electrochemically active Ni-YSZ anode, whereas for Primdhal and Mogensen [250] it was $<20 \mu\text{m}$. Additional results by Kong et al. [251] with a 40-50 μm Ni-YSZ active anode are in contrast with the 5 μm Ni-YSZ reported by Chen et al. [252]. Perovskites used as cathodes have also been studied. Adler et al. [221] estimate a 2-3 μm thick $\text{La}_{0.6}\text{Sr}_{0.4}\text{Co}_{0.2}\text{Fe}_{0.8}\text{O}_{3-\delta}$ electrode, whereas Juhl et al. [253] report a 10 μm thick LSM/YSZ cathode. The variability in results is understood as active electrode thickness depends on manufacturing parameters such as composition (volume fraction) and particle size, but also on the operation conditions of the SOFC. In fine electrode microstructures, the amount of TPB is high and active layer is thin. Making use of this property, most anode-supported cells consist of a coarse Ni-YSZ for mechanical support combined with a $\approx 20 \mu\text{m}$ functional anode with fine Ni-YSZ in the anode/electrolyte interface.

The aim in this section was to optimize cathode and anode thicknesses by estimating the electrochemically active layer for each electrode.

LSF₄₀-SDC composite cathode

Regarding the cathode, early studies summarized in chapter III, demonstrated the superior electrochemical performance of 50 μm thick LSF₄₀-SDC composite cathodes in comparison to 30 μm thick ones in anode-supported cells. Better

performance was a sum of both lower ohmic and polarization resistance and the effect was repeated regardless the cathode sintering temperature.

For metal-supported SOFCs developed in IK4-Ikerlan, similar LSF₄₀-SDC composite cathode is used but typical thicknesses with the standard formulation are thinner, around 25 μm . Given the successful optimization attained by increasing the cathode thickness with anode-supported cells in chapter III, here too, similar approach was pursued. The electrochemical performance of standard metal-supported cells with thicker LSF-SDC cathode was analyzed.

Ni-YSZ cermet anode

Standard Ni-YSZ anode is 40-50 μm thick for G2 cells. According to literature, Ni-YSZ active layer is probably thinner [249, 250, 252]. In addition, less nickel in a fine anode is probably advantageous against nickel diffusion which was identified for G1 cells during co-sintering [102]. Therefore, contrary to the cathode, the strategy was to decrease anode thickness to improve the electrochemical performance of the cell. The idea was to move towards the electrochemically active layer (δ) that is presumably thinner. The electrochemical performance of standard metal-supported cells with thinner Ni-YSZ anode (<40-50 μm) was analyzed.

4.2.5.2 Experimental procedure

Study of LSF₄₀-SDC composite cathodes thickness

Standard metal-supported tubular cells produced in IK4-Ikerlan include a (24.4 ± 3.6) μm thick LSF₄₀-SDC composite cathode. In order to obtain thicker electrodes, LSF₄₀-SDC was dip-coated twice leading to 40-60 μm thick electrodes. However, those cells did not show significant electrochemical improvement. This result contrasts with previously reported better performance of 50 μm thick LSF₄₀-SDC cathodes in anode-supported cells.

Study of Ni-YSZ cermet anodes thickness

Anode thickness was reduced by the systematic dilution of the original Ni-YSZ formulation with 20% vol. in solids. Two new Ni-YSZ slurries were 19% and 18% vol. in solids. Two cells were prepared with each Ni-YSZ slurry: 20%, 19% and 18% vol. in solids, using three different presintered tubes from batch 220. From each tube, two cells were prepared covering every Ni-YSZ slurry combination; %20 and %19 vol. sol. in 220.FP.4, %20 and %18 vol. sol. in 220.FP.7 and %19 and %18 vol. sol. in 220.FP.8 were prepared and subsequently sintered together in the same furnace. This approach was adopted in order to minimize the effect that metal tube and sintering batch may have in the final microstructure. For electrochemical characterization, LSF₄₀-SDC composite cathode and Pt paste were deposited along 2 cm² in the central area of the tube, leading to 7.6–7.7 cm² efficient areas. Optimal

OCV values between 1.09V – 1.1V were registered at 800°C. Summary of cell characteristics is presented in Table IV - 11. (Find detailed information about cells labelling in section 4.1.2.2)

Table IV - 11. Main characteristics of manufactured cells. (OCV is measured at 800°C; anode is fed with 3% humidified 200 ml min⁻¹ H₂ and cathode with ambient air)

FeCr Fraction (μm)	Ts (°C)	LST - Fx	Ni-YSZ slurry			OCV (V)	Efficient area (cm ²)
			Ni-YSZ (%vol. sol.)	η (Pa s)	Cell #		
<45	1350	F1	20	0.307	220.FP.4.1	1.10	7.7
					220.FP.7.1	1.10	7.7
			19	0.158	220.FP.4.2	1.11	7.6
					220.FP.8.1	1.10	7.7
			18	0.126	220.FP.7.2	1.12	7.7
					220.FP.8.2	1.09	7.6

4.2.5.3 Analysis of results

Shrinkage and physical appearance

As Figure IV - 30 demonstrates, cells production was optimal and stainless electrolytes were obtained after the sintering process. This guarantees a fairer comparative for any parameter under study.



Figure IV - 30. Illustration of the stainless electrolyte for batch 220 cells.

Cells exhibited transversal shrinkages between 14-15%. This value is especially low as compared to standard cells with 16% in average (Figure IV - 8). However, transversal shrinkage is still in the 95% confidence interval (CI) as compared to 42 standard cells which showed the following dispersion:

- For standard half-cell: FeCr (<45 μ m)/LST(F1)/Ni-YSZ(%20 vol.sol.) sintered at 1350°C
 - o $\%D_e=(15.9\pm 2.6)\%$

In fact, this is comparable to shrinkages observed for cells with coarse FeCr fraction (< 53 μ m) (Figure IV - 11). For every couple of cells from the same presintered tube, shrinkage increases slightly as anode slurry is diluted. This is in agreement with previous observations with FeCr pins (Figure IV - 9) where a shrinkage decrease is reported as Ni-YSZ anode and YSZ electrolyte are deposited in the FeCr/LST pin.

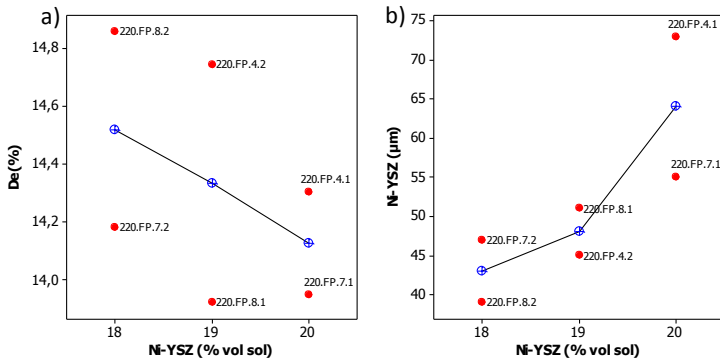


Figure IV - 31. a) Transversal shrinkage, % D_e , and b) anode thickness as a function of the Ni-YSZ vol. solids in the anode slurry.

Microstructural characterization

Thinner anode is successfully obtained by the straightforward dilution of the original Ni-YSZ formulation (Figure IV - 31). As compared to standard 40-50 μ m anodes for G2 cells (Table IV - 6) standard anode is thicker (55-75 μ m) most probably due to the lower transversal shrinkage during co-sintering. With most diluted anode (%18 vol. solids), anode thickness between 35-50 μ m are obtained, 20 μ m thinner than for standard anode.

The microstructural analysis of cells did not reveal significant differences between cells with different anode formulation (Figure IV - 32). Metal-support and DBL are porous for every cell and anode microstructure very similar. In addition, typical electrolyte with closed pores is observed.

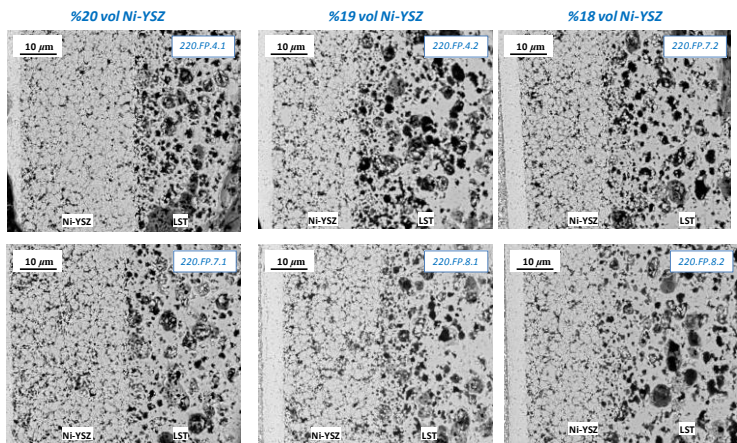


Figure IV - 32. Micrographs of cells for different Ni-YSZ (% vol. sol.) slurries.

Electrochemical characterization

Once that functional layer was measured by SEM, characteristic electrochemical values P , R_o and R_p were analyzed as a function of the anode thickness (Figure IV - 33). Cell performance improves when anode thickness decreases and highest power densities are recorded for finest 40-45 μm anodes. In addition, EIS measurements demonstrate that both ohmic and polarization resistance are lower when anode thickness is reduced in the range between 40-45 μm .

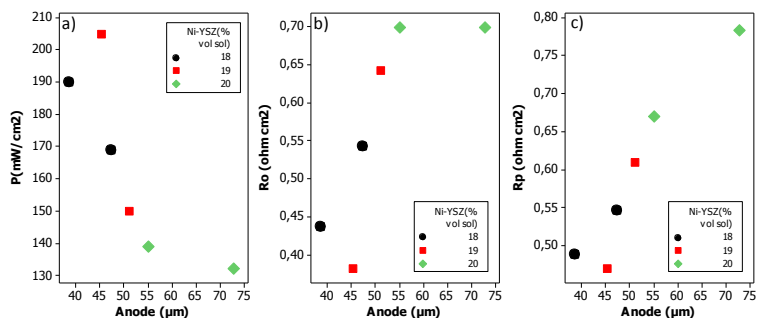


Figure IV - 33. a) Power density, b) ohmic resistance and c) polarization resistance at realistic operation conditions (800°C; 0.7V) as a function of the anode thickness. (Anode is fed with 3% humidified 200 ml min⁻¹ H₂ and cathode with ambient air)

4.2.5.4 Overall discussion and conclusions

In contrast to previous results in anode-supported cells, with similar LSF40-SDC cathode layers, no evidences of an improvement was observed when 40-60 μm thick cathode was used instead of the standard 25 μm thick one. On the other hand, electrochemical efficiency was successfully improved by anode thickness reduction from 70 to 40 μm .

Figure IV - 34 shows schematically, three configurations in which active MIEC electrodes were studied: a) LSF₄₀-SDC in ASC, b) LSF₄₀-SDC in MSC and c) Ni-YSZ in MSC. The main results obtained with these configurations are described as follows:

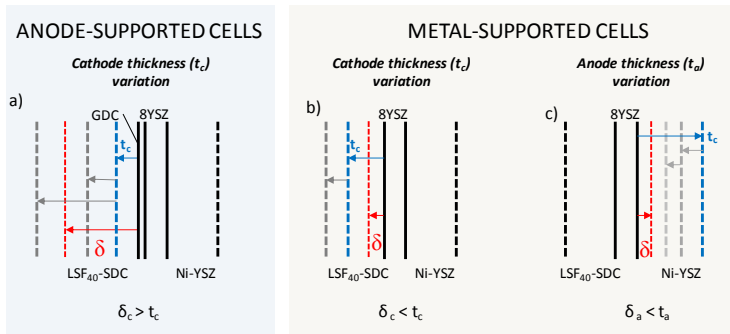


Figure IV - 34. Interpretation of experimental results for cathode, t_c , and anode thickness, t_a , variation on the basis of the electrochemically active layer, δ_c and δ_a , for each electrode, respectively. (Dashed lines in blue correspond to the initial or standard electrode thickness and dashed lines in grey illustrate the increase or decrease of electrode thickness).

LSF₄₀-SDC composite cathode thickness in ASC

In the case of anode-supported cells, better electrochemical performance of 50 μm thick LSF₄₀-SDC cathode was demonstrated as compared to 30 μm thick ones. Lower ohmic and polarization resistance systematically observed for 50 μm thick electrodes. This result was corroborated for cathodes sintered at different temperatures (950°C, 1000°C, 1050°C). This corresponds to a situation where the effective electrochemically active cathode, δ_c , is larger than the physical MIEC electrode (Figure IV - 34). In that case, when electrode thickness increases, more active TPB are available and a faster surface-exchange reaction is traduced in a polarization resistance decrease. In this situation, surface reaction in the cathode is rate limiting. Higher surface reaction in a thicker cell unblocks and regulates the

whole electrochemical reaction in the cell as far as it remains the rate limiting mechanism. Lower ohmic resistance is justified by sheet resistance improvement.

LSF₄₀-SDC composite cathode thickness in MSC

A similar approach with metal-supported cells using the same LSF₄₀-SDC composite cathode did not lead to better performances with 40-60 μm thick cathodes with respect to standard (24.4 ± 3.6) μm electrode. As Figure IV - 34 illustrates, in this case the electrochemically active cathode, δ_c , is thinner than the physical MIEC electrode and when cathode thickness increases beyond the active layer this is not traduced in a significant performance improvement. The outer part is electrochemically inert and acts essentially as a current collector.

The reason of such difference is in all probability originated by the dissimilar rate limiting mechanism in both designs. In the case of anode-supported cells, Ni-YSZ cermet with tailored nanostructure exhibits an excellent electrochemical activity (Figure IV - 35). High-quality anode provides with an efficient distribution of active sites that improve overall cell performance through cathode processing adjustment. The electrochemically active cathode, δ_c , is large and, increasing cathode thickness, better performance is obtained. In the case of metal-supported cells, however, nickel agglomeration during co-sintering deteriorates electrochemical properties in the anode (Figure IV - 35). Electrochemically active cathode, δ_c , is thinner; less performing anode demands lower performance at the cathode, lowering active cathode thickness. In this situation, mechanisms related to the half-reaction in the anode are rate limiting. Summarizing, cathode optimization studies are useless as far as they are combined with poor anode quality. That means that improvements in MSC anode are needed before attempting for cathode optimization.

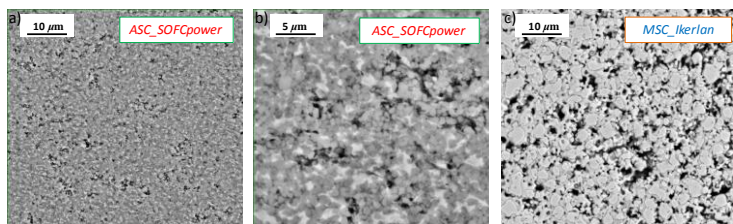


Figure IV - 35. Standard microstructures for a,b) ASC-SOFCpower Ni-YSZ cermet anode compared to c) MSC-IK4-Ikerlan Ni-YSZ cermet anode.

Ni-YSZ cermet anode thickness in MSC

In the case of metal-supported SOFC with coarse Ni-YSZ microstructure developed at IK4-Ikerlan, better performance of finest 40-45 μm Ni-YSZ cermet anode was demonstrated with respect to ≈ 64 μm Ni-YSZ anodes with analogous

microstructures. In this case, the electrochemically active anode thickness, δ_a , is lower than the physical anode, t_a (Figure IV - 34). When anode thickness decreases concentration overpotential reduces and current collection improves. Accordingly, R_p and R_o decrease and better electrochemical efficiency is achieved with 40 μm anode. We assume that few micron thick δ_a reported in literature [249, 250, 252] is thicker here due to the coarser Ni-YSZ microstructure. In a 3D modelling of porous Ni-YSZ microstructure, δ_a between 5-15 μm is predicted for an electrode with particle sizes between 0.5 and 1 μm [254]. Poor quality anode with MSC contains Ni particles in the 3-5 μm range (Figure IV - 35) and therefore we predict an active anode above 20 μm .

To sum up, we have seen that the electrochemical performance of G2 cells is a strong function of anode thickness. G2 cells optimization requires further tailoring by lowering anode thickness till the electrochemically active layer, δ_a . In addition, this conclusion helps to explain the dissimilar electrochemical properties of first and second generation cells; 30 μm thick Ni-YSZ anode for G1 cells will certainly show higher performance than 40-50 μm thick ones for G2 cells (Table IV - 6).

4.3 G2 cells degradation mechanisms during fabrication

4.3.1 Introduction

This section refers specifically to the degradation occurring while co-sintering the half-cell at high temperature (above 1330°C) and under reducing atmosphere required for MSC technology. The MSC fabrication route causes severe degradation of metal substrate, barrier layer and anode. In particular, Ni agglomeration, Ni-Fe-Cr interdiffusion and formation of dark stains have been related to poor electrochemical performance. The detailed analysis of stains is treated in this section.

Significant efforts were addressed all through this work to discover the factor that originates the stains during sintering. In fact, it is hardly understood how plain and stained cells are arbitrarily produced during the standardized manufacturing process. It seems that a subtle factor is in the origin of stain formation. Many factors have been considered and studied.

In early days, titanium diffusion was unidentified but stain formation was observed in the electrolytes and associated to the poor quality of G2 cells. Factors which failed proving any connection with the specific degradation mechanism are the following:

- *Binder quality*
- *Surface interaction in the FeCr substrate/LST interface*
- *Laboratory conditions (T, RH) during dip-coating*

However, during this investigation, as potential factors under the stain formation were rejected one by one, increasing information was collected and stain formation was exclusively related to the co-sintering process. Parameters that guided the investigation and moved closer to the origin of stains are the following:

- *Sintering furnace*
- *pO₂ and dew point (DP) monitoring during co-sintering*
- *Influence of the oxygen getter*

In the following sections, early studies and more specific ones related to the co-sintering processes together with reactivity proofs are presented.

4.3.1.1 Early studies in stain formation

Binder quality

At the very beginning, the potential influence of residual organic components after firing (400°C) was considered in the stain formation. WB4101 binder is a water based with organic additives which is used for LST barrier and anode slurries formulations. This binder is a viscous liquid which is maintained in a tank (20 l). Binder pot (1 l) which is used for slurry processing is filled up periodically with fresh binder from this tank. In fact, binder shows some degradation and small particles solidification after a certain time of use. In order to eliminate binder option as stain former, a new binder pot was prepared from the tank and new slurries and cells were manufactured. New binders showed high viscosity (1.14 Pa s) as compared to the measurements with the old one (\approx 0.8-0.9 Pa s). In contrast, slurries viscosity decreased substantially with the new binder. However, stains appeared once more in the electrolyte surface during co-sintering, this finally rejecting binder influence assumption.

LST penetration in the FeCr substrate

LST barrier penetration in the metal substrate during *dip-coating* was also investigated as a potential source of porous FeCr near surface densification that is observed in stained zones of cells. In order to prevent LST penetration, metal substrate was lubricated with different organic compounds before *dip-coating*. First of all, the wettability of a variety of lubricants was studied. Different pieces of the same FeCr tube were submerged during 10 s in glycerol, vaselin oil, PEG 300, Terpeneol, mineral oil and ethylene glycol. Lubricants with the best wettability, vaselin oil and terpeneol, were select by visual inspection (Figure IV - 36).

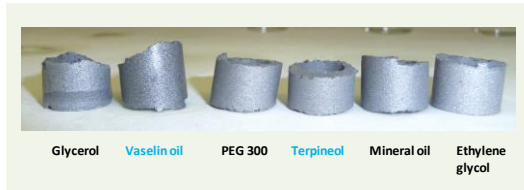


Figure IV - 36. Illustration of the wettability of some organic agents in the FeCr substrate surface. (After 10 s of submersion in the agent).

New G2 cells were produced following the standard manufacturing process of previously lubricated FeCr substrates. Metal tubes were submerged by dip-coating in vaselin oil or terpineol. After LST barrier deposition, surfaces with lubricant were more transparent as compared to a standard cell simultaneously manufactured without wetting agent (Figure IV - 37). Following anode deposition and drying in air, some points became visible in the surface of the cell processed with terpineol, and cells with vaseline oil were radically covered with points. After de-binding at 400°C, cells with vaseline oil exhibited a peeled-off anode. In this phase, difference with stained cells was apparent as stained cells do not show any distinguishing mark prior to co-sintering. However, the process was concluded by electrolyte deposition and co-sintering of two standard cells and other two with terpineol. One of each type was sintered in argon and the other, following the standard sintering cycle with gas change at 1100°C from inert to reducing atmosphere. Regardless the sintering atmosphere, surface of cells with terpineol was completely dark (Figure IV - 37). In contrast, standard cells with good quality had plain surfaces. Cells sintered in argon were brownish as compared to the greyish cell sintered in reducing atmosphere above 1100°C. Most probably, brownish colour is related to the partial reduction of the metal substrate.

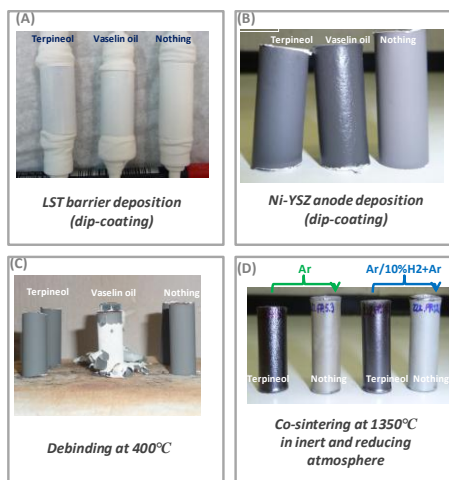


Figure IV - 37. Processing phases of G2 cells with lubricant in the FeCr substrate/LST barrier interface.

For standard cells sintered in argon or following the standard cycle, similar transversal shrinkage was calculated ($\%D_e \approx 15-16\%$). The electrochemical performance was also comparable; 157 and 197 mWcm^{-2} were recorded for cells sintered in argon and standard reducing atmosphere, respectively. Conversely, cells with terpeneol did not show OCV.

Finally, this approach was also rejected in the stain formation investigation.

Laboratory conditions (T, RH) during dip-coating

Local temperature and relative humidity during *dip-coating* of ceramic slurries is usually registered. Potential influence of those parameters in the barrier and anode slurry viscosity and stain formation during co-sintering was also analyzed. However, no correlation was identified.

Furnace influence

During G2 cells manufacturing, three furnaces are used for sintering of half-cells (section 2.3.1.4). In order to analyze if sintering furnace variability is related to stain formation, 12 cells with standard configuration were manufactured from 6 tubes by cutting them into two pieces. Cells processed from the same tube were strategically sintered in different furnaces covering possible combinations (furnace n°1-2, 2-3 and 1-3) twice (

Table IV - 12).

Table IV - 12. Batch, tube and sintering furnace of manufactured cells.

<i>Tube Batch</i>	<i>Tube</i>	<i>Cell #</i>	<i>Furnace (n°)</i>
215	15	215 FP 15 1	1
		215 FP 15 2	2
	16	215 FP 16 1	1
		215 FP 16 2	2
	17	215 FP 17 1	2
		215 FP 17 2	3
	18	215 FP 18 1	2
		215 FP 18 2	3
	19	215 FP 19 1	1
		215 FP 19 2	3
	20	215 FP 20 1	1
		215 FP 20 2	3

From the surface appearance of the half-cells after co-sintering two conclusions can be extracted in Figure IV - 38. First, stain/plain surface of half-cells is independent of the sintering furnace. Second, stain formation is most probably related to sintering process parameters at high temperature. Similar cells manufactured from the same cell tube can appear stained or plain after a different co-sintering process. In the case of tube 17 from batch 215, cell 215.FP.17.1 sintered in the furnace n°2 appears stained, whereas analogous 215.FP.17.2 with similar processing parameters sintered in furnace n°3 is plain. The same holds for partner cells in the sintering cycle 215.FP.18.1 and 215.FP.18.2. Therefore, within the same sintering cycle and independently of the furnace used, the appearance of two cells is mostly influenced by the sintering cycle. That indicates that there are subtle variations within each cycle that markedly influence stain formation. Further analysis of this and other parameters is carefully attempted in the following sections.

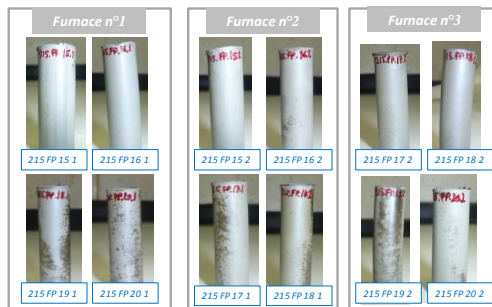


Figure IV - 38. Surface appearance of half-cells as a function of the sintering furnace.

4.3.2 Stains identification

4.3.2.1 Introduction

During the optimization study with second generation of metal supported cells, dark irregular regions were occasionally observed in the electrolyte surface after co-sintering. Sometimes little spots, other times stains and in an extreme situation, completely dark extensions became visible (Figure IV - 39). Besides, cracks were observed in a couple of cells.

In principle, there were no premises against stains. However, after extensive experience with G2 cells, our experimental perception indicated higher performance of stainless cells. According to previous observations (section 4.2.3 and 4.2.4), it is reasonable to think that stains negatively affect the electrochemical performance of G2 cells and create more variability. It is also presumably related to larger shrinkage during co-sintering and enhanced during higher sintering temperatures (1370°C).

In this section, an accurate stain formation analysis is presented. Elemental features related to stains are identified by SEM and EDS and finally, correlation with electrochemical performance is established.

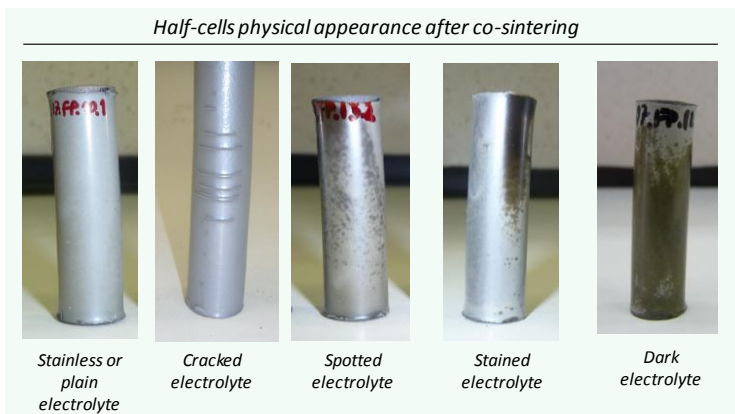


Figure IV - 39. G2 half-cells classification according to the physical appearance after co-sintering.

4.3.2.2 Experimental procedure

One of LST-F1 cells, 209.FP.6.1, initially prepared for experimental work in section 4.2.4, showed particular surface appearance after sintering. Whilst one side was plain the other side appeared completely dark (Figure IV - 26). This singular cell was used to analyze stain formation on electrolyte surface. Results for cell 209.FP.6.1 were then compared with a statistically reliable group of plain/stained G2 cells to confirm that observations match with the general trend for G2 cells.

Procedure was simple; 1cm² of LSF₄₀-SDC cathode was dip-coated in each characteristic zone of cell 209.FP.6.1 prior to Pt-paste application. Pt mesh attached to two Pt wires was stack in each efficient area and 4-point measurement was carried out in both plain and stained zones (Figure IV - 40).

4.3.2.3 Analysis of results

Electrochemical characterization

IV-curves demonstrate the very poor electrochemical characteristics of the stained zone (Figure IV - 40). Whereas in the plain zone 153 mW/cm² were registered at 0.7V, in the dark zone only 18 mW/cm² were collected at 800°C. In addition, optimal OCV of 1.1V in the plain zone contrasts with the low 0.99V in the dark zone. Gas-tightness in the system is guaranteed by the optimal OCV that plain zone exhibited and therefore OCV fall in the stained zone was not caused by an external factor (i.e. poor sealing quality).

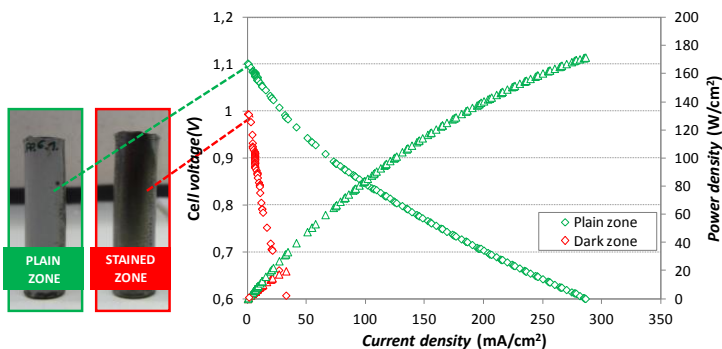


Figure IV - 40. IV-curve at 800°C for plain and stained or dark zone in 209.FP.6.1 cell. (Anode is fed with 3% humidified 200 ml min⁻¹ H₂ and cathode with ambient air)

This result was compared with a statistically reliable G2 cells population. The characteristics of the analyzed group are summarized as follows:

- 8 Batches: 202, 203, 204, 207, 208, 209, 212 and 213
- Crofer fraction: fine (<45 μm) except for two cells with coarse (<53 μm) fraction.
- Sintering temperature: 1350°C except for two cells sintered at 1330°C and other two at 1370°C.
- LST formulation: Standard F1 except for two cells for each F2, F3 and F4 (Refer to section 4.4.2. for F1-F4 labelling details).

Statistical trend is consistent with observations in cell 209.FP.6.1 (Figure IV - 41). While plain cells exhibit high and stable OCVs (1.1V), mean value is lower (1.07V) for stained cells and extensive divergence exist. OCV variation is reasonable given that stains are irregularly distributed over the electrolyte surface. If stains are in truly related to lower OCVs, OCV loss will be more pronounced as stains proliferate in the electrochemically efficient area. Thus, in the dark zone of 209.FP.6.1, extremely low OCV of 0.99V is explicable for a completely stained 1cm² active area. Besides, little number of cells presented cracks in the electrolyte. Even if cracks that are visible by simple inspection are isolated before cathode dip-coating, imperceptible micro-cracks can account for the observed lower OCV of one of the three cells. The negative effect of dark stains in the OCV, however, is extensively corroborated in the statistical population.

On the other hand, better performance of stainless cells is confirmed. Cells with plain electrolyte give 133 mW/cm² power densities in average, whilst those with stains produce around 85 mW/cm² (Figure IV - 41).

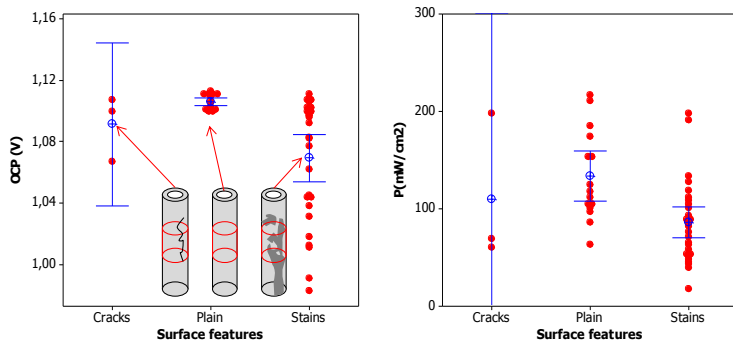


Figure IV - 41. a) Open Circuit Voltage, OCV and b) power density for G2 cells as a function of the surface appearance. (The confidence interval of the mean is of 95% in both cases).

Plain and stained zone of cell 209.FP.6.1 was also studied with EIS technique. Nyquist diagrams at OCV and 0.7V are shown for both plain and stained zones in Figure IV - 42. At OCV, ohmic resistance ($\approx 0.44 \Omega\text{cm}^2$) was similar but higher polarization resistance $\approx 7.5 \Omega\text{cm}^2$ was recorded in the stained zone as compared to the plain zone with $\approx 5 \Omega\text{cm}^2$. Well defined semicircle observed in the plain zone at low frequencies is substituted for a larger semicircle at the spotted zone. At 0.7V, ohmic resistance is slightly different; $0.44 \Omega\text{cm}^2$ in the plain zone is reduced to $0.39 \Omega\text{cm}^2$ in the stained zone. However, polarization resistance diverges substantially; $0.87 \Omega\text{cm}^2$ in the plain zone is converted into the surprisingly high $6.5 \Omega\text{cm}^2$ in the stained zone.

This was again consistent with results from statistical analysis (Figure IV - 43). Comparable ohmic resistance values are slightly lower in stained cells; average $0.65 \Omega\text{cm}^2$ and $0.6 \Omega\text{cm}^2$ are recorded for plain and stained G2 cells, respectively. Conversely, polarization resistances are much higher and dispersed for stained cells; average $0.8 \Omega\text{cm}^2$ for plain and $2.1 \Omega\text{cm}^2$ for stained cells is estimated.

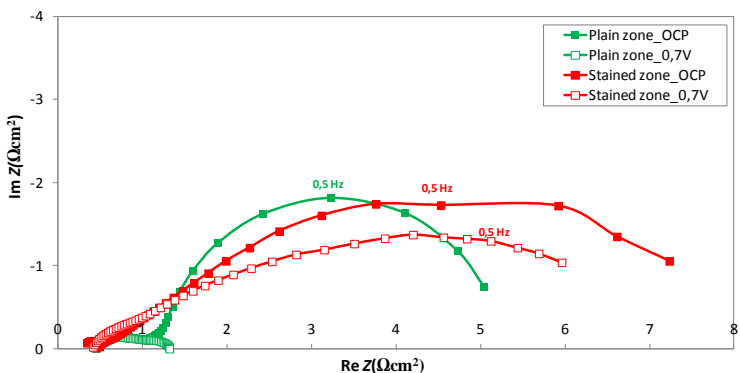


Figure IV - 42. Nyquist diagram for plain and stained zone in cell 209.FP.6.1. Impedances were recorded at OCV and realistic 0.7V between 1KHz - 0.1Hz.

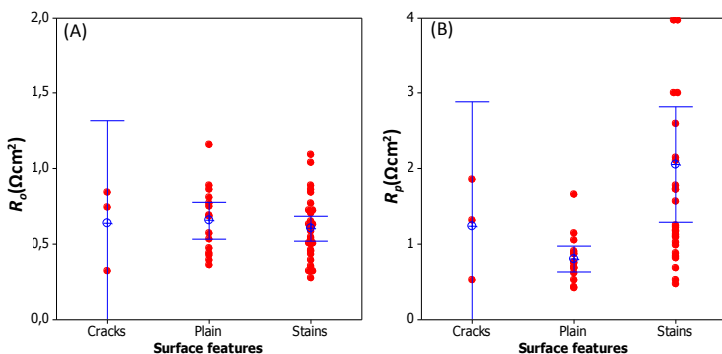


Figure IV - 43. (A) Ohmic and (B) polarization resistance for the analyzed G2 cell population as a function of the surface appearance.

Shrinkage during co-sintering

In cell 209.FP.6.1, plain/stained zones shrinkage could not be independently measured due to shape limitations. Hence, shrinkage trend was directly studied in the G2 cells population. Higher shrinkage of stained G2 cells is suggested. As a general rule, shrinkage variability is high but average $\approx 17\%$ is higher for stained cells in comparison to an average shrinkage of $\approx 15.8\%$ for plain cells (Figure IV - 44).

DBL thickness

In section 4.2.4, stain proliferation was higher for thinnest DBL which was prepared with diluted F4 formulation. This trend was statistically analyzed in the group of plain/stained cells produced with FeCr(<45 μ m)/LST-Fx/Ni-YSZ(20%vol.sol)/YSZ standard configuration, being x=1 or 4 (Figure IV - 44). Plain/stained cells proportions with the standard F1 and most diluted F4 formulations used in the DBL are the following:

$$\frac{\text{Plain}}{\text{Stained}}(LST - F1) = \frac{31}{16} = 1,94$$

$$\frac{\text{Plain}}{\text{Stained}}(LST - F4) = \frac{6}{17} = 0,35$$

For LST-F1, 66% of cells are plain and 34% are stained, against 26% plain and 74% stained for LST-F4. Thus, stain formation is favoured as DBL thickness decreases.

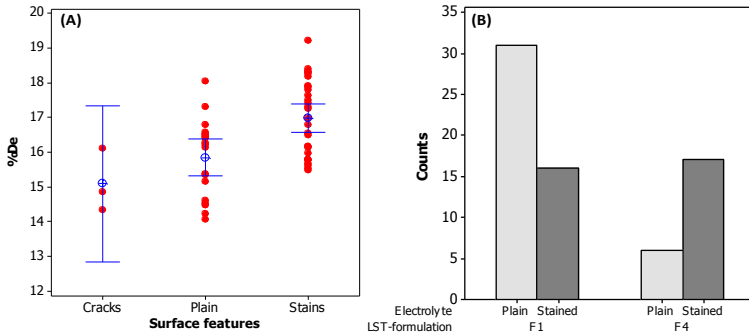


Figure IV - 44. (A) Transversal shrinkage, % D_e , of G2 cells as a function of the physical appearance and (B) number of plain/stained G2 cells as a function of LST barrier formulation. (F1: thicker and F4: diluted and thinner DBL).

Microstructural Characterization

Microstructural differences between plain and stained cells were investigated by post-mortem analysis of the characteristic cell 209.FP.6.1; support and functional layers of plain/stained zones were systematically compared.

Detailed analysis of the metal-support did not reveal any significant difference between plain and stained zones. In Figure IV - 45, central image shows 209.FP.6.1 tube divided in five inspection areas (001-005) in each side. This image was

obtained using a specific SEM application called *Navigation Montage* that permits to construct a general vision of large samples. In this way, metal support was analyzed in each independent zone. FeCr substrate was dense near the active region in some zones but there was no distinction between plain and stained regions.

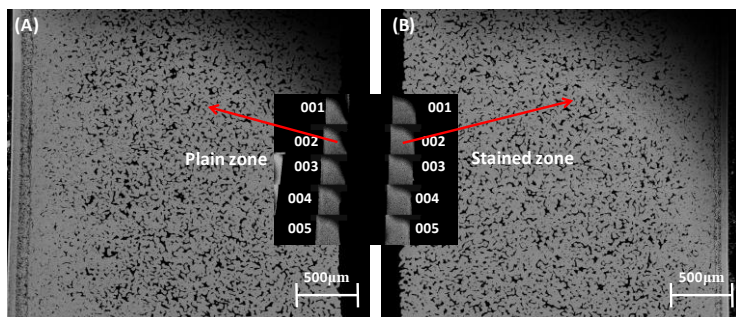


Figure IV - 45. Microstructure of the metal support of (A) plain and (B) stained zones in cell 209.FP.6.1.

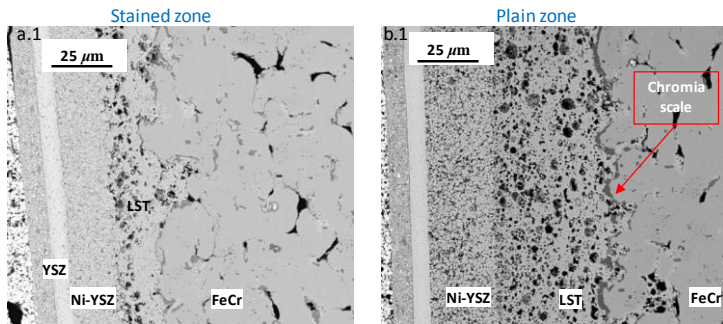
Analysis of ceramic functional layers, however, revealed significant differences between plain and stained zones. In the first row of Figure IV - 46, functional layers appearance in plain/stained zones is presented. Thickness difference of DBL and anode is apparent. Diffusion barrier layer reduces from 86 μm in the plain zone to 49 μm in the stained zone. In addition, the anode is 10 μm thinner in the stained zone with 49 μm . Electrolyte is 15 μm in both cases. Thicknesses of ceramic functional layers are summarized in Figure IV - 47. Significant differences in the metal-support can be pointed out by comparison of first micrographs (Figure IV - 46). In the stained zone, metal-support is slightly denser in the DBL vicinity. More significant is that chromia scale which protects the metal substrate in the plain zone is almost inexistent in the stained zone.

Second row micrographs in Figure IV - 46 compare LST-DBL and Ni-YSZ anode in the stained and plain zones, respectively. Whereas in the plain zone, porous standard microstructure of LST barrier and Ni-YSZ anode is observed, the stained zone shows both layers dense, specially Ni-YSZ anode. This densification yields to thinner LST and Ni-YSZ functional layers (Fig. III - 47).

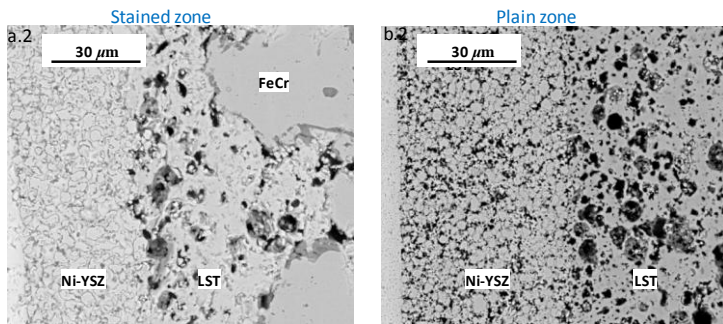
Third row micrographs in Figure IV - 46 illustrate anode and electrolyte in the stained and plain zones, respectively. Anode exhibits the standard porous microstructure with relatively agglomerated nickel particles after co-sintering in the plain zone. In contrast, in the stained zone, nickel particles over agglomeration and YSZ massive sinterization are evident. Anode densification is outstanding with no visible porosity. Surface of nickel particles is covered with dark phases which are identified as chromium, iron and manganese oxides by EDS in the text which follows.

Regarding the electrolyte, typical closed micro pores in the plain zone disappear in the stained zone. The electrolyte is completely dense and grain growth significantly larger.

Functional layers



Anode and DBL



Electrolyte and anode

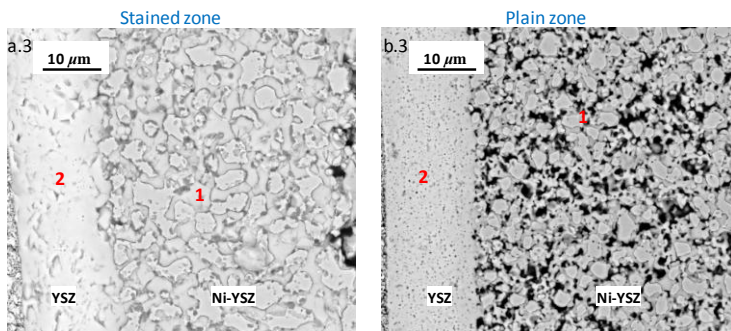


Figure IV - 46. SEM micrographs in the characteristic stained and plain zone in cell 209.FP.6.1.

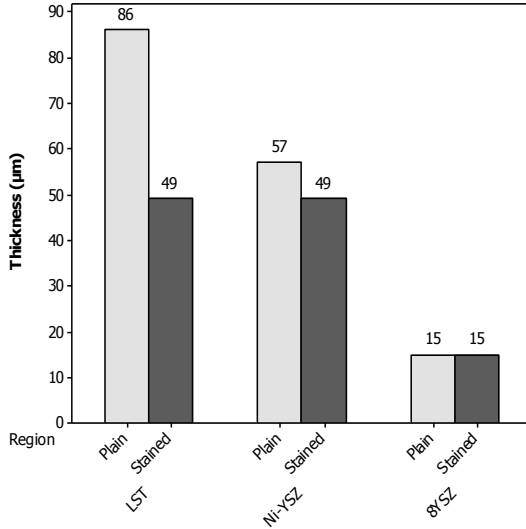


Figure IV - 47. Thickness of functional ceramic layers in plain and stained zones in 209.FP.6.1 cell.

In order to understand the origin of such massive densification in the stained zone, a more exhaustive analysis was carried out in the characteristic zones of cell 209.FP.6.1 by means of EDS.

In the third row of Figure IV - 46, red numbers indicate points in the anode and electrolyte of plain/stained zones whose composition was studied by EDS. Spectrum of those points is presented in Figure IV - 48. In the stained zone (b.3), peaks found around 4.5 keV in the anode (Point 1) and electrolyte (Point 2) are identified as titanium. Note that point 1 is essentially situated on top of YSZ even if little nickel amounts have been observed. Titanium is also observed in the electrolyte (Point 2) but at lower extent. In the stained zone, titanium to zirconia proportion from EDS quantification is the following:

$$\text{Stained zone: } \frac{Ti}{YSZ} (\text{anode}) = 0.1 ; \frac{Ti}{YSZ} (\text{electrolyte}) = 0.06$$

Titanium was also present in the anode of the plain zone. This is evident from EDS spectra examination; there is a titanium peak around 4.5 KeV in the anode. In the electrolyte no titanium was identified but element quantitative analysis accounts for little amounts of titanium. This is an error during element fitting because titanium fitting is asked in a situation where it is not present. As a matter of fact, point analysis

is not a precise quantitative characterization technique. Error is particularly higher when little element concentrations are quantified. In the plain zone, titanium to zirconia ratio from EDS quantification is

$$\text{Plain zone: } \frac{Ti}{YSZ}(\text{anode}) = 0.03 ; \frac{Ti}{YSZ}(\text{electrolyte}) = 0$$

Thus, we conclude that in the stained zone substantial amount of titanium migrates to the electrolyte and especially the anode. In the plain zone, titanium is present just in the anode but to a lesser extent. Titanium incorporation in the electrolyte is most probably associated to the surface darkening.

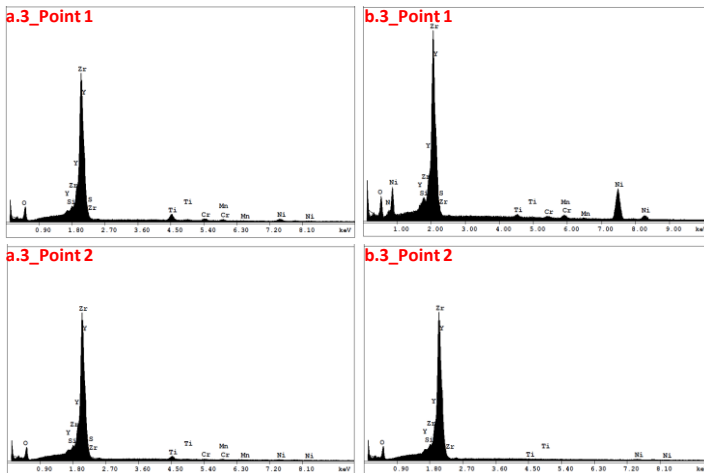


Figure IV - 48. EDS spectra of points specified in a.3 and b.3 images of Figure IV - 46.

Further exhaustive EDS analysis was carried out in the stained zone. The elemental composition of characteristic points in the densified anode (Figure IV - 49) are analyzed in Table IV - 13. The coarse Ni-YSZ microstructure is more apparent. Previously mentioned dark points are essentially chromium oxide, Cr_2O_3 , but manganese is also found and Cr_2MnO_4 spinel additional formation is expected. In point 4, traces of oxygen and iron are also identified in the surface of massively agglomerated nickel particles. Migration of those species has been previously identified in G1 cells [102].

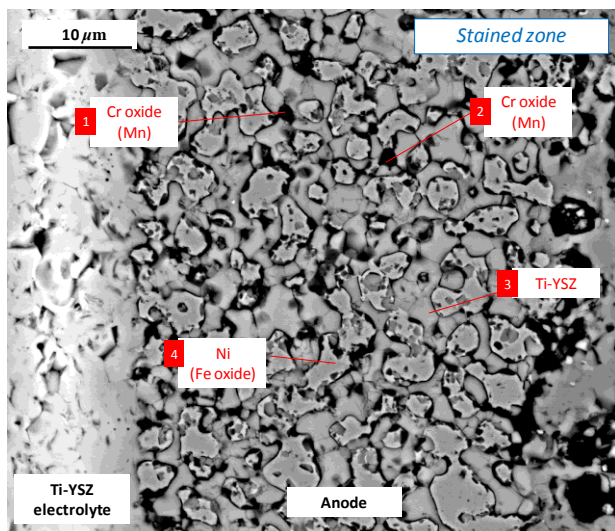


Figure IV - 49. Illustration of anode and electrolyte microstructure in the stained zone of cell 209.FP.6.1.

Table IV - 13. EDS analysis of points in Figure IV - 49.

Element	Point 1 (at%)	Point 2 (at%)	Point 3 (at%)	Point 4 (at%)
OK	47.5	51.46	16.89	7.21
SiK	2.32	1.27	1.42	0.81
SrL	0.49	0.34	1.28	0.11
Y	1.07	0.73	4.62	0.17
P	0.09	0	0.3	0
ZrL	7.37	5.01	32.63	1.87
CaK	0.17	0.18	0.28	0.04
TiK	0.43	0.38	2.21	0.11
LaL	0.03	0.1	0.32	0.06
CrK	20.63	29.67	1.63	0.69
MnK	5.39	3.3	0.64	0.14
FeK	0.6	0.33	0.22	1.73
NiK	13.66	7.24	3.22	87.05

Protective scale in the surface of FeCr substrate contained essentially chromium and titanium as measured in the plain zone of cell 209.FP.6.1 (Figure IV - 50) by EDS (Table IV - 14). This is in agreement with observations for Inconel 601 alloy oxidized in air [255]. The composition of oxide scale formed on its surface included titanium oxides (TiO_2 and $\text{Ti}_2\text{Cr}_7\text{O}_{17}$) and chromia (Cr_2O_3) mixed together. $\text{Mn}_{1.5}\text{Cr}_{1.5}\text{O}_4$ was also detected at the external interface of Inconel 601. This might be related to the unidentified phase including Mn-Cr-Ti-O which was detected by XRD as a minor byproduct of FeCr and LST reactivity at 1350°C [183]. LST barrier layer contained little amounts of chromium (1-2 at%). In the stained zone, chromium was also identified in DBL but concentration was slightly higher in the 2-3 at% Cr range. No nickel was present in the metal substrate.

Therefore, microstructural characteristics of the stained zones can be summarized as follows:

- *Metal-support:*
 - o Densification in the DBL vicinity
 - o Lack of protective chromia scale

- *LST barrier:*
 - o Densification and thickness reduction
 - o Slightly higher chromium incorporation (2-3 at% Cr)

- *Anode:*
 - o Densification and thickness reduction
 - o Ni-YSZ microstructure coarsening
 - Nickel agglomeration
 - YSZ sinterization
 - o Cr, Mn and Fe poisoning in the nickel particles
 - o Ti diffusion to YSZ

- *Electrolyte:*
 - o Overdensification and particle grain growth
 - o Titanium incorporation

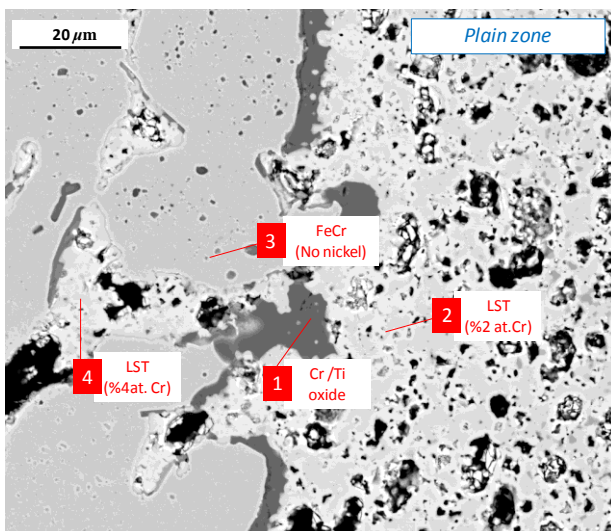


Figure IV - 50. FeCr/LST interface and protective scale in the plain zone of cell 209.FP.6.1.

Table IV - 14. EDS analysis of points analyzed in Figure IV - 50.

Element	Point 1 (at%)	Point 2 (at%)	Point 3 (at%)	Point 4 (at%)
OK	47,.	49.5	7,7	41.14
AlK	1.44	0.72	0.89	0.78
SiK	0.09	0.48	0.68	1.42
SrL	0.03	16.89	0.3	18.86
Y	0	0.78	0.25	1.15
P	0.02	0	0.07	0
ZrL	0.04	0	0.22	0
CaK	0.16	0.13	0.15	0,2
TiK	21.73	20.74	0.27	22.4
LaL	0.38	7.77	0.31	8.96
CrK	27.42	2.73	19.88	4.26
MnK	0.58	0	0	0.09
FeK	0.19	0.17	69.28	0.75
NiK	0	0.1	0	0.07

4.3.2.4 Overall discussion and conclusions

Stain features

Specific characteristics related to stained cells have been identified and corroborated in a statistically reliable G2 cells population. The following conclusions are withdrawn from this analysis:

- *Stains formation is related to OCV loss and lower electrochemical performance.*
- *Stains formation is traduced in little R_o decrease but huge R_p increase at operation conditions (0.7V).*
- *Stains formation is related to a higher transversal shrinkage during co-sintering.*
- *Thinner LST layer increases stain formation probability.*
- *It is most probably favored at higher sintering temperature (1370°C, section)*

SEM analysis provided an explanation to particular features observed with stained cells. Higher transversal shrinkage is reflected in thin and denser functional layers. In particular, massive anode densification with vast agglomeration of Ni and YSZ phases is detrimental for the electrochemical performance of the cell. This blocks fuel transport and the amount of TPB decreases dramatically due to the coarse Ni-YSZ microstructure. Little contact points between agglomerated Ni and YSZ, with practically inexistent porosity is added to the worse catalytic activity of Ni particles due to massive chromium poisoning. The activation barrier for the electrochemical oxidation of hydrogen is high and this is reflected in a huge activation polarization. IV-curve in the characteristic plain/stained zones (Figure IV - 40) of 209.FP.6.1 cell shows that activation losses extend beyond the linear region. At 0.7V, slope should be less abrupt for the stained zone as R_o is slightly lower. However, activation losses predominate and other effects are hindered in the IV-curve. Nevertheless, concentration losses are also expected given the dense anode microstructure.

Stain identification: Ti-YSZ fluorite

Titanium identification in YSZ can be considered as the potential trigger for densification and consequent poor performance of characteristic stained zones. In fact, a detailed work by Mori et al. [256] confirmed these premises. Mori's group studied Ti-YSZ fluorites and Ni-Ti-YSZ cermets structural, electrical, thermal and mechanical properties for SOFC anode application. Concretely, they studied xTi-YSZ system with $x < 10\%$ mol TiO₂. In the text which follows, main properties of Ti-YSZ are discussed, compared to *titanium active* G2 cells and situated in the SOFC framework.

Ti-YSZ crystallography

Firstly, Mori discovered that YSZ fluorite (cubic symmetry) and TiO₂ rutile (tetragonal symmetry) reaction preferentially creates Ti-YSZ fluorites with cubic symmetry. Tetragonal domains were also observed but in a lower degree. In addition, they observed that lattice parameter and cell volume of fluorite decreases increasing TiO₂ content in YSZ ($a=5.1439 \text{ \AA}$) at least up to 10 mol% TiO₂ ($a=5.1238 \text{ \AA}$). This effect was explained as a consequence of the smaller ionic radius of Ti⁴⁺ (88 pm) respect to Zr⁴⁺ (98 pm).

Electrical properties

Secondly, Mori observed that oxide-ion conductivity decreases with increasing Ti content and they related this effect to tetragonal-like domains formation by Ti-doping. However, electrical properties differ in the oxidant and reductive atmosphere. While Ti-YSZ conductivity in air is attributed to simple oxide-ion conduction; in reductive atmospheres, Ti-YSZ works as a mixed ionic-electronic conductor at high temperatures; Ti⁴⁺ can convert to Ti³⁺ ions and ionic valence change is charge compensated via oxygen release and oxygen vacancy formation or by electron hole formation. Therefore, Ti-YSZ acquires mixed conducting properties at reducing atmospheres and ionic conductivity is higher than in oxidizing atmosphere.

Lower R_o observed in stained zones of G2 cells is partially ascribed to the MIEC properties that YSZ acquires when Ti incorporates in the anode; Ti-YSZ works also as a current collector and ohmic resistance is lower. In addition, when Ti incorporates in the electrolyte, mixed ionic-electronic conductivity causes a leakage current that reduces the OCV from the theoretical (Nernst) value. This has been extensively studied with GDC electrolytes [2, 11, 257, 258]. The situation for GDC is analogous to Ti-YSZ above 500°C, as Ce⁴⁺ extensively reduces to Ce³⁺ at reducing atmosphere; GDC becomes a MIEC and OCV loss is acknowledged.

As doped SrTiO₃ perovskites are attracting growing attention as possible SOFC anode materials, titanium diffusion to the YSZ electrolyte is a critical concern. In fact, researchers from Jülich detected Ti diffusion to YSZ electrolyte in a half-cell configuration containing Y-substituted SrTiO₃-YSZ composite anode with infiltrated Ni. Half-cells were sintered in reducing atmosphere at 1400°C for 5h [259]. Even if the novel anode was not electrochemically tested in a cell, possible OCV loss due to mixed conductivity in the electrolyte was contemplated in the article. Existing literature for doped SrTiO₃ anode and YSZ electrolyte was revised but no evidences of OCV decrease were found [26, 27, 260-263]. Finally, it was argued that Ti diffusion was limited in those cases due to either thick electrolytes (50 μm) or different anode processing (i.e. sintered in air at 1200°C). In a recent publication, it was demonstrated that for MIEC electrolytes OCV is strongly related to its thickness [264]. When MIEC GDC electrolyte thickness decreases, OCV and thus the convertible energy also decrease. Hence, if an attempt to use MIEC electrolytes is

made, thickness should not be arbitrarily thin to preserve the OCV. However, in such a case, a compromise between the need of lower ohmic losses and the desire to maximize the convertible energy (OCV) exist. Up to now, MIECs are not considered to be feasible as electrolyte materials.

Sintering behaviour

Mori et al. observed remarkable Ti induced grain growth in the Ni-Ti-YSZ system. That is, Ti-doping enhances the sintering characteristics of YSZ particles. In addition, a recent work by H. Kishimoto et al. [265] demonstrated that TiO₂ doping in YSZ improves the wettability of Ni particles in its surface when Ni particles diameter is larger than ≈ 550 nm. This grain size is comparable to the starting nickel particle ≈ 500 nm in our manufacturing process. Hence, titanium incorporation in the YSZ fluorite causes Ti-YSZ sintering and Ni agglomeration. Thus, evidences are enough to confirm that coarse anode microstructure and electrolyte densification are originated by titanium diffusion at the stained regions of the cell.

Ti migration in YSZ

Kowalski et al. [266] studied titanium diffusion in yttria stabilized zirconia between 1200-1400°C in air and found that grain boundary diffusion ($\approx 10^{-14}$ - 10^{-12} m²/s) is about 5 orders of magnitude faster than bulk diffusion ($\approx 10^{-19}$ - 10^{-17} m²/s). Thus, once that titanium depletion from LST barrier is activated, titanium diffusion should occur preferentially via YSZ grain boundary. Nevertheless, the factor that induces titanium depletion from LST perovskite is unknown up to now.

4.3.3 Titanium activation mechanisms

4.3.3.1 Introduction

In the previous section, titanium diffusion to the anode and electrolyte has been identified as the main degradation mechanism in G2 cells during fabrication. As a result, anode microstructure becomes coarse and dense and electrolyte acquires mixed-conducting properties. For stained or *titanium active* cells, poor protective chromia scale in the FeCr substrate surface and significant chromium poisoning in the anode has also been observed. This poisoning during co-sintering is well known and has been extensively reported in the literature [70, 128, 129]. Conversely, studies about titanium diffusion are not that frequent. Researchers from Jülich have reported Ti diffusion and incorporation in YSZ electrolyte for a Y-substituted SrTiO₃-YSZ anode [259]. The origin of such mechanism is not studied in that work, however, and *titanium activation* mechanism is unidentified as far as it is known by the author.

Earlier studies in this work pointed towards the influence of sintering atmosphere in the formation of stains. Therefore, prevailing conditions in the furnace during the

co-sintering process were analyzed by pO_2 and dew point (DP) measurements in a group of G2 cells. As a matter of fact, hermetical sealing of the furnace is manual and requires physical effort. Difference during sealing can introduce a variability which may affect cell sintering.

Characteristic parameters which are analyzed in pO_2 and DP profiles include the oxidation temperature (T_{ox}), absorption at low temperature (T_{abs}), oxygen partial pressure before gas change at 1100°C , pO_2 (Ar), and oxygen partial pressure and dew point in reducing atmosphere after gas change, pO_2 and DP ($10\%H_2 + Ar$) (section 2.3.1.4). Those parameters are represented in Figure IV - 51 and Figure IV - 52 as a function of stained/plain cells after co-sintering.

At the very beginning, it was thought that oxygen absorption which is sometimes observed at low temperatures could be related to stain formation. However, cells with plain surfaces also exhibited this absorption and this assumption was rejected. Unfortunately, substantial differences between stained and plain cells could not be discerned from this analysis. Dew point measurement after gas change ($t=450$ min) also failed establishing any correspondence with stains (Figure IV - 52).

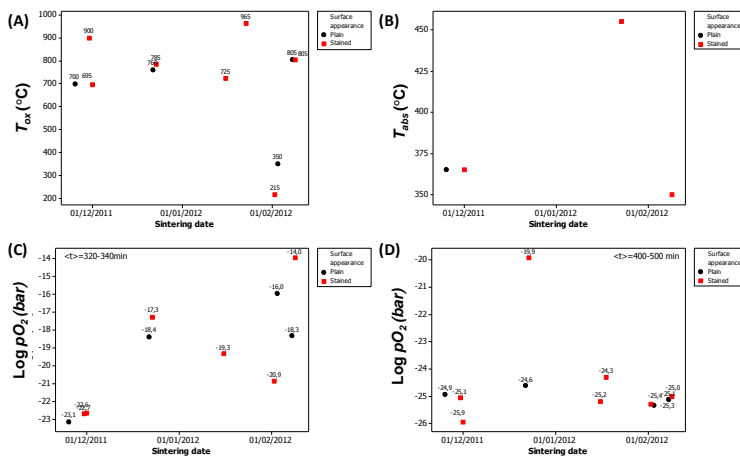


Figure IV - 51. (A) Oxidation temperature, T_{ox} , (B) absorption temperature, T_{abs} , (C) oxygen partial pressure in argon before gas change at 1100°C and (D) in reducing atmosphere ($10\% H_2 + Ar$) after gas change. (Oxygen partial pressure in (C) and (D) is measured in average between 320-340 min and 400-500 min in the thermal cycle, respectively)

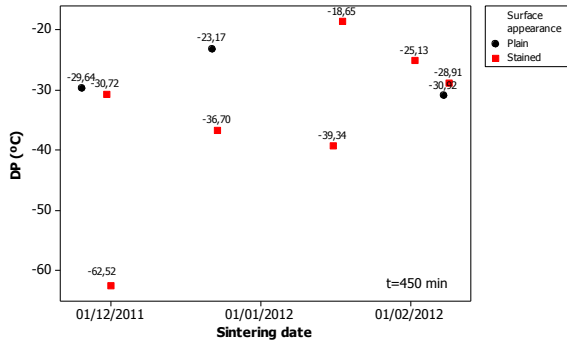


Figure IV - 52. Dew point, (DP) as a function of the surface appearance. (Measurement carried out after gas change, at t=450 min in the thermal cycle).

However, when the influence of the FeCr oxygen getter was looked at closely, experimental results indicated that it could be related to stain formation. FeCr getter is added to the sintering process at the gas inlet; one or two trays of FeCr powder are placed to remove gas impurities. FeCr oxygen getters (<math> < 53 \mu\text{m}</math>) release water as the inert gas is changed to reducing 10% $\text{H}_2 + \text{Ar}$ at 1100°C. Sudden increase in water vapour is reflected in the dew point peak, as illustrated in Figure IV - 53 for cell 2 and 3 which were sintered with FeCr getters. Note that those cells are stained in the top zone of the tube. In contrast, for a single cell sintered with no FeCr getters, there is no such a peak and stainless cell was obtained after co-sintering. This suggests that small water vapour emissions due to reduction of oxygen getters occurring during gas change (1100°C) in the sintering process could be in the origin of the stain formation.

However, it has been observed that stainless cells are obtained even with oxygen getters, indicating that there is a processing parameter still out of control. Dew point is measured periodically but not at every sintering cycle. From dew point measurements, no relation with the surface appearance after co-sintering is discerned (Figure IV - 52).

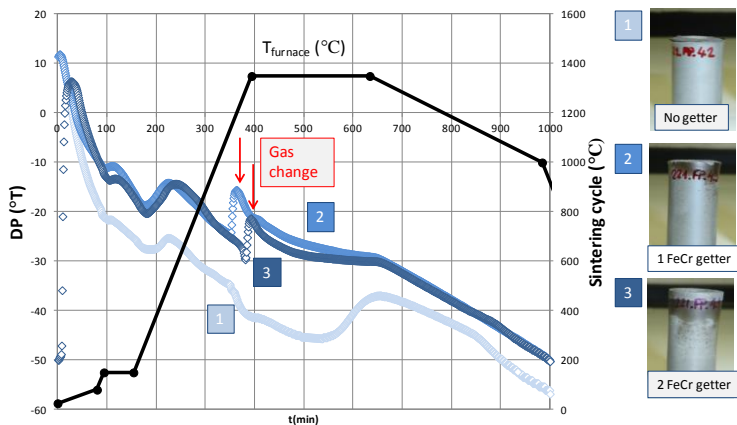


Figure IV - 53. Dew point (DP) evolution during the sintering cycle and final cell surface appearance as a function of the oxygen getter. (Red arrows indicate temperature at which gas change occur. Cell 1 was co-sintered with no oxygen getter whereas cells 2 and 3 had one and two containers of FeCr oxygen getter, respectively)

The identification of titanium diffusion (section 4.3.2) in the origin of stain formation conducted the investigation towards specific reactivity studies of half-cell components. Studies which are presented in this section include:

- Analysis of reactivity of LST and YSZ powders under different sintering atmospheres by XRD
- Analysis of reactivity of FeCr, LST and Ni-YSZ sintering under reducing atmosphere with the presence and absence of water vapour by SEM and EDS

4.3.3.2 Reactivity of LST and YSZ under different atmospheres

Introduction

In this section, reactivity between LST and YSZ was studied by XRD reproducing the thermal cycle during co-sintering under different atmospheres. Two LST+YSZ mixtures were prepared with different weight proportions: 50:50 or 10:90 LST/YSZ and they were sintered at 1350°C and 1400°C, respectively.

XRD patterns recorded for LST/YSZ (50:50 wt.) mixtures, were compared with those recorded for pure LST and YSZ pellets processed under analogous conditions. In addition, cell parameters of YSZ were contrasted with Ti-YSZ system cell parameters [256] under different Ti(%) doping to investigate titanium diffusion into the YSZ fluorite during the sintering process at different atmospheres.

Experimental results

LST-YSZ (50:50 wt.) powder mixture was prepared with 5 g of LST and 5 g of YSZ (TZ-YSZ, 5.8m²/g) which were dispersed in 30 ml of isopropanol and milled with 10 YSZ cylinders during 5h at 500 rpm. LST-YSZ (10:90 wt.) mixture, with 1g of LST and 9g of YSZ was prepared following similar processing conditions. After drying and sieving, powder mixtures were shaped into 1g disks and pressed in a cold uniaxial press at 2 ton for 1 min. LST-YSZ (50:50 wt.) powder was sintered at 1350°C and LST-YSZ (10:90 wt.) at 1400°C. Those samples were sintered under reducing (10% H₂ + Ar), inert (Ar) and oxidizing atmospheres (open furnace) (Table IV - 15).

Table IV - 15. Experimental table of pellets prepared with corresponding composition, sintering temperature and atmosphere. (*) is the average as calculated for two pellets.

<i>T_s</i> (°C)	Composition	Sintering atmosphere	ρ (g/cm ³)
1350	LST-YSZ (50:50 wt.)	10% H ₂ + Ar	4.95*
		Ar	4.1
		Air	4.45*
		Ar/10% H ₂ + Ar (Standard)	4.4*
		10% H ₂ + Ar (3% H ₂ O)	4.9
1350	LST	10% H ₂ + Ar	4.75*
		Ar	3.3
		Air	3.6
		Ar/10% H ₂ + Ar (Standard)	4.75*
		YSZ	10% H ₂ + Ar
Ar	5.5		
Air	5		
Ar/10% H ₂ + Ar (Standard)	5.7		
1400	LST-YSZ (10:90 wt.)		10% H ₂ + Ar
		Ar	5
		Air	5.1
		Ar/10% H ₂ + Ar (Standard)	5
		10% H ₂ + Ar (3% H ₂ O)	4.5

Theoretical densities: ρ (LST= 5.19 g/cm³); ρ (YSZ= 5.9 g/cm³); ρ (LST+YSZ 50:50wt. = 5.55 g/cm³); ρ (LST+ YSZ 10:90wt. = 5.82 g/cm³)

Analysis of results

Pellets color and size after sintering changes depending on the powder (LST, YSZ) and sintering atmosphere. While YSZ powder is clear after sintering (grayish in hydrogen, yellowish in argon and white in air) LST powder is very dark in reducing atmosphere, grey in Argon and yellow-orange when sintering in air. However, color of LST+YSZ cells is a mixture of the characteristic color that LST and YSZ powders exhibit after sintering in each atmosphere. Therefore, simple color inspection of cells

does not reveal any reactivity between LST and YSZ powders. However, there are some differences related to powder proportions and sintering temperature. While LST-YSZ (50:50 wt.) sintered at 1350°C tends more to LST colors, LST-YSZ (10:90 wt.) sintered at 1400°C is grey in hydrogen but yellow when sintered in Argon. This is attributed to YSZ color at 1400°C, which becomes yellow. In Figure IV - 54, however, pure YSZ pellet sintered at 1350°C in Argon is still slightly yellowish.

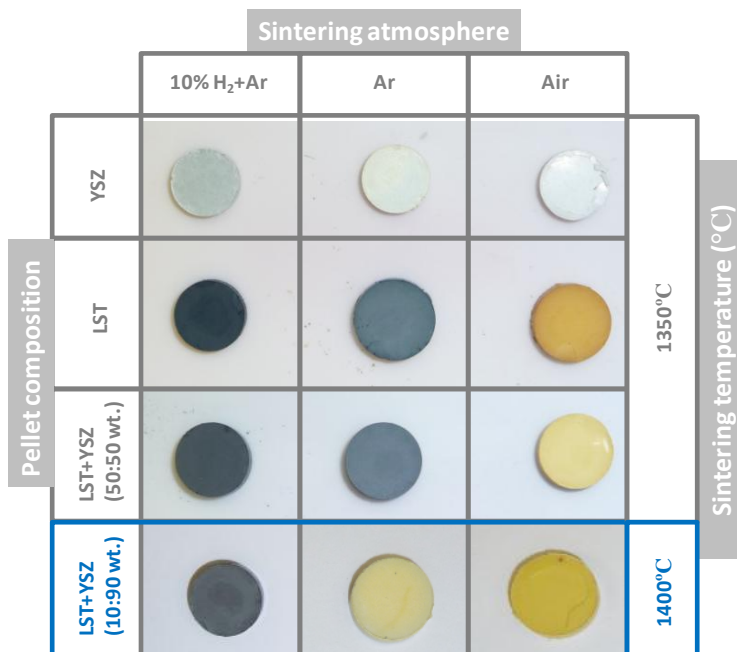


Figure IV - 54. Pellets surface appearance as a function of composition (LST, YSZ or LST+YSZ mixture), sintering temperature and atmosphere.

In order to analyze reactivity, LST+YSZ (50:50 wt.) pellets sintered at 1350°C in three atmospheres (i.e. oxidizing, inert and reducing) were crushed in a mortar and polycrystalline samples were analyzed by XRD diffraction. In addition, untreated LST and YSZ powders were also measured and were used as reference in the posterior analysis.

In the X-ray pattern, YSZ peaks for every sample were fixed at similar Bragg angles. However, LST peaks were shifted to the left for every LST+YSZ (50:50 wt.) pellet as compared to the untreated LST powder. This phenomenon was independent of the sintering atmosphere (Figure IV - 55; Figure IV - 56).

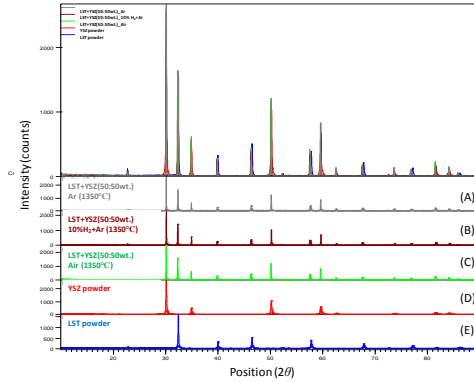


Figure IV - 55. Diffraction patterns of LST+YSZ (50:50 wt.) pellets sintered at 1350°C in (A) Argon, (B) 10% H₂+Ar, (C) air as compared to (D) YSZ and (E) LST commercial powders.

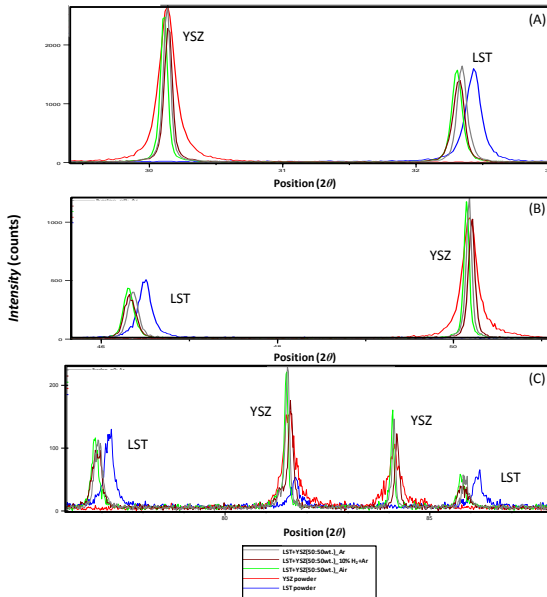


Figure IV - 56. Characteristic LST and YSZ peaks between (A) $2\theta \approx 28-33^\circ$, (B) $2\theta \approx 45-52^\circ$ and (C) $2\theta \approx 75-90^\circ$.

Cell parameters of YSZ fluorite and LST perovskite (i.e. both with cubic structure) were calculated for each sample following Rietveld refinement (Figure IV - 57) carried out in a collaboration with J. Van Duijn (Albacete). As for the observed LST shifting to the left, LST cell parameter for different pellets was in the 3.91- 3.92 Å range after refinement, slightly higher than for untreated LST powder (≈ 3.90 Å). In contrast, YSZ lattice parameter in the 5.141- 5.147 Å range was similar for every sample including the untreated YSZ powder (Table IV - 16).

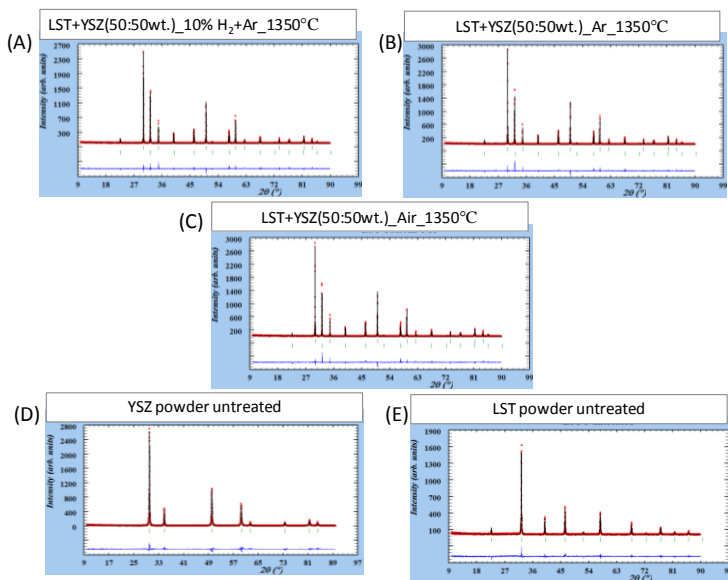


Figure IV - 57. Rietveld refinement of diffraction patterns for LST+YSZ (50:50 wt.) pellets sintered at 1350°C in (A) 10% H₂+Ar, (B) Argon and (C) air and untreated (D) LST and (E) YSZ powder. (For all fits, background, lattice parameters, thermal factor (fixed to be the same for all atoms in one phase) and the usual profile parameters (U, V, W and LY) were fitted. The occupancies were fixed to their theoretical values.)

Therefore, YSZ lattice parameter in the 5.141- 5.147 Å range was compared with data reported by Mori et al. [256] in the Ti-YSZ system. In section 4.3.2, it was mentioned that when Ti incorporates in the YSZ fluorite the lattice parameter decreases due to the lower ionic radius of Ti⁴⁺ (88 pm) as compared to Zr⁴⁺(98 pm). Here, this difference was used to verify if there is any titanium diffusion to the YSZ fluorite and if it depends in the sintering atmosphere. However, theoretical values reported for Ti-YSZ system suggest that there is no titanium diffusion in the LST+YSZ pellets sintered at 1350°C. For lowest 2% Ti-doped YSZ, lattice parameter

is lower than 5.14 Å and it continues decreasing down to 5.12 Å at 10% Ti-YSZ. Experimentally calculated lattice parameter fits perfectly with pure YSZ.

Table IV - 16. (A) Lattice parameter of LST and YSZ powders untreated and after sintering LST+YSZ (50:50 wt.) pellets at 1350°C in reducing, inert and oxidizing atmosphere and (B) lattice parameter of YSZ fluorite as a function of the Ti% doping. (Ti-YSZ lattice parameters calculated after firing at 1600°C for 72h in air).

(A) Experimental data			(B) Ti-YSZ system [256]	
Sample	YSZ-Lattice parameter (Å)	LST-Lattice parameter (Å)	Sample	Lattice parameter (Å)
YSZ powder	5.1446		YSZ	5.1439
LST powder		3.9075	2Ti-YSZ	5.1376
LST+YSZ_%10H ₂ +Ar	5.14719	3.92280	4Ti-YSZ	5.1361
LST+YSZ_Ar	5.14602	3.91985	6Ti-YSZ	5.1310
LST+YSZ_Air	5.14125	3.92129	8Ti-YSZ	5.1301
			10Ti-	
			YSZ	5.1238

Overall discussion and conclusions

LST+YSZ (50:50 wt.) pellets sintered at 1350°C in reducing, inert and oxidizing atmosphere did not show any marked reactivity. By simple visual inspection this was expected as the color of LST+YSZ pellets was a combination of colors that LST and YSZ pellets receive separately. It was concluded that surface coloration of those mixed LST+YSZ pellets depends on the powder proportion, sintering atmosphere and temperature. However, lack of reaction was confirmed by XRD. During stain formation, when titanium incorporates the YSZ fluorite, this is reflected in a lattice parameter decrease due to the lower ionic radius of titanium. Thus, this trend was used to verify if there is some titanium diffusion in our pellets. However, XRD analysis showed fixed YSZ peaks for every pellet regardless the sintering atmosphere. In addition, experimentally calculated lattice parameter for YSZ (Rietveld refinement) corresponds to pure YSZ reported by Mori and collaborators [256]. Hence, there is no titanium diffusion in these pellets. However, diffraction peaks shift to the left and slight increase in the lattice parameter of LST perovskite is observed for every pellet as compared to the untreated LST powder. There is no identification of secondary phases.

From this analysis, it can be concluded that titanium diffusion and incorporation in the YSZ fluorite is not a simple mechanism between YSZ and LST under high temperature and specific atmosphere. There is an unidentified partner that participates to it.

4.3.3.3 Reactivity of FeCr, LST and YSZ under the effect of humidification in reducing atmospheres

On the basis of previous results, there is enough evidence to believe that ambient humidification at high temperatures can be related to stain formation during sintering. In the mentioned work, gradual increase in stain formation was observed as more oxygen getter was used in the sintering process (Figure IV - 53). In contrast, cell surface came out plain when oxygen getter was taken away. On the other hand, in section 4.3.2, microstructural analysis in the stained zone demonstrated chromia scale evaporation and little amounts of chromium in the LST barrier. This suggests that metal substrate interaction with LST barrier could be related to titanium segregation from the perovskite. It is believed that the study of titanium activation mechanisms requires a complete analysis of the half-cell.

In this section, the reactivity of half-cell components FeCr, LST and Ni-YSZ is studied under the effect of moist/dry reducing atmospheres.

Experimental procedure

Three powder blends were prepared by the combination of standard anode Ni-YSZ cermet with little amounts of pure LST and FeCr (<53 μm) powders (Table IV - 17). The first mixture combined the three powders; Ni-YSZ, LST and FeCr. The second one only Ni-YSZ and FeCr. Finally, the third one was a mixture of only Ni-YSZ and LST. Powder mixtures were dispersed in 30 ml of isopropanol and milled with 10 YSZ cylinders during 24h at 500 rpm. After drying and sieving, powder mixtures were shaped into 1g disks and pressed using a cold uniaxial hydraulic pellet press holding 1 ton during 1 min. Pressed disks were sintered at 1400°C during 4h under dry and moist reducing atmospheres. Reducing atmosphere, 10% H₂+Ar, was 3% humidified by passing the fuel through a water bubbler at ambient temperature. Pellets composition and sintering atmosphere are summarized in Table IV - 17.

Table IV - 17. Specifications for pellets combining different anodic cell components under the effect of dry and humidified reducing atmosphere during the sintering process at 1400°C for 4h. (Absolute density (full dense pellets): $\rho(\text{FeCr}+\text{LST}+\text{Ni-YSZ})=7.23\text{g/cm}^3$; $\rho(\text{FeCr}+\text{Ni-YSZ})=7.43\text{g/cm}^3$; $\rho(\text{LST}+\text{Ni-YSZ})=7.18\text{g/cm}^3$.)

<i>T_s</i> (°C)	<i>Atmosphere</i>	<i>Original composition</i>	<i>ρ</i> (g/cm ³)
1400	%10H ₂ +Ar	9g NiO-YSZ+1g FeCr+1g LST	6.41
		9g NiO-YSZ+1g FeCr	6.9
		9g NiO-YSZ+1g LST	6.37
	(%10H ₂ +Ar)(3%H ₂ O)	9g NiO-YSZ+1g FeCr+1g LST	6.4
		9g NiO-YSZ+1g FeCr	6.79
		9g NiO-YSZ+1g LST	6.49

Analysis of results

Samples microstructure

Microstructural characterization of pellets provided interesting information about components reactivity and the influence of humidification in the final microstructure. During pellet processing, crack proliferation within the pellets due to overpressure is usual. However, appearance of FeCr+Ni-YSZ pellets sintered in humidified atmosphere is markedly distinct from others, with localized and evident porosity which is missing in the rest of samples (Figure IV - 58).

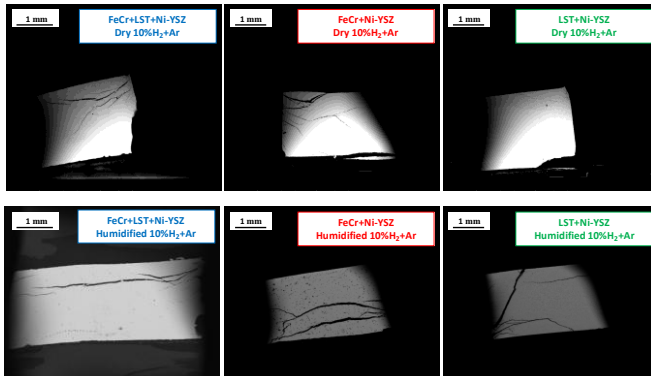


Figure IV - 58. SEM cross section (x50) images for pellets after sintering at 1400°C for 4h. (Mixed material proportions specified in Table IV - 17).

Analysis at higher magnifications made visible nickel and LST clusters formation as shown in Figure IV - 59. Nickel clusters are observed for FeCr+LST+Ni-YSZ and FeCr+Ni-YSZ powder mixtures, regardless the dry/moist reducing atmosphere. However, when humidified atmosphere is introduced, nickel clusters create an empty space in the surroundings. This is especially true for FeCr+Ni-YSZ pellets and accounts for the localized porosities in Figure IV - 58. On the other hand, no Ni clusters are present in LST+Ni-YSZ blend, which points towards the possible influence of FeCr powder in the formation of nickel clusters. Besides, a similar phenomenon is observed with LST clusters. Whereas they are clearly visible in FeCr+LST+Ni-YSZ mixture, for LST+Ni-YSZ pellets, LST agglomeration is smaller. Hence, the possible effect of FeCr in LST agglomeration is also considered. Observations in Figure IV - 59 are summarized as follows:

- Nickel clusters:
 - o Formed in the presence of FeCr

- In humidified sintering atmospheres associated to pore/hole formation
- *LST clusters*:
 - More pronounced in the presence of FeCr

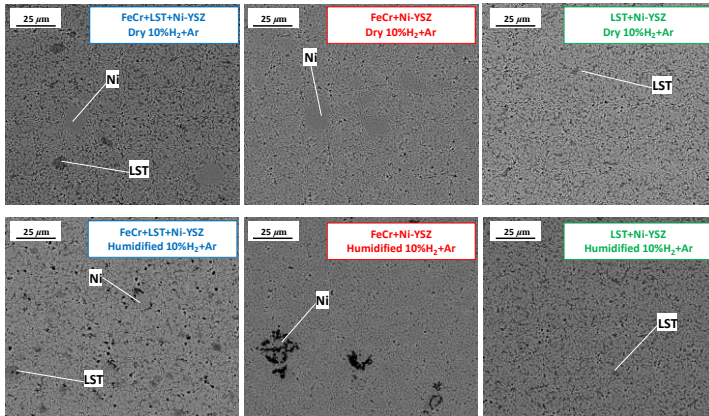


Figure IV - 59. SEM cross sections (x2000) showing nickel and LST clusters formation as a function of powders combinations and sintering under dry or humidified atmosphere.

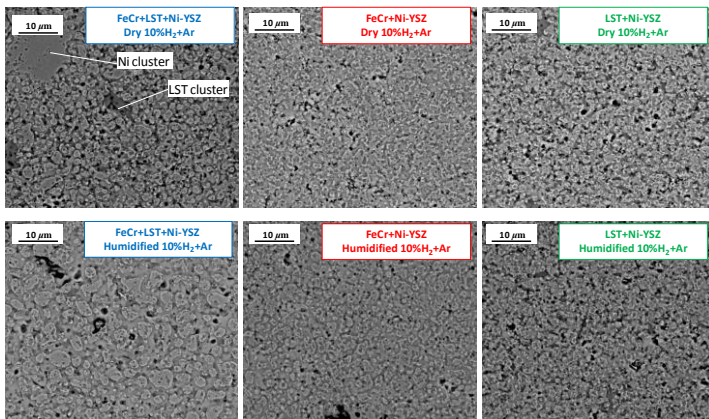


Figure IV - 60. SEM cross sections (x5000) showing pellets background microstructure as a function of powders combinations and sintering under dry or humidified atmosphere.

If nickel and LST clusters are obviated and background microstructure is looked at, additional variation within the pellets is discerned, as shown in Figure IV - 60. Nickel particles wettability and agglomeration increases when FeCr particles are present. Nickel particles grow additionally as FeCr+LST+Ni-YSZ and FeC+Ni-YSZ pellets are sintered in humidified atmosphere as compared to analogous pellets sintered under dry conditions. However, Ni wettability and agglomeration is larger for FeCr+LST+Ni-YSZ mixture as compared to FeCr+Ni-YSZ mixture with no LST, regardless the moist/dry sintering atmosphere. FeCr+LST+Ni-YSZ under humidified sintering atmosphere contains all the ingredients (i.e. FeCr, water and LST) that promote Ni wetting/agglomeration and hence, it shows the largest nickel particles. Observations in Figure IV - 60 are summarized as follows:

- *Nickel agglomeration and wettability:*
 - o Increase when FeCr is present
 - o Under the presence of FeCr, nickel agglomeration increases when sintering atmosphere is humidified
 - o It is further enhanced by the presence of LST

Densification also differs among the different samples. When cells are sintered in dry atmosphere, Ni-YSZ+FeCr is particularly dense in Figure IV - 60. When pellets are sintered in humidified atmosphere, significant modifications are not appreciable, concerning the porosity for FeCr+Ni-YSZ and LST+Ni-YSZ mixtures. However, densification of Ni-YSZ+FeCr+LST pellet is apparent. Those observations are consistent with geometrical density estimations (Table IV - 17). Observations are summarized as follows:

- *Densification*
 - o In dry sintering conditions densification is higher when LST is not present
 - o When LST is present, it increases when sintering atmosphere is humidified
 - o Highest densification for humidified FeCr+LST+Ni-YSZ (above 94%)

Titanium segregation analysis

In order to analyze titanium diffusion, a statistically representative amount of LST clusters (20 points) was analyzed by EDS on every LST containing pellet. EDS analysis and spectrum in LST clusters are illustrated in Figure IV - 61.

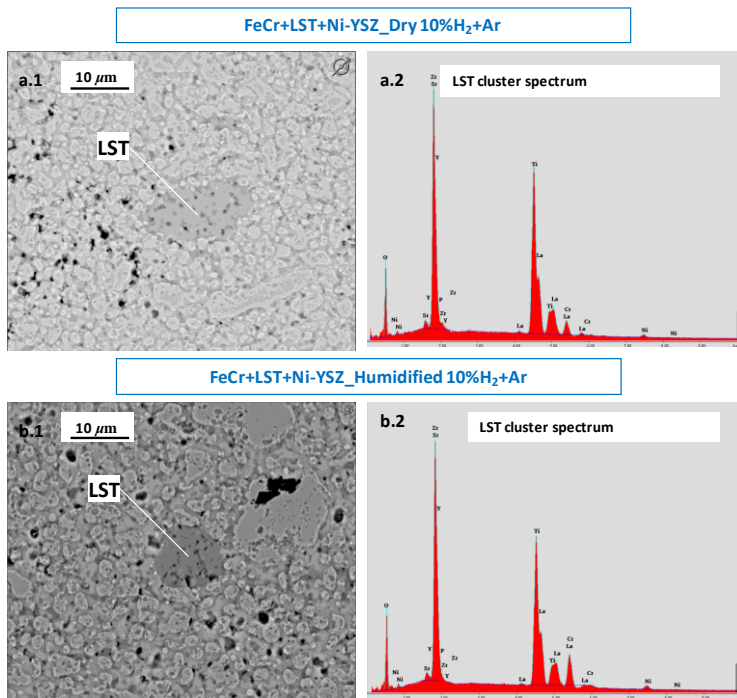


Figure IV - 61. Micrographs illustrating EDS analysis in LST clusters (a.1&b.1) and corresponding EDS spectra (a.2&b.2).

Titanium segregation from the perovskite was estimated making reference to the theoretical stoichiometry $\text{La}_{0.3}\text{Sr}_{0.7}\text{TiO}_x$ [Table IV - 3] and assuming that additional Sr and La segregation does not occur during sintering. If initial LST stoichiometry is preserved, the following relation should be satisfied:

$$\frac{Ti}{Sr + La} = 1$$

However, EDS analysis revealed titanium segregation in every sample (Figure IV - 62). Titanium segregation was 10% in most cases. As an exception, pellets containing FeCr+LST+Ni-YSZ sintered under humidified atmosphere suffered titanium segregation above 20%. In the presence of FeCr, little amounts of chromium were also observed. For FeCr+LST+Ni-YSZ mixture, sintered in moist ambient, chromium concentration is higher as compared to the analogue FeCr+LST+Ni-YSZ sample, sintered in dry atmosphere (Figure IV - 63). This corresponds to 0-2% and

3-6% Cr-concentrations in dry and wet conditions, respectively. Titanium segregation is represented as a function of chromium fraction in Figure IV - 64. A linear trend connecting both phenomena is observable; titanium segregation increases as chromium incorporates into LST clusters. It is well known that SrCrO_3 exhibits, like SrTiO_3 , a cubic perovskite structure and segregation occurs most probably by Cr substitution in the B-site of the LST perovskite. Cr substitution is in 0-5% range in dry atmosphere and 10-23% in wet atmosphere. However, estimations suggest that Cr substitution is lower than Ti segregation. For FeCr+LST+Ni-YSZ mixture sintered in dry atmosphere, 0-5% Cr substitution and 5-13% Ti segregation are calculated. On the other hand, for FeCr+LST+Ni-YSZ mixture sintered in wet atmosphere, 10-23% Cr incorporation and 15-30% Ti segregation is observed. Thus, there is a part of segregated titanium that is necessarily not related to chromium poisoning. This titanium diffusion can be related to the phase shift and increased lattice parameter of LST observed in the LST+YSZ reactivity work (Figure IV - 56; Table IV - 16).

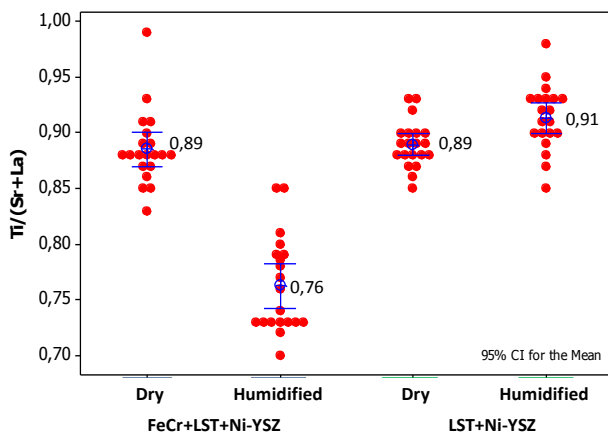


Figure IV - 62. Titanium segregation in LST clusters as a function of powders combinations and sintering under dry or humidified atmosphere.

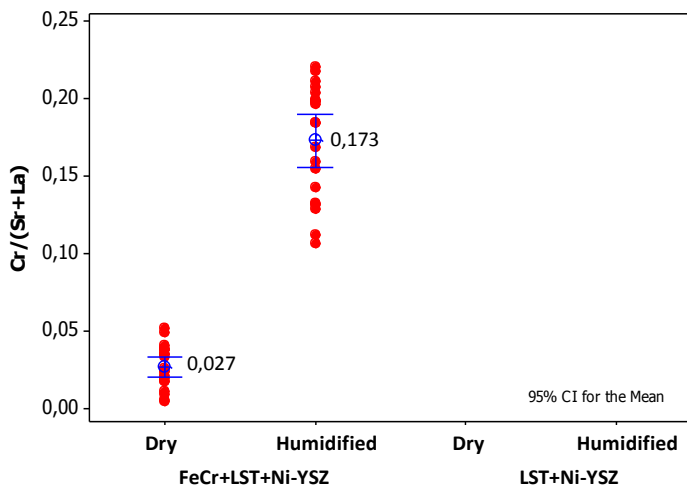


Figure IV - 63. Chromium incorporation in the LST clusters in FeCr+LST+Ni-YSZ samples sintered in dry and humidified reducing conditions.

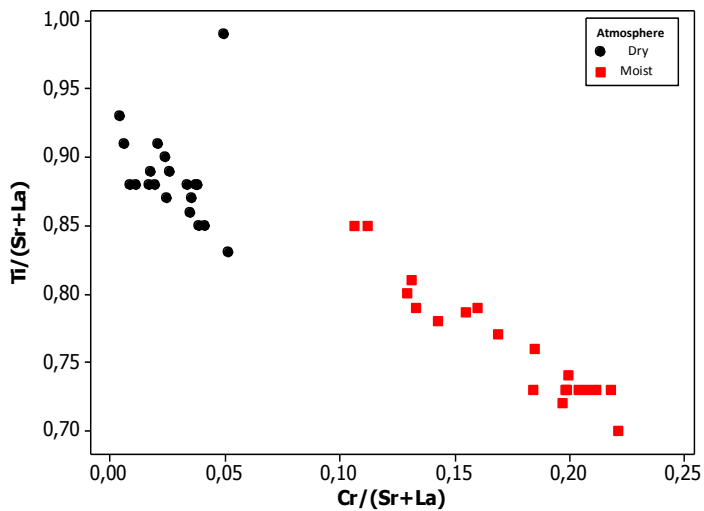


Figure IV - 64. Titanium segregation as a function of chromium incorporation in LST clusters for FeCr+LST+Ni-YSZ samples sintered in dry and humidified reducing conditions.

Nickel clusters analysis

Nickel clusters morphology was different depending on the moist/dry sintering atmosphere (Figure IV - 65). Nickel agglomeration was remarkable under dry sintering conditions. In contrast, when FeCr+LST+Ni-YSZ and FeCr+Ni-YSZ mixtures were sintered in humidified atmosphere, nickel clusters were more irregular and surrounded by empty spaces where chromia particles proliferation was frequently observed. Previously, it has been mentioned that Ni clusters with adjacent void holes are massively distributed in FeCr+Ni-YSZ mixture sintered in humidified atmosphere. Chromia particles proliferation is also more widespread in those samples as evidences Figure IV - 65.

During the elemental analysis, iron and chromium were identified in the nickel particles. In general, iron fraction in the 10-20% range was higher in Ni particles for FeCr+LST+Ni-YSZ mixtures as compared to FeCr+Ni-YSZ blends without LST with iron fraction in the 5-10% range (Figure IV - 66). No correlation connecting iron diffusion and moist/dry sintering atmosphere was established. Moreover, iron concentration difference between background nickel and clusters was not significant.

For FeCr+LST+Ni-YSZ and FeCr+Ni-YSZ samples sintered in dry atmosphere, chromium fraction around 2-3% was similar for background nickel particles and agglomerated ones. In contrast, Cr concentration differed for background/cluster nickel when samples were sintered in humidified atmosphere. Background particles contained little Cr fraction < 0.5% as compared to nickel clusters with higher and more scattered Cr fraction. Difference was more significant in FeCr+Ni-YSZ samples sintered in humidified condition, with Ni clusters containing 0-6% Cr fraction. Furthermore, in this sample, chromia particles massive proliferation was frequently observed in Ni-clusters surroundings (Fig. IV – 65).

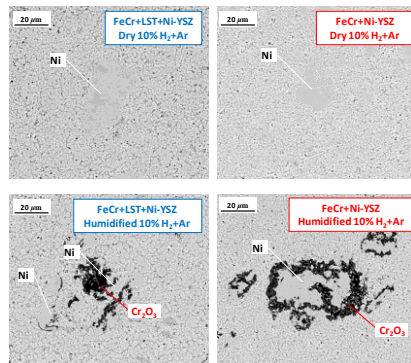


Figure IV - 65. Nickel clusters characteristics as observed for FeCr+LST+Ni-YSZ and FeCr+Ni-YSZ mixtures sintered in dry and humidified reducing 10% H₂ + Ar at 1400°C during 4h.

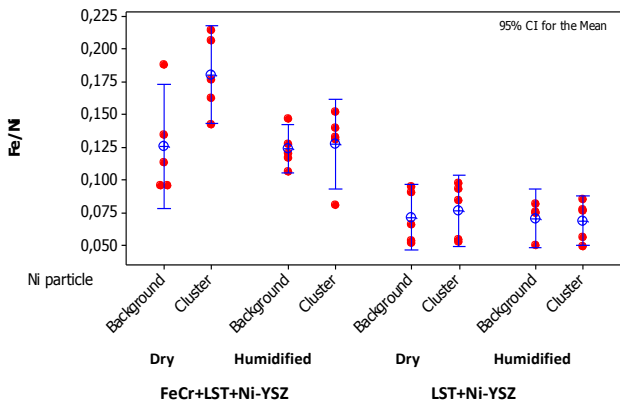


Figure IV - 66. Iron fraction in the nickel particles for FeCr+LST+Ni-YSZ and FeCr+Ni-YSZ samples sintered in dry and humidified atmosphere under reducing conditions.

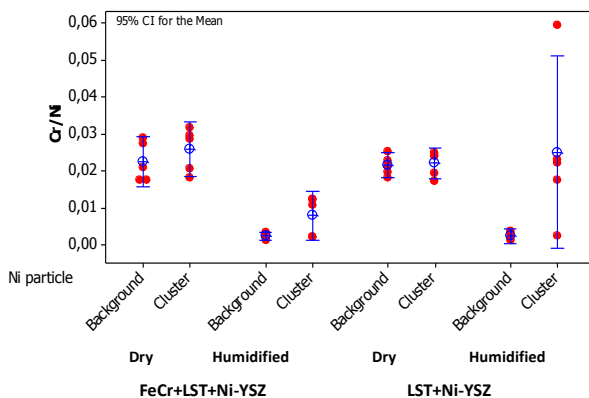


Figure IV - 67. Chromium fraction in nickel particles for FeCr+LST+Ni-YSZ and FeCr+Ni-YSZ samples sintered in dry and humidified atmosphere under reducing conditions.

Overall discussion and conclusions

Titanium segregation during the high temperature co-sintering is related to the effect of vapour. When the reducing atmosphere is humidified, chromium incorporation proliferates in LST clusters and Ti diffusion occurs more probably via chromium substitution at the B-site of the perovskite. It was estimated, in average, that around 24% of titanium leaves LST perovskite when Ni-YSZ, FeCr and LST containing

mixture is sintered in 3% humidified reducing atmosphere at 1400°C. When the same mixture is sintered under dry atmosphere, Ti is also substituted with Cr to some extent and 10% Ti diffusion was estimated. However, Ti segregation is comparable around 10% regardless the moist/dry atmosphere when chromium is not present in the mixture. Therefore, although discrete titanium segregation is observed as a general rule, in a Cr-containing humidified conditions, Ti substitution and segregation from the LST perovskite are favoured. Segregated titanium incorporates in the neighbouring YSZ fluorite and characteristic features already identified in section 4.3.2 are once more detected (microstructure is coarse and denser, Ti-YSZ sinters and Ni wettability and agglomeration increases). In contrast, under dry atmosphere, even if Ti diffusion occurs to some extent, it is not reflected in a significant densification. In fact, in dry atmosphere, denser sample is obtained in the absence of LST. This suggests titanium diffusion becomes critical for the microstructure above a certain concentration in the YSZ fluorite. Thus, little Ti diffusion is not necessarily alarming but water vapor activates massive titanium diffusion which may affect the anode microstructure as it is the case here for FeCr+LST+Ni-YSZ pellet sintered under reducing atmosphere. In a real situation, fuel side components disposition is sequential (FeCr/LST/Ni-YSZ) but FeCr and LST weight is much higher. Hence, G2 cells might be susceptible to even little water contents in the sintering atmosphere.

We conclude, therefore, that titanium massive diffusion is related to the humidification during co-sintering. Titanium segregation mainly occurs due to Cr substitution in the B-site of the LST perovskite. In fact, in the previous section it was observed that in the *titanium active* regions of manufactured cells, protective chromia scale was missing over the surface of FeCr substrate and chromium was identified in the barrier layer. Chromium evaporates preferentially from the chromia scale [124]. Moreover, chromium vaporization is higher in moist air than in dry air [123]. At the high co-sintering temperature, little moisture effect in chromium vaporization is most probably critical as oxygen partial pressure is very low (10^{-22} - 10^{-24} bar). This chromium replaces titanium in the perovskite. Segregated titanium is afterwards incorporated in the YSZ fluorite through the anode and electrolyte. In order to avoid titanium activation, oxygen getters must be removed if standard sintering cycle with gas change at 1100°C is maintained. However, we cannot affirm that titanium massive diffusion and stain formation is completely suppressed with this correcting action. In fact, this should be experimentally proved by the production of a statistically reliable number of G2 cells without oxygen getter and minimizing water vapour during cosintering.

Titanium activation analysis also provided with extra information about fuel side components behaviour. High iron concentrations were detected in the nickel particles regardless the wet/dry sintering atmosphere. When LST was present, iron fraction was especially high with the Fe/Ni ratio in the 10-20% range. Chromium was also

detected in the Ni particles to a lesser extent. Under dry conditions, Cr/Ni ratio in the 2-3% range was found in homogeneously distributed Ni particles. Conversely, when atmosphere was humidified, chromium selective migration was observed. While background nickel particles were Cr free, the Ni clusters showed significant amount of chromium. Cr diffusion to form clusters was also associated to extensive empty spaces where chromia particles regularly formed.

Overall, Ti diffusion into the YSZ produces stain formation. This process is enhanced by the presence of Cr that diffuses from the metal substrate and substitutes Ti in the $\text{La}_{0.7}\text{Sr}_{0.3}\text{TiO}_x$ perovskite barrier layer. This Ti substitution by Cr is furthermore enhanced by the presence of humidity during fabrication. This water vapour may come from gas impurities or can be generated by FeCr oxygen getters reduction during gas change at 1100°C. So far, statistical analysis of cells is required to further corroborate this assumption but the identification of a possible mechanism of stain formation during cell fabrication has been successfully achieved after considering several other alternatives.

4.4 Robustness of second generation cells under operation

4.4.1 Thermal cycles

4.4.1.1 Introduction

Thermal cycling tolerance is a basic prerequisite for SOFC cells especially devised for distributed power generation or auxiliary power units (APU) in transportation applications. Those systems require to be brought into operation rapidly from ambient temperature, preferably in a matter of minutes [156, 267-269]. Hence, in the context of intermittently operating systems, cells must be able to withstand repeated and rapid thermal cycling. However, rapid cycling may cause thermal stress due to temperature gradients and TEC mismatch between adjacent materials.

Metal-supported cells with substrates usually made from stainless steels are much more robust than the ceramic of electrolyte-supported cells or the cermet of anode-supported cells [156]. Furthermore, their thermal conductivity minimizes thermal gradients. Despite the effort to tailor materials properties, ceramics are still thermal shock susceptible. For instance, Rolls Royce Fuel System proprietary IP-SOFC [270], including ceramic-based tubes, shows mechanical failure after 5 thermal cycles [271]. Also for widely adopted anode-supported SOFCs, the porous Ni-YSZ cermet substrate and the thin YSZ film offer relatively low mechanical strength [185].

Tubular design is advantageous for transient operation because it can be sealed more easily and lower stress result from thermal cycles [272]. Rapid thermal cycling for LBNL tubular MS-SOFC, with infiltrated Ni anode as described elsewhere [20, 188], has been demonstrated. First, a braze-sealed cell was subjected to over 30 extremely rapid thermal cycles ($300\text{-}500^\circ\text{C min}^{-1}$) without OCV loss. In contrast, an anode-supported cell subjected to similar thermal cycling exhibited structural failure after only one cycle. In a posterior work, $\approx 100\text{ mWcm}^{-2}$ performance drop after 5 thermal cycles was attributed to fine nickel coarsening and not to thermal cycling [186]. First generation tubular MS-SOFC developed at IK4-Ikerlan have demonstrated excellent thermal shock tolerance. G1 cell was stable at 800°C for at least 2000h under 524 thermal cycles at 10°Cmin^{-1} heating/cooling rates [105, 139]. As far as it is known, this is the most emphatic result reported up till now in the MSC field.

Prospective for second generation cells is hopeful since perovskite-based LST diffusion barrier layer offers better TEC compatibility with adjacent FeCr substrate and anode materials (Table IV - 5). In this section, the first long-lasting proof with second generation cell under thermal cycling is presented.

4.4.1.2 Experimental procedure

G2 cell 222.FP.6.2, tested under thermal cycling, included a standard configuration with a FeCr/LST-F1/Ni-YSZ (20%vol.sol.)/8YSZ half-cell which was co-sintered at 1350°C in reducing atmosphere (10%H₂ + Ar). A specific metal housing made of Crofer 22 APU was used in the experiment (Figure IV - 68). Two alumina tubes were introduced inside the metal housing. The first served to supply fuel to the cell (blue tube) and the second (green tube) contained two nickel wires for current collection. Conventional four-point measurement with Ni mesh+2Ni wires in the anode and Pt mesh+Pt wires in the cathode side respectively, was used. The cell support was brazed to the metal housing and metal tube served for reference voltage measurement. In the text which follows M-T refers to V(-) measure from the metal housing tube and M-W to V(-) measure from nickel wire, as illustrated in Figure IV - 68. Conventional Ceramabond 516 (7.4 ppmK⁻¹) sealing was substituted here by G018-311 (9.8 ppmK⁻¹), a glass-ceramic sealant which is more resistant to thermal shock and compatible with cell materials.

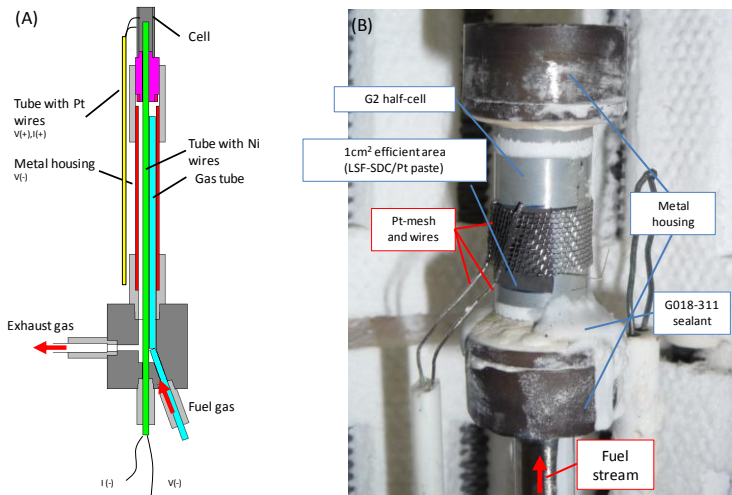


Figure IV - 68. Experimental set-up for thermal cycling: (A) Metal housing design and (B) cell assembly illustration.

Glass-ceramic sealant G018-311 curing was carried out following data sheet specifications; holding times at 450°C (30 min), 850°C (30min) and 810°C (90min) and heating rate of 2°Cmin⁻¹ were used. Thermal cycling was carried out by rising and lowering the temperature through the use of 10°Cmin⁻¹ heating/cooling ramp. Cycling was controlled directly by the furnace program and the high 10°Cmin⁻¹

heating rate permitted to reach the operation temperature at 800°C in merely 1h 20 min. The holding time was 30 min at 800°C and 4h at 0°C cooling stage. One thermal cycle was completed every 7 h 8 min (Figure IV - 69).

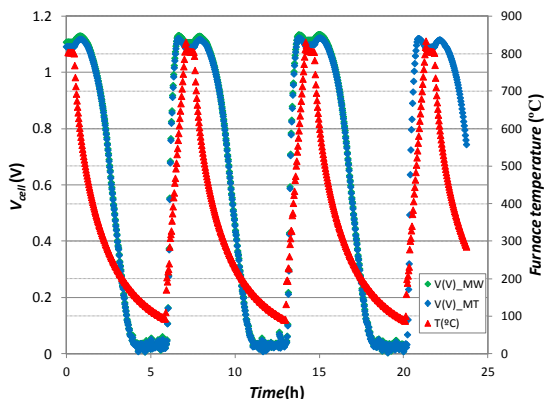


Figure IV - 69. Illustration of the thermal cycling.

4.1.2.2 Analysis of results

G2 cell was stable under rapid thermal cycling during more than 3900 h. 550 thermal cycles were successfully completed with minor OCV loss. In Figure IV - 70, OCV evolution is represented together with temperature upon thermal cycling. Maximal OCV is stable with the exception of two regions where it increases due to water consumption of the bubbler. According to Nernst equation (Eq. 1.4), OCV is higher in dry hydrogen ambient. OCV was recovered by water introduction in the bubbler. During operation, IV-curves and impedance measurements were frequently performed.

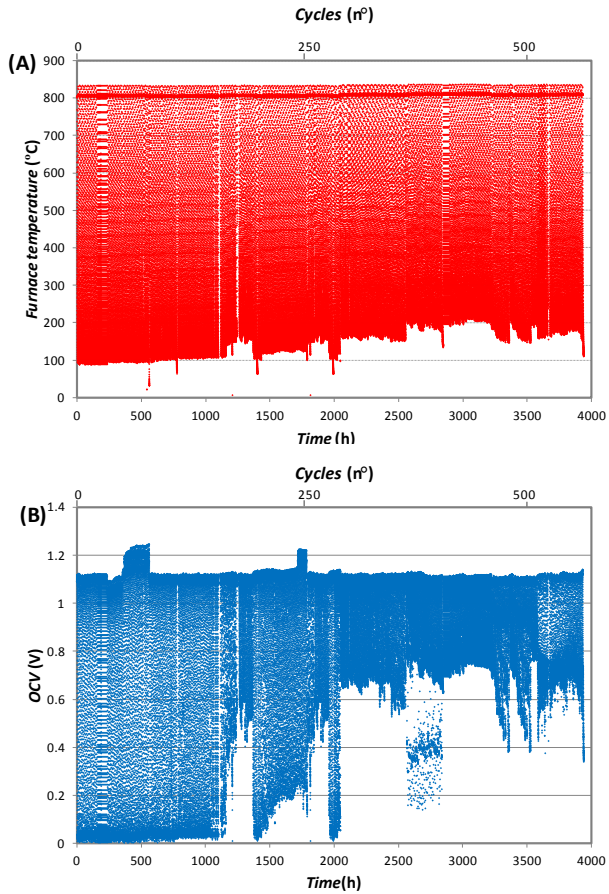


Figure IV - 70. OCV evolution in 550 thermal cycles. (A) Furnace temperature and (B) OCV as measured from the housing metal-tube (M-T) is presented here.

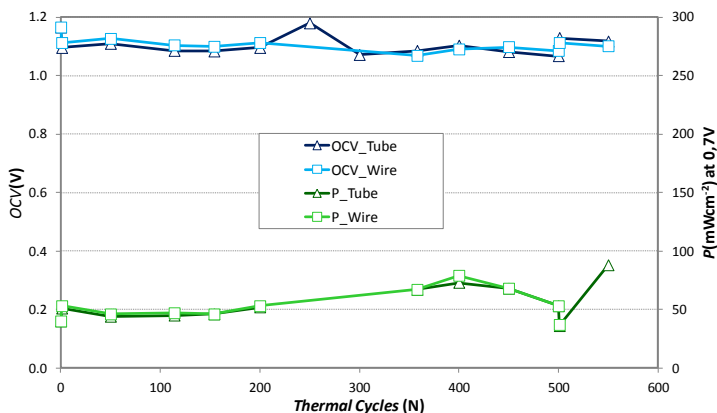


Figure IV - 71. OCV and power density at 800°C as a function of thermal cycles. OCV and measurement from the tube (M-T) or wire (M-W).

Little OCV drop observed from 1.165V to 1.095V during the first thermal cycling is presumably related to sealing and little leakage accommodation. OCV evolution was very stable and after 500 cycles it was still as high as 1.076V. At this point, cell surface appearance was optimal and little OCV loss was attributed to sealing quality degradation. New sealing was applied after 500 thermal cycles and OCV was again optimal around 1.129V (M-W) and 1.112V (M-T) after curing.

Regarding the electrochemical performance, initial power density around 40 mW/cm² is very low as compared to conventional G2 cells but it improves up to 400 thermal cycles giving 76 mW/cm². From here on, power density gradually decreased and after curing at 500 cycles it was comparable to initial performance (37 mW/cm²). However, after 550 thermal cycles best result with 88 mW/cm² was recorded (Figure IV - 71). IV-curves for indicated points in Figure IV - 71 are shown in Figure IV - 72 .

Power density improvement was a consequence of both ohmic and polarization resistance reduction. At 0.7V, $(R_o)_{0tc} = 0.9 \Omega\text{cm}^2$ and $(R_p)_{0tc} = 3.47 \Omega\text{cm}^2$ before thermal cycling reduced to $(R_o)_{550} = 0.41 \Omega\text{cm}^2$ $(R_p)_{550tc} = 1.54 \Omega\text{cm}^2$ after 550 thermal cycles.

Currently, experiment is still ongoing and post-mortem analysis will be done when finalized.

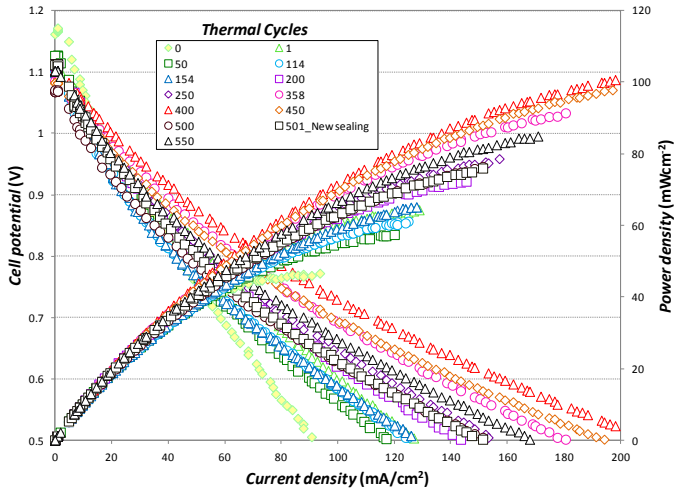


Figure IV - 72. V-I curves and power density at 800°C as a function of the thermal cycles.

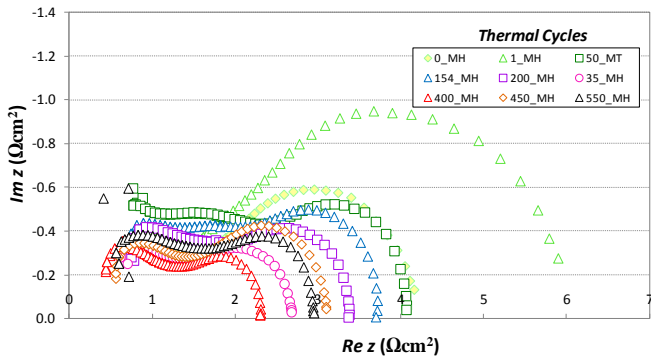


Figure IV - 73. EIS measurements at 800°C and 0.7 V as a function of the thermal cycles.

4.4.1.3 Overall discussion and conclusions

G2 cells robustness under thermal cycling was demonstrated during at least 3900h when the cell was subjected to 550 rapid thermal cycles with 10°Cmin⁻¹

heating/cooling rates among ambient and 800°C operation temperature. Little OCV loss (30mV) after 500 thermal cycles was attributed to the sealing quality degradation and after re-sealing and curing, optimal OCV above 1.12V was recorded at 800°C. This long-lasting experiment demonstrates the excellent mechanical robustness of G2 cells upon thermal cycling. Furthermore, as far as it is known by the author, it contributes with most severe thermal cycling data (550 cycles) ever reported in SOFC's.

4.4.2 Redox tolerance

4.4.2.1 Introduction

In conventional SOFC application conditions, occasional system shut down is unavoidable and RedOx tolerance of the anode is a basic prerequisite for SOFC commercialization. When gas fed is interrupted, system shut down implies that the cell will undergo a complete or partial RedOx cycle. That is, anode oxidation due to air flow during the shutdown by constant air transfer in the electrolyte or leakage in the sealing is followed by the reduction due to system restart and a shut down is traduced in a RedOx cycle. In particular, combined heat and power (CHP) systems demand cells able to survive to a significant number (>5/year) of RedOx cycles without significant degradation [273].

Unfortunately, conventional Ni-YSZ and Ni-GDC cermet anodes are susceptible to Redox cycles due to dimensional instability during oxidation. Nickel suffers an immense expansion (69.9% in solid volume) when it is oxidized [23]. Accordingly, the composite anode expands in dimensions. When NiO is reduced back to metallic Ni, however, the initial state is rarely recovered (i.e. irreversible oxidation). Those dimensional changes generate internal stresses in the anode and stresses in adjacent constituents of the cell. In anode supported cells, cracking through the cathode and/or electrolyte and/or delamination at the anode/electrolyte interface are the main failure modes described in the literature [273-275]. For a given electrolyte thickness, it will crack if the oxidation strain is greater than a critical value. Resulting fuel leak and OCV loss is inadmissible and two approaches can be adopted to overcome this difficulty: system engineering or material development. The former involves extra cost and system complexity and it is not attractive for small applications. The latter is addressed either by alternative materials investigation or by subtle microstructural modifications in the currently used Ni-YSZ cermet. Indeed, stresses at the anode-electrolyte are partially alleviated by modification of the microstructure and distribution of the Ni and YSZ phases within the cermet [103, 273, 276].

Regarding SOFC design, evidences of the superior stability of MSC have been presented by several authors [138] [186]. In contrast, RedOx cycles become critical for anode-supported cells, as the anode works not only as an electrochemically

functional component but also as the mechanical support of the cell. Furthermore, microtubular geometry presents an inferior resistance towards redox cycles as oxidation kinetics are relatively fast due to the small anode thickness in a diffusion limited regime [277]. Nevertheless, even if lower, performance degradation in MSC was unavoidable to date.

In this section, second generation cells tolerance to redox cycles is analyzed. Moreover, implications in the redox behavior of G2 cells which arise due to titanium diffusion during co-sintering are also discussed. In section 4.3.2, stains correlation with titanium diffusion and incorporation into the YSZ fluorite was identified. Ti doping enhances the sinterability of the YSZ particles and forms a solid Ti-YSZ framework in the anode [256]. Furthermore, it improves nickel wetability [265]. Even if Ni-Ti-YSZ provides a coarser microstructure, there is no reason to believe that it cannot be mechanically more resistant to redox cycles, on the contrary; a more solid Ti-YSZ framework may withstand more easily local stresses caused by nickel particles re-oxidation. However, massively agglomerated Ni may suffer oversized growth upon oxidation. Thus, in this part, the redox tolerance of a standard G2 cell is compared to its *titanium active* counterpart.

4.1.2.3 Experimental procedure

Two standard FeCr(<45 μ m)/LST-F1/Ni-YSZ(%20vol.sol.)/8YSZ cells sintered at 1350°C during 4 hours were used to study G2 cells redox tolerance. LSF-SDC composite cathode was dip-coated in 1cm high cell stripes leading to \approx 3.8cm² efficient areas and Pt paste was painted prior to *in-situ* sintering at 950°C. As Figure IV - 74 illustrates, cell 221.FP.4.2 exhibited a plain surface after sintering whilst cell 221.FP.4.1 was covered with stains in the upper part. In the latter, efficient area was deposited in a stain free area to overcome excessive densification of the anode. However, some spots were still present. Samples were systematically prepared and labelled using procedure described in section 4.1.2.2.

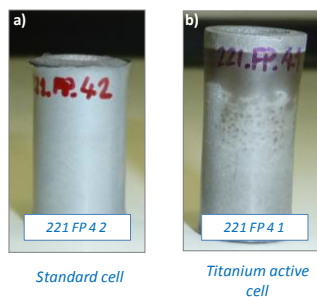


Figure IV - 74. Electrolyte surface of a) standard 221.FP.4.2 and b) *titanium active* 221.FP.4.1 after co-sintering under identical standard conditions.

4.4.2.2 Analysis of results

Voltage evolution during operation is shown in Figure IV - 75 for both tested cells. Steady-state operation tests were performed at 800°C with moderate 200 mA/cm² current load and low fuel utilization (3% H₂) to guarantee stable performance. Current load was removed during redox cycling. IV-curves in Figure IV - 76 and electrochemical characterization in Table IV - 18 correspond to the enumerated points in the voltage evolution diagram (Figure IV - 75).

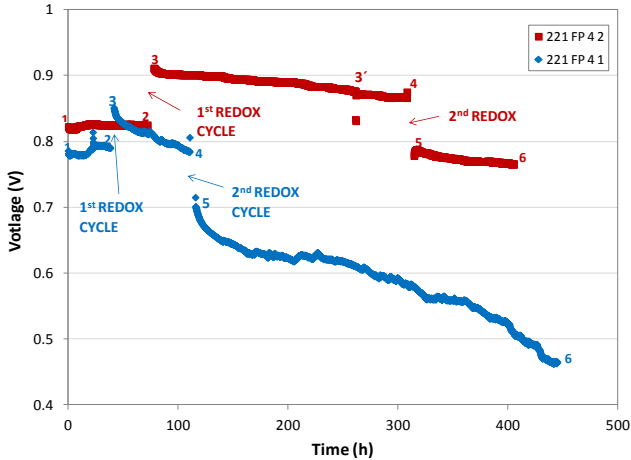


Figure IV - 75. Redox cycle analysis under steady operation at 800°C and 200mA/cm² (3% humidified 200 ml min⁻¹ H₂ in the anode and atmospheric air in the cathode).

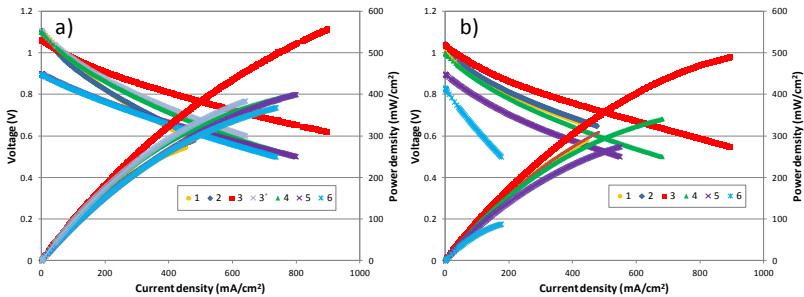


Figure IV - 76. IV curves for a) standard cell 221.FP.4.2 and b) titanium active 221.FP.4.1, corresponding to points in Figure IV - 75.

Table IV - 18. Electrochemical characterization during operation. (Point column corresponds to operation point in Figure IV - 75. Power density and resistances correspond to IV-curve and EIS measurements at realistic operation voltage, 0.7V).

Cell #	Point*	t(h)	OCV(V)	P(mW/cm ²)	R _o (Ωcm ²)	R _p (Ωcm ²)	ASR(Ωcm ²)
222 FP 4 2	1	0	1.105	229	0.55	0.37	0.93
	2	72	1.105	241	0.49	0.37	0.85
	3	72+Redox1	1.06	463	0.21	0.19	0.4
	4	261	1.091	318	0.32	0.32	0.64
	5	307	1.1	294	0.37	0.34	0.71
	6	307+Redox2	0.89	224	0.32	0.32	0.64
	7	405	0.89	220	0.27	0.29	0.56
222 FP 4 1	1	0	1.005	250	0.18	0.45	0.63
	2	37	1.034	265	0.18	0.48	0.66
	3	37+Redox1	1.025	370	0.16	0.33	0.49
	4	110	0.986	219	0.24	1.37	1.61
	5	110+Redox2	0.89	143	0.23	0.48	0.71
	6	445	0.81	43	0.44	1.65	2.1

Standard cell (221.FP.4.2)

First experiment was carried out with the standard cell 221.FP.4.2, which exhibited optimal initial OCV (1.105V) and performance (229 mW/cm²). During the first 70h of operation, performance was stable with small activation (≈ 10 mW/cm²) due to ohmic resistance improvement (Table IV - 18). Cell 221.FP.4.2, was first oxidized in contact with ambient air during 20 minutes and subsequently reduced during 1h in H₂ (3% H₂O). Fuel side was maintained in argon during 30 min in the transitory step between reduction/oxidation and vice versa for safety considerations. After the first redox cycle, an increase of 213mW/cm² was registered. As a matter of fact, the best result with second generation cells up till now, with 463 mW/cm² at 800°C, was recorded. First redox cycle was traduced in an extensive reduction of both R_o and R_p. Nevertheless, it was accompanied by a significant OCV loss (46 mV), even if resultant 1.06V was still acceptable for operation (for operation OCV is considered low under 1.02V). Far above the ground electrochemical efficiency after first redox cycle was not stable and slight degradation commenced when 0.2 A/cm² current load was restored. EIS measurements demonstrated that R_o and R_p gradually increase in this region (point 3, 3', 4 in Table IV - 18). Performance degradation during further 230 h of operation was accompanied by OCV restoration. In point 4, as IV-curve in Figure IV - 76 demonstrates, optimal 1.1 V was attained and cell performance was still about 50 mW/cm² higher than before the redox cycle (point 1 and 2); R_p was roughly the same but R_o was ≈ 0.1 Ω cm² lower (Table IV - 18).

Performance evolution upon redox cycles can be interpreted in the following way. During the first redox cycle, dimensional changes induced in the anode during Ni to NiO oxidation stress the electrolyte and micro-cracks are propagated in the transversal direction. Accordingly, gas leakage through the electrolyte generates the observed OCV loss. When reducing atmosphere is recovered, anode shrinkages and stress in the electrolyte is relaxed permitting those micro-cracks to seal and recover the initial OCV after a certain time. When there is gas leakage and OCV loss, direct combustion of hydrogen makes local temperature higher and therefore higher activity is expected. However, the surprisingly high power density observed cannot be explained by simple combustion of hydrogen. Thus, microstructural refinement in the anode during the redox cycle is most probably in the origin of such electrochemical efficiency improvement. Subsequent performance degradation during ≈ 200 h is in one side attributed to electrolyte sealing and local temperature reduction. However, nickel sintering in reducing atmosphere leads most probably to TPB length reduction in the anode. When gas tight electrolyte is recovered, however, electrochemical performance is still ≈ 50 mW/cm² better than in point 2, before the redox cycle. This demonstrates that microstructural modifications upon the redox cycle improve the electrochemistry in the anode. Lower $R_o \approx 0.2$ Ω cm² observed in point 4 might be related to enhanced Ni percolation.

During the second redox cycle, compressed air (53 mlmin⁻¹cm² air) was introduced in the fuel side during 20 min instead of the atmospheric air. During this time, cell underwent a full re-oxidation and OCV rapidly fell to zero (Figure IV - 77). Once that second redox cycle was completed, OCV fell to 0.89V. This OCV is unacceptable in the SOFC operation threshold. Further operation at 0.2 A/cm² demonstrated that OCV loss due to the second redox cycle was irreversible. In this region, degradation rates were similar to the previous region (0.04 mWcm⁻²h⁻¹).

Titanium active cell (221.FP.4.1)

In the second experiment with the *titanium active* cell (221.FP.4.1), softer redox conditions were adopted but operation conditions were maintained. The scope was to improve cell performance without unchaining the irreversible degradation of the cell during redox cycles (i.e. cracking of the electrolyte, electrolyte/anode interface delamination). With this aim, anode was re-oxidized in argon during 30 min and it was reduced in %10 H₂+Ar during 1 h prior to electrochemical characterization (Figure IV - 77).

Titanium active cell, exhibited excellent initial efficiency (250 mW/cm²) thanks to a very low R_o , which is attributed to the unusually thin electrolyte as it will be seen in the microstructural analysis. OCV (1 - 1.03 V) was low as expected for *titanium active* cells (Figure IV - 76). Nevertheless, it demonstrated to be less resistant to redox cycles than the standard 221.FP.4.2 cell. After the first redox cycle, cell performance improved ≈ 110 mW/cm². Both R_o and R_p were lower and OCV was

reduced 9 mV. Trend was similar to that observed with the standard cell 221.FP.4.2. When current load was restored, however, cell exhibited significant degradation rates ($0.17 \text{ mWcm}^{-2}\text{h}^{-1}$) and additional OCV loss which lead to inadmissible 0.98 V after 110 h operation. At this point cell degradation was permanent but after a second redox cycle, huge OCV dropped to 0.89 V and performance to 143 mWcm^{-2} . Further operation was detrimental and after 445 h of operation, in point 6, power density was as low as 43 mWcm^{-2} (Figure IV - 76, Table IV - 18).

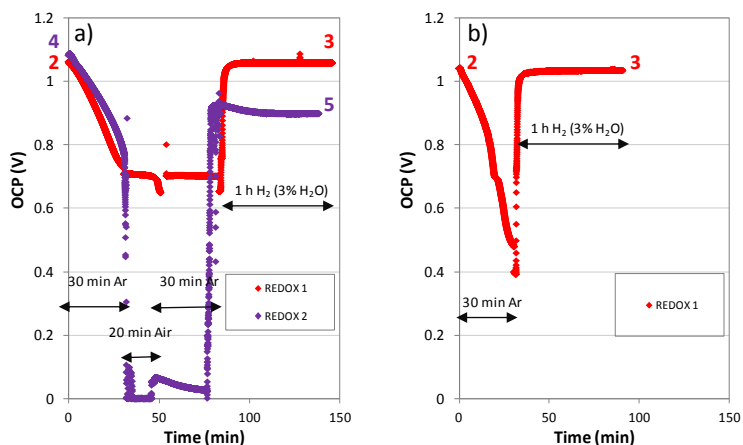


Figure IV - 77. OCV evolution during the redox cycles for a) 221.FP.4.2 and b) 221.FP.4.1 cells. (Enumeration corresponds to the evolution in Figure IV - 75).

Microstructural characterization

Post-mortem inspection revealed extensive crack proliferation over the surface of 221.FP.4.2 standard cell, as shown in Figure IV - 78. In contrast, for titanium active cell (221.FP.4.1), plain electrolyte was in one piece whereas *titanium active* dark zone at the top suffered the catastrophic oxidation of the metal-support. In Figure IV - 79, SEM analysis illustrates the characteristic electrolyte cracking for cell 221.FP.4.2. Cracks which form in the anode/electrolyte interface, propagate perpendicularly through the electrolyte and cathode and it is evenly distributed all through the electrolyte surface. On the other hand, in the plain zone of *titanium active* cell (221.FP.4.1) no micro-crack proliferation was detected but the anode/electrolyte interface delamination was broadly extended (Figure IV - 80a). Note that electrolyte ($4 \mu\text{m}$) is especially thin.

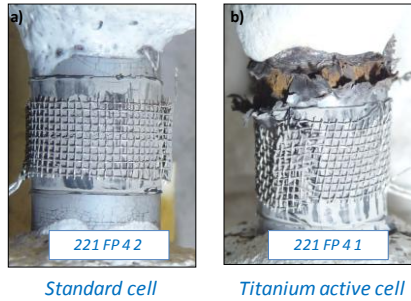


Figure IV - 78. Post-mortem appearance of a) standard 221.FP.4.2 and b) *titanium active* 221.FP.4.1 cells.

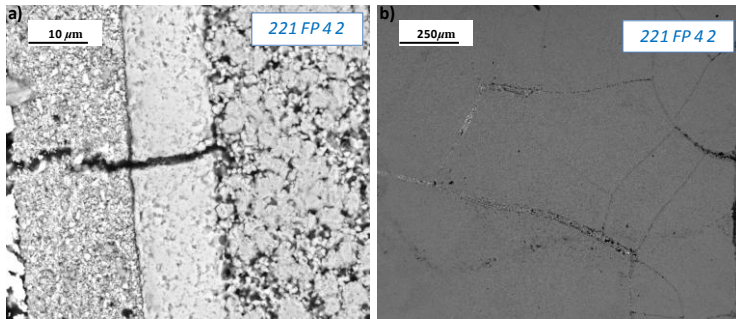


Figure IV - 79. Degradation mechanism under redox cycles for the standard cell 221.FP.4.2: crack proliferation in the electrolyte as illustrated by SEM images in the a) cross-section and b) electrolyte surface.

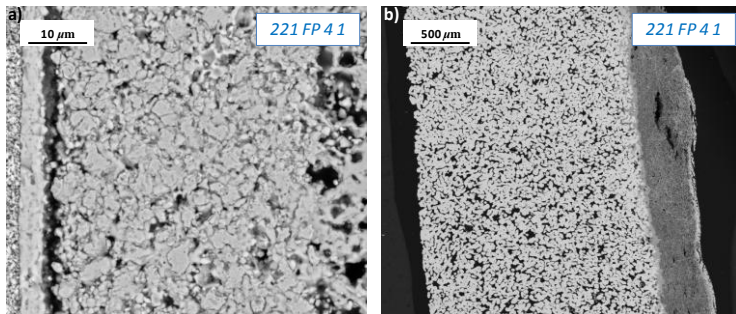


Figure IV - 80. Degradation mechanisms under redox cycles for the *titanium active* cell 221.FP.4.1: a) electrolyte delamination and b) oxidation of the metal-support.

4.4.2.3 Overall discussion and conclusions

Ni-YSZ refinement via redox cycle

Electrochemical improvement upon redox cycles in MSCs has already been reported by Blennow et al. [138]. In the cited work, performance improvement upon redox cycles (1 min redox cycle) was moderate and no interest was addressed to explain the mechanism under this effect. In this work, however, after the first redox cycle, power density was about 200 and 100 mW/cm² higher for standard and *titanium active* cells, respectively, compared to the initial performance. We promptly hypothesized that this could be related to modifications in the Ni-YSZ cermet microstructure during the redox cycle, as we know that the electrochemical performance of our cells is highly susceptible to microstructural changes in the anode. Revision of an early experiment with cell 202.FP.14.1, which was accidentally left without flux during 10 h, demonstrated our premises. For this cell, power density increased from 110mW/cm² to 230 mW/cm² during the accidental redox cycle but OCV was 0.89 V after reduction. In Figure IV - 81, anode microstructure after the redox cycle is compared with that for a standard cell after co-sintering. In cell 202.FP.4.1, fine Ni-YSZ microstructure is observed after the first redox cycle in comparison to the typical anode microstructure with agglomerated nickel already after co-sintering. Thus, we conclude that Ni-YSZ microstructure refinement during the first redox cycle is reflected in a power density improvement. Current collection improves due to a better percolated nickel matrix and R_o is reduced. In addition, TPB length extends in the anode and this is reflected in lower R_p .

Therefore, nickel agglomeration due to co-sintering at high temperatures and reducing atmosphere can be partially diminished by tailored nickel reoxidation. If nickel reoxidation kinetics were controlled in such a way to suppress mechanical damage (i.e. crack proliferation in the electrolyte), we could design a protocol with a sequence of rapid redox cycles to fine tune Ni-YSZ microstructure. As a result, more performing cells with improved tolerance to full redox cycles would probably be achieved.

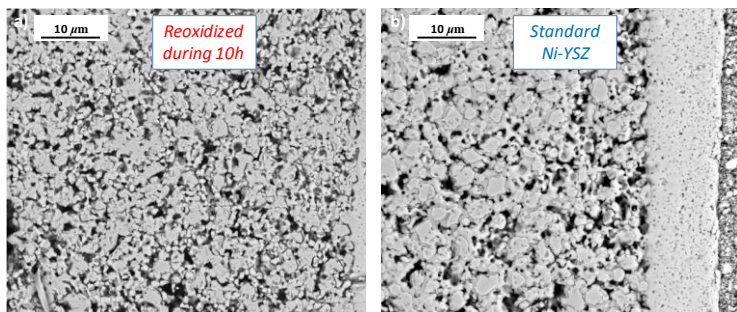


Figure IV - 81. Ni-YSZ microstructure for a) a standard cell (202.FP.14.1) oxidized during 10 h and b) standard cell (220.FP.4.1) after co-sintering. (First photograph reproduced with the permission of Laida Otaegui)

Conventional degradation mechanisms

Tensile stress exerted in the electrolyte as a result of dimensional changes in the anode was manifested in different ways in the two types of cells tested under redox cycling conditions. In the standard cell (221.FP.4.2), stored elastic energy during redox was released by electrolyte cracking, whereas anode/electrolyte interface delamination was observed for the *titanium active* cell (221.FP.4.1). There are two possible explanations for the different degradation mechanism observed in both cells. Firstly, dissimilar redox cycling conditions were used. Secondly, electrolyte is much thinner ($\approx 4 \mu\text{m}$) for *titanium active* cell. The criterion for cracking (i.e. channel cracking) for a single layer on a thick substrate states that, for a given anode oxidation strain, the electrolyte will crack if it is thicker than a critical thickness, h_c [278]. Given that electrolyte is 3 times thinner for *titanium active* cell, it is reasonable to think that as the electrolyte is mechanically more resistant, criterion of cracking is not satisfied in this situation. Thus, as it demands less energy, delamination in the electrolyte/anode interface is favoured. Of these degradation mechanisms, however, the most significant for the cell is electrolyte cracking, since through-crack results in air leaking to the fuel side. Thin electrolytes, however, are difficult to manufacture systematically under high yield for this technology. It is difficult, in practise, to reproduce thin electrolytes without surface defects (i.e. gas leakage).

Susceptibility of titanium active cells

Highest degradation rate for *titanium active* cell (221.FP.4.1) was attributed to the rapid oxidation of the metal-support in the stained zone (Figure IV - 80). In section 4.3.3, detailed analysis in stained cells and titanium diffusion issues demonstrated that it is related to massive chromium diffusion. Metal-support

becomes vulnerable to corrosion as the protective chromia scale and the Cr content of the alloy decrease.

Ti diffusion is activated due to chromium incorporation to the LST perovskite of the barrier, but chromium and little amounts of iron and manganese also migrate to the anode. This situation is analogue to that observed with G1 cells [102]. However, no traces of nickel were identified in the FeCr substrate of G2 cells up to now. Stained zones exhibit partially bare metal-support. In view of that, poor resistance of *titanium active* zones to fuel utilization is also predicted.

Comparison with other MS-SOFC developments

At first sight, one could conclude that cell failure only after two redox cycles is a negative result. However, when compared to recent advances reported by competitive manufactures in the MSC field, they do not seem to be necessarily that discouraging. Blennow and collaborators [138] at Risoe accounted a MSC which withstands 100 redox cycles without detrimental degradation. Active anode comprised a FeCr-YSZ cermet backbone that was infiltrated with 10 wt. % Ni-GDC20 after sintering. Cell improved during the first redox 50 cycles (1 min redox cycles) and little OCV loss was reported. In the following 50 redox cycles (10 min redox cycles) cell showed a 20% degradation in power density and OCV loss. On the other hand, Tucker et al. [186] at LBNL, presented a MSC concept that does not fail after 5 redox cycles (10-15 min redox cycles). Tubular MSC comprising porous FeCr/porous YSZ/dense YSZ/porous YSZ/ was infiltrated with NiO and LSM perovskite in the anode and cathode side, respectively. Performance loss of 200 mW/cm² after 5 cycles was attributed to Ni coarsening. Note that in both cases, Blennow [138] and Tucker [186] use much softer redox conditions than those reported here.

In close collaboration along with Materials Science Division at Berkeley, an attempt to produce an analogous Ni-infiltrated MSC was performed at IK4-Ikerlan few years ago. However, infiltration did not lead to promising results. Given the extra complexity introduced in cells manufacturing and unsatisfactory preliminary results obtained, infiltration was promptly abandoned in favor of a new DBL development.

Despite the constraints related to manufacturing, nano-scale Ni-infiltration offers many advantages. More performing cells with infiltrated Ni exhibit improved tolerance towards redox conditions. TPB concentration is higher and since nickel does not work as a structural element, mechanical stability is superior. However, infiltrated Ni rapidly agglomerates upon redox cycles or even during steady operation. As Ni agglomerates, the anode becomes progressively more susceptible to redox cycles. Therefore, Ni-infiltration solves only partially the limitations related to redox cycles.

4.4.3 Performance and stability under fuel utilization

4.4.3.1 Introduction

Fuel utilization is one of the most important parameters for fuel cells and has a significant impact on the cell output voltage and system efficiency (section 1.2.3). Even if ferritic stainless steel is the preferred material for metal-supported SOFC, little information is available in the literature about fuel utilization effect on MSC technology. Good results have been reported for cells containing ANSI-430 (Fe17Cr) or SUS-447J (Fe-30Cr-2Mo) (not specified in the article) ferritic stainless steels and ceria-based functional electrolyte and anode [147]. Cell operated at 600°C was stable for at least 1400h in hydrogen with 50% water vapor. However, no degradation values were specified.

Alternative SOFC configurations did not demonstrate better results with high fuel utilization to date. Rolls Royce proprietary integrated planar design, IP-SOFC [270], underwent 1.3 and 1.5% degradation at 900°C with 14% fuel utilization [271]. This configuration consisted of two ceramic-based tubes including YSZ electrolyte and Ni-YSZ anode functional layers. An anode-supported tubular SOFC with conventional Ni-YSZ/YSZ/LSM-YSZ configuration was tested at 70% FU and 800°C but steady operation resulted for very short period of just 50 h [279]. Also the stack developed by Ceres Power operated at rather low 35% fuel utilization on simulated reformat gas with 4.2% loss in performance over 960 hours of operation [150].

The primary scope with tubular metal-supported SOFC developed at IK4-Ikerlan is to reach stability at high 70% fuel utilization. However, this objective is directly correlated to a good performing DBL between the FeCr substrate and Ni-YSZ anode. In the introduction of this chapter (section 4.1.1), a detailed description of tubular MS-SOFC progress was presented. First generation cells with ceria-based DBL did not succeed; fuel utilization stability failed as a result of a deficient DBL which allows element interdiffusion during co-sintering. Thus, operating even at low fuel utilization catastrophic corrosion of the metal-support rapidly occurred (Figure IV - 2). New perovskite-based DBL, LST, was considered as an attractive candidate thanks to its high electronic conductivity and optimal TEC under reducing atmospheres. In fact, already during preliminary testing, a qualitative leap was made and performance was stable during more than 700 h at reasonable high 25-50% fuel utilization conditions (Figure IV - 1).

Research with second generation cells, which adopted this new DBL, has been reported all through this chapter. Processing parameters optimization, susceptibility to titanium diffusion and robustness were studied. However, G2 cells must demonstrate the real long-stability at high fuel utilization. This is the principal challenge that perovskite-based DBL faces prior to its ultimate implementation in the tubular MS-SOFC technology concept definition.

Ellingham diagram

At the fuel side, as increasing hydrogen is electrochemically consumed more water concentration is generated in the atmosphere. Nevertheless, high water production can affect the chemical stability of the fuel side components. Phase stability of elements was studied using an Ellingham diagram [280] that is presented in Figure IV - 82. In the anode side, oxygen partial pressure fluctuates between 10^{-24} – 10^{-26} bar O_2 and typical H_2/H_2O ratios vary from 3 at rather low 25% FU to 0.43 at high 70% FU.

From the Ellingham diagram the following conclusions can be extracted:

- Low pO_2 (10^{-24} – 10^{-26} bar) is sufficient for a stable protective scale to form in the FeCr substrate surface via chromium and manganese oxidation [65].
- Metallic nickel is not oxidized by water. At 800°C , extremely high humidifications, $H_2/H_2O \approx 10^{-2}$ – 10^{-4} , would be necessary to cause nickel oxidation at simple reducing conditions.
- Iron becomes susceptible to corrosion around 50% of H_2O

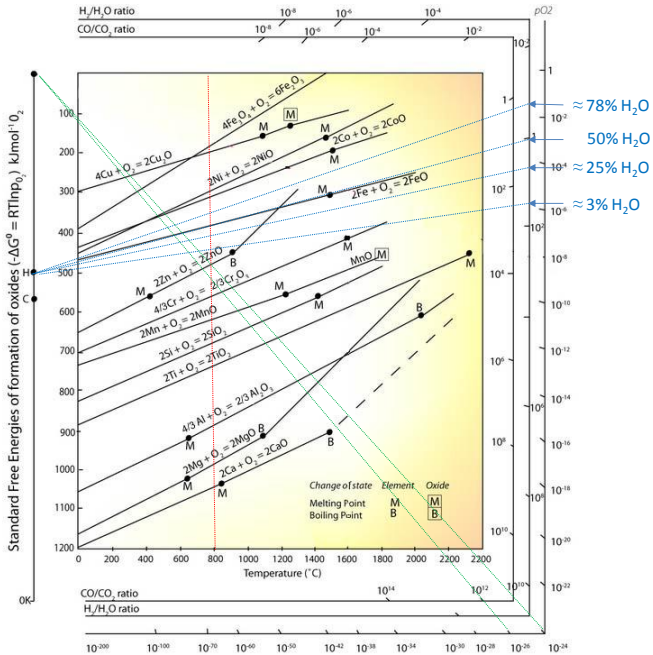


Figure IV - 82. Ellingham diagram [280] for the possible operation conditions in the fuel-side atmosphere using H_2 as fuel and considering several levels of utilization.

Therefore, metal support is vulnerable under high fuel utilization due to the high humidification which prevails in the atmosphere. Even if protective chromia scale forms in the surface of ferritic stainless steel during the co-sintering process, passivation before operation under fuel utilization can be beneficial to further protect the metal support.

4.4.3.2 Experimental procedure

Fuel utilization stability of G2 cells has been analyzed in the totality of eight experiments. Most cells had the standard FeCr (<45 μm)/LST-F1/Ni-YSZ (%20 vol sol)/8YSZ configuration and were sintered at 1350°C in reducing atmosphere as described in section 4.1.2.2. As an exception, cell 207.FP.9.1 comprised a thinner DBL by dip-coating of the most diluted F4 formulation (Figure IV - 23) and cell 222.FP.5.3 was sintered fully under Argon. In addition, cell 222.FP.18.3 and 222.FP.5.3 were passivated prior to the FU experiment by passing 250 mA during 100 h at very low fuel utilization conditions (1% FU). In this period, cells showed little activation and power density improved 26 and 38 mW/cm² for cell 222.FP.18.3 and 222.FP.5.3, respectively.

Every cell exhibited a plain electrolyte except cell 221.FP.8.1, which was partially stained after co-sintering. In order to avoid the titanium active zone, just 1 cm² of efficient area was dip-coated in a stain free zone. At first electrochemical characterization, optimal OCV was recorded for every cell. Main characteristics of cells used in FU experiments are summarized in Table IV - 19. Cells 199.FP.38.2 and 202.FP.14.1, in orange, are those initially tested by Laida Otaegui [102]. (Find detailed information about cells labelling in section 4.1.2.2).

Table IV - 19. Initial characteristics of G2 cells tested in FU experiments. (*) indicates previous passivation at 1% FU by 250 mA current load during 100h at 800°C.

FeCr (μm)	Ts (°C)	Sintering atmosphere	LST-Fx	Cell #	Surface appearance	Efficient area (cm ²)	OCV (V)	P (mW/cm ²)
<45	1350	%10 H ₂ + Ar	F1	199 FP 38 2	Plain	7.45	1.117	108
				202 FP 14 1	Plain	7.46	1.111	111
				213 FP 4 1	Plain	7.46	1.102	217
				213 FP 5 1	Plain	7.46	1.106	211
				221 FP 8 1	Stained	1	1.115	340
			222 FP 18 3*	Plain	3.78	1.107	223	
			F4	207 FP 9 1	Plain	7.64	1.101	174
			F1	222 FP 5 3*	Plain	3.76	1.0925	195

4.4.3.3 Analysis of results

Humidification and temperature effect

The effect of fuel humidification in cell performance was investigated in the 700°C-800°C range with cell 222.FP.18.3. Different water concentrations (25%, 35%, 50% and 78%) were introduced in the fuel stream through a CEM. IV curves are represented in Figure IV - 83 as a function of water content and temperature.

Nernst equation relates temperature and reactant/product concentrations to the OCV (Eq. 1.4). Temperature has a negative effect in the OCV and it decreases as temperature increases from 700°C to 800°C. However, significant influence of temperature is not discernible here in the OCV (Figure IV - 83). When dry fuel is used, OCVs above 1.2 V are recorded. Those values are theoretically forbidden and are attributed to the CEM measuring system, which introduces an experimental error due to internal currents in the mA range.

According to Nernst equation (Eq. 1.4), fuel humidification has also a negative influence in the OCV. This is observed in Figure IV - 83 regardless the temperature as fuel humidification increases from 0% to 78%.

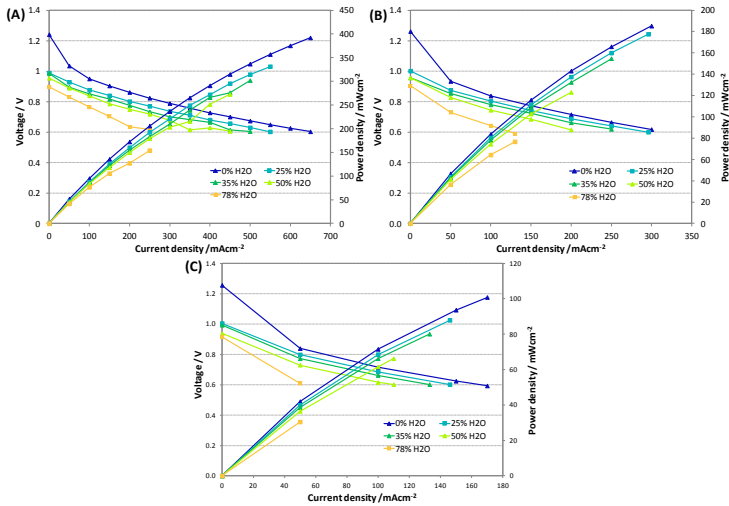


Figure IV - 83. Effect of water concentration on the performance of cell 222.FP.18.3 at different temperatures: (A) 800°C, (B) 750°C and (C) 700°C.

The effect of temperature and fuel humidification (*simulated* fuel utilization) in performance is more visible in Figure IV - 84A, where characteristic power density at 0.7 V is represented as a function of both parameters. An increase in water concentration from 0% to 78% H₂O results in a performance decrease of

approximately 65% at 800°C. However, when temperature decreases from 800°C to 700°C, performance decreases 75%. At 800°C, performance is also compared with a G1 cell. Even if G2 cell is more performing in dry atmosphere, G1 and G2 cells follow a similar trend as fuel is humidified above 35% H₂O.

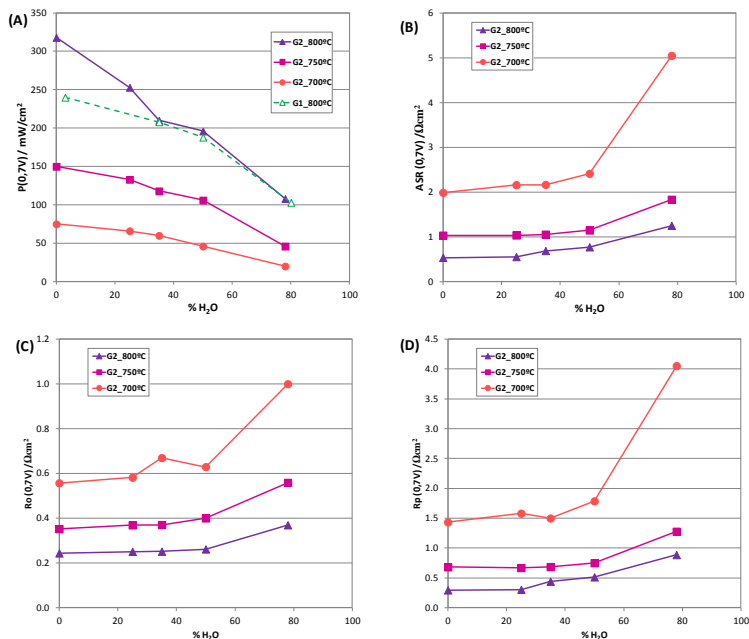


Figure IV - 84. Effect of temperature and fuel humidification in (A) power density, p , (B) area specific resistance, ASR, (C) ohmic resistance, R_o , and (D) polarization resistance, R_p , at realistic operation conditions at 0.7V.

ASR and R_o in Figure IV - 84B,C are measured from the slope of the IV-curves linear region (Figure IV - 83) and EIS at 0.7V, respectively. R_p in Figure IV - 84D is calculated by ASR- R_o subtraction as a simple estimation of R_p with EIS is difficult due to fluctuations that high water levels produce at low frequencies.

The increase in water concentration from 0% to 78% H₂O results in a R_o and R_p increase of approximately 54% and 200% at 800°C, respectively. On the other hand, when temperature decreases from 800°C to 700°C, R_o and R_p increase 133% and 393%, respectively. The influence of both parameters is huge in the final performance but temperature is more significant. In addition, performance degradation is mainly connected to polarization losses, which become highly activated at low temperature and high water vapour, above 50%.

Steady operation fuel utilization experiments

In this section, fuel utilization experiments have been performed in two ways. In one side, *real* fuel utilization experiments were accomplished by lowering the hydrogen flow from 200 to 30 mlmin⁻¹cm⁻². Nevertheless, the stoichiometric H₂ flux required to run cells with moderate performances is much lower than the experimental capacities in the laboratory; G2 cells require just 1-3 mlmin⁻¹cm⁻² to reach power densities between 100-300 mW/cm². Our mass flow controller works with accuracy in the range between 30-300 ml and thus it is not possible to control high fuel utilizations with this instrument. The alternative option is to *simulate* high fuel utilization conditions by introducing hydrogen with high water vapour contents in the anode side. This is attained via a CEM, from which gas mixture is delivered at temperatures around 100°C at the gas entrance to avoid water condensation (section 2.1.3). In both *real* and *simulated* FU experiments, cells were operated at 800°C and 0.7V.

FU experiments with G2 cells are summarized in Table IV - 20, with the corresponding operation conditions and degradation rates. The FU approach, whether by *real* or *simulated* (CEM) operation is expressly indicated for each experiment. Performance evolution/degradation is expressed in %Vkh⁻¹, the relative voltage evolution in 1000 h.

Table IV - 20. Fuel utilization conditions and degradation rates for G2 cells tested using real and simulated (CEM) fuel utilization.

Cell #	FU	Φ _{H₂} (ml/min)	J (mA/cm ²)	%H ₂ /%H ₂ O (i)	Real FU (%)	%H ₂ O (out)	Δt	%Kh ⁻¹
199 FP 38 2	Real	45	181	97/3	21	23	650	-3.8
	CEM	600	115	50/50	1	51	100	-8.2
202 FP 14 1	CEM	600	137	50/50	1	51	912	-3.5
213 FP 4 1	Real	30	270	97/3	47	48	620	-9.9
213 FP 5 1	Real	30	250	97/3	43	45	620	-21.9
221 FP 8 1	Real	15	460	97/3	21	24	69	-62.3
		15	300	97/3	14	17	96	-12.6
222 FP 18 3	CEM	600	250	50/50	1	51	1000	-1.0
							1161	-11.6
207 FP 9 1	Real	30	195	97/3	35	37	1000	-8.5
							1510	-14.1
222 FP 5 3	CEM	600	182	50/50	1	51	313	-11.7

Note that cell 199.FP.38.2, which was tested by Laida Otaegui [102] in the starting point, used both methods. During the first 650 h, cell was operated at *real* 21% fuel utilization leading to 3.8% kh⁻¹ voltage degradation. Then, fuel gas was introduced with a CEM and it was operated under *simulated* 50% FU by passing 600 ml H₂ and 29 ml H₂O giving 50%H₂/50%H₂O ratio. During this period, the

degradation rate increased to $8.2\% \text{ Kh}^{-1}$, presumably due to the higher water concentration in the fuel atmosphere. For cell 202.FP.14.1, also tested by Laida Otaegui [102], stability was superior during 912 h at similar *simulated* %50 FU and converted degradation was $3.5\% \text{ Kh}^{-1}$. This result was considered a very good starting point of the following experiments performed within this work.

Three cells with plain surface (i.e. 213.FP.4.1 and 213.FP.5.1 and 207.FP.9.1) were tested under *real* fuel utilization conditions in the 35%-47% FU range (Figure IV - 85). Two experiments exhibited high degradation rates (9.9% and $21.9\% \text{ kh}^{-1}$) in 620 h long tests. One of those cells underwent a rapid deterioration after 400 h of operation (213.FP.5.1). A third cell (207.FP.9.1) reached 1500 h of operation. During the first 1000 h cell voltage decreased 8.5% under 35% FU. For G1 and G2 cells, this is the first true degradation value in 1000 h under fuel utilization. However, degradation augmented to $14\% \text{ Kh}^{-1}$ after 1500 h of operation.

Other two cells with plain surface were operated at *simulated* 50% FU in the CEM. Those cells correspond to the previously passivated ones (222.FP.18.3 and 222.FP.5.3). The cell sintered in argon (222.FP.5.3) exhibited rapid deterioration ($>10\% \text{ kh}^{-1}$). After 300 h of operation experiment was concluded due to an abrupt gas leakage that irremediably oxidized the cell. In contrast, cell 222.FP.18.3, sintered in the standard reducing atmosphere, exhibited excellent stability and voltage degraded just 1.0% during the first 1000 h of operation under 50% *simulated* FU. However, this cell suffered a rapid degradation after reaching 1100 h of operation.

Stained cell suffered out of range $62\% \text{ Kh}^{-1}$ degradation rate. It was very unstable already with moderate 21% FU during 69h. In a second part of the experiment, cell was running at lower 14% FU; degradation decreased to $12\% \text{ Kh}^{-1}$ but it was still high.

In Figure IV - 86, G2 cells potential degradation is expressed as a function of the exit water concentration. The majority of cells show degradation rates between $1\text{-}15\% \text{ Kh}^{-1}$ regardless the *real/simulated* FU and water concentration. In contrast, the stained cell is completely out of range with highest degradation rates between $60\text{-}70\% \text{ Kh}^{-1}$ at relatively low fuel utilizations.

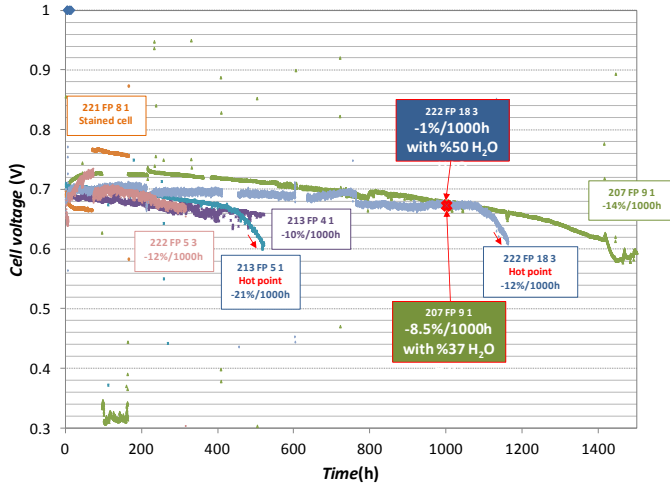


Figure IV - 85. G2 cells steady state operation with fuel utilization variable conditions at 800°C.

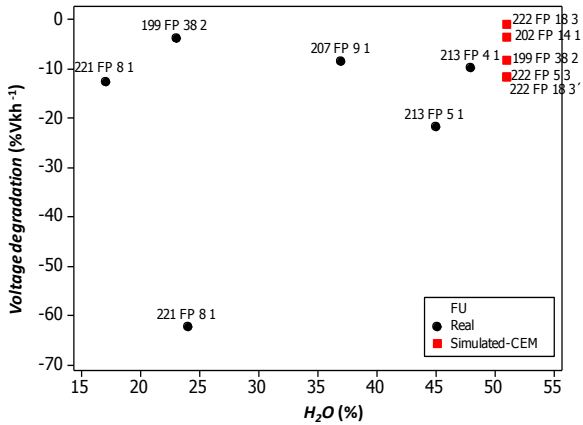


Figure IV - 86. Degradation rates of G2 cells as a function of the water concentration at the cell outlet. (222.FP.18.3 and 222.FP.18.3' indicate degradation measurement at 1000 h and 1161 h of operation, respectively)

Surface appearance after the FU experiment

Whilst the physical appearance of one cell (213.FP.4.1) was perfectly normal after the FU experiment, the remaining cells showed specific signs of severe degradation (Figure IV - 87). Two cells (213.FP.5.1 and 222.FP.18.3) exhibited an oxidized metal-support through the top region and ceramic layers which were all together peeled off. However, peeling was clean and proliferated around a hot point. Localized defects or sealing (Ultra-Temp 516, Aremco) stress are most probably in the origin of those hot points and account for the abrupt degradation which was observed for both cells after a certain time of operation (Figure IV - 85). As a matter of fact, it is observed that hot points form in the contact zone with sealing.

The metal-support of cell which underwent an accidental fuel leakage (222.FP.5.3) was also oxidized but this time oxidation was homogeneous through the whole cell.

At first sight, good surface quality of stained cell was observed. The stainless zone was clean and the efficient area seemed to be intact. However, when platinum mesh was removed, the whole cathode delaminated. In addition, even if this cell included a limited zone with stained electrolyte, more accurate inspection revealed clusters formation in its surface (Figure IV - 87).

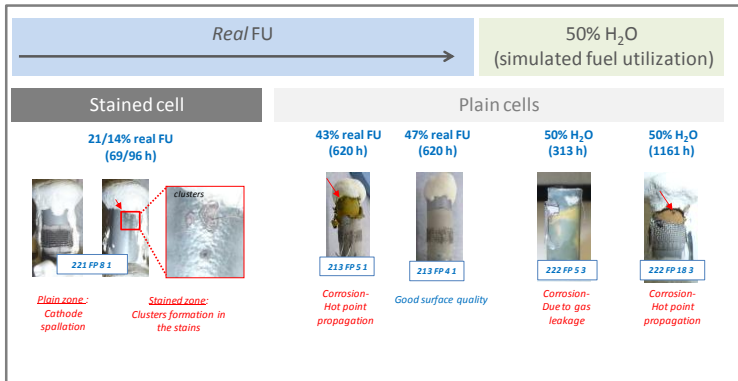


Figure IV - 87. Surface appearance of G2 cells after operation under *real* and *simulated* fuel utilization conditions (except for cell 209.FP.7.1).

Microstructural characterization

G2 cells which were used for FU experiments had different processing parameters (i.e. passivation, LST barrier thickness, sintering atmosphere). Furthermore, they were tested under different conditions (i.e. FU, Δt). Accordingly, it is difficult to correlate different microstructures. Therefore, we limited our analysis to the microstructure of passivated cell with stable performance under high FU

(222.FP.18.3) and specific degradation mechanisms in the titanium active cell (221.FP.8.1).

Passivated cell with 1.0% kh⁻¹ degradation

Passivated cell 222.FP.18.3 exhibited excellent stability under 50% *simulated* FU with 1.0% voltage degradation in 1000h of operation. However, after reaching this point fast degradation occurred due to hot point propagation through the top region and the metal-support appeared partially oxidized after cooling down.

The microstructural characterization of the cell revealed that degradation due to metal substrate corrosion was limited to a small area. In general, cell exhibited suitable microstructural properties; porous metal substrate, good adherence of the oxide-scale, porous LST and Ni-YSZ anode and gas-tight electrolyte with typical closed pores (Figure IV - 88). However, some oxidation clusters were recognized in the metal substrate. In addition, extensive cathode delamination was observed. In fact, cathode delamination was also identified in G2 cells after operation under fuel utilization by Laida Otaegui [179].

Protective oxide scale morphology and thickness was evaluated in the FeCr substrate/LST-DBL interface to analyze the effect of passivation (Figure IV - 88). 3 μm thick chromia scale exhibited a multilayered microstructure and no signs of spallation. Chromia scale adhesion to the metal substrate and LST barrier was excellent.

Inspection of the anode microstructure showed partial sinterization of YSZ that occurs in the DBL neighbouring region. This is attributed to moderate titanium diffusion with incorporation in the YSZ fluorite. In the sintered zone, chromium poisoning of nickel particles is also apparent. However, this was a plain cell and the electrolyte still preserved the characteristic closed porosity with no Ti contamination.

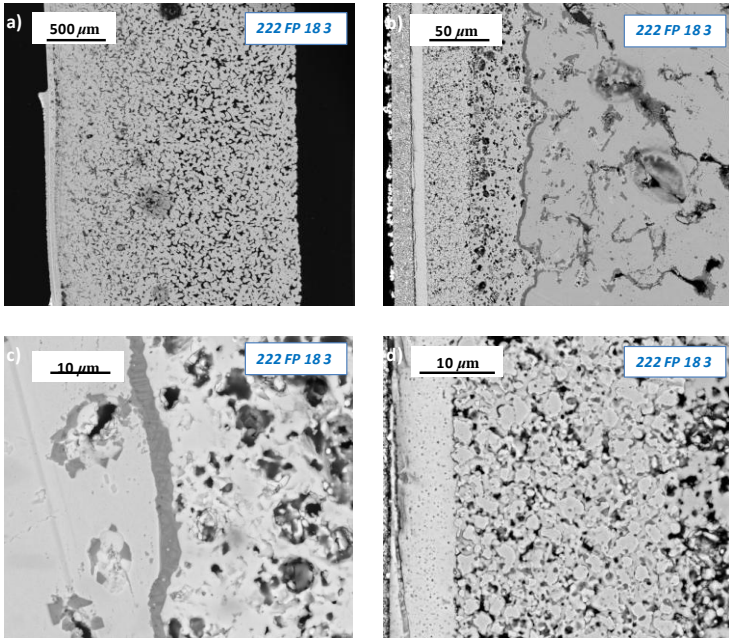


Figure IV - 88. SEM images for passivated cell 222.FP.18.3 after the fuel utilization experiment (50% H₂O; 1161 h): a) metal-support, b) functional ceramic layers, c) chromia scale and d) Ni-YSZ anode.

Titanium active cell

The microstructural analysis of stained cell 221.FP.8.1 is presented in Figure IV - 89. General observations in the stain free zone are first revised. Metal-support was overdensified but chromia scale in the contact surface with LST barrier layer was 4 μm thick in average. Electrolyte delamination and crack proliferation through the electrolyte and cathode were observed. In the anode, little nickel agglomeration was detectable.

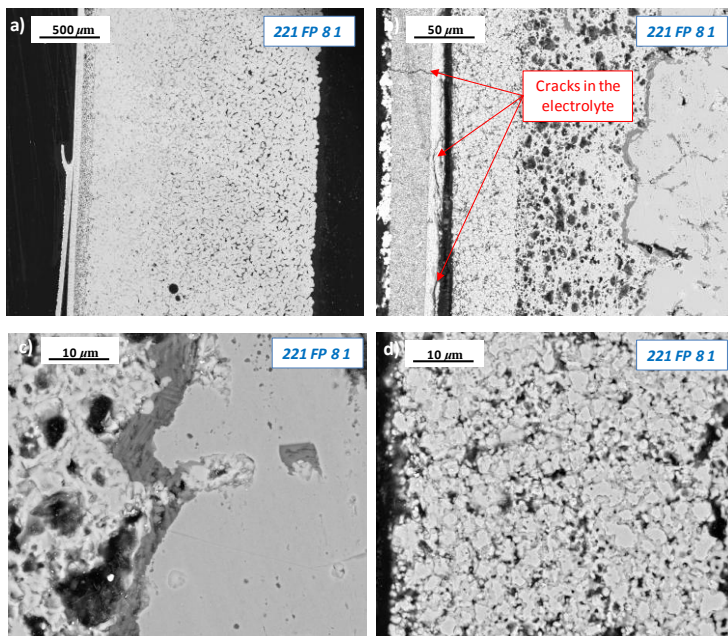


Figure IV - 89. SEM images in the plain zone for cell 221.FP.8.1 after the fuel utilization experiment (21% FU; 69 h and 14% FU; 96 h): a) metal-support, b) functional ceramic layers, c) chromia scale and d) Ni-YSZ anode.

Microstructure was completely different in the stained zone. Metal-support was also dense but little protective chromia scale was present in its surface. A reconstruction of the corrosion process in the stained zone is presented in Figure IV - 90. In phase 1, a dark phase proliferates between the anode and electrolyte. This new phase pushes and lifts the electrolyte away. Above a certain bending force, electrolyte does not withstand the stress and it breaks into pieces. In a second phase, dark phase propagates within the anode and electrolyte disappears below. In a third phase, also anode vanishes and only the dark layer is discernible in the surface of the LST barrier layer.

Dark phase and functional layers were analyzed in the propagation zone to study the exact mechanism that produces the catastrophic degradation (Figure IV - 91). Anode microstructure was extremely coarse and massively poisoned. Oversintering of YSZ particles and huge amounts of titanium were identified. Nickel particles were also agglomerated and radically poisoned with chromium. In the electrolyte, multiple micro crack propagation was observed. Typical closed pores were missing and EDS indicated huge amounts of titanium also in the electrolyte.

The dark face between the anode and electrolyte was nickel surrounded by huge amounts of chromium oxide but iron was also detected to a lesser extent.

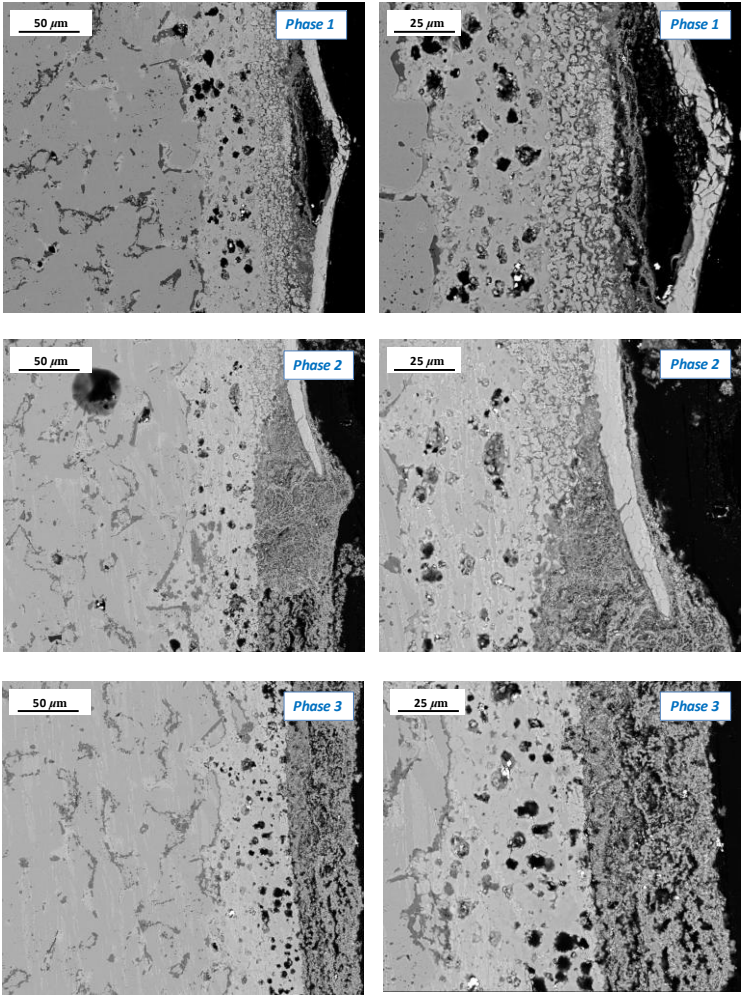


Figure IV - 90. Degradation caused during the fuel utilization experiment (21% FU; 69 h and 14% FU; 96 h) in the stained zone of cell 221.FP.8.1.

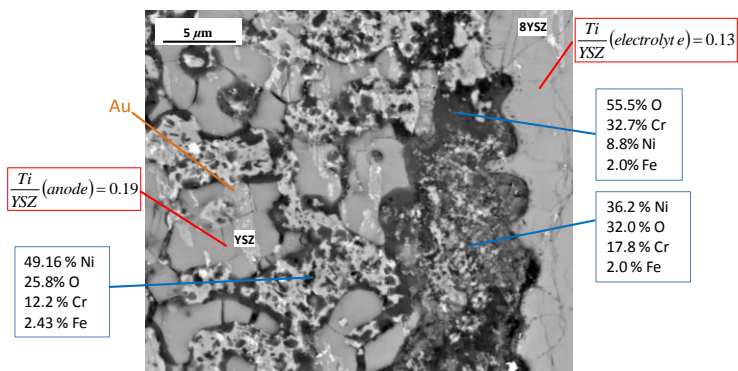


Figure IV - 91. EDS analysis of the degradation propagation through the anode in the stained zone of cell 221.FP.8.1 caused during the fuel utilization experiment (21% FU; 69 h and 14% FU; 96 h).

This section has illustrated the catastrophic effect of titanium diffusion and stain formation in the posterior operation under rather low fuel utilization. However, the exceptional stability that G2 cells with good property (i.e. free of defects) have demonstrated under high fuel utilization (50% H₂O) must be highlighted.

4.4.3.4 Overall discussion and conclusions

Stability was succeeded at *simulated* 50% fuel utilization with only 1.0% voltage degradation in 1000 h. This excellent result is partially attributed to the improved corrosion resistance of the previously passivated metal-support prior to increasing FU. In fact, passivation under a less humidified atmosphere allows the formation of a more protective chromia scale as already reported by Kofstad [126]. SEM analysis revealed that chromia scale adhesion and quality was very good for the passivated cell still after 1400 h of operation. In contrast, cells which were tested under FU without previous passivation exhibited more irregular multilayered chromia scale and spallation on the FeCr/LST interface. A second cell was also passivated and sintered in argon. However, this cell demonstrated unstable performance and underwent substantial degradation in 300h of *simulated* 50% FU. Degradation mechanisms could not be further investigated due to the accidental fuel leakage and total oxidation that this cell suffered.

It is demonstrated that, in general, water concentration is not the principal factor that triggers the stability during operation under fuel utilization. When the metal-support is well protected, as it is the case of passivated cell 222.FP.18.3, it exhibits excellent stability under high fuel utilization. Nevertheless, if chromia scale evaporates substantially from the FeCr substrate, the metal-support becomes vulnerable to fuel utilization. Those cells are susceptible to even very low vapour

concentrations and therefore degrade rapidly under fuel utilization. This is the case of *titanium active* cells as it was confirmed in a FU experiment with the stained cell 221.FP.8.1. This cell exhibited surprisingly high degradation rates at relatively low 24% FU. In the stained zone, protective chromia layer was missing and massive chromium and titanium diffusion occurred. Titanium incorporated into the YSZ fluorite in the anode and electrolyte layers, this causing Ti induced YSZ densification. Furthermore, chromia migrated to the anode and massively deposited in vastly agglomerated nickel particles. Above a certain value, saturated and overdensified anode suffered dimensional changes that stressed the electrolyte, causing the final breakdown of the electrolyte. At this point, oxygen entered the anode and accelerated cell degradation; oxidation of nickel, chromium and iron occurred. Experiment was stopped at this point but in the final phase, the catastrophic corrosion of the metal-support is expected.

In conclusion, second generation cells with *good quality* (i.e. stain and defect free) demonstrate an optimal response under fuel utilization. Excellent stability, with 1.0% voltage degradation in 1000h, has been experimentally proved for a passivated cell. However, *titanium active* cells confirm high instability under even low levels of fuel utilization. In addition, operation under *simulated* FU has demonstrated to be a useful approach to reproduce real operation conditions under high fuel utilization with similar trends observed under *simulated* and *real* FU.

Chapter V

CONCLUSIONS AND FUTURE PERSPECTIVES

The present thesis work was divided in two parts: (i) analysis of cathode stability under studies in planar anode-supported SOFCs and (ii) fabrication and operation of tubular metal-supported SOFCs. Conclusions drawn from both studies together with future perspectives are reported in this section.

Cathodes stability in planar anode-supported cells

In the first part of this thesis work, the stability of ferritic cathode LSF-SDC and LSCF-GDC, used at intermediate temperatures was studied during operation. Long-term tests were performed using highly reproducible anode-supported cells using a specific design of experiments through Taguchi methodology (L_{18}). This powerful technique allowed evaluating the influence of three cathode processing parameters (i.e. composition, thickness and sintering temperature) and five operation conditions (i.e. temperature, current density, air flow rate, air humidification and chromium presence) in eighteen 500 h durability tests. Anode-supported cells include conventional Ni-YSZ anode, YSZ electrolyte and GDC barrier.

Initially, the influence of cathode processing parameters on cell electrochemical performance was studied. Thicker electrodes (50 μm) demonstrated higher power

density as a result of enhanced current collection and catalytic activity. Generally, higher power densities were observed for high cathode sintering temperatures (1050°C) as contact between cathode and GDC barrier layer was favoured. LSCF-GDC cathode composition showed highest power densities.

During operation, some cells exhibited a substantial performance increase during the initial period. This activation was mainly related to operation under high current density and lower cathode sintering temperatures. In contrast, performance degradation was mainly caused by extrinsic factors (i.e. chromium poisoning and air humidification).

It is well known that contact with chromium vapours affect cathodes stability notoriously. The negative effect was shown to increase at high temperature (800°C) as chromia evaporation and deposition in the cathode were promoted. Characteristic SrCrO_4 formation in the ferritic cathode surface was observed. However, chromium vapours interacted with potassium in Ceramabond 571 sealing and $\text{K}_2\text{Cr}_2\text{O}_7$ deposits in the cathode surface and interface with GDC barrier were also detected. Deposition of such insulating phase at the interface between cathode and GDC barrier resulted, above all, the most harmful degradation mechanism during operation. It was concluded that the use of Ceramabond 571 and potassium-containing sealings is incompatible with chromia-based ferritic steels which are used as interconnect at intermediate temperatures, unless Cr volatile species are eliminated by protective coating of steels.

Although not systematically, high humidification of air (20%) has shown to be detrimental on the performance of some cells including ferritic cathodes. In fact, air humidification was classified, after chromium poisoning, as the second crucial factor inducing degradation. Microstructural characterization revealed instability in the cathode and GDC barrier interface (i.e. cathode delamination, crack propagation in the GDC barrier surface). The exact effect of air humidification was not fully understood and requires further investigation. Nevertheless, dry air is certainly beneficial for the stability of air side components.

Operation temperature effect was also significant, especially in the presence of chromium vapours. It was classified as the third factor influencing degradation and stability was improved at lowest 700°C. Further improvement on stability was attained operating at lower current loads (0.25 Acm^{-2}) and intermediate air flow ($0.75 \text{ mlcm}^{-2}\text{min}^{-1}$) through the cathode. The effect of cathode composition was minimal but the stability was slightly superior for LSF-SDC composite cathode and high sintering temperature (1050°C).

Overall, long-term experiments performed by varying control factors through a specific design of experiment (DoE-Taguchi matrix) approach demonstrated to be a powerful technique to study the influence of the maximal impact factors while minimizing the number of experiments. This approach provided with "safe" conditions for stable operation after screening a variety of cathode processing and operation

conditions. In fact, using the “one factor at a time” approach, collection of individual effects and impact of control factors that are reported here would have required much more time and experimental effort.

To minimize the impact of Cr poisoning, similar ASC configurations were studied in realistic operation conditions, using MCO spinel and LNC perovskite coated Crofer 22 APU meshes as current collector at the air side. A factorial experimental design was used for a small experimental matrix. Initial electrochemical characterization demonstrated excellent contact properties for Crofer 22 APU mesh coated with LNC. Power densities as high as 1640 mW/cm² were recorded at 800°C for LSCF-GDC cathode composition. Posterior results obtained in the stability tests were comparable to those reached with MCO coating and thus, also encouraging for LNC material. In fact, during the evolution of this work, Nextech Materials has patented LNC perovskite as coating material for metal alloys protection.

Fabrication and operation of tubular metal-supported SOFCs

The second part of this thesis work was devoted to the development of a second generation tubular MS-SOFC. This cell includes a porous tubular substrate composed of a ferritic stainless steel, Crofer 22 APU, which is processed following an innovative technique called *free-fall powder*. Ceramic functional layers are subsequently deposited by industrially scalable “wet” colloidal techniques which include dip-coating and spray-coating. Cells consist of conventional Ni-YSZ cermet anode and 8YSZ electrolyte. The innovative aspect of this second generation of cells is a nickel free lanthanum doped SrTiO₃ (LST) perovskite barrier which is placed between the metal substrate and anode to avoid Ni, Cr and Fe element interdiffusion during the high co-sintering temperatures required for YSZ electrolyte densification.

Progress with this MS-SOFC technology in the last two years has been significantly demonstrated throughout this work. Research lines included performance optimization, degradation mechanisms under fabrication and robustness of G2 cells under operation.

With the aim at improving the electrochemical efficiency, the influence of basic processing parameters (i.e. Crofer particle fraction and sintering temperature) and functional layers thickness (LST barrier, Ni-YSZ anode and LSF40-SDC cathode) were studied. In this sense, sintering temperature was set at 1350°C. On the other hand, tubes with coarse FeCr (<53 μm) exhibited modest results and fine fraction (<45 μm) was finally selected.

Performance optimization was also pursued by making ceramic layers strictly as thin as necessary. In the fuel side, standard LST-DBL (70-90 μm) and Ni-YSZ cermet anode (40-50 μm) were reduced by the straightforward dilution of the colloidal suspension prior to dip-coating. Conversely, in the air side, initially thin LSF40-SDC cathode (15-30 μm) was made thicker by dip-coating.

Contrary to expectations, better electrochemical performance was obtained with standard LST-F1 barrier layer (70-90 μm) as compared to thin LST-F4 ($\approx 50 \mu\text{m}$). In addition, a connection between the DBL thickness and surface appearance after co-sintering was pointed out. Stains proliferated in the electrolyte surface as thinner DBL was used. Finally, standard LST-F1 DBL was maintained in the manufacturing process.

In reference to the electrodes, electrochemical performance turned out to be a strong function of the anode thickness. Power density was systematically improved when anode was reduced from 60 μm to 40-45 μm . In contrast, power density was similar regardless the thickness variation of the LSF₄₀-SDC cathode at the air side. This is attributed to nickel agglomeration during co-sintering and resulting coarse anode microstructure which limits the electrochemical performance.

During the manufacturing process of G2 half-cells, stain formation was frequently observed in the electrolyte surface after co-sintering. That is to say, plain and stained cells were arbitrarily produced in the *a priori* standardized manufacturing process. In one hand, stain free cells microstructure is satisfactory; porous FeCr/LST/Ni-YSZ and gas-tight 8YSZ electrolyte with typical closed pores is obtained after co-sintering. OCV around 1.1V is optimal and power densities in the 150-250 mW/cm² range are systematically recorded at 800°C. On the contrary, stained cells microstructure undergoes a severe densification during co-sintering. Ceramic layers and FeCr substrate near to the active region are dense. Ni-YSZ microstructure is particularly coarse and dense. In addition, full dense 8YSZ electrolyte with missing closed pores is observed. OCV is lower and power densities below 100 mW/cm² are registered.

Detailed SEM and EDS analysis revealed that stains formation and densification are related to titanium diffusion. Titanium is segregated from LST barrier during co-sintering and migrates first to the anode and then to the electrolyte easily incorporating into the YSZ fluorite structure. This phenomenon implies an abrupt transformation of the electrical properties as well as the sintering behaviour of YSZ. In practice, anode densification originates huge activation losses and poor performing cells.

Further analysis revealed that massive Ti diffusion is related to humidification during co-sintering. Ti segregates mostly via chromium substitution at the B-site of LST perovskite, though some intrinsic Ti segregation is also detected. At high temperatures required for G2 cells co-sintering (1350°C), massive chromium evaporation is promoted under humidified atmosphere. This chromium migrates through the barrier and substitutes titanium at the B-site of LST perovskite. Finally, segregated titanium is transferred and incorporated into the YSZ fluorite within the anode and electrolyte. Massive Cr diffusion leaves behind a Cr depleted metal-support, with poor protective chromia scale.

In principle, G2 cells co-sintering is performed under dry conditions. However, oxygen getter (FeCr) which is used in the process liberates water at 1100 °C, when gas is changed from inert Ar to reducing 10%H₂ + Ar atmosphere. On the basis of the experimental results reported here, better cell quality is expected for a getter free half-cell processing. In fact, this was corroborated for similar half-cells which were co-sintered in the presence and absence of oxygen getters.

In this work, G2 cells robustness under severe operation conditions was studied by accelerated ageing techniques which include thermal and redox cycles and high fuel utilization stability studies.

A long-lasting experiment demonstrated the excellent mechanical robustness of G2 cells upon thermal cycling. Cell was stable and OCV remained high (1.12V) under 550 rapid thermal cycles (10°Cmin⁻¹ heating/cooling rates) during at least 3900 h. This result is particularly significant in the MSC research field. It constitutes with 550 rapid thermal cycles, the most rigorous proof of mechanical stability reported to date.

Poor redox tolerance of G2 cells was confirmed by testing a stainless and stained cell. Both cells failed after 2 full redox cycles under 20 min in air or Ar, respectively.

Fuel utilization experiments provided excellent results for G2 cells. Exceptional stability of a stainless cell was proved under simulated high 50% fuel utilization. During the first 1000h of operation, only 1.0% voltage degradation was registered. This result might be related to previous passivation and resultant good quality of chromia scale. However, further experimentation is necessary to confirm this tendency.

Second generation (G2) tubular MSCs are promising candidates for power generation applications where cost and robustness under steady and transient conditions are critical. However, further understanding of processing, performance optimization and reliable and competitive stability are still needed.

Future perspectives

A more detailed analysis of the influence of air humidification in cathode stability under real operation conditions is envisaged. LNC and MCO coatings should be further evaluated.

Reliable reproducibility of stainless G2 cells without FeCr oxygen getters, thus minimizing the effect of humidity during cosintering, must be demonstrated.

Anode microstructure and resulting poor redox stability are still limiting cell performance and life. Future work may go on the following directions:

- *Thinner anodes with optimized microstructure*
- *Fine tuning redox cycles may be used as cell conditioning to improve anode microstructure and hence, performance and redox resistance*
- *Alternative anodes: finding nickel free anodes with high catalytic activity and redox resistance is a primary challenge.*

LIST OF ABBREVIATION AND ACRONYMS

<i>AFC</i>	Alkaline Fuel Cell
a_i	Coded variables in the Taguchi matrix
A_i	Natural variables in the Taguchi matrix
<i>APU</i>	Auxiliary Power Unit
<i>ASC</i>	Anode-supported cell
<i>ASR</i>	Area specific resistance / Ωcm^{-2}
<i>AS-SOFC</i>	Anode-supported SOFC
<i>CHP</i>	Combined Heat and Power
d_{50}	Median grain size diameter / μm
<i>DBL</i>	Diffusion barrier layer
E_0	Standard potential
<i>EDS</i>	Energy Dispersive X-ray Spectroscopy
<i>EMF</i>	Electromotive force
<i>EIS</i>	Electrochemical Impedance Spectroscopy
<i>F</i>	Faraday constant
<i>FU</i>	Fuel utilization
ΔG	Gibbs free energy
<i>G1</i>	First generation fuel cells
<i>G2</i>	Second generation fuel cells
<i>GDC</i>	Gadolinium doped ceria
<i>LNC</i>	Nickel substituted lanthanum cobaltite / $\text{La}_{0.5}\text{Ni}_{0.6}\text{Co}_{0.4}\text{O}_3$
<i>LSC</i>	Strontium substituted lanthanum cobaltite / $\text{La}_{0.5}\text{Sr}_{0.5}\text{CoO}_3$
<i>LSCF</i>	Strontium substituted lanthanum cobaltite and ferrite / $(\text{La}_{0.6}\text{Sr}_{0.4})_{0.995}\text{Co}_{0.2}\text{Fe}_{0.8}\text{O}_{3-\delta}$
<i>LSF</i>	Lanthanum and strontium ferrite / $(\text{La}_{0.6}\text{Sr}_{0.4})_{0.95}\text{FeO}_{3-\delta}$
<i>LSF₄₀</i>	Strontium substituted lanthanum ferrite / $(\text{La}_{0.6}\text{Sr}_{0.4})_{0.95}\text{FeO}_{3-\delta}$
<i>LST</i>	Lanthanum substituted strontium titanate / $(\text{La}_{0.3}\text{Sr}_{0.7})\text{TiO}_{3-\delta}$
<i>HT-SOFC</i>	High temperature SOFC
<i>IT-SOFC</i>	Intermediate temperature SOFC
<i>J</i>	Current density / Acm^{-2}
<i>MCFC</i>	Molten Carbonate Fuel Cell
<i>MCO</i>	Manganese and cobalt spinel / $\text{Mn}_{1.5}\text{Co}_{1.5}\text{O}_4$
<i>MIC</i>	Metal interconnect
<i>MIEC</i>	Mixed Ionic Electronic Conductor
<i>MSC</i>	Metal-supported cell
<i>MS-SOFC</i>	Metal-supported SOFC
<i>OCV</i>	Open Circuit Voltage / V

p (%)	Porosity / %
P	Power density / Wcm^{-2}
PAFC	Phosphoric Acid Fuel Cell
PEFC	Polymer Electrolyte Fuel Cell
PEM	Polymer Electrolyte Membrane
PVD	Physical Vapor Deposition
RH	Relative humidity
R_o	Ohmic resistance / Ωcm^{-2}
R_p	Polarization resistance / Ωcm^{-2}
SEM	Scanning Electron Microscope
SOFC	Solid Oxide Fuel Cell
SDC	Samaria doped ceria
SSA	Surface Area Resistance / m^2g^{-1}
t	Cathode thickness / μm
t_i	Initial time / h^{-1}
t_f	Final time / h^{-1}
T	Operation temperature / $^{\circ}\text{C}$
T_d	Dew point / $^{\circ}\text{C}$
T_s	Sintering temperature / $^{\circ}\text{C}$
TEC	Thermal expansion coefficient
TPB	Triple Phase Boundary
V_{cell}	Cell voltage / V
XRD	X-ray diffraction
X_i	Certain resistance (ASR, R_p or R_o) at t_i / Ωcm^{-2}
X_f	Certain resistance (ASR, R_p or R_o) at t_f / Ωcm^{-2}
YDC	Yttrium doped ceria / $\text{Y}_{0.2}\text{Ce}_{0.8}\text{O}_{1.9}$
YST	Yttrium substituted strontium titanate
YSZ	Yttria stabilized zirconia / $(\text{ZrO}_2)_{1-x}(\text{Y}_2\text{O}_3)_x$
ZDC	Zirconium doped ceria / $(\text{Zr}_{0.1}\text{Ce}_{0.9}\text{O}_2)$
Φ_{air}	Air flux / $\text{ml cm}^{-2} \text{min}^{-1}$
ΔX	Certain resistance percentual increment / %
ΔASR	Area specific resistance percentual increment / %
ΔR_p	Polarization resistance percentual increment / %
ΔR_o	Ohmic resistance percentual increment / %
η	Viscosity / Pa s
ρ_s	Geometrical density / gm^{-3}
$\%D_e$	Transversal shrinkage / %
ε	Efficiency
ε_R	Reversible efficiency
ε_V	Voltage efficiency
ε_U	Fuel utilization

REFERENCES

- [1] Ivers-Tiffée E, Weber A, Herbstritt D. *Materials and technologies for SOFC-components*. Journal of the European Ceramic Society **2001**;21:1805-11.
- [2] Brett DJL, Atkinson A, Brandon NP, Skinner SJ. *Intermediate temperature solid oxide fuel cells*. Chemical Society Reviews **2008**;37:1568-78.
- [3] <http://www.hydrogenandfuelcells.energy.gov>. Comparison of Fuel Cell Technologies.
- [4] Kendall K. *Progress in microtubular solid oxide fuel cells*. International Journal of Applied Ceramic Technology **2010**;7:1-9.
- [5] Crawley G. *Opening doors to fuel cell commercialisation*. Fuel Cell Today – January 2007, **2007**.
- [6] Thorstensen B. *Parametric study of fuel cell system efficiency under full and part load operation*. Journal of Power Sources **2001**;92:9-16.
- [7] H. Yokokawa NS. *Handbook of Fuel Cells Fundamentals Technology and Application*: John Wiley a& Sons; **2003**.
- [8] S.C. Singhal KK. *High Temperature Solid Oxide Fuel Cells: Fundamentals, Design and Applications*. Oxfor, UK: Elsevier Ltd.; **2003**.
- [9] Cowin PI, Petit CTG, Lan R, Irvine JTS, Tao S. *Recent progress in the development of anode materials for solid oxide fuel cells*. Advanced Energy Materials **2011**;1:314-32.
- [10] Sammes NM, Tompsett GA, Näfe H, Aldinger F. *Bismuth based oxide electrolytes - Structure and ionic conductivity*. Journal of the European Ceramic Society **1999**;19:1801-26.
- [11] Steele BCH. *Material science and engineering: The enabling technology for the commercialisation of fuel cell systems*. Journal of Materials Science **2001**;36:1053-68.
- [12] Steele BCH, Heinzel A. *Materials for fuel-cell technologies*. Nature **2001**;414:345-52.
- [13] Männer R. i-T, and Wersing W. In: Zegers P, editor. *Proceedings 2nd International Symposium on SOFC 1991*. p. 715-25.
- [14] Arachi Y, Sakai H, Yamamoto O, Takeda Y, Imanishai N. *Electrical conductivity of the $ZrO_2-Ln_2O_3$ ($Ln = \text{lanthanides}$) system*. Solid State Ionics **1999**;121:133-9.
- [15] Nomura K, Mizutani Y, Kawai M, Nakamura Y, Yamamoto O. *Aging and Raman scattering study of scandia and yttria doped zirconia*. Solid State Ionics **2000**;132:235-9.
- [16] Kharton VV, Marques FMB, Atkinson A. *Transport properties of solid oxide electrolyte ceramics: A brief review*. Solid State Ionics **2004**;174:135-49.
- [17] Fergus JW. *Doping and defect association in oxides for use in oxygen sensors*. Journal of Materials Science **2003**;38:4259-70.
- [18] Pomprasertsuk R, Ramanarayanan P, Musgrave CB, Prinz FB. *Predicting ionic conductivity of solid oxide fuel cell electrolyte from first principles*. Journal of Applied Physics **2005**;98.
- [19] Mogensen M, Sammes NM, Tompsett GA. *Physical, chemical and electrochemical properties of pure and doped ceria*. Solid State Ionics **2000**;129:63-94.

- [20] Tucker MC. *Progress in metal-supported solid oxide fuel cells: A review*. Journal of Power Sources **2010**;195:4570-82.
- [21] Joshi AV, Steppan JJ, Taylor DM, Elangovan S. *Solid electrolyte materials, devices, and applications*. Journal of Electroceramics **2004**;13:619-25.
- [22] Fergus JW. *Electrolytes for solid oxide fuel cells*. Journal of Power Sources **2006**;162:30-40.
- [23] Sarantaridis D, Atkinson A. *Redox cycling of Ni-based solid oxide fuel cell anodes: A review*. Fuel Cells **2007**;7:246-58.
- [24] Zhu WZ, Deevi SC. *A review on the status of anode materials for solid oxide fuel cells*. Materials Science and Engineering A **2003**;362:228-39.
- [25] Rasmussen JFB, Hagen A. *The effect of H₂S on the performance of Ni-YSZ anodes in solid oxide fuel cells*. Journal of Power Sources **2009**;191:534-41.
- [26] Marina OA, Canfield NL, Stevenson JW. *Thermal, electrical, and electrocatalytical properties of lanthanum-doped strontium titanate*. Solid State Ionics **2002**;149:21-8.
- [27] Hui S, Petric A. *Electrical conductivity of yttrium-doped SrTiO₃: Influence of transition metal additives*. Materials Research Bulletin **2002**;37:1215-31.
- [28] Huang X, Zhao H, Shen W, Qiu W, Wu W. *Effect of fabrication parameters on the electrical conductivity of YxSr1-xTiO₃ for anode materials*. Journal of Physics and Chemistry of Solids **2006**;67:2609-13.
- [29] Li X, Zhao H, Gao F, Zhu Z, Chen N, Shen W. *Synthesis and electrical properties of Co-doped Y_{0.08}Sr_{0.92}TiO_{3-δ} as a potential SOFC anode*. Solid State Ionics **2008**;179:1588-92.
- [30] Sun XF, Guo RS, Li J. *Preparation and properties of yttrium-doped SrTiO₃ anode materials*. Ceramics International **2008**;34:219-23.
- [31] Karczewski J, Bochentyn B, Molin S, Gazda M, Jasinski P, Kusz B. *Solid oxide fuel cells with Ni-infiltrated perovskite anode*. Solid State Ionics **2012**;221:11-4.
- [32] Puengjinda P, Muroyama H, Matsui T, Eguchi K. *Stability of solid oxide fuel cell anodes based on YST-SDC composite with Ni catalyst*. Journal of Power Sources **2012**;216:409-16.
- [33] Ikebe T, Muroyama H, Matsui T, Eguchi K. *Stability of Ni/Y-doped SrTiO₃-YSZ anode in reduction-oxidation cycles*. 2 PART 3 ed. Vienna **2009**. p. 1993-2002.
- [34] Sun C, Hui R, Roller J. *Cathode materials for solid oxide fuel cells: A review*. J Solid State Electrochem **2010**;14:1125-44.
- [35] McEvoy AJ. *Activation processes, electrocatalysis and operating protocols enhance SOFC performance*. Solid State Ionics **2000**;135:331-6.
- [36] Haanappel VAC, Mertens J, Rutenbeck D, Tropartz C, Herzhof W, Sebold D, et al. *Optimisation of processing and microstructural parameters of LSM cathodes to improve the electrochemical performance of anode-supported SOFCs*. Journal of Power Sources **2005**;141:216-26.
- [37] Jiang SP, Love JG, Zhang JP, Hoang M, Ramprakash Y, Hughes AE, et al. *Electrochemical performance of LSM/zirconia-yttria interface as a function of a-site non-stoichiometry and cathodic current treatment*. Solid State Ionics **1999**;121:1-10.
- [38] Clausen C, Bagger C, Bilde-Sørensen JB, Horsewell A. *Microstructural and microchemical characterization of the interface between La_{0.85}Sr_{0.15}MnO₃ and Y₂O₃-stabilized ZrO₂*. Solid State Ionics **1994**;70-71:59-64.
- [39] Kostogloudis GC, Vasilakos N, Ftikos C. *Preparation and characterization of Pr_{1-x}Sr_xMnO_{3±δ} (x = 0, 0.15, 0.3, 0.4, 0.5) as a potential SOFC cathode material*

- operating at intermediate temperatures (500-700°C). Journal of the European Ceramic Society **1997**;17:1513-21.
- [40] Rim HR, Jeung SK, Jung E, Lee JS. Characteristics of $Pr_{1-x}M_xMnO_3$ ($M=Ca, Sr$) as cathode material in solid oxide fuel cells. Materials Chemistry and Physics **1998**;52:54-9.
- [41] Yue X, Yan A, Zhang M, Liu L, Dong Y, Cheng M. Investigation on scandium-doped manganate $La_{0.8}Sr_{0.2}Mn_{1-x}Sc_xO_{3-\delta}$ cathode for intermediate temperature solid oxide fuel cells. Journal of Power Sources **2008**;185:691-7.
- [42] Weber A, Ivers-Tiffée E. Materials and concepts for solid oxide fuel cells (SOFCs) in stationary and mobile applications. Journal of Power Sources **2004**;127:273-83.
- [43] Zhu C, Liu X, Xu D, Yan D, Wang D, Su W. Preparation and performance of $Pr_{0.7}Sr_{0.3}Co_{1-y}Cu_yO_{3-\delta}$ as cathode material of IT-SOFCs. Solid State Ionics **2008**;179:1470-3.
- [44] Chen W, Wen T, Nie H, Zheng R. Study of $Ln_{0.6}Sr_{0.4}Co_{0.8}Mn_{0.2}O_{3-\delta}$ ($Ln = La, Gd, Sm$ or Nd) as the cathode materials for intermediate temperature SOFC. Materials Research Bulletin **2003**;38:1319-28.
- [45] Fukunaga H, Koyama M, Takahashi N, Wen C, Yamada K. Reaction model of dense $Sm_{0.5}Sr_{0.5}CoO_3$ as SOFC cathode. Solid State Ionics **2000**;132:279-85.
- [46] Ralph JM, Rossignol C, Kumar R. Cathode materials for reduced-temperature SOFCs. Journal of the Electrochemical Society **2003**;150:A1518-A22.
- [47] Simner SP, Bonnett JF, Canfield NL, Meinhardt KD, Shelton JP, Sprenkle VL, et al. Development of lanthanum ferrite SOFC cathodes. Journal of Power Sources **2003**;113:1-10.
- [48] Coffey G, Hardy J, Marina O, Pederson L, Rieke P, Thomsen E. Copper doped lanthanum strontium ferrite for reduced temperature solid oxide fuel cells. Solid State Ionics **2004**;175:73-8.
- [49] Anderson MD, Stevenson JW, Simner SP. Reactivity of lanthanide ferrite SOFC cathodes with YSZ electrolyte. Journal of Power Sources **2004**;129:188-92.
- [50] Yokokawa H, Sakai N, Horita T, Yamaji K, Brito ME, Kishimoto H. Thermodynamic and kinetic considerations on degradations in solid oxide fuel cell cathodes. Journal of Alloys and Compounds **2008**;452:41-7.
- [51] Mai A, Haanappel VAC, Uhlenbruck S, Tietz F, Stover D. Ferrite-based perovskites as cathode materials for anode-supported solid oxide fuel cells Part I. Variation of composition. Solid State Ionics **2005**;176:1341-50.
- [52] Kim JY, Canfield NL, Chick LA, Meinhardt KD, Sprenkle VL. Chromium poisoning effects on various cathodes. In: Bansal NP, editor. 4 ed. Cocoa Beach, FL **2005**. p. 129-38.
- [53] Orui H, Watanabe K, Chiba R, Arakawa M. Application of $LaNi(Fe)O_3$ as SOFC cathode. Journal of the Electrochemical Society **2004**;151:A1412-A7.
- [54] Jiang SP. A comparison of O_2 reduction reactions on porous $(La,Sr)MnO_3$ and $(La,Sr)(Co,Fe)O_3$ electrodes. Solid State Ionics **2002**;146:1-22.
- [55] Ullmann H, Trofimenko N, Tietz F, Stöver D, Ahmad-Khanlou A. Correlation between thermal expansion and oxide ion transport in mixed conducting perovskite-type oxides for SOFC cathodes. Solid State Ionics **2000**;138:79-90.
- [56] Teraoka Y, Zhang HM, Okamoto K, Yamazoe N. Mixed ionic-electronic conductivity of $La_{1-x}Sr_xCo_{1-y}FyO_{3-\delta}$ perovskite-type oxides. Materials Research Bulletin **1988**;23:51-8.

- [57] Kindermann L. PF, Larsen PH, Nickel H, Hilpert K. *3rd European Forum on SOFC*. Switzerland: Stevens P; **1998**. p. 123-32.
- [58] Tai LW, Nasrallah MM, Anderson HU, Sparlin DM, Sehlin SR. *Structure and electrical properties of $La_{1-x}Sr_xCo_{1-y}Fe_yO_3$. Part 2. The system $La_{1-x}Sr_xCo_{0.2}Fe_{0.8}O_3$* . *Solid State Ionics* **1995**;76:273-83.
- [59] Chiba R, Yoshimura F, Sakurai Y. *Investigation of $LaNi_{1-x}Fe_xO_3$ as a cathode material for solid oxide fuel cells*. *Solid State Ionics* **1999**;124:281-8.
- [60] Xia CR LM. *Advanced materials* **2002**;15.
- [61] Sahibzada M BS, Rudkin RA, Kilner JA (1995) *Solid. State Ionics*
- [62] EG&G Technical Services I. *Fuel Cell Handbook*. Morgantown, West Virginia **2004**.
- [63] Shaigan N, Qu W, Ivey DG, Chen W. *A review of recent progress in coatings, surface modifications and alloy developments for solid oxide fuel cell ferritic stainless steel interconnects*. *Journal of Power Sources* **2010**;195:1529-42.
- [64] Zhu WZ, Deevi SC. *Development of interconnect materials for solid oxide fuel cells*. *Materials Science and Engineering A* **2003**;348:227-43.
- [65] Fergus JW. *Metallic interconnects for solid oxide fuel cells*. *Materials Science and Engineering A* **2005**;397:271-83.
- [66] Quadackers WJ, Piron-Abellan J, Shemet V, Singheiser L. *Metallic interconnectors for solid oxide fuel cells- A review*. *Materials at High Temperatures* **2003**;20:115-27.
- [67] J. Piron Abellan VS, F. Tietz, L. Singheiser, W.J. Quadackers, . *Ferritic Steel Interconnect for Reduced Temperature SOFC*. *Proceeding The Electrochemical Society* **2001**;2001-16.
- [68] Yang Z. *Recent advances in metallic interconnects for solid oxide fuel cells*. *International Materials Reviews* **2008**;53:39-52.
- [69] Fontana S, Amendola R, Chevalier S, Piccardo P, Caboche G, Viviani M, et al. *Metallic interconnects for SOFC: Characterisation of corrosion resistance and conductivity evaluation at operating temperature of differently coated alloys*. *Journal of Power Sources* **2007**;171:652-62.
- [70] Villarreal I, Rivas M, Rodriguez-Martinez LM, Otaegi L, Zabala A, Gomez N, et al. *Tubular metal supported SOFC development for domestic power generation*. *ECS Transactions: Solid Oxide Fuel Cells XI. 2 PART 1* ed. Vienna **2009**. p. 689-94.
- [71] Kei Hosoi MN. Status of National Project for SOFC Development in Japan. In: S.C. Singhal HY, editor. *ECS Transactions: Solid Oxide Fuel Cells XI*. Vienna, Austria: The Electrochemical Society; **2009**. p. 11-20.
- [72] Besette N. Status of the Acumentrics SOFC Program. SECA 2004 Annual Meeting and Core Program Review. Boston: US DOE NETL **2004**.
- [73]http://www.nextechmaterials.com/energy/index.php?option=com_content&view=article&id=14&Itemid=12.
- [74] <http://www.netl.doe.gov/technologies/coalpower/fuelcells/seca/industry.html>.
- [75] http://www.toto.co.jp/company/profile_en/technology/sofc/index.htm.
- [76] AIST Today. 2007;7.
- [77] Beckel D, Bieberle-Hütter A, Harvey A, Infortuna A, Muecke UP, Prestat M, et al. *Thin films for micro solid oxide fuel cells*. *Journal of Power Sources* **2007**;173:325-45.

- [78] Suzuki T, Yamaguchi T, Fujishiro Y, Awano M. *Fabrication and characterization of micro tubular SOFCs for operation in the intermediate temperature*. Journal of Power Sources **2006**;160:73-7.
- [79] Evans A, Bieberle-Hütter A, Rupp JLM, Gauckler LJ. *Review on microfabricated micro-solid oxide fuel cell membranes*. Journal of Power Sources **2009**;194:119-29.
- [80] Sarkar P, Yamarte L, Rho H, Johanson L. *Anode-supported tubular micro-solid oxide fuel cell*. International Journal of Applied Ceramic Technology **2007**;4:103-8.
- [81] Dhir A, Kendall K. *Microtubular SOFC anode optimisation for direct use on methane*. Journal of Power Sources **2008**;181:297-303.
- [82] Singhal SC. *Solid oxide fuel cells*. *Electrochemical Society Interface* **2007**;16:41-4.
- [83] Cologna M. *Advances in the production of planar and Micro-Tubular Solid Oxide Fuel Cells*. Trento: University of Trento; **2009**.
- [84] Schuler A. *An Intermediate Report on the Way to a Near-Series Sulzer Hexis Fuel Cell System*. *Sixth European Solid Oxide Fuel Cell Forum*. Luzern, der Schweiz **2004**.
- [85] E. Batawi WK, M. Janousek, B. Boggwiler and R. Diethelm. *Electrochemical Society* **1999**;99-19.
- [86] L. Blum WAM, H. Nabelek, R. Steinberg-Wilckens. *Worldwide SOFC technology overview and benchmark*. Cocoa Beach, FL **2005**.
- [87] Blum L, Meulenberg WA, Nabelek H, Steinberger-Wilckens R. *Worldwide SOFC technology overview and benchmark*. International Journal of Applied Ceramic Technology **2005**;2:482-92.
- [88] George RaAC. *Developments in Siemens Westinghouse SOFC Program*. *2003 Fuel Cell Seminar*. Miami Beach, FL, USA.: Department of Energy; **2003**.
- [89] Fujii H. *Status of National project for SOFC Development in Japan*. *Solid Oxide Fuel Cells Meeting* **2002**.
- [90] Nimomiya HFaT. *Status of the National Project for SOFC Development in Japan*. In: J. Huijsmans UB, Oberrohrdorf, editor. *Proceedings of the European Fuel Cell Forum*. Lucerne, Switzerland **2002**. p. 700-7.
- [91] Nakanishi A, et al *Development of MOLB Type SOFC*. *ECS Transactions: Solid Oxide Fuel Cells (SOFC VIII)*. Paris, France: The Electrochemical Society; **2003**.
- [92] Yokokawa H, Tu H, Iwanschitz B, Mai A. *Fundamental mechanisms limiting solid oxide fuel cell durability*. Journal of Power Sources **2008**;182:400-12.
- [93] A.C. Müller AW, D. Herbstritt, E. Ivers-Tiffée. In: Singhal M. D, editor. *Proceedings of the Eighth International Symposium on Solid Oxide Fuel Cells (SOFC-VIII)*. Pennington, NJ: *The Electrochemical Society*; **2003**. p. 196-9.
- [94] Ioselevich A, Kornyshev AA, Lehnert W. *Statistical geometry of reaction space in porous cermet anodes based on ion-conducting electrolytes patterns of degradation*. *Solid State Ionics* **1999**;124:221-37.
- [95] Liu J, Barnett SA. *Operation of anode-supported solid oxide fuel cells on methane and natural gas*. *Solid State Ionics* **2003**;158:11-6.
- [96] Takeguchi T, Kani Y, Yano T, Kikuchi R, Eguchi K, Tsujimoto K, et al. *Study on steam reforming of CH₄ and C₂ hydrocarbons and carbon deposition on Ni-YSZ cermets*. Journal of Power Sources **2002**;112:588-95.
- [97] Mitterdorfer A, Gauckler LJ. *La₂Zr₂O₇ formation and oxygen reduction kinetics of the La_{0.85}Sr_{0.15}Mn_yO₃, O₂(g)|YSZ system*. *Solid State Ionics* **1998**;111:185-218.

- [98] Simner SP, Anderson MD, Engelhard MH, Stevenson JW. *Degradation mechanisms of La-Sr-Co-Fe-O₃ SOFC cathodes*. *Electrochem Solid State Lett* **2006**;9:A478-A81.
- [99] Jiang SP, Zhang S, Zhen YD. *Deposition of Cr species at (La,Sr)(Co,Fe)O₃ cathodes of solid oxide fuel cells*. *Journal of the Electrochemical Society* **2006**;153:A127-A34.
- [100] Taniguchi S, Kadowaki M, Kawamura H, Yasuo T, Akiyama Y, Miyake Y, et al. *Degradation phenomena in the cathode of a solid oxide fuel cell with an alloy separator*. *Journal of Power Sources* **1995**;55:73-9.
- [101] Batfalsky P, Haanappel VAC, Malzbender J, Menzler NH, Shemet V, Vinke IC, et al. *Chemical interaction between glass-ceramic sealants and interconnect steels in SOFC stacks*. *Journal of Power Sources* **2006**;155:128-37.
- [102] L. Otaegui LMR-M, M. A. Alvarez, F. Castro, I. Villarreal. *Development of improved tubular metal-supported Solid Oxide Fuel Cells towards high fuel utilization stability*. *Advances in Solid Oxide Fuel Cells VIII - Ceramic Engineering and Science Proceedings* **2012**;33.
- [103] Waldbillig D, Wood A, Ivey DG. *Thermal analysis of the cyclic reduction and oxidation behaviour of SOFC anodes*. *Solid State Ionics* **2005**;176:847-59.
- [104] Bujalski W, Dikwal CM, Kendall K. *Cycling of three solid oxide fuel cell types*. *Journal of Power Sources* **2007**;171:96-100.
- [105] Lide M, Rodriguez-Martinez LO, Amaia Aregi, Mario A. Alvarez, Igor Villarreal. *Tubular metal supported solid oxide fuel cell resistant to high fuel utilization*. 10th European SOFC Forum 2012.
- [106] Yokokawa H, Watanabe T, Ueno A, Hoshino K. *Investigation on degradation in long-term operations of four different stacks/modules*. 1 PART 1 ed **2007**. p. 133-40.
- [107] D.-S. Lee WSK, S.H. Choi, J. Kim, H.-W. Lee, J.-H. Lee. *Characterization of ZrO₂ co-doped with Sc₂O₃ and CeO₂ electrolyte for the application of intermediate temperature SOFCs*. *Solid State Ionics* **2005**;176:33-9.
- [108] Brown M, Primdahl S, Mogensen M. *Structure/performance relations for Ni/yttria-stabilized zirconia anodes for solid oxide fuel cells*. *Journal of the Electrochemical Society* **2000**;147:475-85.
- [109] Dees DW, Claar TD, Easler TE, Fee DC, Mrazek FC. *Conductivity of porous Ni/ZrO₂-Y₂O₃ cermets*. *Journal of the Electrochemical Society* **1987**;134:2141-6.
- [110] Itoh H. *Research and Development on High Performance Anode for Solid-Oxide Fuel Cells - Improvement of the microstructure for New Long Life Anode*. CRIEPI Report **1995**.
- [111] Gong M, Liu X, Tremblay J, Johnson C. *Sulfur-tolerant anode materials for solid oxide fuel cell application*. *Journal of Power Sources* **2007**;168:289-98.
- [112] Vels Jensen K, Wallenberg R, Chorkendorff I, Mogensen M. *Effect of impurities on structural and electrochemical properties of the Ni-YSZ interface*. *Solid State Ionics* **2003**;160:27-37.
- [113] Tu H, Stimming U. *Advances, aging mechanisms and lifetime in solid-oxide fuel cells*. *Journal of Power Sources* **2004**;127:284-93.
- [114] M. J. Heneka El-T. *Proceedings of the 26th Risø International Symposium on Materials Science*. In: S. Linderoth AS, N. Bonanos, A. Hagen, L. Mikkelsen, K. Kammer, D. Lybye, P.V. Hendriksen, F.W. Poulsen, M. Mogensen, W.G. Wang, editor. **2005**. p. 215-22.

- [115] Hagen A, Barfod R, Hendriksen PV, Liu YL, Ramousse S. *Degradation of anode supported SOFCs as a function of temperature and current load*. Journal of the Electrochemical Society **2006**;153:A1165-A71.
- [116] G. Orsello GD, K. Litzinger, R. Basel, M. Cali, M. Santrelli. *7th European SOFC Forum Oberrohrdorf, Switzerland 2006*.
- [117] Mai A, Becker M, Assenmacher W, Tietz F, Hathiramani D, Ivers-Tiffée E, et al. *Time-dependent performance of mixed-conducting SOFC cathodes*. Solid State Ionics **2006**;177:1965-8.
- [118] Tietz F, Mai, A., Stöver, D. . *From powder properties to fuel cell performance - A holistic approach for SOFC cathode development* Solid State Ionics **2008** ;179:1509-15.
- [119] Matsuzaki Y, Yasuda I. *Electrochemical properties of a SOFC cathode in contact with a chromium-containing alloy separator*. Solid State Ionics **2000**;132:271-8.
- [120] Simner SP, Anderson MD, Xia GG, Yang Z, Pederson LR, Stevenson JW. *SOFC performance with Fe-Cr-Mn alloy interconnect*. Journal of the Electrochemical Society **2005**;152:A740-A5.
- [121] Konyshova E, Penkalla H, Wessel E, Mertens J, Seeling U, Singheiser L, et al. *Chromium poisoning of perovskite cathodes by the ODS alloy Cr5Fe1 Y2 O3 and the high chromium ferritic steel Crofer 22 APU*. Journal of the Electrochemical Society **2006** ;153:A765-A73.
- [122] Yokokawa H, Horita T, Sakai N, Yamaji K, Brito ME, Xiong YP, et al. *Thermodynamic considerations on Cr poisoning in SOFC cathodes*. Solid State Ionics **2006**;177:3193-8.
- [123] Caplan D, Cohen M. *The Volatilization of Chromium Oxide*. Journal of the Electrochemical Society **1961**;108:438-42.
- [124] Zaplatynsky I. *Volatilization of oxides during oxidation of some superalloys at 1200°C*. Oxidation of Metals 1977;11:289-305.
- [125] Ebbinghaus BB. *Thermodynamics of gas phase chromium species: The chromium oxides, the chromium oxyhydroxides, and volatility calculations in waste incineration processes*. Combustion and Flame **1993**;93:119-37.
- [126] Kofstad P, Bredesen R. *High temperature corrosion in SOFC environments*. Solid State Ionics **1992**;52:69-75.
- [127] Jiang SP, Zhang JP, Foger K. *Deposition of chromium species at Sr-doped LaMnO₃ electrodes in solid oxide fuel cells. II. Effect on O₂ reduction reaction*. Journal of the Electrochemical Society **2000**;147:3195-205.
- [128] Franco T, Brandner M, Rüttinger M, Kunschert G, Venskutonis A, Sigl LS. *Recent development aspects of metal supported thin-film SOFC*. 2 PART 1 ed. Vienna **2009**. p. 681-8.
- [129] Franco T, Schibinger K, Ilhan Z, Schiller G, Venskutonis A. *Ceramic diffusion barrier layers for metal supported SOFCs*. 1 PART 1 ed **2007**. p. 771-80.
- [130] Ebbinghaus BB. *Thermodynamics of gas phase chromium species: The chromium oxides, the chromium oxyhydroxides, and volatility calculations in waste incineration processes*. Combustion and Flame **1993**;93:119-37.
- [131] K.R. Williams JGS. *Fuel Cell with Solid State Electrolytes* 1969;US3.
- [132] Momma A, Kaga Y, Okuo T, Fujii K, Hohjyo K, Kanazawa M. *Improvement of the electrode performance of alloy substrate-type tubular SOFC - development and*

application of the intermediate layer. Denshi Gijutsu Sogo Kenkyusho Iho/Bulletin of the Electrotechnical Laboratory **1999**;63:1-11.

[133] Schiller G, Henne RH, Lang M, Ruckdäschel R, Schaper S. *Development of vacuum plasma sprayed thin-film SOFC for reduced operating temperature*. Fuel Cells Bulletin **2000**;3:7-12.

[134] Bance P, Brandon NP, Girvan B, Holbeche P, O'Dea S, Steele BCH. *Spinning-out a fuel cell company from a UK University - 2 years of progress at Ceres Power*. Journal of Power Sources **2004**;131:86-90.

[135] Villarreal I, Jacobson C, Leming A, Matus Y, Visco S, De Jonghe L. *Metal-supported solid oxide fuel cells*. Electrochemical and Solid-State Letters **2003**;6:A178-A9.

[136] Ansar A, Szabo P, Arnold J, Ilhan Z, Soysal D, Costa R, et al. *Metal supported solid oxide fuel cells and stacks for auxiliary power units - Progress, challenges and lessons learned*. 1 PART 1 ed. Montreal, QC**2011**. p. 147-55.

[137] Leah RT, Brandon NP, Aguiar P. *Modelling of cells, stacks and systems based around metal-supported planar IT-SOFC cells with CGO electrolytes operating at 500-600°C*. Journal of Power Sources **2005**;145:336-52.

[138] Blennow P, Hjelm J, Klemensø T, Ramousse S, Kromp A, Leonide A, et al. *Manufacturing and characterization of metal-supported solid oxide fuel cells*. Journal of Power Sources **2011**;196:7117-25.

[139] Rodriguez-Martinez LM, Otaegi L, Alvarez MA, Rivas M, Gomez N, Zabala A, et al. *Degradation studies on tubular metal supported SOFC*. 2 PART 1 ed. Vienna **2009**. p. 745-52.

[140] Tietz F. *Thermal expansion of SOFC materials*. Ionics **1999**;5:129-39.

[141] Mori M, Yamamoto T, Itoh H, Inaba H, Tagawa H. *Thermal expansion of nickel-zirconia anodes in solid oxide fuel cells during fabrication and operation*. Journal of the Electrochemical Society **1998**;145:1374-81.

[142] Antepará I, Villarreal I, Rodríguez-Martínez LM, Lecanda N, Castro U, Laresgoiti A. *Evaluation of ferritic steels for use as interconnects and porous metal supports in IT-SOFCs*. Journal of Power Sources **2005**;151:103-7.

[143] Franco T, Haydn M, Mücke R, Weber A, Rüttinger M, Büchler O, et al. *Development of metal-supported solid oxide fuel cells*. 1 PART 1 ed. Montreal, QC**2011**. p. 343-9.

[144] Kleinlogel C, Gauckler LJ. *Sintering and properties of nanosized ceria solid solutions*. Solid State Ionics **2000**;135:567-73.

[145] Lewis GS, Atkinson A, Steele BCH, Drennan J. *Effect of Co addition on the lattice parameter, electrical conductivity and sintering of gadolinia-doped ceria*. Solid State Ionics **2002**;152-153:567-73.

[146] Nicholas JD, De Jonghe LC. *Prediction and evaluation of sintering aids for Cerium Gadolinium Oxide*. Solid State Ionics **2007**;178:1187-94.

[147] Oishi N, Yoo Y. *Fabrication of cerium oxide based SOFC having a porous stainless steel support*. 2 PART 1 ed. Vienna **2009**. p. 739-44.

[148] Steele BCH. *Appraisal of Ce_{1-y}Gd_yO_{2-y/2} electrolytes for IT-SOFC operation at 500 °C*. Solid State Ionics **2000**;129:95-110.

[149] Brandon NP, Blake A, Corcoran D, Cumming D, Duckett A, El-Koury K, et al. *Development of metal supported solid oxide fuel cells for operation at 500-600 °C*. Journal of Fuel Cell Science and Technology **2004**;1:61-5.

- [150] Ltd. CP. *Development of innovative metal-supported IT-SOFC technology*. DTI Technology Programme: New and Renewable Energy, Future Energy Solutions **2005**.
- [151] Vaßen R, Hathiramani D, Mertens J, Haanappel VAC, Vinke IC. *Manufacturing of high performance solid oxide fuel cells (SOFCs) with atmospheric plasma spraying (APS)*. Surface and Coatings Technology **2007**;202:499-508.
- [152] Vaßen R, Kaßner H, Stuke A, Hauler F, Hathiramani D, Stöver D. *Advanced thermal spray technologies for applications in energy systems*. Surface and Coatings Technology **2008**;202:4432-7.
- [153] Lang M, Franco T, Schiller G, Wagner N. *Electrochemical characterization of vacuum plasma sprayed thin-film solid oxide fuel cells (SOFC) for reduced operating temperatures*. Journal of Applied Electrochemistry **2002**;32:871-4.
- [154] Lang M, Szabo P, Ilhan Z, Cinque S, Franco T, Schiller G. *Development of solid oxide fuel cells and short stacks for mobile application*. Journal of Fuel Cell Science and Technology **2007**;4:384-91.
- [155] Schiller G, Ansar A, Lang M, Patz O. *High temperature water electrolysis using metal supported solid oxide electrolyser cells (SOEC)*. Journal of Applied Electrochemistry **2009**;39:293-301.
- [156] Wang Z, Berghaus JO, Yick S, Decès-Petit C, Qu W, Hui R, et al. *Dynamic evaluation of low-temperature metal-supported solid oxide fuel cell oriented to auxiliary power units*. Journal of Power Sources **2008**;176:90-5.
- [157] Hui S, Yang D, Wang Z, Yick S, Decès-Petit C, Qu W, et al. *Metal-supported solid oxide fuel cell operated at 400-600 °C*. Journal of Power Sources **2007**;167:336-9.
- [158] Szabo P, Arnold J, Franco T, Gindrat M, Refke A, Zagst A, et al. *Progress in the metal supported solid oxide fuel cells and stacks for APU*. 2 PART 1 ed. Vienna **2009**. p. 175-85.
- [159] Henne R. *Solid oxide fuel cells: A challenge for plasma deposition processes*. Journal of Thermal Spray Technology **2007**;16:381-403.
- [160] Blennow P, Hjelm J, Klemensø T, Persson Å, Brodersen K, Srivastava AK, et al. *Development of planar metal supported SOFC with novel cermet anode*. 2 PART 1 ed. Vienna **2009**. p. 701-10.
- [161] Blennow P, Klemensø T, Persson ÅH, Brodersen K, Srivastava AK, Sudireddy BR, et al. *Metal-supported SOFC with ceramic-based anode*. 1 PART 1 ed. Montreal **2011**, QC2011. p. 683-92.
- [162] Klemensø T, Nielsen J, Blennow P, Persson ÅH, Stegk T, Hjalmarsson P, et al. *Development of long-term stable and high-performing metal-supported SOFCs*. 1 PART 1 ed. Montreal, QC**2011**. p. 369-78.
- [163] Blennow P, Hansen KK, Wallenberg LR, Mogensen M. *Strontium titanate-based composite anodes for solid oxide fuel cells*. 26 ed. Phoenix, AZ **2008**. p. 181-94.
- [164] Rüttinger M, Mücke R, Franco T, Büchler O, Menzler NH, Venskutonis A. *Metal-supported cells with comparable performance to anode-supported cells in short-term stack environment*. 1 PART 1 ed. Montreal, QC**2011**. p. 259-68.
- [165] T. Franco RR, et al. *7th European Solid Oxide Fuel Cell Forum Proceedings*. 7th European Solid Oxide Fuel Cell Forum. Lucerne, Switzerland .
- [166] T. Franco RHea. In: S.C. Singhal MD, editor. *Solid Oxide Fuel Cell VIII (SOFC VIII, Paris)*. Paris **2003**. p. 923-32.

- [167] Tucker MC, Sholkapper TZ, Lau GY, DeJonghe LC, Visco SJ. *Progress in metal-supported SOFCs*. 2 PART 1 ed. Vienna **2009**. p. 673-80.
- [168] Webber J. *Oxidation of Fe-Cr alloys in O₂/3% H₂O*. Corrosion Science **1976**;16:499-504.
- [169] Hänsel M, Quadackers WJ, Young DJ. *Role of water vapor in chromia-scale growth at low oxygen partial pressure*. Oxidation of Metals **2003**;59:285-301.
- [170] Hou PY, Stringer J. *The effect of reactive element additions on the selective oxidation, growth and adhesion of chromia scales*. Materials Science and Engineering A **1995**;202:1-10.
- [171] Holt A, Kofstad P. *Electrical conductivity and defect structure of Cr₂O₃*. II. Reduced temperatures (<~1000°C). Solid State Ionics **1994**;69:137-43.
- [172] Larring Y, Haugsrud R, Norby T. *HT corrosion of a Cr-5 wt % Fe-1 wt % Y₂O₃ alloy and conductivity of the oxide scale. Effects of water vapor*. Journal of the Electrochemical Society **2003**;150:B374-B9.
- [173] Brandner M, Bram M, Froitzheim J, Buchkremer HP, Stöver D. *Electrically Conductive Diffusion barrier layers for Metal-Supported SOFC*. Solid State Ionics **2008**;179:1501-4.
- [174] J. Froitzheim LN, M. Bradner, L. Singheiser and W.J. Quadackers. *Anode side diffusion barrier coating for solid oxide fuel cells interconnects*. Journal of Fuel Cell science and Tecnology **2010**;7:0310201.
- [175] Franco T, Hoshidar Din Z, Szabo P, Lang M, Schiller G. *Plasma sprayed diffusion barrier layers based on doped perovskite-type LaCrO₃ at substrate-anode interface in solid oxide fuel cells*. Journal of Fuel Cell Science and Technology **2007**;4:406-12.
- [176] S. J. Visco CPJ. *8th International Symposium on Solid Oxide Fuel Cells*. Paris, France: Electrochemical Society Proceedings; **2003**. p. 1040/50.
- [177] Chen CY, Lyu YR. *Effect of NiO addition on properties of bulk yttria-doped ceria sintered from their spray pyrolyzed powder*. Ceramics International **2012**;38:3291-300.
- [178] Van Herle J, Horita T, Kawada T, Sakai N, Yokokawa H, Dokiya M. *Low temperature fabrication of (Y,Gd,Sm)-doped ceria electrolyte*. Solid State Ionics **1996**;86-88:1255-8.
- [179] L. O. *Desarrollo de celdas de combustible de tipo SOFC tubulares de soporte metálico: tecnun - Universidad de Navarra*; **2013**.
- [180] Zengwu Y, Min F, Xingeng L, Xuelei T. *High temperature oxidation behavior of TP304H steel coated with CeO₂ in water vapor*. Oxidation of Metals **2010**;74:157-65.
- [181] Hussey RJ, Papaicovou P, Shen J, Mitchell DF, Graham MJ. *Effect of ceria coatings on the high-temperature oxidation of iron-chromium alloys*. Materials Science and Engineering A **1989**;A120-1:147-51.
- [182] Pérez-Coll D, Aguadero A. *Electrochemical performance of La₂NiO₄-based cathode for solid oxide fuel cells. Single cell test*. Fuel Cells **2011**;11:91-101.
- [183] Reynaud M. *Etude de trois oxydes solides pour leur application en tant que barrière à la diffusion du chrome entre l'anode et le support métallique de la SOFC* École nationale supérieure de chimie de Paris; **2010**.
- [184] Li X, Zhao H, Gao F, Chen N, Xu N. *La and Sc co-doped SrTiO₃ as novel anode materials for solid oxide fuel cells*. Electrochemistry Communications **2008**;10:1567-70.

- [185] Matus YB, De Jonghe LC, Jacobson CP, Visco SJ. *Metal-supported solid oxide fuel cell membranes for rapid thermal cycling*. Solid State Ionics **2005**;176:443-9.
- [186] Tucker MC, Lau GY, Jacobson CP, DeJonghe LC, Visco SJ. *Stability and robustness of metal-supported SOFCs*. Journal of Power Sources **2008**;175:447-51.
- [187] Iwanschitz B, Holzer L, Mai A, Schütze M. *Nickel agglomeration in solid oxide fuel cells: The influence of temperature*. Solid State Ionics **2012**;211:69-73.
- [188] Tucker MC, Lau GY, Jacobson CP, DeJonghe LC, Visco SJ. *Performance of metal-supported SOFCs with infiltrated electrodes*. Journal of Power Sources **2007**;171:477-82.
- [189] M.C. Tucker CPJ. *Cu-based cermet for high-temperature fuel cell*. **2009**.
- [190] Minic D. *Hydrogen Energy - Challenges and Perspectives*.
- [191] Keys LNMaLK. *Studies on Adsorption of Oxygen on γ -Alumina. Nature of Adsorbed Species*. Journal of the American Chemical Society **1965**;87:6.
- [192] Pier Francesco Rossi GOaMB. *Heat of Water Chemisorption on α -Al₂O₃ at 200-400°C*. Journal of the Chemical Society, Faraday Transactions **1994**;90:363-7.
- [193] Peri JB. *Infrared and Gravimetric Study of Surface Hydration of γ -Alumina*. Journal of Physical Chemistry **1965**;69:211-9.
- [194] www.vaisala.com. Humidity Conversion Formulas. In: Vaisala, editor. 2010.
- [195] Jülich F. Crofer 22 APU Material Data Sheet. TV GmbH, Editor 2010.
- [196] <http://www.sofcpower.com>.
- [197] Bertoldi M, Bucheli O, Modena S, Larrain D, Ravagni A. *Manufacturing and market-oriented development of SOFC generators at SOFCpower SpA*. 1 PART 1 ed. Montreal, QC **2011**. p. 127-38.
- [198] <http://enefield.eu/>.
- [199] Bertoldi M, Bucheli O, Ravagni A, Autissier N, Signorini M, Modena S. *Status report of SOFC development and pilot manufacturing at SOFCpower Srl*. 2 PART 1 ed. Vienna **2009**. p. 105-14.
- [200] Bouwmeester HJM, Den Otter MW, Boukamp BA. *Oxygen transport in La_{0.6}Sr_{0.4}Co_{1-x}Fe_xO_{3-delta}*. J Solid State Electrochem **2004**;8:599-605.
- [201] Mai A, Becker M, Assenmacher W, Tietz F, Hathiramani D, Ivers-Tiffée E, et al. *Time-dependent performance of mixed-conducting SOFC cathodes*. Solid State Ionics **2006**;177:1965-8.
- [202] Kim WH, Song HS, Moon J, Lee HW. *Intermediate temperature solid oxide fuel cell using (La,Sr)(Co,Fe)O₃-based cathodes*. Solid State Ionics **2006**;177:3211-6.
- [203] C. Gindorf LS, K. Hilpert, M. Schroeder, M. Martin, H. Greiner, F. Richter. *Chromium vaporization from metallic interconnect and retention by perovskite layers*. In: S.C. Singhal MD, editor. Solid Oxide Fuel Cells VI. Pennington, NJ: Electrochemical Society; **1999**. p. 774-82.
- [204] Matsuzaki Y, Yasuda I. *Dependence of SOFC Cathode Degradation by Chromium-Containing Alloy on Compositions of Electrodes and Electrolytes*. Journal of the Electrochemical Society **2001**;148:A126-A31.
- [205] Hilpert K, Das D, Miller M, Peck DH, Weiß R. *Chromium vapor species over solid oxide fuel cell interconnect materials and their potential for degradation processes*. Journal of the Electrochemical Society **1996**;143:3642-7.
- [206] Li JQ, Xiao P. *Fabrication and characterisation of La_{0.8}Sr_{0.2}MnO₃/metal interfaces for application in SOFCs*. Journal of the European Ceramic Society **2001**;21:659-68.

- [207] Jiang SP, Zhang JP, Apateanu L, Foger K. *Deposition of chromium species at Sr-doped LaMnO₃ electrodes in solid oxide fuel cells. I. Mechanism and kinetics.* Journal of the Electrochemical Society **2000**;147:4013-22.
- [208] Nielsen J, Hagen A, Liu YL. *Effect of cathode gas humidification on performance and durability of Solid Oxide Fuel Cells.* Solid State Ionics **2010**;181:517-24.
- [209] Bucher E, Sitte W, Klauser F, Bertel E. *Oxygen exchange kinetics of La_{0.58}Sr_{0.4}Co_{0.2}Fe_{0.8}O₃ at 600 °C in dry and humid atmospheres.* Solid State Ionics **2011**;191:61-7.
- [210] Bucher E, Sitte W, Klauser F, Bertel E. *Impact of humid atmospheres on oxygen exchange properties, surface-near elemental composition, and surface morphology of La_{0.6}Sr_{0.4}CoO_{3-δ}.* Solid State Ionics **2012**;208:43-51.
- [211] Copeland WD, Swalin RA. *Studies on the defect structure of strontium oxide.* Journal of Physics and Chemistry of Solids **1968**;29:313-25.
- [212] Mehrotra PN, Chandrashekar GV, Rao CNR, Subbarao EC. *Phase transformations of rare earth sesquioxides La₂O₃, Nd₂O₃, Pr₂O₃ and Y₂O₃.* Transactions of the Faraday Society **1966**;62:3586-90.
- [213] R. Steinberger-Wilckens ICV, L. Blum, L.G. J. de Haart, J. Rimmel, F. Tientz, W.J. Quadackers. *6th European Solid Oxide Fuel Cell Forum* **2004**:11-9.
- [214] Tai LW, Nasrallah MM, Anderson HU, Sparlin DM, Sehlin SR. *Structure and electrical properties of La_{1-x}Sr_xCo_{1-y}Fe_yO₃. Part 1. The system La_{0.8}Sr_{0.2}Co_{1-y}Fe_yO₃.* Solid State Ionics **1995**;76:259-71.
- [215] Petric A, Huang P, Tietz F. *Evaluation of La-Sr-Co-Fe-O perovskites for solid oxide fuel cells and gas separation membranes.* Solid State Ionics **2000**;135:719-25.
- [216] Kim SH, Shim KB, Kim CS, Chou JT, Oshima T, Shiratori Y, et al. *Degradation of solid oxide fuel cell cathodes accelerated at a high water vapor concentration.* Journal of Fuel Cell Science and Technology **2010**;7:0210111-6.
- [217] A.Hagen RB, P.Van Hendriksen, Y.L. Liu, S. Ramousse. *Journal of the Electrochemical Society* **2006** 153:A1165-A71.
- [218] M.J. Heneka El-T. *Influence of high current cycling on the performance of SOFC single cells.* In: M.J. Heneka El-T, in: S. Linderoth, A.Smith, N. Bonanos, A. Hagen, L. Mikkelsen, K. Kammer, D. Lybye, P.V. Hendriksen, F.W. Poulsen, M. Mogensen, W.G. Wang editor. *26th Risoe International Symposium on Materials Science* **2005**. p. 215-22.
- [219] Timmermann H. *International workshop on Degradation Issues in Fuel Cell* **2007**.
- [220] Bouwmeester HJM, Kruidhof H, Burggraaf AJ. *Importance of the surface exchange kinetics as rate limiting step in oxygen permeation through mixed-conducting oxides.* Solid State Ionics **1994**;72:185-94.
- [221] Adler SB, Lane JA, Steele BCH. *Electrode kinetics of porous mixed-conducting oxygen electrodes.* Journal of the Electrochemical Society **1996**;143:3554-64.
- [222] Falamaki C, Veysizadeh J. *Taguchi design of experiments approach to the manufacture of one-step alumina microfilter/membrane supports by the centrifugal casting technique.* Ceramics International **2008**;34:1653-9.
- [223] Wahdame B, Candusso D, François X, Harel F, Kauffmann JM, Coquery G. *Design of experiment techniques for fuel cell characterisation and development.* International Journal of Hydrogen Energy **2009**;34:967-80.

- [224] Liu M. *Equivalent circuit approximation to porous mixed-conducting oxygen electrodes in solid-state cells*. Journal of the Electrochemical Society **1998**;145:142-54.
- [225] S. Bebelis NK, A. Mai, F. Tietz. *Electrochemical characterization of perovskite-based SOFC cathodes*. Journal of Applied Electrochemistry **2007**;37:15-20.
- [226] Ingram BJ, Cruse TA, Krumpelt M. *Potassium-assisted chromium transport in solid oxide fuel cells*. Journal of the Electrochemical Society **2007**;154:B1200-B5.
- [227] Sharma VI, Yildiz B. *Degradation Mechanism in $La_{0.8}Sr_{0.2}CoO_3$ as Contact Layer on the Solid Oxide Electrolysis Cell Anode*. Journal of the Electrochemical Society **2010**;157:B441-B8.
- [228] Sakamoto S, Yoshinaka M, Hirota K, Yamaguchi O. *Fabrication, mechanical properties, and electrical conductivity of Co_3O_4 ceramics*. Journal of the American Ceramic Society **1997**;80:267-8.
- [229] Weakley TJR, Ylvisaker ER, Yager RJ, Stephens JE, Wiegel RD, Mengis M, et al. *Phase transitions in $K_2Cr_2O_7$ and structural redeterminations of phase II*. Acta Crystallographica Section B: Structural Science **2004**;60:705-15.
- [230] Steinberger-Wilckens R, Vinke IC, Blum L, de Haart LGJ, Rimmel J, Tietz F, et al. *Progress in SOFC Stack Development at Forschungszentrum Jülich*. Proc 6th European Solid Oxide Fuel Cells Forum **2004**;1:11-9.
- [231] Backer M, Mai A, Ivers-Tiffée E, Tietz F. *Long-term measurements of anode-supported solid oxide fuel cells with Iscf cathodes under various operating conditions*. In: Singhal SC, Mizusaki J, editors. Quebec **2005**. p. 514-23.
- [232] Sakai N, Horita T, Yamaji K, Xiong YP, Kishimoto H, Brito ME, et al. *Material transport and degradation behavior of SOFC interconnects*. Solid State Ionics **2006**;177:1933-9.
- [233] Brittain RD, Lau KH, Hildenbrand DL. *Mechanism and Thermodynamics of the vaporization of K_2CrO_4* . Journal of the Electrochemical Society **1987**;134:2900-4.
- [234] Larring Y, Norby T. *Spinel and perovskite functional layers between Plansee metallic interconnect (Cr-5 wt% Fe-1 wt% Y_2O_3) and ceramic ($La_{0.85}Sr_{0.15}O_{0.91}MnO_3$) cathode materials for solid oxide fuel cells*. Journal of the Electrochemical Society **2000**;147:3251-6.
- [235] Yang Z, Xia GG, Maupin GD, Stevenson JW. *Conductive protection layers on oxidation resistant alloys for SOFC interconnect applications*. Surface and Coatings Technology **2006**;201:4476-83.
- [236] Mikkelsen L, Chen M, Hendriksen PV, Persson Å, Pryds N, Rodrigo K. *Deposition of $La_{0.8}Sr_{0.2}Cr_{0.97}V_{0.03}O_3$ and $MnCr_2O_4$ thin films on ferritic alloy for solid oxide fuel cell application*. Surface and Coatings Technology **2007**;202:1262-6.
- [237] Huang K, Hou PY, Goodenough JB. *Characterization of iron-based alloy interconnects for reduced temperature solid oxide fuel cells*. Solid State Ionics **2000**;129:237-50.
- [238] Chen L, Sun EY, Yamanis J, Magdefrau N. *Oxidation kinetics of $Mn_{1.5}Co_{1.5}O_4$ -coated Haynes 230 and Crofer 22 APU for solid oxide fuel cell interconnects*. Journal of the Electrochemical Society **2010**;157:B931-B42.
- [239] Yang Z, Xia G, Nie Z, Templeton J, Stevenson JW. *Ce-modified $(Mn,Co)_3O_4$ spinel coatings on ferritic stainless steels for SOFC interconnect applications*. Electrochemical and Solid-State Letters **2008**;11:B140-B3.

- [240] Montero X, Tietz F, Sebold D, Buchkremer HP, Ringuede A, Cassir M, et al. *MnCo_{1.9}Fe_{0.1}O₄ spinel protection layer on commercial ferritic steels for interconnect applications in solid oxide fuel cells*. Journal of Power Sources **2008**;184:172-9.
- [241] Matthew M. Seabaugh SI, Scott L. Swartz. *Protective coatings for metal alloys and methods incorporating the same*. In: (US) CO, editor. **2012**.
- [242] S. Visco CJ, L. De Joghe, A. Leming, Y. Matus, L. Yang, I. Villarreal, L. Rodriguez-Martinez. *Ionic and Mixed Conducting Ceramics IV*.
- [243] GmbH TV. Crofer APU Data Sheet No. 4046. http://www.thyssenkruppvdm-fareast.com/media/download/datasheets/heatres/new/crofer22apu_e.pdf **2005**.
- [244] K. Hilpert WJQ, L. Singheiser. *Interconnects Handbook of Fuel Cells - Fundamentals, Technology and Applications* **2003**.
- [245] Sarasketa-Zabala E, Otaegi L, Rodriguez-Martinez LM, Alvarez MA, Burgos N, Castro F, et al. *High temperature stability of porous metal substrates under highly humidified hydrogen conditions for metal supported Solid Oxide Fuel Cells*. Solid State Ionics **2012**;222-223:16-22.
- [246] Kim SG, Yoon SP, Nam SW, Hyun SH, Hong SA. *Fabrication and characterization of a YSZ/YDC composite electrolyte by a sol-gel coating method*. Journal of Power Sources **2002**;110:222-8.
- [247] Faes A, Wullemijn Z, Tanasini P, Accardo N, Modena S, Schindler HJ, et al. *Design of experiment approach applied to reducing and oxidizing tolerance of anode supported solid oxide fuel cell. Part II: Electrical, electrochemical and microstructural characterization of tape-cast cells*. Journal of Power Sources **2011**;196:8909-17.
- [248] Kurokawa H, Kawamura K, Maruyama T. *Oxidation behavior of Fe-16Cr alloy interconnect for SOFC under hydrogen potential gradient*. Solid State Ionics **2004**;168:13-21.
- [249] Moon H, Kim SD, Park EW, Hyun SH, Kim HS. *Characteristics of SOFC single cells with anode active layer via tape casting and co-firing*. International Journal of Hydrogen Energy **2008**;33:2826-33.
- [250] Primdahl S, Mogensen M. *Oxidation of hydrogen on Ni/yttria-stabilized zirconia cermet anodes*. Journal of the Electrochemical Society **1997**;144:3409-19.
- [251] Kong J, Sun K, Zhou D, Zhang N, Mu J, Qiao J. *Ni-YSZ gradient anodes for anode-supported SOFCs*. Journal of Power Sources **2007**;166:337-42.
- [252] Chen K, Chen X, Lü Z, Ai N, Huang X, Su W. *Performance of an anode-supported SOFC with anode functional layers*. Electrochimica Acta **2008**;53:7825-30.
- [253] Juhl M, Primdahl S, Manon C, Mogensen M. *Performance/structure correlation for composite SOFC cathodes*. Journal of Power Sources **1996**;61:173-81.
- [254] Cai Q, Adjiman CS, Brandon NP. *Investigation of the active thickness of solid oxide fuel cell electrodes using a 3D microstructure model*. Electrochimica Acta **2011**;56:10809-11.
- [255] Buscaill H, Perrier S, Josse C. *Oxidation mechanism of the Inconel 601 alloy at high temperatures*. Materials and Corrosion **2011**;62:416-22.
- [256] Mori M, Hiei Y, Itoh H, Tompsett GA, Sammes NM. *Evaluation of Ni and Ti-doped Y₂O₃ stabilized ZrO₂ cermet as an anode in high-temperature solid oxide fuel cells*. Solid State Ionics **2003**;160:1-14.
- [257] Steele BCH. *Ceramic ion conducting membranes*. Current Opinion in Solid State and Materials Science **1996**;1:684-91.
- [258] Haile SM. *Fuel cell materials and components*. Acta Materialia **2003**;51:5981-6000.

- [259] Ma Q, Tietz F, Sebold D, Stöver D. *Y-substituted SrTiO₃-YSZ composites as anode materials for solid oxide fuel cells: Interaction between SYT and YSZ*. Journal of Power Sources **2010**;195:1920-5.
- [260] He H, Huang Y, Vohs JM, Gorte RJ. *Characterization of YSZ-YST composites for SOFC anodes*. Solid State Ionics **2004**;175:171-6.
- [261] Huang X, Zhao H, Qiu W, Wu W, Li X. *Performances of planar solid oxide fuel cells with doped strontium titanate as anode materials*. Energy Conversion and Management **2007**;48:1678-82.
- [262] Kurokawa H, Yang L, Jacobson CP, De Jonghe LC, Visco SJ. *Y-doped SrTiO₃ based sulfur tolerant anode for solid oxide fuel cells*. Journal of Power Sources **2007**;164:510-8.
- [263] Kim G, Gross MD, Wang W, Vohs JM, Gorte RJ. *SOFC anodes based on LST-YSZ composites and on Y_{0.04}Ce_{0.48}Zr_{0.48}O₂*. Journal of the Electrochemical Society **2008**;155:B360-B6.
- [264] Duncan KL, Lee KT, Wachsman ED. *Dependence of open-circuit potential and power density on electrolyte thickness in solid oxide fuel cells with mixed conducting electrolytes*. Journal of Power Sources **2011**;196:2445-51.
- [265] Kishimoto H, Suzuki A, Shimonosono T, Brito ME, Yamaji K, Horita T, et al. *Agglomeration behavior of nickel particles on YSZ and TiO₂-doped YSZ electrolytes*. Journal of Power Sources **2012**;199:174-8.
- [266] Kowalski K, Bernasik A, Sadowski A. *Bulk and grain boundary diffusion of titanium in yttria-stabilized zirconia. Dedicated to the memory of Professor Jan Janowski*. Journal of the European Ceramic Society **2000**;20:951-8.
- [267] Chen MH, Jiang TL. *The analyses of the start-up process of a planar, anode-supported solid oxide fuel cell using three different start-up procedures*. Journal of Power Sources **2012**;220:331-41.
- [268] Lin PH, Hong CW. *Cold start dynamics and temperature sliding observer design of an automotive SOFC APU*. Journal of Power Sources **2009**;187:517-26.
- [269] Petruzzi L, Cocchi S, Fineschi F. *A global thermo-electrochemical model for SOFC systems design and engineering*. Journal of Power Sources **2003**;118:96-107.
- [270] Gardner FJ, Day MJ, Brandon NP, Pashley MN, Cassidy M. *SOFC technology development at Rolls-Royce*. Journal of Power Sources **2000**;86:122-9.
- [271] Almutairi G, Kendall K, Bujalski W. *Cycling durability studies of IP-SOFC*. International Journal of Low-Carbon Technologies **2012**;7:63-8.
- [272] Antepará I, Díaz L, Rivas M, Otaegi L, Gomez N, Villarreal I, et al. *Electrochemical behavior of metal-supported SOFCs under high fuel utilization and their durability*. Journal of Fuel Cell Science and Technology **2012**;9.
- [273] G. Robert AKaEB. *Anode substrate Design for RedOx-Stable ASE Cells*. 6th European Solid Oxide Fuel Cell Forum **2004**.
- [274] Cassidy M, Lindsay G, Kendall K. *The reduction of nickel-zirconia cermet anodes and the effects on supported thin electrolytes*. Journal of Power Sources **1996**;61:189-92.
- [275] Malzbender J, Wessel E, Steinbrech RW. *Reduction and re-oxidation of anodes for solid oxide fuel cells*. Solid State Ionics **2005**;176:2201-3.
- [276] Kim SD, Moon H, Hyun SH, Moon J, Kim J, Lee HW. *Performance and durability of Ni-coated YSZ anodes for intermediate temperature solid oxide fuel cells*. Solid State Ionics **2006**;177:931-8.

- [277] Monzón H, Laguna-Bercero MA. *Redox-cycling studies of anode-supported microtubular solid oxide fuel cells*. International Journal of Hydrogen Energy **2012**;37:7262-70.
- [278] Beuth Jr JL. *Cracking of thin bonded films in residual tension*. International Journal of Solids and Structures **1992**;29:1657-75.
- [279] Zhou L, Cheng M, Yi B, Dong Y, Cong Y, Yang W. *Performance of an anode-supported tubular solid oxide fuel cell (SOFC) under pressurized conditions*. Electrochimica Acta **2008**;53:5195-8.
- [280] http://www.doitpoms.ac.uk/tlplib/ellingham_diagrams/contents.php.

SCIENTIFIC PRODUCTION

Amaia Arregui, Laida Otaegui and Lide M. Rodriguez-Martinez, *Stability under severe operation of tubular metal supported SOFCs*, In preparation.

Arregui A., Rodriguez-Martinez LM., Modena S., Bertoldi M., van Herle J., Sglavo VM., *Cathode degradation mechanisms by potassium/chromium poisoning and air humidification*. Fuel Cells (Accepted).

Lide M. Rodriguez-Martinez, Laida Otaegui, Amaia Arregui, Mario A. Alvarez, Igor Villarreal, *Tubular metal supported solid oxide fuel cell resistant to high fuel utilization*, 10th European SOFC Forum, **2012**, A0905.

Arregui A., Rodriguez-Martinez LM., Modena S., Bertoldi M., van Herle J., Sglavo VM., *Stability of ferritic perovskite cathodes in anode-supported solid oxide fuel cells under different processing and operation parameters*. Electrochimica Acta **2011**;58;312-21.

Arregui A., Rodriguez-Martinez LM, Modena S., Bertoldi M., van Herle J., Sglavo VM., *Influence of operational parameters on LSF and LSCF cathodes degradation*. The American Ceramic Society's Ceramic Engineering and Science Proceedings **2011**;32.

PARTICIPATION TO CONGRESSES, SCHOOLS AND WORKSHOPS

Lide M. Rodriguez-Martinez, Laida Otaegui, Amaia Arregui, Mario A. Alvarez, Igor Villarreal,

10th European SOFC Forum

Tubular metal supported solid oxide fuel cell resistant to high fuel utilization, Lucerne Switzerland, June 26-29 2012. Oral co-author

Amaia Arregui, Lide M. Rodriguez-Martinez, Stefano Modena, Massimo Bertoldi, Jan van Herle and Vincenzo M. Sglavo

ECeS XII 12th Conference of the European Ceramic Society

Influence of operational parameters in LSCF and LSF cathodes degradation, Stockholm Sweden, June 19-23 2011. Oral presentation

7th International Solid Oxide Fuel Cell Summer School

"Introduction to SOFC Science and Technology", Thessaloniki Greece 29th August – 2nd September 2010. Attende

Scuola Estiva Nazionale, Edizione Speciale ESOF 2010

SCIENZA APERTA – "Ricerca e Società: analisi dell'efficacia Comunicativa di un grande evento", Torino Italy, July 01-06 2010. Attende

Amaia Arregui, Lide M. Rodriguez-Martinez, Stefano Modena, Massimo Bertoldi, Jan van Herle and Vincenzo M. Sglavo

34th International Conference and Exposition on Advanced Ceramics and Composites

Influence of operational parameters on LSCF and LSF stability in anode-supported SOFC, Daytona Beach, January 24 -29, 2010. Poster session

OTHER ACTIVITIES

This research activity is a result of a collaboration initiated by IK4-IKERLAN in Spain and SOFCpower in Italy, as a way to reinforce the understanding of degradation in intermediate temperature cathodes of common interest. Amaia Arregui has been the main driver of this established international collaboration between Ikerlan and SOFCPower Srl and Department of Materials Engineering and Industrial Technologies of Trento (DIMTI) and EPFL – Swiss Federal Institute of Technology, LENI (Lausanne, Switzerland).

As a result, Amaia went to SOFCpower to initiate cathode stability analysis as well as to follow the doctoral program in the University of Trento, between January 2009 and April 2011. The main activities included experimental set up for long term testing of anode supported cells, analysis of degradation of fuel cell components and design of experiments and statistical analysis. Thorough characterization of degradation and materials interactions was carried out using the facilities at University of Trento.

Afterwards, she went to IK4-Ikerlan and continued her research in the following subjects: Implementation of planar fuel cell experimental set up (Technology transfer from SOFCPower), standardisation of testing protocols amongst Institutes and the development of a new generation of tubular metal supported cell technology which must be highlighted in this period.

ACKNOWLEDGMENTS

I would like to begin by thanking Dr. Lide Rodriguez, Dr. Massimo Bertoldi and Dr. Stefano Modena, for giving me the opportunity of working in the SOFC field in collaboration between SOFCpower and IK4-Ikerlan, during these four years. I would also like to acknowledge prof. Vincenzo M. Sglavo for supporting my research activity within the University of Trento and Dr. Jan van Herle for his valuable contribution in the experimental design in the first stage of this work.

I would like to thank SOFCpower for allocating test benches and producing specific cells for my experiments, Nextech Materials for providing me with coated interconnect meshes for stability tests, CIC Energigune for the access to SEM utilities and Joost van Duijn and Rocio Ruiz Bustos, in UCLM, for diffraction measurements.

Nei primi due anni a Trento ho incontrato tanta gente all'Università ma anche in azienda, a Mezzolombardo. Con il mio fresco diploma in Fisica Teorica, conoscevo solo la matita e le equazioni ed ero una principiante rispetto alle scienze sperimentali. Infatti, ero un pò disorientata in questo nuovo paese fra le montagne.

Non posso dimenticare i colleghi del laboratorio di Ceramurgia, che mi hanno aiutato con pazienza e mi hanno fatto sentire come a casa. Nel primo anno Marco, Aylin, Anna, Vincenzo, Francesca e Marzio. Nel secondo anno Tatiana, Alessandro ed Elisa. E sempre Lorenzo alle ore più imprevedibili. Da voi ho vissuto tanti momenti belli in laboratorio, ma anche fuori, scoprendo il Trentino e il teroldego.

In Sofcpower ho imparato di giorno in giorno come funziona un' azienda ma anche come sono i trentini. Adesso che ci penso, non tanto differenti dai baschi. Grazie a Stefano per guidare il mio lavoro, ma anche a Lorenzo, Michele e gli altri. Da tutti ho imparato qualcosa. Per ultima, non posso dimenticare Zora. Non potrei immaginare SOFCpower senza di te.

Me gustaría dar las gracias a todos los compañeros de la Unidad de Energía de IK4-Ikerlan, por estos años en los que, entre idas y venidas, he trabajado a vuestro lado. Siempre me he sentido respaldada y vuestra ayuda ha sido incondicional. No sé cómo será el resto de empresas, pero trabajar en Ikerlan ha sido un placer.

Me gustaría agradecer a los compañeros del proyecto de pilas su ayuda. Igor y Lide al frente y Nuria, Laida, Mikel y Mario con quienes he compartido el día a día en

el laboratorio. El asunto de los borboteadores dejó claro que venía con mucho que aprender. Me enseñasteis todo desde cero.

Me gustaría también recordar a mis compañeros de desayunos, risas y confidencias, Genelva, Mikel, Laida y Ruth. Sin vosotros, me hubiera costado mucho más levantarme por las mañanas. A Madalena, le agradezco enormemente su ayuda con el coche. En este último periodo, vuestro apoyo ha sido esencial.

Mis más sinceros agradecimientos a Lide y Laida, por su especial implicación en mi tesis. A Lide, por dirigirla en todos los aspectos, por sus visión, espíritu crítico y por corregirla con puntos y comas. Laida, lan esperimentalean zehar zure laguntza eta aholkuak ezinbestekoak izan dira neretzat. Neurri handi batean, zuk ere gidatu dezu lan hau. Nadie sabe mejor que vosotras de qué hablan estas páginas.

Azkenik, tesia familiari dedikatu diodanez, lagunei eskerrak eman nahiko nizkieke. A Caterina y las Julias, con quien empecé a volar en Grenoble. A Monica, que apareció en mi vida en Trento y espero que nunca se marche. Jara eta Leireri, lau urte hauetan zehar bizitako abentura guztietan nere alboan egon zeratelako. Mila esker Trentora ni salbatzera etortzeagatik. Unairi, Gasteizen berriz ere nere bizitzan agertzeagatik. Koadrilakoei, beti hor egoteagatik. Zuen maitasunak eman dit beti aurrera egiteko indarra.